Dynamic analysis of mechanical systems with Coulomb friction

Luca Marino

Lincoln College

University of Oxford

A thesis submitted for the degree of

Doctor of Philosophy

Michaelmas 2021

Preface

This thesis is submitted for the degree of Doctor of Philosophy in the University of Oxford. The research presented in this work was carried out by the author between January 2018 and December 2021 in the Department of Engineering Science, under the supervision of Professor Alice Cicirello and Professor David A. Hills.

To the best of my knowledge and belief, the work described in this dissertation is original, except where due reference has been made, acknowledging the work of others. Nothing has been included that is the outcome of work done in collaboration. No part of this dissertation, or any similar to it, has been or is currently being submitted for any degree at this or any other university. This thesis is less than 250 pages in length.

The work presented herein has been partially published in the following journal papers:

- Marino, L., Cicirello, A., Hills, D.A.: Displacement transmissibility of a Coulomb friction oscillator subject to joined base-wall motion. Nonlinear Dyn. **98**, 2595-2612 (2019)
- Marino, L., Cicirello, A.: Experimental investigation of a single-degree-of-freedom system with Coulomb friction. Nonlinear Dyn. **99**, 1781-1799 (2020)
- Marino, L., Cicirello, A.: Multi-degree-of-freedom systems with a Coulomb friction contact: analytical boundaries of motion regimes. Nonlinear Dyn. **104**, 35–63 (2021)
- Marino, L., Cicirello, A.: Dynamic response of multi-degree-of-freedom systems with a Coulomb friction contact under harmonic excitation. Nonlinear Dyn. **106**, 1675–1709 (2021)

Luca Marino
Oxford, UK
December 15^{th}, 2021

To my father's memory

Acknowledgements

First and foremost, I would like to express my gratitude towards my supervisor Professor Alice Cicirello for her endless support and guidance during these years. Without her suggestions, constant motivation and our - almost daily - discussions, this thesis would have not been possible. I would like to thank my supervisor Professor David A. Hills for the helpful discussions and advices. To both my supervisors, my deepest appreciation for giving me the unique opportunity to carry out my doctoral studies at the University of Oxford and for the freedom they granted me in pursuing my research ideas.

I am very grateful to EPSRC and Rolls Royce for funding my DPhil project through the industrial CASE postgraduate scholarship 16000036. Their generous support also allowed me to attend several training courses and conferences, improving my research skills and knowledge and discussing my findings with the leading scientists in the field.

I am deeply thankful to my friends and colleagues Alessandro Cabboi, Andrea Patanè, Andrea Piccione, Enrico Salvati, Felipe Igea, Filippo Giunta, Luca Laurenti and Michele Tricarico for proofreading the chapters of this thesis and for their valuable suggestions.

At the end of this four years journey, I would like to thank all those who contributed to make it a memorable experience, despite all the difficulties encountered. Thanks to Andreea, Bruno, Felipe, Filippo and all the other current and former members of the Dynamics, Vibration and Uncertainty laboratory, not only for the interesting scientific discussions, but also for the numerous happy moments we have shared in the lab. Thanks to Bruno, Filippo and Sergio for their friendship and support during the earliest days of my Oxford life. Special thanks go to my friends Laurenti, Patanè, Piccione, Salvati and Tricarico, who have been my Oxford family during these years. Their support has been essential, especially during the hardest days of the pandemic.

Last but not least, my final thanks go to my family. Thanks to my mother and to my brother Claudio for their unconditioned support and encouragement throughout all these years. And thanks to my father, your lessons and your belief in my potential kept motivating me towards the completion of this work, which I am sure you would be proud of.

Abstract

Friction damping is commonly used in engineering structures for dissipating energy and reducing vibrations. However, friction can also introduce undesired effects such as the periodic or permanent sticking between the contacting parts or the magnification of the response amplitude. These behaviours need to be accounted for during the early design stages, where these structures are modelled as discrete single (SDOF) or multi-degree-of-freedom (MDOF) systems. However, even when Coulomb friction and simplified mechanical models are considered, the dynamic analysis of these systems is complicated by the nonlinearity of the friction forces.

In this thesis, the dynamic response of different lumped mechanical systems including a Coulomb friction contact and subjected to harmonic excitation is investigated analytically, numerically and experimentally, aiming at establishing how their response features and motion regimes are affected by the presence of multiple DOFs and by the motion of the contacting components.

Exact solutions are derived for the continuous steady-state response of these systems and validated numerically. These solutions enable the exploration of the Coulomb friction effects on response features such as resonant, low- and high-frequency behaviours, the presence of invariant points and inversions of the transmissibility curves. Moreover, the analytical boundaries among continuous, stick-slip and permanent sticking regimes are represented in a two-dimensional parameter space, allowing for a quick prediction of the motion regimes during the design stage.

An experimental investigation of the response of SDOF and MDOF systems is carried out by using a base-excited shear frame setup with a brass-to-steel contact, leading to the validation of the theoretical results and the evaluation of different metrics for measuring friction from the dynamic response.

The main findings of this thesis are that: (1) MDOF systems exhibit significantly different behaviours depending on whether the friction and the harmonic forces are applied to the same or different masses; (2) the friction generated by a contact between oscillating components can magnify the response of the system at high frequencies; (3) Coulomb friction model is generally suitable for describing the dynamic behaviour of structures with a metal-to-metal contact.

Contents

List of Figures

List of Abbreviations

AFT . . . . . Alternating frequency-time domain.

DOF . . . . . Degree of freedom.

FE . . . . . Finite element

HB . . . . . Harmonic balance.

IHB . . . . . Incremental harmonic balance.

MHB . . . . . Multi-harmonic balance.

MDOF . . . . Multi degree of freedom.

SDOF . . . . . Single degree of freedom.

List of Symbols

$\dot{\square}$	Derivative with respect to time
$\square'$	Derivative with respect to the non-dimensional time τ
$\square^*$	Quantity referred to permanent sticking conditions
$\hat{\square}$	Modal quantity
$\square_A$	Quantity referred to the lower of two masses in contact
$\square_B$	Quantity referred to the upper of two masses in contact
$\square_i$	Quantity referred to the generic i-th vibrating mode
$\square_j$	Quantity referred to the mass in contact
$\square_k$	Quantity referred to the generic k-th degree of freedom
$\square_l$	Quantity referred to the excited mass
c	Viscous damping coefficient
$\mathbf{C}$	Viscous damping matrix
f	Frequency of the harmonic excitation
$\mathbf{f}$	Friction force vector
f_n	Natural frequency
F	Amplitude of the kinetic friction force
F_f	Friction force
F_n	Normal force in a contact
F_s	Static friction force
g	Stribeck function in LuGre friction model
g_i	Second damping function of the i-th vibrating mode
G	Second damping function in systems with mixed damping
J	Cost function
k	Stiffness
$\mathbf{K}$	Stiffness matrix

m . . . . . Mass

$\mathbf{M}$ . . . . . Mass matrix

N . . . . . Number of degrees of freedom

N_{cyc} . . . . . Number of excitation periods

P . . . . . Amplitude of the harmonic force

$\mathbf{p}$ . . . . . Harmonic force vector

r . . . . . Frequency ratio of a SDOF system

r_1 . . . . . Frequency ratio of a MDOF system

$r_{n,i}$ . . . . . Frequency ratio of the i-th resonant peak

R_i . . . . . i-th modal frequency ratio

s_i . . . . . Function defined in Eq.(5.56)

S . . . . . Function defined in Eq.(2.27)

t . . . . . Time

u_i . . . . . Damping function of the i-th vibrating mode

U . . . . . Damping function in Coulomb damped systems

u_{di} . . . . . First damping function of the i-th vibrating mode

U_d . . . . . First damping function in systems with mixed damping

v_r . . . . . Relative velocity in a contact

v_s . . . . . Stribeck velocity

v_i . . . . . Response function of the i-th vibrating mode

V . . . . . Response function

v_{di} . . . . . Complex response function of the i-th vibrating mode

V_d . . . . . Complex response function

x . . . . . Displacement of the mass m

x_c . . . . . Displacement of the centroid

$\mathbf{x}$ . . . . . Displacement vector

X . . . . . Amplitude of the displacement of the mass m

$\overline{X}_{\mathrm{fft}}$ . . . . . Frequency-based displacement transmissibility

y . . . . . Base displacement

Y . . . . . Amplitude of the base displacement

z . . . . . Internal state variable in rate-and-state friction models

z . . . . . Relative displacement in a contact

Z . . . . . Amplitude of the relative displacement in a contact

β . . . . . Friction ratio

β_{lim} . . . . . Friction ratio at the boundary between continuous and stick-slip regimes

β^*_{lim} . . . . . Friction ratio at the boundary between sliding and permanent sticking regimes

$\beta_{n,i}$ . . . . . Boundary friction ratio at $r_1 = r_{n,i}$

β_0 . . . . . Boundary friction ratio at $r_1 = 0$

β_∞ . . . . . Boundary friction ratio at $r_1 \to \infty$

γ . . . . . Mass ratio

γ_{AB} . . . . . Ratio between two masses in contact

δ . . . . . Kronecker delta

ζ . . . . . Viscous damping ratio

η . . . . . Modal coordinate

$\boldsymbol{\eta}$ . . . . . Vector of the modal coordinates

κ . . . . . Stiffness ratio

λ . . . . . Shape factor in LuGre friction model

μ . . . . . Ratio between the static and the kinetic friction forces

μ_d . . . . . Kinetic friction coefficient

μ_s . . . . . Static friction coefficient

σ_0 . . . . . Stiffness of the bristle in rate-and-state friction models

σ_1 . . . . . Damping of the bristle in LuGre friction model

σ_2 . . . . . Viscous damping coefficient in LuGre friction model

Σ . . . . . Amplitude of the sum of the non-inertial forces acting in a contact

τ . . . . . Non-dimensional time

ϕ . . . . . Phase angle between the maxima of excitation and response

ϕ_{fft} . . . . . Frequency-based phase angle

ϕ_z . . . . . Phase angle between the maxima of excitation and relative displacement

ψ_{ki} . . . . . k-th component of the i-th mode shape

$\boldsymbol{\psi}$ . . . . . Mode shape

$\boldsymbol{\Psi}$ . . . . . Modal matrix

ω . . . . . Angular frequency of the harmonic excitation

ω_i . . . . . i-th angular natural frequency

Ω_i . . . . . i-th non-dimensional natural frequency

Some men see things as they are, and say "Why?". I dream of things that never were, and say "Why not?"

— George Bernard Shaw

1 Introduction

Contents

1.1 Friction damping in engineering structures

The development of a fundamental understanding of the role played by friction damping in engineering structures is nowadays one of the most pressing challenges in structural dynamics. In fact, friction joints and interfaces are found in a wide variety of engineering systems, ranging from aerospace vehicles to civil buildings, turbomachines and robotic devices.

Friction can be defined as the force resisting the motion between solid bodies in contact. To distinguish it from the forces generated between fluid layers or in lubricated contacts, this force is also often referred to as dry friction. When subject to dynamic loadings, the friction generated by the relative motion between

the structural components in contact can have detrimental effects. Phenomena such as noise, excessive wear and energy loss can reduce the performance and the efficiency of jointed structures [1]. More importantly, friction can also lead to serious consequences such as structural damage and component failures. This can occur, for instance, in the dovetail joints found in the roots of the gas-turbines blades, where even small amounts of relative motion between the blade and the central hub can lead to cracking over time due to fretting fatigue [2]. However, friction can also enhance the performance of vibrating structures, if used for purposes such as energy dissipation, vibration control and isolation [3, 4]. Friction dampers, devices that use dry friction to dissipate energy, are often introduced in engineering structures to limit their vibratory response. These dampers present many advantageous properties, such as the ability to perform in harsh or inaccessible environments, to operate simultaneously along different directions and to adapt to a wide excitation bandwidth without tuning [5]. For this reason, their use is common in several engineering structures, particularly in large civil buildings, where they are used for achieving seismic isolation [6, 7], and in gas-turbines, where they are capable of providing energy dissipation despite the extreme temperatures encountered [3, 8]. Further applications of friction dampers can be found in suspension systems [9, 10], robotic devices [11, 12], energy harvesters [14], airplane taxing systems [15] and satellites [16]. Finally, structures with a large amount of friction joints, such as bolted frames and truss structures, often rely on friction as the major source of damping without requiring the introduction of ad-hoc dampers [3, 5].

Despite the widespread presence of friction in engineering structures, the current understanding of its effect on the dynamic behaviour of mechanical systems is still limited. The difficulties surrounding the analysis of these systems are mostly related to the following issues.

- *The lack of a universal and predictive friction model.* The development of such a model represents one of the main goals of the research community in this field. However, this research is complicated by the insufficient knowledge

of the multiscale physics and of the several physical parameters governing the friction process [2].

- *The nonlinear nature of the friction forces.* Even the simplest models used for describing the friction forces, including Coulomb's law, are highly nonlinear since they lead to a discontinuous or nonsmooth behaviour in the dynamic response which does not allow the use of perturbation methods and linearisation techniques in proximity of an equilibrium condition [3]. In addition, the performance and accuracy of numerical approaches using time integration are also hindered by the nonsmoothness of the friction forces [3].

- *The unrepeatable nature of the friction phenomenon.* The properties of a friction contact are known to change depending on several external factors, such as temperature, condensation and humidity. Moreover, friction itself alters the properties of the surfaces in contact over time, due to effects such as wear and debris formation [2]. As a result, experimental studies often offer poor reproducibility and the performance of friction contacts differ between experimental and operational conditions [3].

All these aspects make it difficult to achieve a reliable prediction of the performance of friction damped systems, limiting the exploration of innovative and efficient engineering design solutions involving friction dampers. Furthermore, in large scale systems, including gas-turbine engines and civil buildings, characterising the effect of friction contacts on the dynamic response of the structure is also complicated by the presence of other nonlinearities (localised or distributed [17, 18]), complex geometries and fluctuating loads [3]. Therefore, during the earliest stages of the mechanical design, it is common to represent these structures as discrete mass-spring systems, aiming to capture some of the fundamental characteristics of their dynamic behaviour [19], produce analytical results or perform numerical simulations with a reduced computational cost [20]. In particular, analytical solutions can speed-up the exploration of suitable designs, avoiding the use of more complicated and computationally expensive models while carrying out parameter investigations,

optimisations and statistical model updating. However, even when Coulomb friction and simplified mass-spring models are considered, deriving analytical solutions for the response of these systems is a complex task due to the nonlinearity of the problem. For this reason, the available solutions in the literature are mostly limited to the case of a harmonically excited single-degree-of-freedom (SDOF) system where friction is generated in the contact between the mass and a ground-fixed wall and modelled according to Coulomb's law (see, e.g., [21, 22, 23]). In this case, the availability of closed-form solutions allowed for the development of a general understanding of how friction can affect the dynamic response, introducing different motion regimes or altering features such as the behaviour of the system at resonance. Nevertheless, this simple model cannot account, even at a high level, for the behaviour of structures where a contact occurs between two vibrating components, such as in the dovetail joints connecting gas-turbines blades to the central hub or in the friction dampers located between two different floors of a building. Moreover, a single DOF is often not enough to achieve even a very simplified model of a structure, e.g. in assemblies with multiple components or when more vibrating modes need to be taken into account; in these cases, multi-degree-of-freedom (MDOF) models are required [24]. Understanding how the motion regimes and the features of the dynamic response of friction damped systems evolve depending on the physical parameters of the problem, when a contact between oscillating parts or multiple DOFs are involved, is the focus of this thesis.

1.2 Research challenges

In this thesis, the response of SDOF and MDOF models is firstly investigated: (i) assuming that a single friction contact is the only source of damping in the system; (ii) using Coulomb's law for modelling dry friction in the contact; (iii) considering a harmonic loading as source of excitation. These assumptions enable the derivation of analytical solutions and the development of numerical approaches which can be used to explore the motion regimes and the response features of friction damped systems. However, in order to determine if these assumptions are acceptable, it is essential to

verify whether the dynamic behaviour described by analytical and numerical results can be observed in a real structure, at least in experimental conditions. The inherent challenge is the development of an experimental procedure which allows a systematic observation of the damping effects due to the presence of a Coulomb friction contact in a vibrating structure. A further step towards a more comprehensive description of the behaviour of engineering structures with friction joints consists in overcoming the assumption (i) and including other forms of damping in the mechanical models, aiming to understand if they can alter the dynamic behaviour generated by Coulomb friction. All these research challenges are briefly discussed in what follows.

1.2.1 Motion regimes

One of the most relevant consequences of the nonlinearity of friction damped systems is that their dynamic response is not always continuous. In fact, periodic or permanent sticking can be observed in the relative motion between the two surfaces of a friction joint.

The alternance of sliding and sticking phases in the response, known as *stick-slip* motion, is typically an undesired phenomenon in engineering applications, since it can lead to consequences such a noise, wear and excessive periodic stresses on the mechanical components, increasing the risk of fatigue failure [4, 25].

The occurrence of permanent sticking in a friction contact is instead associated to two main effects: (i) a strong reduction of the damping levels in the structure, due to the absence of the energy dissipation generated by the macroscopic sliding between the contacting surfaces [5]; (ii) a change in the dynamic properties of the system, including different resonant frequencies and mode-shapes [26]. It is worth underlying that permanent sticking, unlike stick-slip, does not always represent an undesired effect. For instance, in gas-turbines it is desirable that no relative motion occurs in joints located more closely to the rotating axis, such as dovetail and fir-tree roots, to avoid excessive wear and fretting fatigue. Conversely, the occurrence of permanent sticking in the underplatform dampers and, more generally, in the joints located in proximity of the outer shell, would prevent them from

dissipating energy and reducing vibration [2]. In civil structures, relative motion in the friction dampers is only activated where they receive an amount of excitation such to overcome a certain threshold, known as slip load [27].

The ability to predict if the response of a mechanical systems will be characterised by a continuous, stick-slip or permanent sticking regime is of paramount importance since the early design stages, where different solutions can be explored to obtain the desired structural behaviour. However, little information is currently available on how different motion regimes can occur depending on parameters such as the amplitudes of the excitation and of the friction force and designers need to rely on expensive numerical computations when carrying out parameter investigations.

1.2.2 Features of the dynamic response

Friction dampers are usually introduced in engineering structures to reduce vibration amplitudes and, in particular, to avoid excessive stress levels when resonances occur [8]. Therefore, it is essential to characterise the effect of Coulomb damping on the resonant behaviour of mechanical systems and, more in general, on their response amplitude. In the SDOF case, the analytical solutions available in the literature [21] show that Coulomb friction is only effective at reducing the amplitude of resonant peaks either when stick-slip occurs or when viscous damping is also included in the model. These behaviours are also expected in MDOF systems. However, the current knowledge of the resonant behaviour of these systems is still limited due to the absence of analytical solutions.

Although the reduction or suppression of the resonant peaks is one of the main purposes of friction dampers, an adequate attenuation of the vibration may also be required at non-resonant frequencies when Coulomb friction is used for isolation purposes [28]. However, in MDOF systems, it is known that the occurrence of permanent sticking in a friction contact can lead to a different dynamic configuration of the system, usually referred as stuck mode or configuration, and to the onset of new resonant peaks [26]. Moreover, previous studies on SDOF systems with a contact between the mass and a vibrating wall [28] suggest that Coulomb damping

might lead to a magnification of the response amplitude at high frequencies, similarly to that observed in base-excited SDOF systems with viscous damping (see, e.g., [29]). Therefore, further investigation is needed to understand how the response amplitude of mechanical systems is affected by the Coulomb friction generated in a contact between two vibrating components.

1.2.3 Experimental investigation

The experimental investigations carried out in this thesis have the primary scope of validating theoretical results based on the Coulomb friction model. This validation is not only required for assessing whether the assumptions introduced in the current studies can be acceptable in experimental conditions. In fact, establishing a link between theoretical and experimental results is also important for identifying friction damping during dynamic testing.

The challenges of this experimental investigation are mainly related to the necessity of isolating the Coulomb damping effects on the dynamic response. This requires, in the first place, the limitation of those effects, such as wear and debris formation, which are not accounted by Coulomb's law. In fact, these effects can alter the surface properties during and between experimental tests. Secondly, it is also needed to determine which metrics are better-suited for measuring friction from the dynamic response of the test rig.

While previous experiments mostly focused on the investigation of the resonant behaviour [21, 30] and of the stick-slip responses [31] of SDOF systems with a fixed wall, to the best of the author's knowledge, vibrating walls or multiple DOFs have not been investigated experimentally. These cases will be addressed in this thesis.

1.3 Aim and scope of the thesis

The work presented in this thesis aims at advancing the fundamental research on friction damping in vibrating systems by improving the current understanding of how dry friction can affect their dynamic response: (1) altering features such

as the resonant, the low- and the high-frequency behaviours; (2) introducing different motion regimes.

To achieve this purpose, a series of case-studies is investigated using analytical, numerical and experimental approaches and assuming the simplest forms for the mechanical model, the friction model and the external dynamic loading. Specifically, in these case-studies, SDOF and MDOF systems with a Coulomb friction contact are subjected to a harmonic excitation, either applied to one of the masses of the system or through a base motion. Different configurations are explored for the contact, which can occur between: (i) a mass and a fixed wall; (ii) a mass and wall vibrating jointly to the harmonically excited base; (iii) two different masses.

The following questions arise from the research challenges introduced in the previous section:

1. Which different motion regimes (continuous, stick-slip, permanent sticking) occur depending on the main parameters of the system, of the dynamic loading and of the friction contact.

2. How quantities such as the features of dynamic response would differ in the presence of multiple DOFs, of a contact occurring between two oscillating parts or when different locations are considered for the excitation and friction sources.

3. How the dynamic behaviour of discrete mechanical systems with a Coulomb friction contact can be reproduced in experimental conditions and which metrics should be considered for evaluating Coulomb damping from the response signatures of a structure.

4. How the inclusion of modal damping in the mechanical models can alter the damping effects due to Coulomb friction.

These research questions have been addressed in this thesis, leading to:

1. The formulation of closed-form expressions for the boundaries among continuous, stick-slip and permanent sticking motion regimes and their representation in a two-dimensional parameter space for varying non-dimensional exciting frequencies and friction forces. This representation provides an useful tool for predicting the occurrence of periodic or permanent sticking in the response of the system since the early stages of the design.

2. The derivation of exact solutions for the continuous steady-state response of harmonically excited mechanical systems with a Coulomb friction contact, holding for: (a) any number of DOFs; (b) any of the contact configurations specified above; (c) any location of the harmonic loading and of the friction force, and enabling the analytical investigation of their response features. Numerical approaches based on time integration are also developed to validate these results and evaluating stick-slip responses.

3. The development of an experimental framework and of a procedure for validating the analytical and the numerical results obtained for the displacement transmissibilities and the phase angles of SDOF and MDOF systems with Coulomb friction and investigating the behaviour of such systems.

4. The extension of the above solutions for the continuous response of systems with combined modal and Coulomb damping, the investigation of their response features and, in particular, of their resonant behaviour.

1.4 Outline of the thesis

This thesis is composed of 8 chapters. A general background on friction models and on the existing analytical, numerical and experimental techniques developed for dealing with friction damped systems is provided in Chapter 2. Chapter 3 presents an investigation of the dynamic response of SDOF systems with a friction contact between the mass and a vibrating wall. In Chapter 4, an experimental investigation is carried out for SDOF systems with either a fixed or an oscillating wall. An exact

solution for the continuous response of MDOF systems with a Coulomb friction contact is derived in Chapter 5. In Chapter 6, this analytical solution, along with numerical and experimental approaches, is used for investigating the features of the response of MDOF systems. Closed-form solutions are also derived for systems with combined modal and Coulomb damping and used for investigating their response features in Chapter 7. Finally, Chapter 8 presents the conclusions of the work carried out in this thesis and the future research directions.

Trying to divide systems into linear and nonlinear, is like trying to divide the world into bananas and non-bananas.

— R. M. Rosenberg

2

Review of modelling and solution techniques for friction damped systems

Contents

2.1 Introduction

The aim of this chapter is to review the methodologies used for modelling and investigating the behaviour of mechanical systems with friction damping. The chapter is structured as follows. Section 2.2 presents an overview of the main friction models. Section 2.3 deals with the nonlinear behaviour introduced by

friction in the mechanical systems, reviewing the most common analytical, semi-analytical and numerical approaches used for exploring their dynamic response. Section 2.4 focuses on the experimental investigation of the dynamic behaviour of vibrating systems with friction damping. Finally, in Section 2.5, Den Hartog's solution for SDOF systems with a Coulomb friction contact between the mass and a fixed wall [21] is described in detail and an overview of the most significant extensions of his approach to different lumped mechanical models is provided.

2.2 Friction models

The development of an accurate model for describing the friction forces generated in the contact between two bodies is one of the most compelling challenges in the study of mechanical systems. As a real-life phenomenon, friction has been a topic of scientific and technological attention since ancient times [25]. The earliest characterisation of the friction force is attributed to Leonardo da Vinci [32], who suggested that the amplitude of the friction force F_f might evaluated as:

$$F_f = 0.25F_n \tag{2.1}$$

where F_n is the normal force acting between the surfaces in contact, while its direction would always oppose the motion. This model was later generalised by Amontons and Coulomb [33], whose work resulted in the famous law of proportionality between the friction force and the normal force amplitudes:

$$F_f = \mu_d F_n \tag{2.2}$$

where μ_d is the friction coefficient and, differently from the constant value reported in Da Vinci's law, depends on the material of the surfaces in contact. A further step towards a more comprehensive understanding of the friction phenomenon was the introduction of the concept of stiction or static friction, firstly proposed by Euler [34] and in Segner [35]. While Eq.(2.2) refers to the force generated by the sliding between two surfaces in contact and can be referred to as kinetic friction force, the static friction force is the force required to initiate a motion from rest

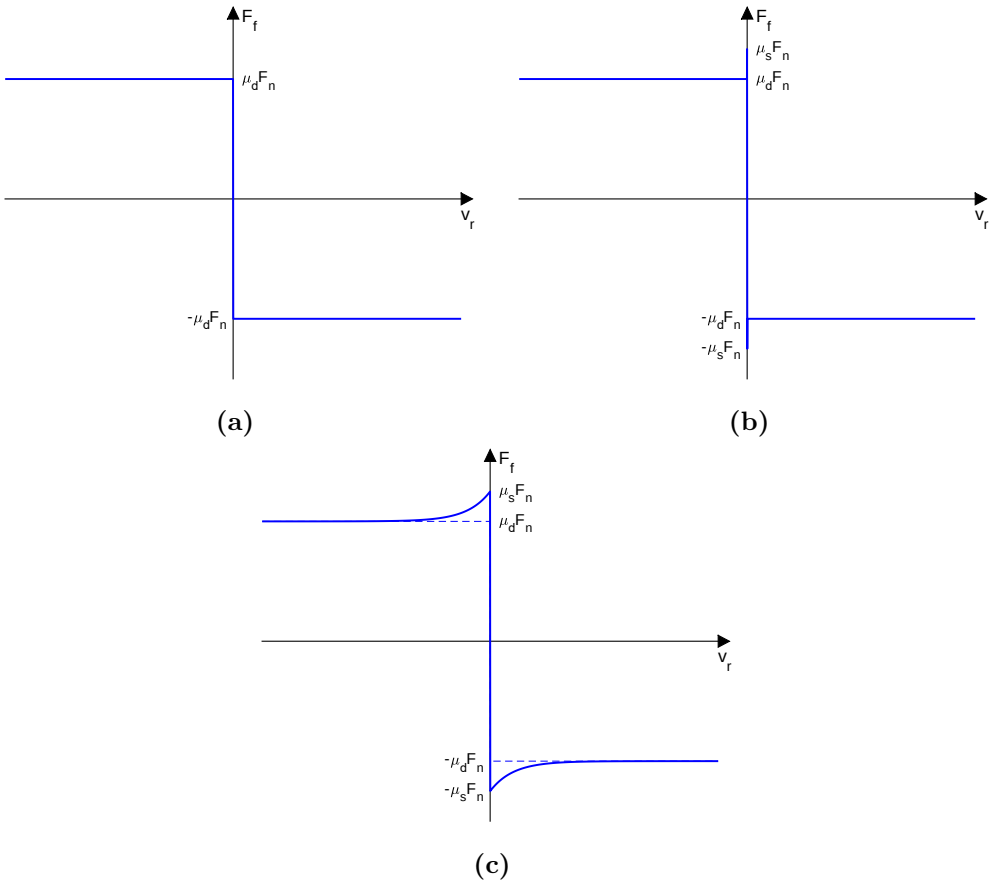

Figure 2.1: Friction force dependence on the relative velocity between the bodies in contact according to Coulomb model (**a**), Coulomb model with stiction (**b**) and Stribeck model (**c**).

and it is generally greater than the kinetic force [36]. Therefore, an appropriate mathematical formulation of the Coulomb friction model can be given as:

$$F_f = \begin{cases} \mu_d F_n & \text{if } \mathrm{v}_r < 0 \\ [-\mu_s F_n,\ \mu_s F_n] & \text{if } \mathrm{v}_r = 0 \\ -\mu_d F_n & \text{if } \mathrm{v}_r > 0 \end{cases} \tag{2.3}$$

where μ_s is defined as static friction coefficient and v_r is the relative velocity between the bodies in contact. The force-velocity relations expressed in Eqs.(2.2) and (2.3) are represented in Figs.2.1a and b, respectively.

In Coulomb model, the friction coefficient is completely independent of the sliding speed. However, according to Awrejcewicz [37], this statement is only acceptable when a contact between metals and low or medium relative velocities are considered. A first step towards a better characterisation of the dependence of

the friction force on v_r is due to the experiments performed by Thurston, Martens and Stribeck [38], which revealed a rapid decrease of the friction force amplitude at low relative velocities, followed by a slower decrease at higher values of v_r. This phenomenon was formalised in the so-called Stribeck's law [39, 40]:

$$F_f = -\left[\mu_d - (\mu_s - \mu_d)e^{-\left|\frac{v_r}{v_s}\right|}\right] F_n \mathrm{sgn}(v_r) \tag{2.4}$$

where v_s is a further parameter of the model, defined as Stribeck velocity. Stribeck's law allows for a smooth transition between the static and the kinetic value of the friction forces, as shown in Fig.2.1c; for this reason, it is often provided as an alternative to the Coulomb model in commercial softwares for finite element modelling [41]. Several friction models proposing different laws for the dependency of the friction force on the sliding velocity, including smooth Coulomb models using different types of smoothening functions to eliminate the discontinuity occurring at $v_r = 0$ [42, 43, 44, 45], velocity-based models such as that presented in [46], and the Karnopp friction model [47].

In all the above models, the friction force only depends on the sliding velocity, implying that any variations in v_r would be followed by an instantaneous change in the value of F_f. However, it is well-known that in reality changes in the friction force follow those in the relative velocity with some delay [48], leading to the so-called frictional memory. To account for this hysteresis effect, rate-and-state models were developed in the last decades. In these models, the friction force is not only a function of the sliding velocity, but also of one or more state variables [49].

The simplest rate-and-state model was formulated by Dahl [50, 51]. Dahl model can be seen as Coulomb friction model with a lag in the change of friction force during the switching of the direction of motion [41]. A simple graphical description of this model is achieved in Fig.2.2a, according to the bristle analogy: under the action of an applied load, the bristle will initially deform elastically and return to its initial position after the load is removed; however, if the load exceeds its elastic resistance, the entire bristle will move. Thus, the Dahl friction force can be expressed as:

$$F_f = -\sigma_0 z \tag{2.5}$$

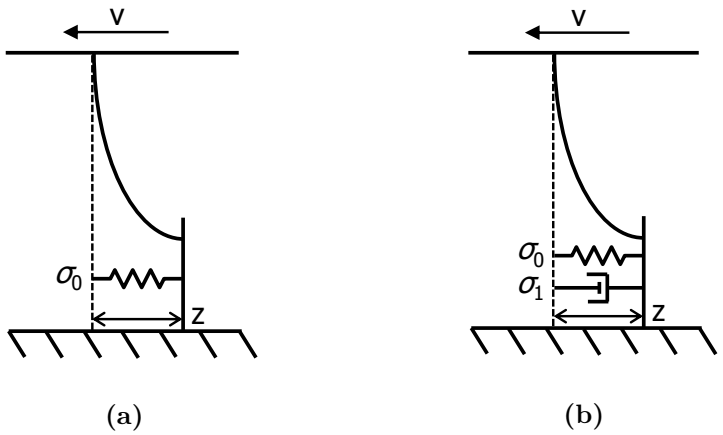

Figure 2.2: The bristle analogy for the Dahl (**a**) and the LuGre (**b**) friction models.

where σ_0 is the stiffness of the bristle and z the internal state variable corresponding to the relative displacement. This variable can be obtained from the equation:

$$\dot{\mathrm{z}} = \mathrm{v}_r \left(1 - \frac{\sigma_0 \mathrm{z}}{F} \mathrm{sgn}(\mathrm{v}_r)\right)^{\alpha} \tag{2.6}$$

where F is the amplitude of the kinetic friction force and α a shape factor.

The LuGre model [49, 52] is a modified version of Dahl model which also accounts for the Stribeck effect. In this model, the friction force is expressed as:

$$F_f = \sigma_0 \mathrm{z} + \sigma_1 \dot{\mathrm{z}} + \sigma_2 \mathrm{v}_r \tag{2.7}$$

where, according to the bristle analogy shown in Fig.2.2b, σ_1 is the damping of the bristle, while σ_2 simply represents the viscous damping of the system. Similarly to Dahl model, the state variable can be determined from the equation:

$$\dot{\mathrm{z}} = \mathrm{v}_r \left(1 - \frac{\sigma_0 \mathrm{z}}{\mathrm{g}(\mathrm{v}_r)} \mathrm{sgn}(\mathrm{v}_r)\right) \tag{2.8}$$

where the function:

$$\mathrm{g}(\mathrm{v}_r) = F - (F_s - F) e^{-\left|\frac{\mathrm{v}_r}{\mathrm{v}_s}\right|^{\lambda}} \tag{2.9}$$

allows the introduction of the Stribeck effect in the model. In the above equation, F_s is the static friction force and λ is a shape factor. Thanks to its passivity properties and ability to match experimental data [49], LuGre model is often considered in high-precision control applications [53, 54, 55].

Several rate-and-state models have been proposed over the years, mostly as modified or improved versions of the LuGre model, such as the Bouc-Wen [56, 57], the elastoplastic [58] and the Maxwell-slip [59] models. All these friction models are well-suited for describing specific phenomena and applications, but the goal of developing an universal friction model is still far and perhaps unrealistic [2]. Nonetheless, when it comes to the modelling of the damping effects due to friction, difficulties arise in the dynamic analysis even when the Coulomb model is considered. As specified in Section 1.1, these complications are mostly related to the strong nonlinearity introduced by the friction forces, which leads to the need of resorting to different analytical and numerical techniques from those standardly used for investigating linear systems, as discussed in the following section.

2.3 Solution techniques for friction damped systems

In mathematics and science, a system is referred to as nonlinear when a change in its input does not lead to a proportional change in the output. Nonlinearity is often encountered in engineering structures: according to Worden and Tomlinson, all the real structures are nonlinear to some extent [60]. Typical sources of nonlinearity in structures are the following [17]:

- geometrical nonlinearities are observed when large deformations occur in flexible structures such as beams, plates and shells;
- material nonlinearities are displayed by materials whose constitutive law relating stresses and strains is not linear, such as plastics and foams;
- most types of damping models are nonlinear, including the dissipation occurring in friction joints or internally in the materials due, e.g., to plastic deformations or the magnetostriction effect;

- nonlinearities in the boundary conditions can be due to free surfaces in fluids, vibro-impacts due to loose joints or contacts, clearances or imperfectly bonded elastic bodies.

One of the most characterising features of nonlinear systems is that they do not satisfy the superposition principle. In structural dynamics, this implies that popular methods such as modal analysis and the modal superposition approach cannot be used to determine the natural frequencies, the mode-shapes and the time response of MDOF systems. For this reason, a common approach for dealing with nonlinear problems is the linearisation method. However, while approximating nonlinear systems with linear equation allows the use of the most common and consolidated engineering techniques, linearised systems fail to predict nonlinear phenomena such as jumps, bifurcations, subharmonic, superharmonic and internal resonances, modal interactions and chaos [17, 18]. In addition, strongly nonlinear systems, such as those affected by dry friction, vibro-impact oscillations and certain geometric nonlinearities do not generally admit linearisation [17]. As mentioned in Section 1.1, the strong nonlinearity of friction damped systems is due to the discontinuities and/or nonsmoothness present in most friction laws [3], such as that found at $v_r = 0$ in the Coulomb model, shown in Figs.2.1a-b. Therefore, several analytical and numerical techniques have been explored over the years for investigating the dynamic response of these systems, as reported in what follows.

2.3.1 Exact solution technique

Despite the nonlinearity of the governing equations of friction damped systems, exact analytical solutions can sometimes be derived for their dynamic response under specific assumptions.

The seminal work in this research area was performed by Den Hartog [21, 63] in the earliest 1930s. Den Hartog derived an exact solution for the continuous steady-state response of a harmonically excited SDOF system with a Coulomb friction contact between the mass and a ground-fixed wall, also providing closed-form expressions for the response amplitude and phase and a formulation for the

boundary between continuous and stick-slip motion regimes. Furthermore, Den Hartog extended his solution to deal with stick-slip responses with two-stop per excitation period and to systems with combined viscous and Coulomb damping. Den Hartog's solution is considered a milestone in the field and the majority of the analytical developments proposed in the following decades until today, including those presented in this thesis, are strongly based on his work, which is therefore reported in detail in Section 2.5.1.

The dynamic behaviour of Coulomb friction oscillators with a ground-fixed contact has lately been explored by several authors. Hong and Liu [22] proposed a different procedure for deriving analytically the steady-state response of a base-excited system with Coulomb damping only; although the expression obtained for the displacement transmissibility coincides with that proposed by Den Hartog [21], their method also enables the evaluation of the velocity transmissibility and of its phase angle with respect to the harmonic excitation. Moreover, a different formulation from Den Hartog's is provided for the upper bound of the continuous motion regime. In reference [64], the same authors provided a piecewise analytical solution for stick-slip responses with multiple stops per cycle; multi-stop motions have also been investigated by Papangelo and Ciavarella [65], in the attempt of establishing the link between the low-frequency behaviour described by the dynamic solution and quasi-static approaches, such as that proposed in [66]. Shaw [23] extended Den Hartog's solution to address different static and kinetic friction forces, also accounting for positive and negative viscous damping, which can be viewed as a crude model of destabilizing aerodynamic forces. Furthermore, he carried out a stability analysis of the periodic response of Coulomb friction oscillators. Other relevant works on the stability of the response of these systems can be found in [67, 68, 69]. The analytical solutions provided in [21, 23] also enabled the investigation of features of the dynamic response such as the resonant, the subresonant and the low- and high-frequency behaviours [69, 70]. Due to their piecewise-smooth nature, Coulomb friction oscillators belong to the class of the so-called Filippov-type dynamical systems [71] and several authors (see, e.g., [72, 73])

investigated their sliding bifurcations, typical of these systems, using analytical and numerical techniques. Other mathematical approaches to the study of friction damped systems are based on the reformulation of the frictional problem as a linear complementarity problem [74] or the application of the theory of maximal monotone operators [75]. Finally, during the last decade, fundamental research on SDOF systems with dry friction has mostly focused on the research of asymmetric and chaotic solutions [76, 77], the introduction of more complex friction models in the dynamic analysis [77, 78] and the investigation of the energy dissipation in friction damped systems [79, 80].

While most analytical developments on friction damped systems focus on the case of a SDOF system with a fixed wall, some authors also investigated different contact configurations and systems with more DOFs. Levitan [28] obtained a monoharmonic approximation of the continuous response of a SDOF system where the wall in contact with the mass oscillates jointly to the base. Hundal [81] extended Den Hartog's solution to address the continuous and the two-stop responses of a base-excited system with combined viscous and Coulomb damping. Yeh [82] also extended Den Hartog's approach to deal with 2DOF systems with a contact between the lower mass and a fixed wall. More recently, Pascal investigated the dynamic behaviour of 2DOF systems with one [83, 84] or both masses [85] in contact with a belt moving at a constant velocity.

Analytical solutions offer several advantages over other techniques. In fact, they can be used for performing dynamic analyses with a reduced computational cost and, even more importantly, they are essential for the development of a fundamental understanding of the friction damping effects. Nonetheless, their availability is currently limited to harmonically excited SDOF and 2DOF systems with a Coulomb friction contact. Therefore, semi-analytical and numerical approaches must be used when dealing with more complicated systems.

2.3.2 Semi-analytical methods

One of the most popular techniques for solving systems with friction damping is the harmonic balance (HB) method [86]. This method can be used to obtain approximated expressions for the amplitude and the phase of the frequency response of mechanical systems subjected to harmonic excitation in steady-state conditions; therefore, it is widely used when dealing with rotating systems such as bladed-disks [5].

In the simplest implementation of the HB method, also referred to as first-order HB [3], it is assumed that the steady-state response of a harmonically excited system is also harmonic and with the same frequency as that of excitation, while the response amplitude and phase are obtained by solving a set of nonlinear algebraic equations, which are written by grouping the harmonic coefficients [60, 87]. This approach has been used by some authors for determining the response amplitude of friction damped systems of moderate complexity. In particular, Griffin and Sinha [88, 89] investigated the base-excited SDOF system with a flexible damper, obtained as the series of a spring and Coulomb element. This model was first introduced by Griffin in [8] for representing a blade-to-ground underplatform damper; the combination of the spring and the Coulomb element is sometimes referred to as hysteretic spring friction model [3] and its use is common in the turbomachinery field. Other authors used the first-order HB method to investigate the behaviour of continuous multi-modal systems connected to a SDOF friction damper [90, 91, 92].

Although first-order HB offers a general overview of the dynamic behaviour of a friction damped system, its use can lead to significant errors, particularly at low excitation frequencies [87] and for high ratios between the amplitudes of the friction and the exciting forces [3]. Therefore, many authors (see, e.g., [93, 94, 95]) describe the excitation and the steady-state response of the system as a sum of sinusoids, expressing them in terms of Fourier series [87]. This approach is usually referred to as multi-harmonic balance (MHB) method and leads to a better agreement with the results obtained via numerical integration [87], since more harmonics are taken into account. Nonetheless, including several harmonics in the response can lead to the

necessity of solving complicated systems of nonlinear algebraic equations, therefore requiring the use of further numerical approaches. An extension of the HB method, called incremental harmonic balance (IHB), combines the HB method with the Newton-Raphson method [96], leading to an iterative procedure where the number of harmonics can be changed at each iteration, reducing the computational effort [97].

Harmonic balance methods are often unable to capture the nonlinearities in the response and in the friction force [87]; for instance, they cannot be used to determine if stick-slip occurs in the response. Based on the observation that, despite the higher efficiency of frequency domain-based methods, nonlinearity are better described in the time domain [87], Cameron and Griffin [98] introduced the alternating frequency-time domain (AFT) method, in the attempt of combining the advantages related to both time domain- and frequency domain-based approaches. Although it is currently regarded as the most suitable semi-analytical approach for the investigation of friction damped systems, AFT method can also have a slow convergence, limiting its advantages on time integration approaches [87].

Finally, it is worth mentioning that, while harmonic balance methods are preferred for approximating the forced response of harmonically excited systems, other semi-analytical approaches have also been explored for investigating the behaviour of different types of friction damped systems. For instance, Thomsen and Fidlin successfully used the averaging method for studying the stick-slip oscillations of a mass-spring system with a contact between the mass and a moving belt [99].

2.3.3 Numerical methods

The main complications in the numerical time integration of the governing equations of friction damped systems are related to the discontinuous nature of most friction models. As observed in Section 2.2, this discontinuity occurs when the relative velocity in the contact is equal to zero and causes the friction force to switch direction with every time step. Moreover, if stick-slip occurs in the response, the transition between the sliding and the sticking phases typically occurs very rapidly. On the one hand, when automatic step-size controls are used, this leads to high

computation times; on the other hand, there will be a loss of accuracy if the step-size is constant [3]. This numerical stiffness problem can be dealt with implementing specialised stiff solvers [100]. Nonetheless, several authors prefer to use standard numerical integration techniques and impose that the conditions for the transition from a sliding to a sticking phase are checked every time that the relative velocity crosses the zero [3]. In addition to these event-driven approaches, techniques based on the so-called time-stepping, such as the Moreau–Jean's scheme [101, 102], are also commonly used for integrating nonsmooth dynamical systems [103]. Further approaches, such as the singular perturbation technique [104], have been explored for dealing with the further stiffness problems caused by models where both fast and slow dynamics need to be captured.

The stiffness of the problem is not the only issue affecting the numerical treatment of friction damped systems. In fact, while one of the advantages of the time integration is the possibility to capture transient behaviours, this can also lead to high computational costs in lightly-damped systems if the steady-state response is of interest, since hundreds of excitation periods can be needed for transient to die out [3]. Other difficulties may arise from the presence of multiple contacts. In this case, several and interdependent sticking conditions must be checked after each time step, notably increasing the complexity of the implementation [105, 106, 107]. Finite element (FE) models are also often used, particularly in the industry, to deal with more complicated problems, where several contacts or multiple sliding directions are involved. Numerical algorithms for the treatment of friction in FE models have been proposed by Barber *et al.* in [108, 109, 110]. Finally, a common numerical tool for carrying out bifurcation analyses in nonlinear dynamical systems is the continuation method [111]. This approach can also deal with nonsmooth systems [112] and has recently been used for the investigation of friction damped systems [77].

In conclusion, numerical time integration can be used determine the dynamic response of those mechanical systems for which, due to their complexity, analytical solutions are not available in literature. Moreover, it enables the investigation of transient behaviours and of nonlinear phenomena such as stick-slip motion,

which are often missed by the semi-analytical methods reviewed in Section 2.3.2. Nonetheless, the stiffness of the numerical problem, the presence of long transients or of multiple contacts can affect the efficiency and the accuracy of the numerical integration. Both analytical and numerical solutions are clearly affected by the models assumed for the structure and for the friction forces. However, even the most advanced friction laws and very detailed mechanical models cannot fully account for the complexity of the friction processes. Therefore, a complete understanding of the behaviour of friction damped systems can only be obtained combining theoretical results with experimental observations.

2.4 Experimental investigation of friction damped systems

Experimental testing has an essential role in friction modelling and in the evaluation of friction damping effects in vibrating structures. In fact, not only the development of friction models is usually based on experimental observations, but experiments are also needed for estimating the parameters to be used in such models, including the measurement of the kinetic [113, 114] and static [115, 116] friction coefficients, the Stribeck velocity [117, 118] and the many parameters found in more advanced models [119, 120, 121]. Furthermore, experimental tests are often carried out for purposes such as identifying [13], comparing [122, 123] and validating [124, 125] the existing models.

Since the focus of this thesis is on friction damped mechanical systems, particular attention is here given to experiments investigating the friction effects on their dynamic response. The earliest experiments regarding the response of systems with friction damping were performed by Jacobsen [30, 126] in 1930, who used a vibrating table setup to measure the amplitude and the phase of a SDOF system with a constant Coulomb friction force and for varying harmonic centrifugal excitation. In the same year, Den Hartog [21] carried out a series of tests on a torsional-vibration damper apparatus, measuring the response amplitude at resonance of a SDOF system for varying ratios between the amplitudes of the friction force and of the

harmonic excitation. Several years later, Marui and Kato [31] investigated the response of a base-excited SDOF system at low ratios between the exciting and the natural frequencies, observing an excellent agreement between theoretical and experimental results in the time and in the frequency domains.

Several experimental investigations focused on identifying viscous and Coulomb damping from the response of mechanical systems. Various approaches were developed for estimating viscous and dry friction from the free response, exploiting the well-established knowledge about the exponential and the linear decays respectively observed in the presence of each of these forms of damping [127, 128, 129, 130]. In particular, it was found that, while viscous damping effect is dominating in large amplitude oscillations, Coulomb friction prevails at smaller amplitudes [127]. The main limit of these approaches is that they can only be considered if the overall damping acting in the system is relatively small; differently, a very small number of periods of oscillation would occur before the final equilibrium is reached. Therefore, many authors investigated different metrics, aiming to directly estimate the damping parameters in forced oscillators. Tomlinson and Hibbert [131] estimated the friction coefficient and the loss factor looking at the power dissipation of a Coulomb damped system. Tomlinson also proposed different approaches for estimating Coulomb friction using the receptance plots [132] or the frequency response functions in terms of displacement, velocity and acceleration [133]. Iourtchenko [134] resorted to the use of HB method to generate identifying equations. Yao et al. [135] implemented a recursive nonlinear least-squares approach to identify viscous and Coulomb damping parameters. Liang and Feeny developed an identification method for estimating the same parameters by using the analytical solutions from Den Hartog [21] and Hundal [81] for the continuous response of a SDOF system excited near resonance. More recently, different response metrics have been investigated in the attempt to overcome the well-known reliability and repeatability problems related to experiments involving friction. An example is the frictional frequency response function (i.e. the ratio between the dynamic component of the friction force and sliding velocity fluctuations) considered in references [119, 124, 137, 138].

In conclusion, it has been highlighted how theoretical and experimental studies on friction damped systems are closely interconnected. In particular, the analytical solutions for dynamic response of these systems available in the literature have been repeatedly used for developing experimental approaches for estimating parameters such as the viscous damping ratios or the amplitude of the friction forces. These existing solutions are presented in detail in the following section.

2.5 Steady-state response of mechanical systems with Coulomb friction

This section reviews the current understanding of the dynamic behaviour of lumped mechanical models with Coulomb friction. In Section 2.5.1, Den Hartog's solution for the continuous steady-state response of a SDOF system a Coulomb friction contact between the mass and a fixed wall [21, 63] is described in detail, and its implications on the features of dynamic response and on the boundaries of motion regimes, which have been investigated by several authors throughout the years, are also debated. Section 2.5.2 will instead focus on the more significant extensions of Den Hartog's theory to systems with contacts between oscillating parts or multiple DOFs.

2.5.1 Den Hartog's approach for SDOF systems with a fixed wall

Continuous response of systems with Coulomb damping only

Let us consider a mass-spring system, where the mass and the stiffness of the spring are referred to as m and k respectively, subjected to a harmonic load of amplitude P and frequency ω, as shown in Fig.2.3a. The mass m rubs against a fixed wall producing a friction force of amplitude F. The governing equation of this system can be written as:

$$m\ddot{x} + kx + F\mathrm{sgn}(\dot{x}) = P\cos(\omega t) \tag{2.10}$$

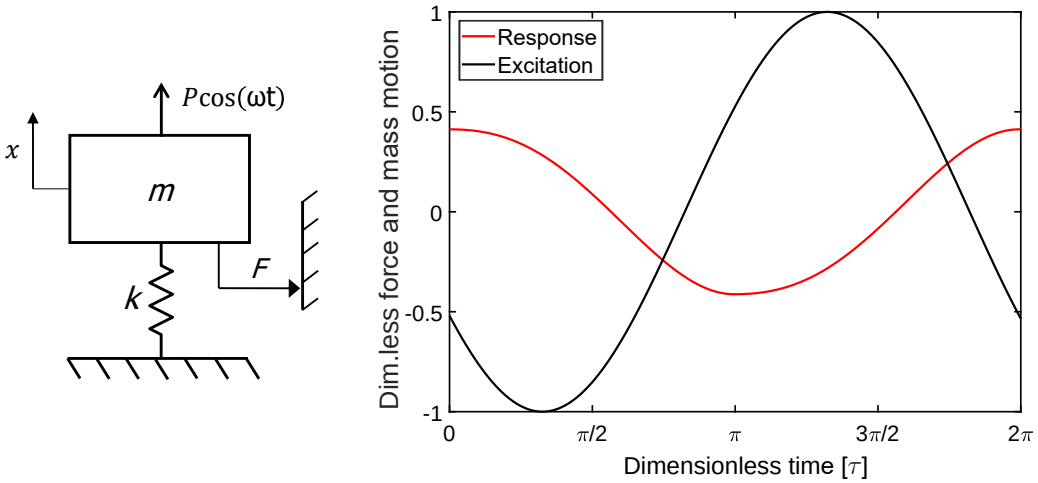

(a) **(b)**

Figure 2.3: SDOF system with a Coulomb friction contact between the mass and a fixed wall (**a**) and its continuous steady-state response to harmonic excitation (**b**).

The following definition of the sgn() function will be considered throughout this thesis:

$$\text{sgn}(\dot{x}) = \begin{cases} 1 & \text{if } \dot{x} > 0 \\ [-\mu, \mu] & \text{if } \dot{x} = 0 \\ -1 & \text{if } \dot{x} < 0 \end{cases} \tag{2.11}$$

where $\mu \geq 1$ is the ratio between the static and the kinetic values of the friction force. The so-defined function is mathematically undetermined when $\dot{x} = 0$. The value assumed in this static condition, included between -μ and μ, will be such that the system is in equilibrium when the mass m is stuck on the wall. While this definition of the sgn() function can accommodate different static and kinetic friction coefficients, Den Hartog does not consider the stiction phenomenon in his work and, therefore, it will be hereby assumed that $\mu = 1$. Furthermore, in order to reduce the number of parameters of the problem to its minimum, it is useful to rewrite Eq.(2.10) in a non-dimensional form. Let us then introduce the non-dimensional time and mass displacement as:

$$\tau = \omega t \tag{2.12}$$

and:

$$\bar{x} = \frac{x}{P/k} \tag{2.13}$$

respectively. Substituting Eqs.(2.12) and (2.13) into Eq.(2.10) and dividing it by P, it is possible to obtain following the non-dimensional form of the governing equation:

$$r^2\bar{x}'' + \bar{x} + \beta \mathrm{sgn}(\bar{x}') = \cos\tau \tag{2.14}$$

where the symbol ' denotes the derivative with respect to τ. The following non-dimensional groups have been introduced in the above equation:

- the *frequency ratio* is the ratio between the driving and the natural frequencies

$$r = \omega\sqrt{\frac{m}{k}} \tag{2.15}$$

- the *friction ratio* is the ratio between the amplitudes of the friction and of the harmonic forces

$$\beta = \frac{F}{P} \tag{2.16}$$

As specified in reference [139], it is possible to demonstrate that the response of the system can be fully described referring to these two parameters only. In fact, the solution of Eq.(2.10) depends on six independent variables (t, m, k, F, P, ω), but only three dimensions are required to describe such quantities, i.e. [kg], [m] and [s]. Therefore, according to the generalised Buckingham's theorem [140], a suitable non-dimensional form of this solution can be expressed by using three non-dimensional groups. In the present problem, this means that the non-dimensional response $\bar{x}$ can be expressed as a function of τ, r and β. Since the first is simply a non-dimensional form of the time variable, the frequency and the friction ratios will fully determine the response of the system.

Den Hartog derived his solutions under the following assumptions:

- a steady-state condition has been reached;
- the response has the same fundamental period of the excitation, which is equal to 2π if the non-dimensional forcing function is considered;
- no stops occur in the response, which is therefore continuous.

Den Hartog also implicitly assumed that the response of the system is symmetric in time and in displacement, i.e. that the second half of steady-state response period must match the negative of the first half, as shown in Fig.2.3b; this type of symmetry is often referred as anti-periodicity. However, the symmetry of the non-sticking solutions has only been demonstrated several years later by Csernak and Stepan [69]. Under these assumptions, Eq.(2.14) will be linear in each interval included between two subsequent stationary points of the response, since no change occurs in the sign of the velocity $\bar{x}'$ of the mass. If the non-dimensional time interval $[0, \pi]$ is considered, where $\tau = 0$ coincides with a maximum of the response and $\tau = \pi$ with the subsequent minimum, $\bar{x}'$ will be equal to zero at both ends of the interval and negative in all the internal points. Therefore, the friction ratio will be constant within the interval and equal to $-\beta$. Thus, it will be possible to rewrite Eq.(2.14) as:

$$r^2 \bar{x}'' + \bar{x} - \beta = \cos(\tau + \phi) \tag{2.17}$$

where it is assumed that an unknown phase angle ϕ is present between the excitation and the response due to friction damping. It is worth underlining that this phase angle refers to the maxima of these functions, while that between their zero will be generally different, since the response is not assumed to be harmonic. Eq.(2.17) is a linear second-order ordinary differential equation (ODE), whose solution can be written as:

$$\bar{x} = A \cos\left(\frac{\tau}{r}\right) + B \sin\left(\frac{\tau}{r}\right) + \beta + V \cos(\tau + \phi) \tag{2.18}$$

where A and B are two unknown constants and V is the *response function* of an undamped SDOF system:

$$V = \frac{1}{1 - r^2} \tag{2.19}$$

Den Hartog determined the unknown values A, B and ϕ from Eq.(2.18) by imposing the initial and final conditions on the displacement and the velocity of the mass within the half-period $[0, \pi]$, which can be expressed as:

$$\begin{cases} \bar{x}(0) = \overline{X} & \text{(2.20a)} \\ \bar{x}'(0) = 0 & \text{(2.20b)} \end{cases}$$

and:

$$\begin{cases} \bar{x}(\pi) = -\overline{X} & \text{(2.21a)} \\ \bar{x}'(\pi) = 0 & \text{(2.21b)} \end{cases}$$

respectively. In the above conditions, $\overline{X}$ is the non-dimensional amplitude of the response, which is also unknown at this stage. Therefore, Den Hartog's problem presents four unknown values which can be fully determined using the four conditions introduced in Eqs.(2.20) and (2.21). The final expression obtained for the mass motion in the time interval $[0, \pi]$ is:

$$\bar{x} = \overline{X}\cos\tau + \beta U \sin\tau + \beta\left[1 - \cos\left(\frac{\tau}{r}\right) - Ur\sin\left(\frac{\tau}{r}\right)\right] \tag{2.22}$$

where the response amplitude and phase can be evaluated as:

$$\overline{X} = \sqrt{V^2 - (\beta U)^2} \tag{2.23}$$

and:

$$\cos\phi = \frac{\overline{X}}{V} \qquad\qquad \sin\phi = -\frac{\beta U}{V} \tag{2.24}$$

respectively. In the above expressions, the *damping function*:

$$U = \frac{\sin(\pi/r)}{r[1 + \cos(\pi/r)]} \tag{2.25}$$

has been introduced.

The analytical expressions reported in Eqs.(2.22), (2.23) and (2.24) only hold when the mass motion is continuous. This has been imposed in Den Hartog's procedure by assuming that $\bar{x}' < 0$ in all the internal points of the time interval $[0, \pi]$. Thus, it is possible to determine the domain of validity of the solution by substituting the derivative of the mass displacement described in Eq.(2.22) into this condition. This results in the following inequality:

$$\beta < \sqrt{\frac{V^2}{U^2 + \left(\frac{S}{r^2}\right)^2}} \tag{2.26}$$

where:

$$S = \max_{0<\tau<\pi} \frac{r\sin(\tau/r) + Ur^2[\cos\tau - \cos(\tau/r)])}{\sin\tau} \tag{2.27}$$

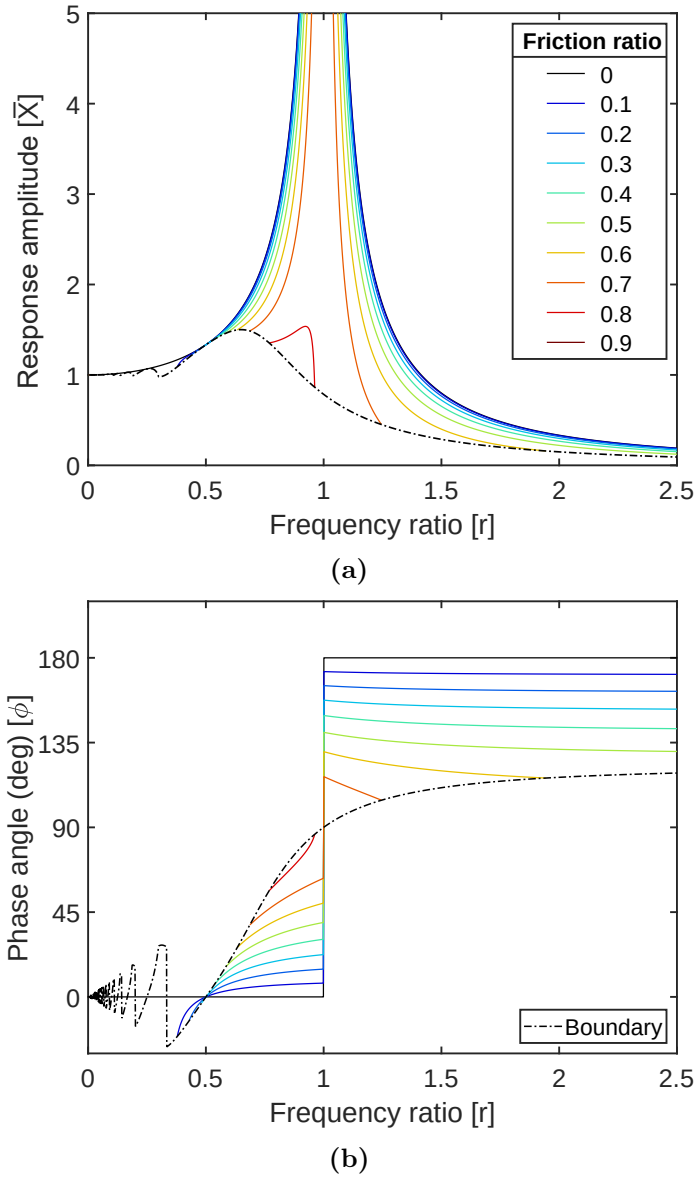

Figure 2.4: Non-dimensional amplitude (**a**) and phase angle (**b**) of the continuous steady-state response of a harmonically excited SDOF system with a Coulomb friction contact between the mass and a fixed wall.

The RHS of Eq.(2.26) represents the value of the friction ratio at the boundary between continuous and stick-slip motion regimes, which will be referred as β_{lim} in the remaining of this thesis. This boundary can also expressed in terms of the response amplitude and phase by simply substituting β_{lim} into Eqs.(2.23) and Eq.(2.24). In

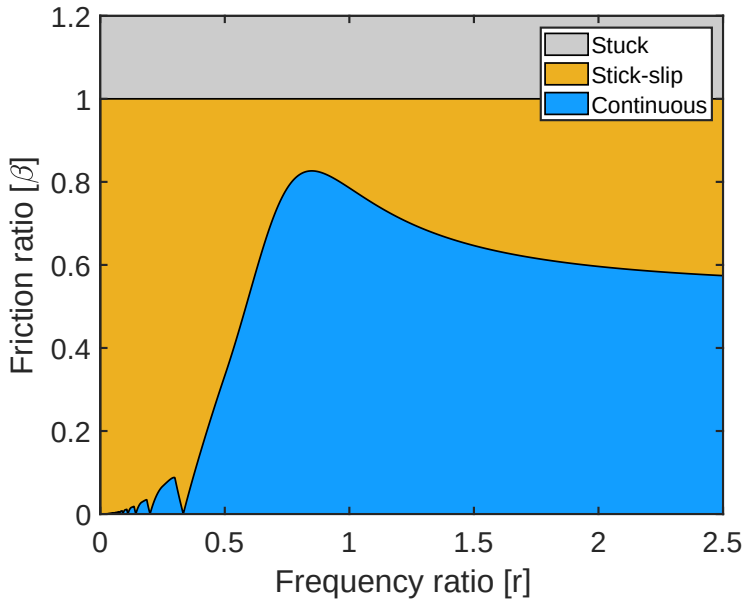

Figure 2.5: Motion regimes of a harmonically excited SDOF system with a Coulomb friction contact between the mass and a fixed wall.

particular, the expression obtained for the boundary response amplitude is:

$$\overline{X} > \sqrt{\frac{V^2}{1+\left(\frac{Ur^2}{S}\right)^2}} \tag{2.28}$$

It is worth mentioning that the function S expressed in Eq.(2.27) must be evaluated numerically. Therefore, although based on Den Hartog's theory, the boundary between continuous and stick-slip regimes is here determined by a semi-analytical approach.

Results and discussion

The response amplitude and phase expressed Eqs.(2.23) and (2.24) have been plotted in Figs.2.4a-b in the frequency ratio range $0:2.5$ for varying friction ratios; their respective boundaries also reported in these figures. The boundary between continuous and stick-slip regimes has been represented in Fig.2.5 in the same range of values of r. It is worthwhile underlining that a steady-state mass motion can only be observed, whatever in continuous or stick-slip regimes, when the amplitude of the harmonic excitation is larger than that of the static friction force. In the

assumption of $\mu = 1$, this only happens if:

$$\beta < 1 \tag{2.29}$$

The RHS of the above inequality indicates the boundary between the sliding (continuous and stick-slip) and the permanent sticking regimes and will be denoted, in general, as β^*_{lim}. This boundary is also reported in Fig.2.5.

Some noteworthy behaviours can be observed from Figs.2.4 and 2.5 and will be commented in what follows.

- Among the cases observed, the resonant peak at $r = 1$ is infinite for all the curves, except that for $\beta = 0.8$. In fact, according to Den Hartog's theory, Coulomb damping leads to finite resonant peaks only if:

$$\beta > \frac{\pi}{4} \tag{2.30}$$

  This was mathematically proved by Csernak *et al.* in [69] by evaluating the limit of the response amplitude for $r \to 1$, while in [139] this value is obtained by evaluating the same limit for β_{lim}. This shows that the resonant peak becomes finite only when stick-slip occurs at resonance. In this case, as can been seen in Fig.2.4a, the finite peak will be shifted on the left, i.e. towards lower values of r.

- The amplitude of the mass motion always decreases with the friction ratio, while the phase angle is always increased by friction for $r < 1$ and decreased for $r > 1$. The only exceptions occurs at those frequency where the damping function is equal to zero or tends to infinity. The condition $U = \infty$ occurs in correspondence of the odd sub-harmonic resonant frequency ratios, i.e. when $r = 1/(2n+1), n = 1; 2; ...$; at these frequencies, also the boundary between continuous and stick-slip regimes from Eq.(2.26) is equal to zero, meaning that sticking is expected to occur in the mass motion for any value of β and Den Hartog's solution is therefore not valid. Differently, the condition $U = 0$ occurs for $r = 1/(2n), n = 1; 2; ...$. In reference [23], Shaw observed that unstable

behaviours may occur in SDOF systems with dry friction and zero or positive viscous damping in correspondence of these subresonant frequencies; further investigation by Csernak *et al.* [70] showed that a one-parameter continuum of marginally stable asymmetric solutions actually exists in correspondence of the even sub-harmonic resonances.

- As can be seen in Fig.2.5, at low frequency ratios the dynamic response is usually characterised by the occurrence of stick-slip. This can also be shown mathematically by evaluating the limit value of the boundary between continuous and stick-slip regimes from Eq.(2.26) for $r \to 0$. The presence of stick-slip at low exciting frequencies is a well-known phenomenon. However, it can also be observed in Fig.2.5 that β_{lim} tends to an asymptotic value when $r \to \infty$, showing that stick-slip can occur at high frequency ratios if the friction ratio exceeds a certain threshold value. This value has been calculated in reference [70], also taking into account different values for static and kinetic friction forces, and it is equal to:

$$\beta_{\infty} = \frac{2}{\sqrt{4\mu + \pi^2}} \tag{2.31}$$

which is equal to 0.537 if $\mu = 1$, as also reported in [139] and shown in Fig.2.5.

Extension to two-stop stick-slip responses

Den Hartog's approach can also be extended, as shown in [21], to deal with stick-slip motions as long as they are characterised by the presence of two sticking phases during each response period. Each period of a two-stop motion is characterised by the presence of two sliding phases. The sliding phase with a negative slope can be studied similarly to that included between a maximum and the subsequent minimum of a continuous response. However, it must be considered that duration of this sliding phase will be shorter than a half-period, meaning that it will be included between $\tau = 0$ and a certain time instant $\tau_0 < \pi$, as shown in Fig.2.6. Therefore, the final conditions in Eq.(2.21) will be applied at $\tau = \tau_0$, rather than at $\tau = \pi$; conversely, the initial conditions in Eq.(2.20) will remain unchanged. To

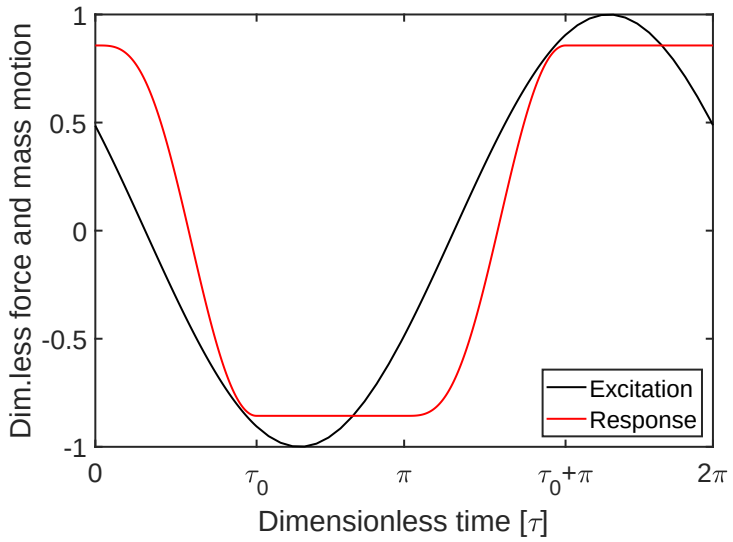

Figure 2.6: two-stop stick-slip response of a harmonically excited SDOF system with a Coulomb friction contact between the mass and a fixed wall.

deal with the introduction of this unknown value τ_0 in the problem, Den Hartog considered a further condition: since the origin of the time interval coincides with the transition from a sticking to a sliding stage, the static equilibrium must be verified at $\tau = 0$. Considering that $\bar{x} = \overline{X}$ at $\tau = 0$, and substituting these values into Eq.(2.17), this condition can be written as:

$$\beta + \cos\phi - \overline{X} = 0 \tag{2.32}$$

in Den Hartog's assumption of $\mu = 1$. The final solution cannot be expressed explicitly and can only be obtained via numerical calculation. Therefore, it does not offer significant analytical insights on the response features of SDOF systems. Nonetheless, it represents a handy alternative to semi-analytical approaches and numerical time integration when multi-stop and/or asymmetric responses are not expected.

Systems with combined viscous and Coulomb damping

A more general formulation of Den Hartog's solution, reported in [21], can account for the case of mixed viscous and Coulomb damping. Let us consider the SDOF model shown in Fig.2.7a, where a viscous dashpot has been included between the

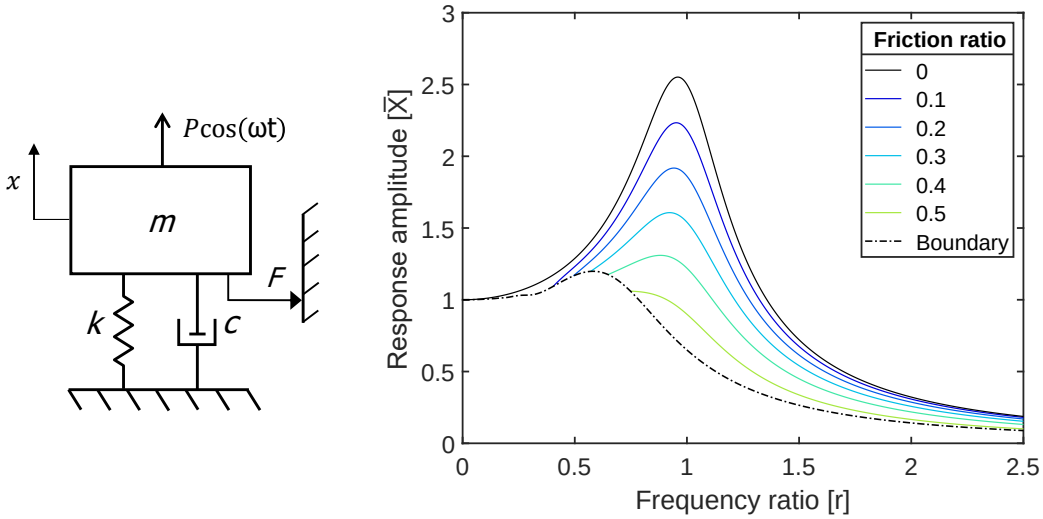

(a) **(b)**

Figure 2.7: SDOF system with combined viscous and Coulomb damping (**a**) and its non-dimensional response amplitude for $\zeta = 0.2$ (**b**).

ground and the mass. The governing equation of this system can be written as:

$$m\ddot{x} + c\dot{x} + kx + F\text{sgn}(\dot{x}) = P\cos(\omega t) \tag{2.33}$$

The addition of the term $c\dot{x}$ does not violate any of the Den Hartog's assumptions reported above. Therefore, the corresponding solution can be obtained using the same mathematical procedure, which is not reported here for sake of brevity. The following expression was derived by Den Hartog for the non-dimensional amplitude of the continuous steady-state response:

$$\overline{X} = -\beta G + \sqrt{|V_d|^2 - (\beta U_d)^2} \tag{2.34}$$

In the above equation, the complex response function:

$$V_d = \frac{1}{1 - r^2 + i2\zeta r} \tag{2.35}$$

and the damping functions:

$$U_d = \frac{\sin\left(\dfrac{\pi\sqrt{1-\zeta^2}}{r}\right)}{r\sqrt{1-\zeta^2}\left[\cosh\left(\dfrac{\zeta\pi}{r}\right) + \cos\left(\dfrac{\pi\sqrt{1-\zeta^2}}{r}\right)\right]} \tag{2.36}$$

$$G = \frac{\sinh\left(\frac{\zeta\pi}{r}\right) - \frac{\zeta}{\sqrt{1-\zeta^2}}\sin\left(\frac{\pi\sqrt{1-\zeta^2}}{r}\right)}{\cosh\left(\frac{\zeta\pi}{r}\right) + \cos\left(\frac{\pi\sqrt{1-\zeta^2}}{r}\right)} \tag{2.37}$$

have been introduced, while $\zeta = c/(2\sqrt{km})$.

The curves resulting from Eq.(2.34) for different values of β are reproduced in Fig.2.7b for the case $\zeta = 0.2$.

2.5.2 Extensions to different contact configurations and multiple DOFs

The idea of extending Den Hartog's approach to different and more complex mechanical models was firstly proposed by the author himself in [63]. In fact, among the possible extensions of his work, Den Hartog mentioned that his solution for SDOF systems with Coulomb damping only can be used to obtain the response of a base-excited system with a fixed wall (Fig.2.8a) and that of a system where both base and wall are harmonically excited (Fig.2.8b); furthermore, he suggested that his approach could also be generalised to systems with two or more DOFs (Fig.2.8c).

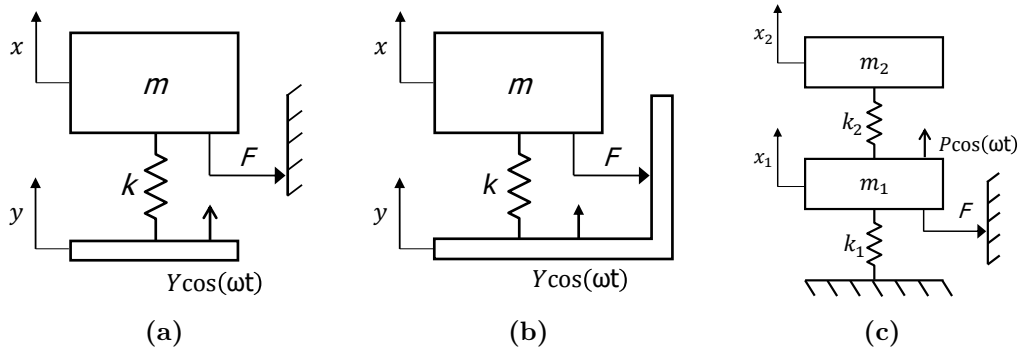

Figure 2.8: Harmonically excited mass-spring systems with a Coulomb friction contact: (**a**) SDOF system with a fixed wall under base excitation, (**b**) SDOF system under joined base-wall excitation, (**c**) 2DOF system with excitation and contact acting on m_1.

In the absence of viscous damping, the dynamic response of a SDOF system with a fixed wall will be exactly the same whether the harmonic excitation is due to a load of amplitude P directly applied to the mass or to a base excitation of amplitude Y; in fact, as in the case of an undamped SDOF system (see, e.g., [29]), the two problems are identical for $P = kY$. Nonetheless, independently of the presence of

dry friction, these two problems will present different solutions if a viscous dashpot is included in the system, between the mass and the excited base. Hundal [81] derived a closed-form solution for the steady-state response of this system by applying the same approach as Den Hartog. Hundal's solution holds for continuous and for two-stop motion regimes and reduces to Den Hartog's solution when $c = 0$.

The dynamic response of a SDOF system where the friction contact occurs between the mass and a wall rigidly connected to the excited base, as shown in Fig.2.8b, can only be partially described using Den Hartog's solution. As specified by the author, in the absence of viscous damping, the problem is equivalent to that discussed in Section 2.5.1 for $P = kYr^2$. However, the dependency of the amplitude of the dynamic load acting on the mass on the frequency ratio changes significantly the behaviour of the system. Furthermore, only the relative motion between the mass and the wall in contact can be described with this approach. A more complete solution was derived by Levitan in [28], who also considered the presence of viscous damping in the system. Differently, from Den Hartog, Levitan addressed the absolute motion of the mass, obtaining a closed-form solution for the displacement transmissibility. A major limitation of Levitan's solution is that the mass motion is assumed to be monoharmonic. Although Levitan's expressions are able to capture interesting dynamic phenomena such as an inversion of transmissibility curves at high frequencies, the error in the evaluation of the displacement transmissibility is too large in a wide frequency range. Therefore, this problem will be addressed in this thesis, aiming to derive an exact solution for the absolute mass motion and to develop a more complete understanding of the dynamic behaviour of these systems.

Den Hartog's approach cannot handle systems with multiple nonlinearities due to its piecewise linear nature [87]. Nonetheless, his approach can also be used for dealing with MDOF systems if a single friction contact is considered. Den Hartog himself suggests that, once determined a half-period time interval where the sign of the relative velocity between the parts in contact does not change, the problem can still be solved by considering $2N$ initial conditions and $2N$ final conditions, where N is the number of DOFs of the system [63]. This approach is successfully

applied by Yeh [82] for deriving an exact solution for the response of a harmonically base-excited 2DOF system where the masses are interconnected by two springs and two viscous dampers in parallel and a Coulomb contact is applied to the lower mass. Yeh's solution is not expressed in an explicit form, even when a continuous non-sticking response is considered, due to the mathematical complexity of the procedure. Therefore, even if the procedure proposed by Den Hartog and Yeh can, in principle, be applied to MDOF systems with a larger number of masses, the calculation would become more and more complicated as the number of DOFs increases, as also suggested by Ferri and Dowell in [93]. In addition, the solution should be derived *ex novo* for each different MDOF system investigated, meaning that significant changes would be introduced in the procedure not only if a different number of DOFs is considered, but also if the harmonic or the friction forces are applied to different masses of the system. Finally, the absence of explicit closed-form solutions renders difficult to draw more general conclusions on the features of the dynamic response of these systems. These gaps will be addressed in this thesis.

2.6 Concluding remarks

This chapter has provided an overview of the research advances in the areas of the modelling and of the dynamic analysis of friction damped systems.

Firstly, the main models used for describing analytically the friction process have been reviewed. Although an universal and predictive friction model is not available in the literature and its development might be unrealistic, several models have been proposed and are able to address efficiently specific friction-related phenomena. While the most advanced laws, such as the LuGre model, are of interest for high-precision applications, the Coulomb friction model is still considered in most studies regarding the damping effects introduced by dry friction in mechanical vibrating systems.

A plethora of analytical, numerical and experimental approaches have been developed for investigating the nonlinear behaviour of friction damped systems. While analytical solutions can offer significant advantages in terms of computational

cost and of the possibility of developing a mathematical understanding of the behaviour of these systems, their derivation is a complex task and, therefore, they are only available for very simple mechanical models. Semi-analytical approaches, which are mostly based on the harmonic balance method, can be used to investigate more complex systems but are often unable to capture nonlinearities in the dynamic response; the most advanced approaches can overcome this limitation by switching between the time and the frequency domains, but this also lead to a loss of efficiency in terms of computational cost. Therefore, the numerical time integration still remains the reference approach for the investigation of complex nonlinear systems and of transient behaviours.

Analytical and numerical approaches are strongly limited by the assumptions inherent to the choice of the friction and mechanical models; therefore, a complete understanding of the behaviour of systems with dry friction can only be achieved combining theory and experiments. Moreover, experimental testing is required to estimate the parameters of the friction models and to identify viscous and Coulomb damping in vibrating systems.

Finally, the existing analytical solutions for the response of mechanical systems with Coulomb friction and the current understanding of their dynamic behaviour have been reviewed. While the behaviour of SDOF systems with a Coulomb friction contact between the mass and a fixed wall is generally well-understood, more research effort is needed to develop the same level of understanding for mechanical systems including a contact between two oscillating components and/or multiple DOFs. This will be the focus of the next chapters of this thesis.

All intelligent thoughts have already been thought;
what is necessary is only to try to think them again.

— Johann Wolfgang von Goethe

3

Dynamic response of a Coulomb friction oscillator under joined base-wall motion

Contents

3.1 Introduction

This chapter investigates the steady-state response of SDOF mass-spring systems with a Coulomb friction contact between the mass and a harmonically oscillating wall. The goal of this investigation is to provide an insight of how the dynamic performances of Coulomb damped systems change when the friction contact occurs

between two oscillating components, as it is typically the case in friction dampers and isolation systems.

Closed-form expressions are derived in continuous steady-state conditions for both the relative motion between the mass and wall in contact and the absolute mass motion. The amplitude and the phase of these motions are evaluated for varying non-dimensional exciting frequencies and friction forces; different static and kinetic friction forces are also taken into account. In addition, an analytical formulation is also obtained for the boundaries among the continuous, stick-slip and motion regimes. Finally, a numerical approach is introduced for validating the analytical results and investigating the dynamic response of the system when stick-slip occurs.

A general formulation of the problem is presented in Section 3.2, where the dynamic load acting in the contact is also determined. In Section 3.3, analytical solutions are derived for the time response, amplitude and phase of the relative motion in the contact. The domain of validity of these solutions and the boundaries among the motion regimes are determined in Section 3.4. Section 3.5 deals with the absolute mass motion and presents an in-depth discussion on the response features of the system in continuous regime. Finally, Section 3.6 presents the numerical validation of the above results and an overview of the dynamic behaviour of the system across the different motion regimes.

3.2 General formulation and equivalent dynamic loading

Let us consider the SDOF mass-spring system shown in Fig.3.1a. The wall rubbing against the mass m is rigidly jointed to the base, forming an external support, and displays the same harmonic motion of amplitude Y and frequency ω. In other words, the motion of the excited base is transmitted to the mass by the parallel of a spring of stiffness k and a Coulomb contact, where a friction force of amplitude F is generated by relative motion between mass and wall, as shown in Fig.3.1b.

In this thesis work, this problem will be referred to as *joined base-wall* excitation. The governing equation of this system can be written as:

$$m\ddot{x} + k(x - y) + F\text{sgn}(\dot{x} - \dot{y}) = 0 \tag{3.1}$$

where the coordinates x and y describe the position of the mass and the base, respectively. The function sgn is here introduced according the definition given in Eq.(2.11); no assumption is made here regarding the ratio μ between the static and kinetic friction forces, which can therefore assume different values.

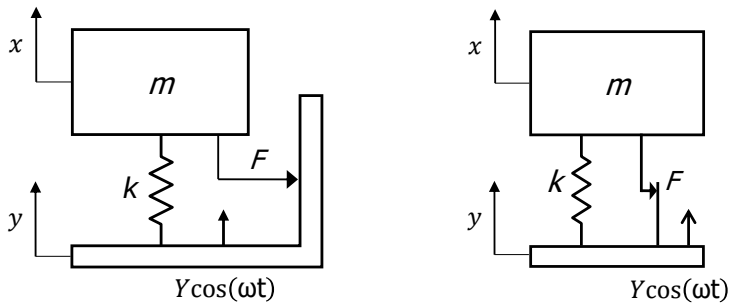

Figure 3.1: Two equivalent representations of a SDOF mass-spring system with a friction contact under harmonic joined base-wall excitation, showing (**a**) the mass in contact with a wall jointed to the base and (**b**) the parallel between the spring and the friction contact.

Let us define a new variable $z = x - y$ to account for the relative motion between the mass and the wall. Introducing z and the explicit expression $y = Y\cos(\omega t)$ of the base motion, it is possible to rewrite the above equation as:

$$m\ddot{z} + kz + F\text{sgn}(\dot{z}) = mY\omega^2\cos(\omega t) \tag{3.2}$$

Finally, introducing the definition of frequency ratio from Eq.(2.15) into Eq.(3.2), it is obtained that:

$$m\ddot{z} + kz + F\text{sgn}(\dot{z}) = kYr^2\cos(\omega t) \tag{3.3}$$

Eq.(3.3) is written in the same form as the governing equation of a SDOF with a fixed wall, reported in Eq.(2.10). In particular, the exciting term of this equation can be seen as the equivalent dynamic load acting in the contact. The amplitude of this load is equal to kYr^2, in agreement with the Den Hartog's annotation [63]

mentioned in Section 2.5.2, which is hereby demonstrated. Despite the similarity between Eqs.(2.10) and (3.3), in the latter the dependency of the harmonic load amplitude on the frequency ratio leads to significantly different results. Thus, the relative motion between mass and wall in the system shown in Fig.3.1 is investigated in the following section.

3.3 Relative motion in the contact

In order to study the relative motion in the contact, it is convenient to rewrite Eq.(3.3) in non-dimensional terms, so that the smallest number of independent parameters is considered [139]. Introducing the non-dimensional variable $\bar{z} = z/Y$ and the non-dimensional time τ from Eq.(2.12), the following expression is obtained:

$$r^2 \bar{z}'' + \bar{z} + \beta \mathrm{sgn}(\bar{z}') = r^2 \cos\tau \tag{3.4}$$

where the friction ratio has been introduced as $\beta = F/(kY)$. Den Hartog's approach [21] can be used to derive an exact solution of Eq.(3.4) if the same assumptions considered in Section 2.5.1 are applied. Specifically, it will be assumed that a steady-state condition has been reached and that the relative motion $\bar{z}$ is continuous and antiperiodic, with the same period of oscillation 2π as the non-dimensional forcing function. The existence of a unique steady-state response, independent of the initial conditions, has been studied by several authors (see, e.g, [23, 67, 70]) for SDOF systems with a fixed wall, as discussed in Section 2.5.1; however, to the best of the author's knowledge, stability properties have not been explored for the contact configuration investigated in this chapter. Nevertheless, the numerical investigations carried out in this study have shown a convergence of the response to a unique steady-state solution for most sets of parameters. Specific exceptions include the resonant and sub-resonant frequencies; these will be discussed in Section 3.6.

Under these assumptions, Eq.(3.4) can be written, within the non-dimensional time interval $[0, \pi]$ included between a maximum of the steady-state relative displacement $\bar{z}$ and the subsequent minimum, as:

$$r^2 \bar{z}'' + \bar{z} - \beta = r^2 \cos(\tau + \phi_z) \tag{3.5}$$

where ϕ_z is the phase angle introduced between the maxima of the excitation and of the relative motion $\bar{z}$ by Coulomb damping. The second-order ODE in Eq.(3.5) is linear and its solution is:

$$\bar{z} = A\cos\left(\frac{\tau}{r}\right) + B\sin\left(\frac{\tau}{r}\right) + \beta + \frac{r^2}{1-r^2}\cos(\tau+\phi_z) \tag{3.6}$$

where the unknown values A, B and ϕ_z, as well as the non-dimensional response amplitude $\overline{Z}$, can be found by imposing the initial conditions:

$$\begin{cases} \bar{z}(0) = \overline{Z} & \text{(3.7a)} \\ \bar{z}'(0) = 0 & \text{(3.7b)} \end{cases}$$

and:

$$\begin{cases} \bar{z}(\pi) = -\overline{Z} & \text{(3.8a)} \\ \bar{z}'(\pi) = 0 & \text{(3.8b)} \end{cases}$$

Eq.(3.6) is written in the same form as Eqs.(2.18), with $\bar{z}$ replacing $\bar{x}$ and with:

$$V_z = \frac{r^2}{1-r^2} = V - 1 \tag{3.9}$$

replacing the response function V. Therefore, it is possible to write the final solution by simply applying the same substitutions to Eq.(2.22):

$$\bar{z} = \overline{Z}\cos\tau + \beta U\sin\tau + \beta\left[1 - \cos\left(\frac{\tau}{r}\right) - Ur\sin\left(\frac{\tau}{r}\right)\right] \tag{3.10}$$

where:

$$\overline{Z} = \sqrt{(V-1)^2 - (\beta U)^2} \tag{3.11}$$

while the phase angle ϕ_z can be determined as:

$$\cos\phi_z = \frac{\overline{Z}}{V-1} \qquad\qquad \sin\phi_z = -\frac{\beta U}{V-1} \tag{3.12}$$

The amplitude and phase of the non-dimensional relative displacement between mass and wall, expressed in Eqs.(3.11) and (3.12) respectively, are depicted in Figs.3.2a-b in the frequency ratio range $0:2.5$ for varying friction ratio. It can be observed that, in both figures, all the curves are delimited by a boundary curve. In fact, the expressions reported in the above equations are only valid within the assumption of continuous non-sticking motion. The boundaries between continuous and stick-slip regimes, as well as the condition for the presence of a sliding motion in the contact, will be derived in what follows.

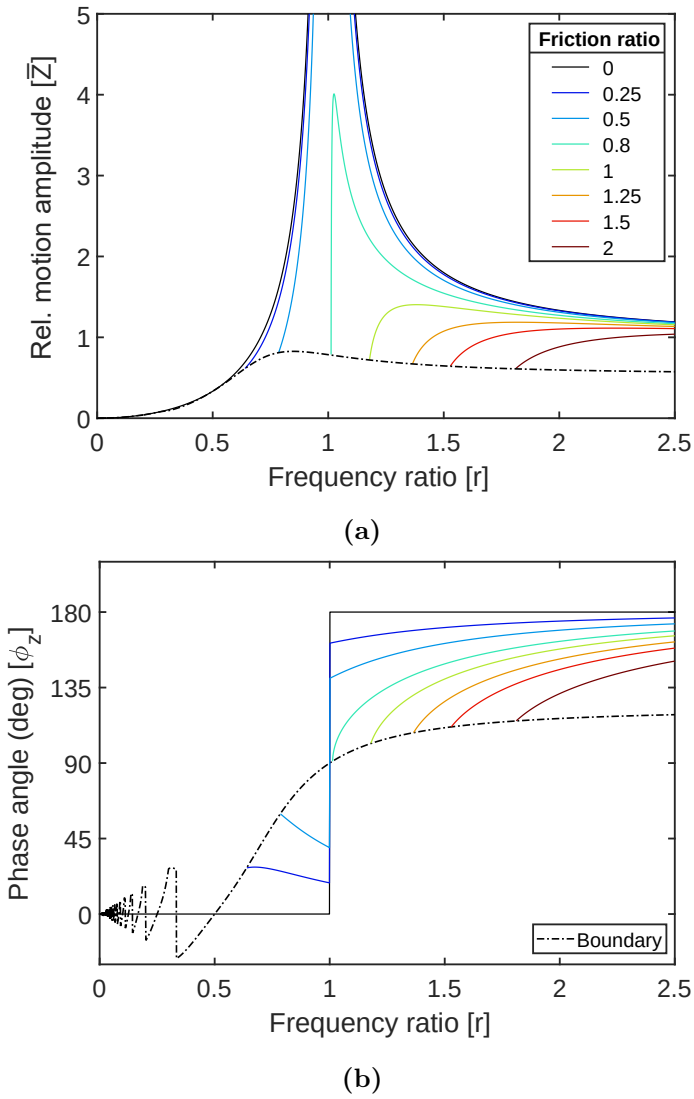

Figure 3.2: Relative motion in the contact for a SDOF system with Coulomb friction under joined base-wall excitation: non-dimensional amplitude (**a**) and phase angle (**b**).

3.4 Boundaries of motion regimes

3.4.1 Boundary between continuous and stick-slip regimes

The solutions presented in Section 3.3 have been derived under the assumption of continuous non-sticking relative motion between mass and wall. This assumption leads to a negative relative velocity and, consequently, to a constant friction force in all the internal points of the half-period $[0, \pi]$. However, the condition $\bar{z}' < 0$ is not sufficient by itself to rule out the occurrence of stops in the steady-state solution. In fact, it is well known that a sticking phase takes place when, simultaneously, the

relative velocity between the components in contact is zero and overall dynamic loading acting in this contact does not overcome the static friction forces. This second sticking condition needs to be imposed explicitly at both ends of the interval, where $\bar{z}' = 0$. Therefore, the conditions for a continuous non-sticking motion can be written as:

$$\begin{cases} \bar{z}' < 0 & \text{if } 0 < \tau < \pi \quad (3.13a) \\ |\bar{z} - r^2 \cos(\tau + \phi_z)| > \mu\beta & \text{if } \tau = 0 \text{ or } \tau = \pi \quad (3.13b) \end{cases}$$

These two conditions can be used to evaluate the maximum value of the friction ratio for which the relative motion is continuous, as well as to determine the boundaries represented in Figs.3.2a-b. Substituting the derivative of Eq.(3.10) into Eq.(3.13a), it is obtained that:

$$-\overline{Z} \sin\tau + \beta U \cos\tau + \beta \left[\frac{1}{r} \sin\left(\frac{\tau}{r}\right) - U \cos\left(\frac{\tau}{r}\right) \right] < 0 \tag{3.14}$$

from which:

$$\overline{Z} > \frac{\beta}{r^2} \frac{r \sin(\tau/r) + U r^2 [\cos\tau - \cos(\tau/r)]}{\sin\tau} \tag{3.15}$$

The above inequality must be verified for each time instant $0 < \tau < \pi$; therefore, considering the maximum of the RHS within this interval and introducing the function S defined in Eq.(2.27), it is possible to write that:

$$\overline{Z} > \frac{\beta S}{r^2} \tag{3.16}$$

and, substituting Eq.(3.11) into the above expression, that:

$$\beta < \sqrt{\frac{(V-1)^2}{U^2 + \left(\frac{S}{r^2}\right)^2}} \tag{3.17}$$

Let us now consider the second non-sticking condition. Due to the symmetry of the response, it is only necessary to impose this condition in the time instant $\tau = 0$. Therefore, Eq.(3.13b) can be rewritten as:

$$\left| \overline{Z} - r^2 \cos\phi_z \right| > \mu\beta \tag{3.18}$$

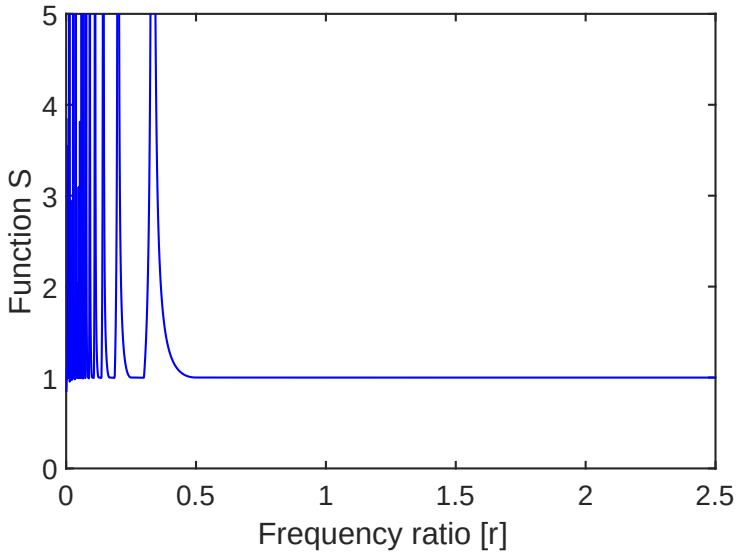

Figure 3.3: Evolution of the function S with respect to the frequency ratio r.

from which, substituting Eq.(3.12a) and rearranging, it is obtained that:

$$\overline{Z} > \frac{\mu\beta}{r^2} \tag{3.19}$$

Introducing Eq.(3.11), the above inequality can be expressed as:

$$\beta < \sqrt{\frac{(V-1)^2}{U^2 + \left(\frac{\mu}{r^2}\right)^2}} \tag{3.20}$$

Finally, merging Eqs.(3.17) and (3.20), it is possible to express the domain of validity of the analytical solution presented in this chapter as:

$$\beta < \sqrt{\frac{(V-1)^2}{U^2 + \left[\frac{\max(S,\mu)}{r^2}\right]^2}} \tag{3.21}$$

where the RHS represents the boundary value of the friction ratio between continuous and stick-slip regimes. Introducing Eq.(3.21) into Eq.(3.11), it is also possible to express the same inequality in terms of the amplitude of the relative motion as:

$$\overline{Z} > \sqrt{\frac{(V-1)^2}{1 + \left[\frac{Ur^2}{\max(S,\mu)}\right]^2}} \tag{3.22}$$

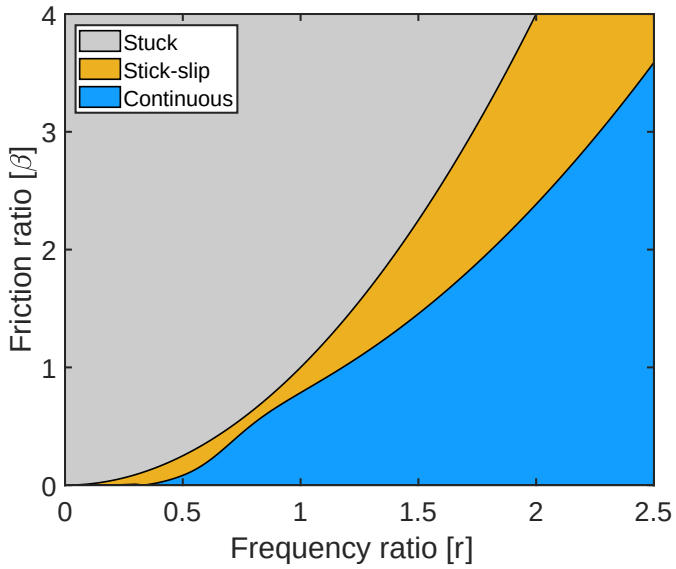

Figure 3.4: Motion regimes of a SDOF system with Coulomb friction under harmonic joined base-wall excitation for varying frequency and friction ratios .

It is worth noting that, in order to plot the boundaries described by Eqs.(3.21) and (3.22), it is required to compute the function S for each value of r. Given the time-dependent expression of such a function, described in Eq.(2.27), and the necessity of evaluating numerically its maximum value in the interval $0 < \tau < \pi$, this can increase the computational cost of the process. Alternatively, an approximated expression of the boundaries can be used. In fact, observing the evolution of the function S with respect to the frequency ratio, shown in Fig.3.3, it can be observed that this function is always unitary when $r > 0.5$; therefore, since $\mu \geq 1$, the ratio μ can directly be used instead of $\max(S, \mu)$ when different frequency ratio ranges are investigated.

The boundary described in Eq.(3.22) is represented by the dotted line in Fig.3.2a, while the boundary friction ratio from Eq.(3.21) is shown in the parameter space $r - \beta$ in Fig.3.4. Finally, the boundary phase angle shown in Fig.3.2b can be obtained by substituting the boundary value of the friction ratio into Eq.(3.12). All the boundaries have been plotted assuming, for simplicity, $\mu = 1$; the effect of the static friction force will instead be discussed in Section 3.4.3.

3.4.2 Boundary between sliding and permanent sticking regimes

In Fig.3.4, a second boundary between the stick-slip and the permanent sticking regions is also shown. In friction damped systems, the relative motion between the components in contact only occurs when the amplitude dynamic load acting on this contact exceeds the static friction force. For instance, in SDOF systems with a fixed wall, the mass motion is only possible if $P > F$ and, therefore, the upper bound for the sliding motion is expressed as $\beta < 1/\mu$. In Section 2.5.1, this boundary is shown in Fig.2.5 for the case of $\mu = 1$. Differently from the fixed-wall case, the boundary shown in Fig.3.4 shows a dependency on the frequency ratio. This can be explained recalling that, as demonstrated in Section 3.1, the amplitude of the harmonic loading acting in the contact depends on r^2. This leads to the following condition for the presence of steady-state relative motion in the contact:

$$kYr^2 > \mu F \tag{3.23}$$

from which:

$$\beta < \frac{r^2}{\mu} \tag{3.24}$$

where the RHS represents the boundary β^*_{lim} between the sliding and the permanent sticking motion regimes. This result has two important implications:

- at low frequencies, the mass will be stuck against the wall even when small amounts of friction are considered;
- at high frequencies, the sliding motion between the mass and the wall in contact will be possible for any value of the friction ratio, as long as the driving frequency overcomes the threshold value:

$$\omega > \sqrt{\frac{\mu F}{mY}} \tag{3.25}$$

which can easily be derived from Eq.(3.23).

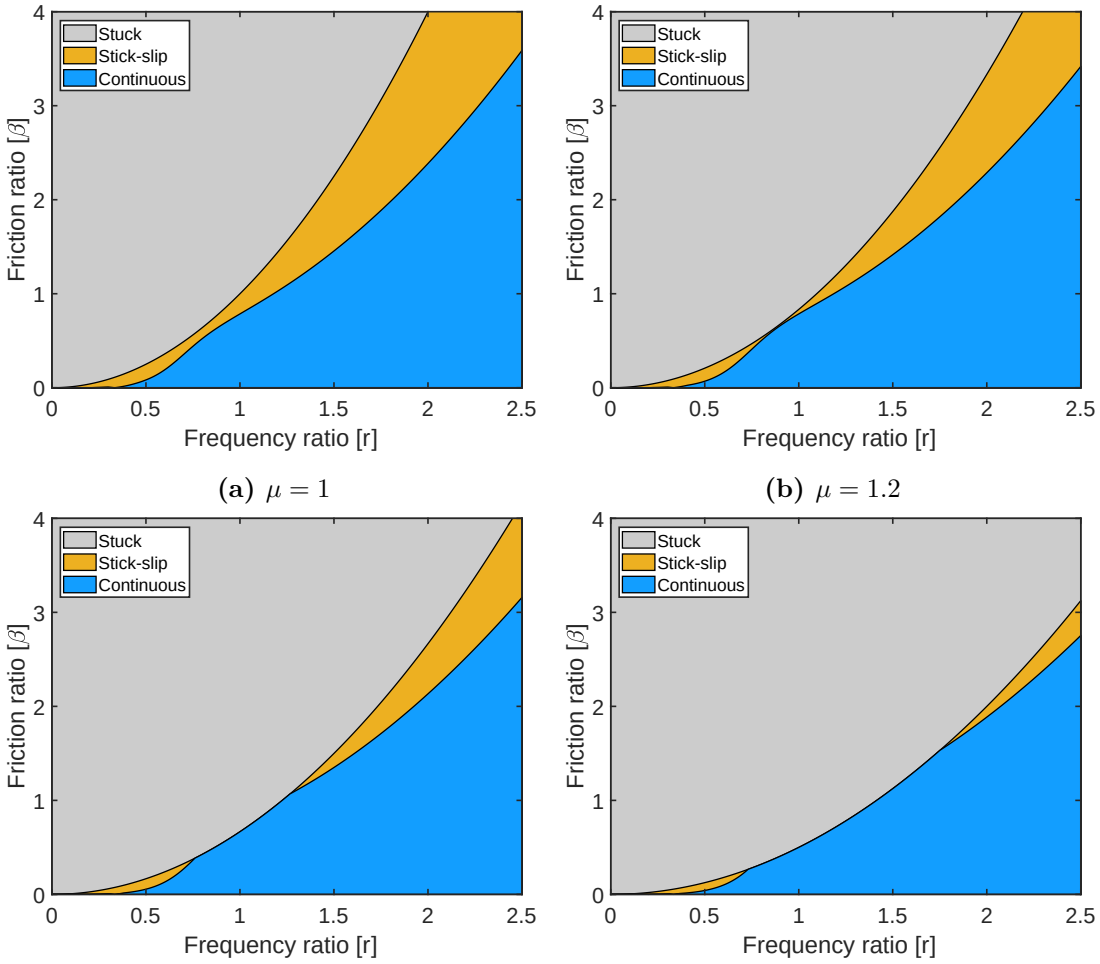

(a) $\mu = 1$ **(b)** $\mu = 1.2$

(c) $\mu = 1.5$ **(d)** $\mu = 2$

Figure 3.5: Motion regimes of a SDOF system with Coulomb friction under harmonic joined base-wall excitation in the parameter space $r - \beta$ for varying ratio between static and kinetic friction forces.

3.4.3 Discussion of the results

Fig.3.4 shows as, in the case $\mu = 1$, the boundaries described by Eqs.(3.21) and (3.24) divide the parameters space $r - \beta$ into three regions associated to the main motion regimes: continuous, stick-slip and permanent sticking. It is noteworthy that the boundaries show no intersections, except that for $r = 0$. Nonetheless, the stick-slip region appears rather narrow if compared to that shown in Fig.2.5 for the fixed-wall case. It can be observed that, for varying frequency ratio, the width of this region, i.e. the local difference between β_{lim} and β^*_{lim}, increases starting from the origin until $r \cong 0.55$, decreases within the interval $0.55 < r < 0.79$ and then increases again

starting from the local minimum found at $r \cong 0.79$. Nevertheless, these patterns will change if different values are considered for static and kinetic friction forces.

The effect of the parameter μ on the boundaries of the motion regimes is shown in Fig.3.5. As the ratio between static and kinetic friction forces is increased, it can be observed that:

- the boundary between continuous and stick-slip regimes maintains the same shape but the value of β_{lim} gradually decreases across the different frequency ratios;
- similarly, the boundary between sliding and sticking regimes has still a quadratic shape but permanent sticking occurs at smaller values of the friction ratio, as can easily be deduced from Eq.(3.24).

Despite both boundaries are reduced by effect of the static friction force, β^*_{lim} decreases with μ more quickly than β_{lim}. As a result, starting approximatively from $\mu = 1.2$, there will be an intersection between them and direct transitions from continuous to permanent sticking regimes will be observed, while the extension stick-slip region will further decrease. It is worth underlining that, in case of intersection between the boundaries, the boundary between sliding and permanent sticking regimes prevails, since relative motion can never occur above this curve; this is also confirmed by the numerical results shown in Fig.3.12b in Section 3.6.

3.5 Absolute mass motion

Whereas the relative motion between mass and wall can be studied as an extension of Den Hartog's solution, this is not true for the absolute motion of the mass. The analytical expression of the steady-state response of the system in the time interval $[0, \pi]$ can be obtained as the sum of the relative motion $\bar{z}$, expressed in Eq.(3.10) and of the base motion $\cos(\tau + \phi_z)$, which yields:

$$\bar{x} = \frac{1}{r^2}\left(\overline{Z}\cos\tau + \beta U \sin\tau\right) + \beta\left[1 - \cos\left(\frac{\tau}{r}\right) - Ur\sin\left(\frac{\tau}{r}\right)\right] \qquad (3.26)$$

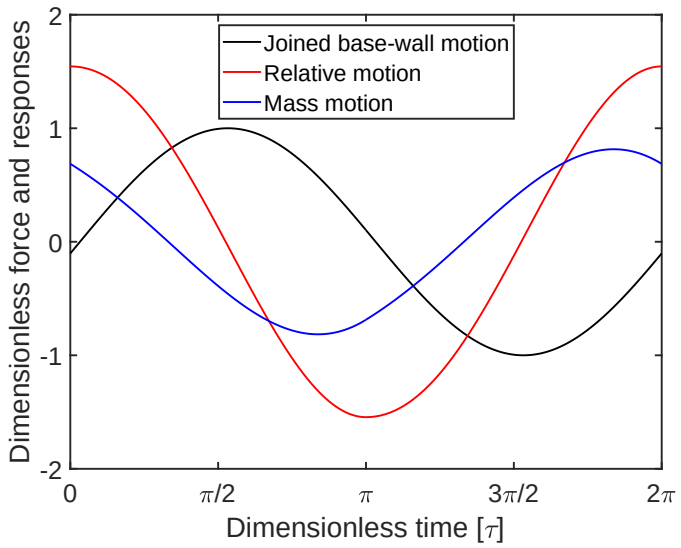

Figure 3.6: Steady-state continuous response of a SDOF system with Coulomb friction under joined base-wall motion in the non-dimensional time period $[0, 2\pi]$.

considering the expression of ϕ_z given in Eq.(3.12). However, closed-form expressions cannot easily be derived for the amplitude and the phase angle of this mass motion. In fact, Fig.3.6 shows clearly that the functions $\bar{x}$ and $\bar{z}$ are neither in phase or phase-opposition; therefore, the initial value of the mass motion does not coincide with its amplitude as in the case of the relative motion. To determine such an amplitude, it is required to evaluate the maximum absolute value of $\bar{x}$ within the time interval $[0, \pi]$; however, due to the transcendental form of this function, the calculation can only be carried out numerically.

The non-dimensional response amplitude has therefore been evaluated using the max function in Matlab [141] in the frequency ratio range 0:2.5 for varying friction ratio; the resulting curves are portrayed in Figs.3.7a-b. Since $\bar{x} = x/Y$, the amplitude $\overline{X}$ corresponds to the ratio between the amplitudes of the mass and of the base motions, which is defined as *displacement transmissibility* [143]; in this thesis work, the quantity $\overline{X}$ will therefore be referred to as non-dimensional response amplitude or displacement transmissibility indifferently. The boundary line represented in Fig.3.7 has been obtained by substituting the boundary value of the friction ratio from Eq.(3.21) into Eq.(3.26) and then evaluating numerically the maximum of the latter expression in $[0, \pi]$.

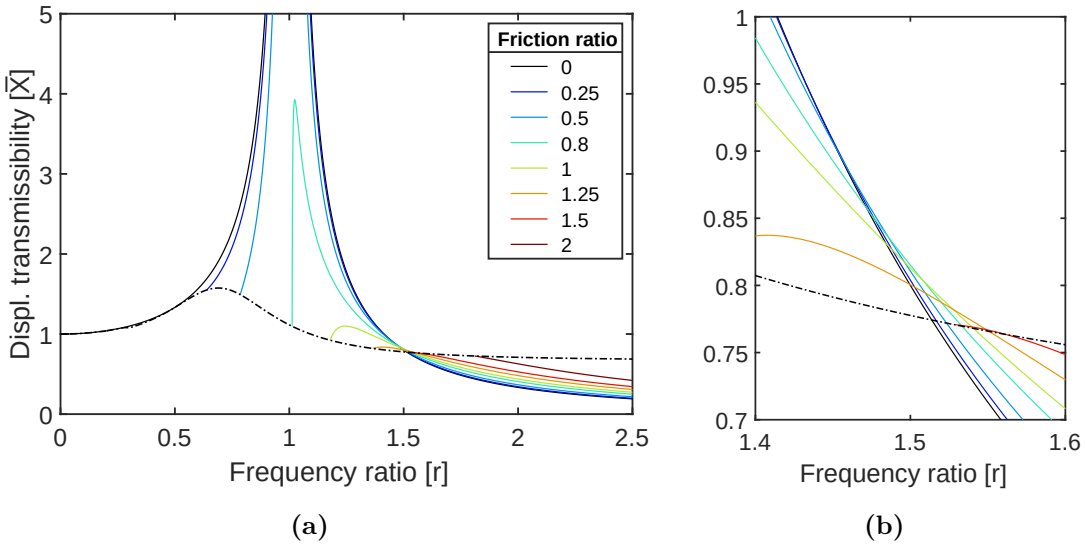

Figure 3.7: Displacement transmissibility of a SDOF system with Coulomb friction under joined base-wall excitation (**a**) and detail of the inversion of the curves (**b**).

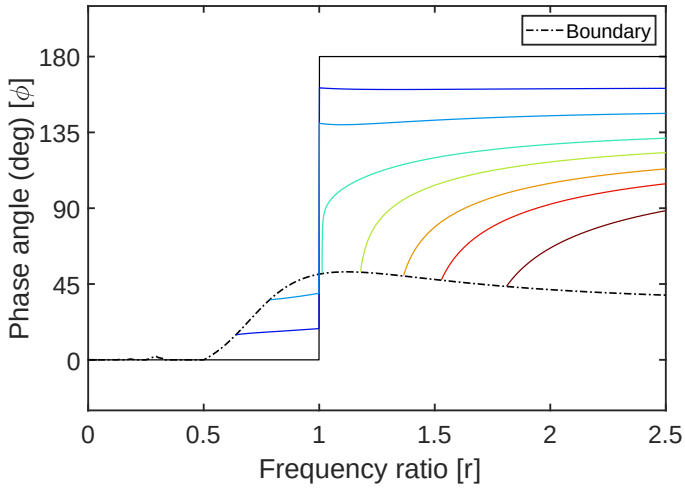

Figure 3.8: Phase angle between excitation and response of a SDOF system with Coulomb friction under joined base-wall excitation.

The phase angle ϕ between the excitation and the response can also be evaluated as follows. The first step consists in the numerical evaluation of the time instant $\tau_{\max}$ where the maximum absolute value of the mass motion is reached within the half-period $[0, \pi]$. The phase angle between the relative motion $\bar{z}$ and the mass motion $\bar{x}$ will be equal to the non-dimensional time lag between their maxima. Thus, since the maximum of $\bar{z}$ coincides with the instant $\tau = 0$, this phase angle ϕ_{zx} will be equal to $\tau_{\max}$ or $\tau_{\max} + \pi$ depending on whether $\bar{x}(\tau_{\max})$ is a maximum or a minimum of the mass motion. Finally, the phase angle ϕ is obtained by

summing the angles ϕ_z and ϕ_{zx}:

$$\begin{cases} \phi = \phi_z + \tau_{\max} & \text{if } \bar{x}(\tau_{\max}) \geq 0 \quad (3.27a) \\ \phi = \phi_z + \tau_{\max} + \pi & \text{if } \bar{x}(\tau_{\max}) < 0 \quad (3.27b) \end{cases}$$

where ϕ_z can be evaluated from Eq.(3.12). Also in this case, the boundary between continuous and stick-slip motions can be obtained by imposing $\beta = \beta_{\lim}$ in Eq.(3.27).

A discussion on the results shown in Figs.3.7 and 3.8 is presented in what follows.

- As in the fixed-wall case discussed in Section 2.5.1, the resonant peaks shown in Fig.3.7a, as well as in Fig.3.2a, are only finite when the friction ratio is larger than $\pi/4$. This behaviour can be explained analytically by calculating the value assumed by the boundary friction ratio from Eq.(3.21) when $r \to 1$:

$$\beta_n = \lim_{r\to 1} \sqrt{\frac{(V-1)^2}{U^2 + \left(\frac{S}{r^2}\right)^2}} = \lim_{r\to 1} \left| \frac{\frac{1}{1-r^2}}{\frac{\sin(\pi/r)}{r[1+\cos(\pi/r)]}} \right| = \frac{\pi}{4} \qquad (3.28)$$

  As can be seen from Fig.3.4, the transition from continuous to stick-slip regime occurs at higher and higher frequency ratios as the friction ratio is increased. This implies that the continuous transmissibility curves in Fig.3.7a start at higher values of r for increasing values of β. When $\beta > \pi/4$, this starting value becomes larger than unity and, as a consequence, the infinite resonance is eliminated from the curve. The resulting effect is that the resonant peak becomes finite and shifts towards higher values of r. This peak eventually disappears when high values of the friction ratio are considered, as discussed in detail in Section 3.6.

- Fig.3.7a clearly shows that all the transmissibility curves tend to zero when $r \to \infty$, meaning that as the driving frequency is increased at much larger values than the natural frequency of the system, the mass will display more and more narrow oscillations till getting asymptotically stationary. However, a major difference with the fixed-wall case emerges looking at the motion regimes exhibited at high frequencies. From Fig.3.4, it is evident that both

boundaries tend to infinity when $r \to \infty$; this can also be easily shown analytically. As a result, the response of the system will always be continuous at very high frequencies. It is worthwhile observing that, while the mass motion has a negligible amplitude, the relative motion between mass and wall is still significant at high frequencies. This is also shown by Fig.3.2a, where it can be observed than the non-dimensional amplitude of the relative motion tends asymptotically to 1 when $r \to \infty$, independently of the friction ratio.

- One of the most interesting elements highlighted in Fig.3.7a is the presence of an inversion of the transmissibility curves, also shown in details in Fig.3.7b. This inversion occurs in a very narrow region localised around the frequency ratio $r = 1.5$; starting from here, Coulomb damping amplifies the response of the system. The inversion also affects the role of the boundary curve; in fact, when the transmissibility increases with β, this curve represents an upper bound for the continuous transmissibility curves rather than a lower bound. Even though this amplification effect may appear as counter-intuitive, a similar behaviour is notoriously shown by base-excited viscous SDOF systems. It is worth noting that in the system shown in Fig.3.9a the vibration is transmitted from the base to the mass through the parallel of the spring and of a damper, exactly as in the system studied in this chapter. In the viscous case, as shown in Fig.3.9b, the inversion of the transmissibility curves occur at $r = \sqrt{2}$, where the displacement transmissibility is unitary independently of the damping ratio. Conversely, in Coulomb damped systems the inversion occurs at slightly higher frequencies and in a narrow frequency ratio range, approximatively $1.4 < r < 1.55$, rather than in a single point. Furthermore, the value of the displacement transmissibility in this region is smaller than unity, as can be seen in Fig.3.7b. A mathematical explanation of this inversion phenomenon can be obtained introducing the monoharmonic approximation $\bar{z} \cong \overline{Z} \cos \tau$ considered in Levitan's work [28]. If this approximated formulation is taken

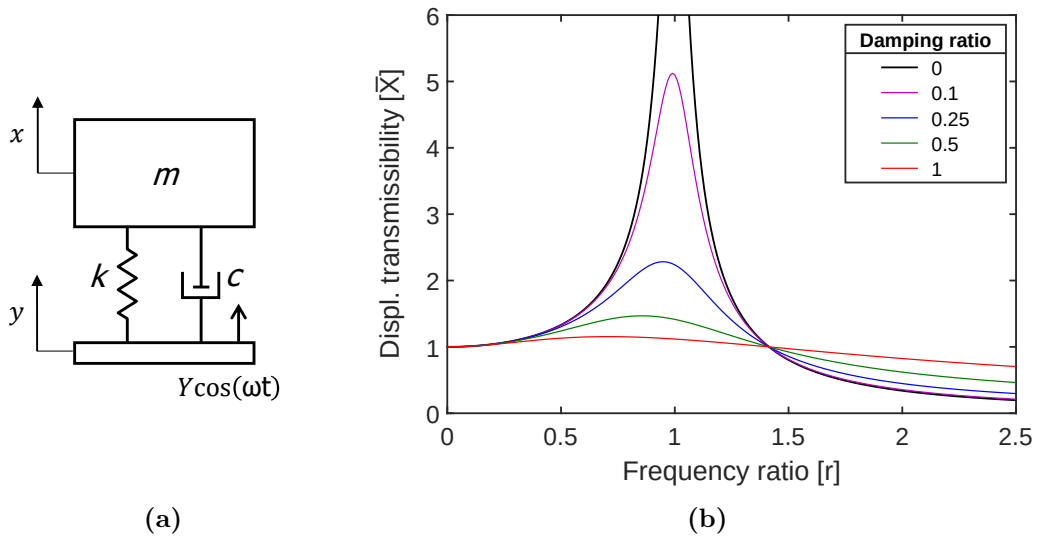

(a) **(b)**

Figure 3.9: SDOF system with viscous damping under harmonic base motion (**a**) and its displacement transmissibility for varying viscous damping ratio (**b**).

into account instead of the complete expression of the relative motion given in Eq.(3.10), the time response of the system can be written as:

$$\bar{x} \cong \overline{Z}\cos\tau + \cos(\tau + \phi_z) \cong \frac{1}{r^2}\left(\overline{Z}\cos\tau + \frac{\beta U}{V}\sin\tau\right) \tag{3.29}$$

The amplitude of this harmonic function can be evaluated analytically, yielding:

$$\overline{X} \cong \sqrt{V^2 - \left(\frac{2-r^2}{r^2}\right)(\beta U)^2} \tag{3.30}$$

consistently with the result presented by Levitan [28]. Eq.(3.30) shows that, if the response of the system were monoharmonic, there would be an inversion of the transmissibility curves occurring at $r = \sqrt{2}$ and $\overline{X} = 1$, exactly as in the viscous case. However, the transmissibility curves represented in Figs.3.7a-b show that the other harmonic components of the response have a non-negligible effect on this inversion phenomenon.

All the results presented in this chapter so far are limited to the case of continuous non-sticking relative motion between mass and wall; the domain of validity of these solutions has also been derived. To complete the dynamic analysis of the system, a numerical investigation of the stick-slip response is presented in the following section.

3.6 Numerical validation and extension to stick-slip regime

This section introduces a numerical approach for the evaluation of the time response, displacement transmissibility and phase angle for SDOF systems with Coulomb friction, with the scope of providing a numerical validation of the results presented in the previous sections and achieving a complete overview of the dynamic behaviour of SDOF systems under joined base-wall motion, including stick-slip responses.

3.6.1 Description of the numerical approach

The main challenge in the numerical time integration of the governing equation reported in Eq.(3.4) is doubtlessly related to the occurrence of stick-slip in the response. In fact, while continuous responses can be calculated with standard numerical solvers, stick-slip motions are characterised by the presence of rapid variations due to the transitions between the sticking and the sliding phases and lead, as discussed in Section 2.3.3, to numerical stiffness in the problem. The approach proposed in this section consists in using standard integration methods by setting explicit conditions to account for the transition between different regimes.

A schematic representation of the implemented numerical algorithm is given in Fig.3.10 and the major steps are detailed in what follows.

- As explained in Section 2.5.1 with respect to the fixed-wall case, the response of this system is completely determined by three non-dimensional parameters, i.e. the frequency ratio, the friction ratio and the ratio between static and kinetic friction forces. These parameters can be selected by the user, as well as the initial conditions for the displacement and the velocity and the number of excitation periods N_{cyc}. Since the length of each period is equal to 2π in the current formulation, the final time will be equal to $2\pi N_{cyc}$.

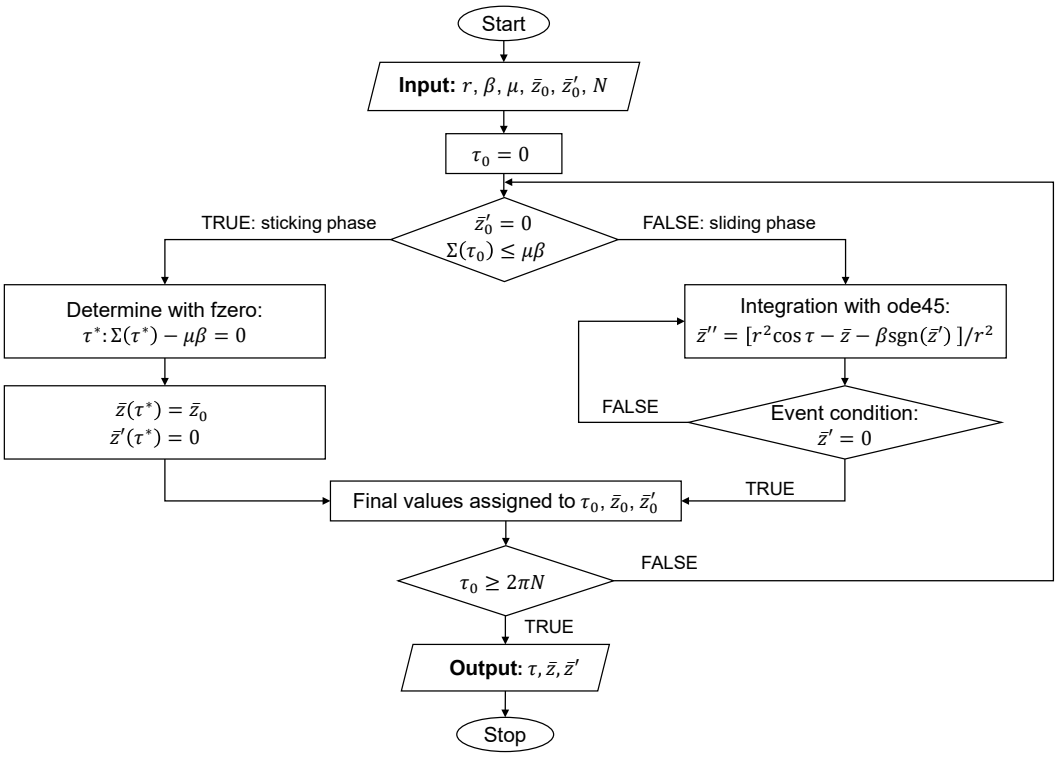

Figure 3.10: Flowchart of the numerical algorithm implemented for the calculation of the response of a SDOF system with Coulomb friction under joined base-wall excitation.

- As a first step, the algorithm checks if the sticking conditions:

$$\begin{cases} \bar{z}' = 0 & \text{(3.31a)} \\ \Sigma \leq \mu\beta & \text{(3.31b)} \end{cases}$$

  are verified. In the above equations, the function:

$$\Sigma = |\bar{z} - r^2 \cos\tau| \tag{3.32}$$

  denotes the amplitude of the overall dynamic loading acting in the contact. A sticking or a sliding phase will take place depending on whether these conditions are met or not.

- During the sliding phases, the relative motion $\bar{z}$ is continuous and the solution is nonstiff. Therefore, the governing equations are integrated by using a variable-step Runge-Kutta (4,5) method, implemented in the Matlab function ode45 [141]. These phases are terminated by the event condition $\bar{z}' = 0$;

when this happens, the algorithm checks if the second sticking condition, from Eq.(3.32)b, is also verified to determine if the following phase will be sticking or sliding.

- During the sticking phases, the relative displacement between mass and wall will be unchanged and the relative velocity will remain equal to zero. The stop will end when the dynamic force acting in the contact exceeds the static friction force, i.e. when $\Sigma > \mu\beta$. The final time instant of the sticking phase can therefore be evaluated by using the Matlab function fzero [141], as shown in Fig.3.10.

- The simulation will end when the final time $2\pi N_{cyc}$ is reached. The time response of the system can simply be obtained as the sum of the relative motion and the non-dimensional base motion $\cos\tau$. The response amplitude can be determined as the maximum absolute value within the time interval $[2\pi(N_{cyc}-1), 2\pi N_{cyc}]$, corresponding to the last excitation period. Similarly, given that the initial time of this interval corresponds to a maximum of the excitation, the phase angle can be determined as the non-dimensional time instant where the maximum displacement occurs. However, when stick-slip occurs, the maximum response usually coincides with a sticking phase rather than a single point and the definition of phase angle considered in this chapter cannot be applied. Therefore, the numerical evaluation of the phase angle has not been carried out for the case discussed in this chapter. Nonetheless, a different definition will be provided in Chapter 4 for overcoming this issue and comparing numerical and experimental phase angles also in stick-slip regime.

3.6.2 Results and discussion

Steady-state time response

The steady-state relative and absolute mass motions, described by Eqs.(3.10) and (3.26) respectively, have been compared to the numerical results obtained with the algorithm introduced in the previous section for different sets of the parameters r,

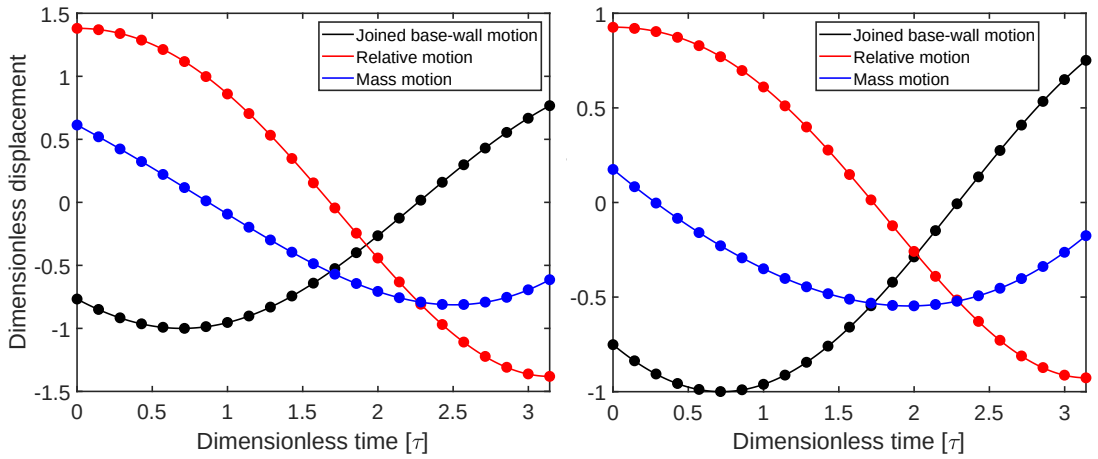

(a) $r = 1.5$, $\beta = 1$, $\mu = 1$ **(b)** $r = 2.3$, $\beta = 2.3$, $\mu = 2$

Figure 3.11: Steady-state time response of a SDOF system with Coulomb friction under joined base-wall excitation for varying parameters r, β and μ: analytical (continuous lines) vs numerical (round markers).

β and μ. An excellent agreement has been observed for all the cases investigated, as shown in Figs.3.11a-b for two specific combinations of these parameters. In particular, the numerical responses have been evaluated setting a number of cycles equal to $N = 200$ and zero initial conditions for the relative displacement and velocity. It has been observed that most responses converge to a steady-state solution for a significantly lower number of cycles. During the integration process, the absolute and relative tolerances were set to 10^{-6} and 10^{-12} respectively. The harmonic excitation $\cos(\tau + \phi_z)$ is also represented in the non-dimensional interval $[0, \pi]$ and appears perfectly aligned to the numerical forcing function, showing that a very good agreement is also achieved for the phase angle ϕ_z.

Motion regimes

Figs.3.12-3.13 shows the motion regimes observed numerically in the parameter space $r - \beta$, also including the evaluation of the number of stops displayed in the steady-state response. The numerical simulation were carried out for $r = 0 : 0.02 : 2.5$, $\beta = 0 : 0.01 : 4$ and considering two different values of the ratio μ. In Fig.3.12, it is possible to appreciate the agreement between the analytical and the numerical boundaries of these motion regimes. Furthermore, it can be observed that two-stop motions are widely predominating in the stick-slip region; the direct transition

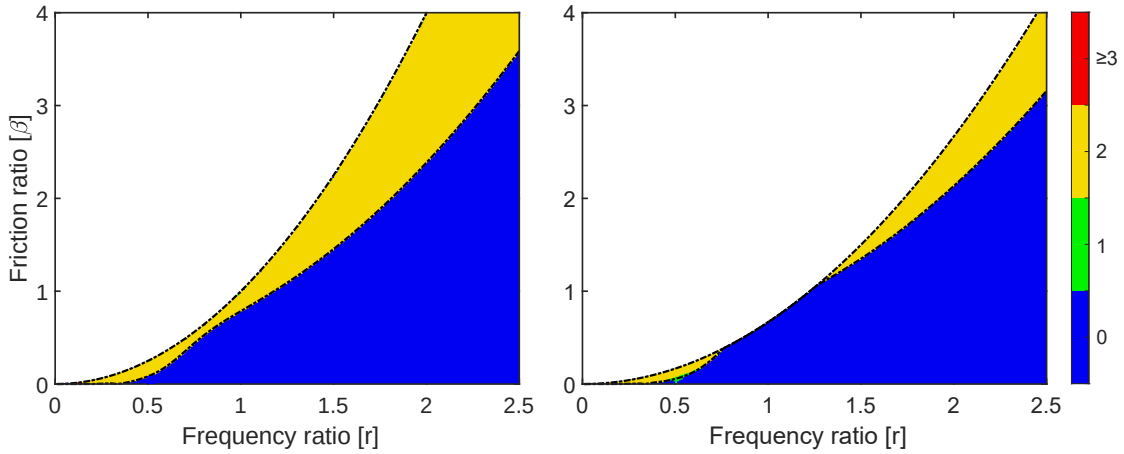

(a) $\mu = 1$ **(b)** $\mu = 1.5$

Figure 3.12: Number of stops of the steady-state response a SDOF system with Coulomb friction under harmonic joined base-wall excitation in the parameter space $r-\beta$ for varying ratio between static and kinetic friction forces. The dashed black lines represent the analytical boundaries of the motion regimes.

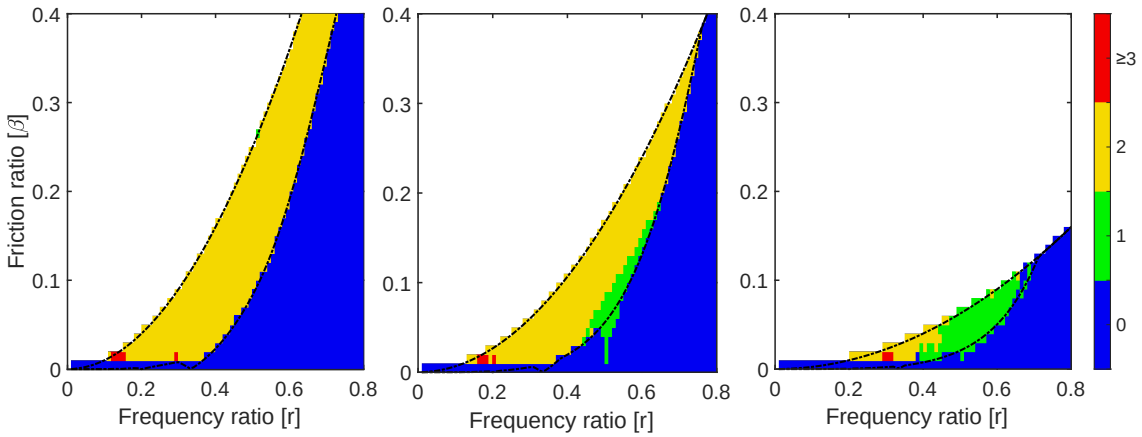

(a) $\mu = 1$ **(b)** $\mu = 1.5$ **(c)** $\mu = 4$

Figure 3.13: Detail of the number of stops in the low-frequency region of parameter space $r - \beta$ for varying ratio between static and kinetic friction forces.

from the continuous to the permanent sticking regime, forecast in Section 3.4.3 for $\mu > 1$, can also observed in Fig.3.12b for the case $\mu = 1.5$. In Fig.3.13, the motion regimes in the low-frequency region can be observed in more detail. Particularly, it can be seen that:

- multi-stop motions, i.e. stick-slip motions with more than two stops per cycle, can occur under joined base-wall excitation, although they have only been observed for a very limited number of parameter combinations;

- asymmetric one-stop motions occurs in a small region around the frequency ratio $r = 0.5$ when $\mu > 1$. The extension of this region increases with μ and one-stops motions can become predominant in the stick-slip region for high values of this parameter, as shown in Fig.3.13c.

- one-stop motions have not been detected for the case of $\mu = 1$; however, asymmetric non-sticking responses have been observed at $r = 0.5$.

The latter behaviour appear very similar to those observed by Csernak et al. [70] for SDOF systems with a fixed wall in the case of $\mu = 1$. In the fixed-wall case, as specified in Section 2.5, a one-parameter continuum of asymmetric solutions exists in correspondence of the even sub-resonant frequencies when:

$$\beta \leq \frac{1}{4n^2 - 1} \tag{3.33}$$

where $n = 2, 4, 6, ...$ In the joined base-wall motion case, it has been observed from numerical results that these asymmetric solutions occur for:

$$\beta \leq \frac{r^2}{4n^2 - 1} \tag{3.34}$$

which leads to $\beta < 0.083$ in the case of $r = 0.5$. Due to the dependency on r^2, the RHS of Eq.(3.33) assumes very small values for the other sub-resonant frequencies, so that asymmetric non-sticking responses can realistically be observed only for the above value of the frequency ratio.

Displacement transmissibility

The analytical and numerical response amplitudes have been compared in the frequency ratio range $0 : 2.5$ for varying friction ratio and $\mu = 1$. The results, shown in Figs.3.14a-b, show an excellent agreement. In addition, stick-slip response amplitudes have been plotted, allowing for the following considerations.

- The stick-slip responses observed immediately after the transition from the permanent sticking to the sliding regime present a drop below unity in the displacement transmissibility. This phenomenon becomes more and more visible as the friction ratio is increased.

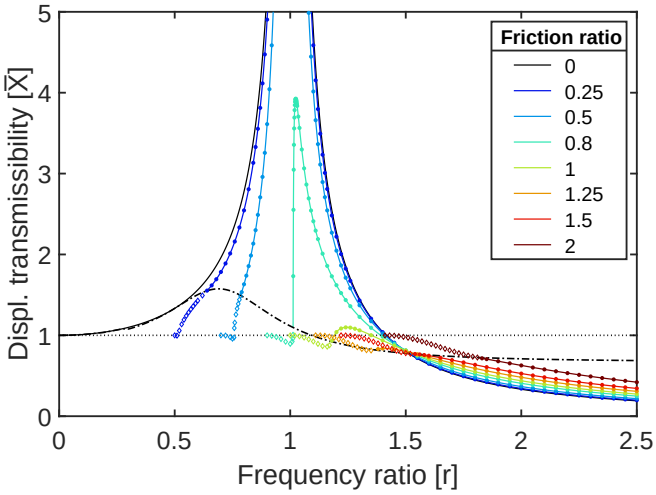

(a)

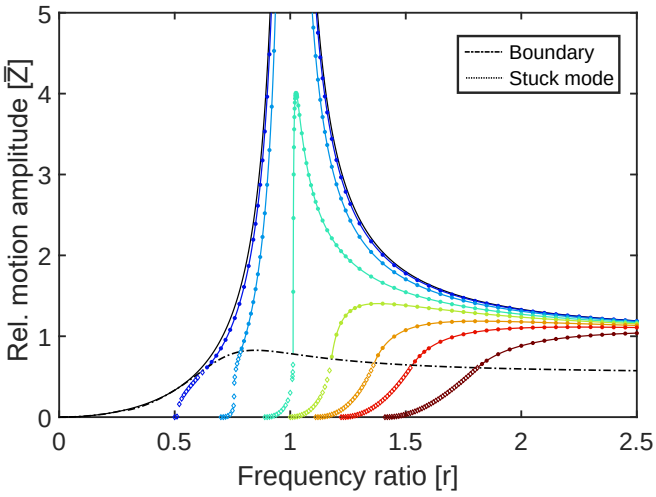

(b)

Figure 3.14: Non-dimensional response amplitude of a SDOF system with Coulomb friction under joined base-wall excitation: absolute mass motion (**a**) and relative motion in the contact (**b**). Analytical results are represented by the continuous lines, while numerical results are represented with round (continuous motion) and with diamond markers (stick-slip motion).

- The transition from stick-slip to continuous regime is characterised by different behaviours depending on the friction ratio. For lower values, such as in the case $\beta = 0.2$, there is a gradual increase of the response amplitude both before and after the transition, with the continuous transmissibility curve displaying a very similar pattern to the undamped case. At intermediate values, represented by the cases of $\beta = 0.5$ and $\beta = 0.8$, the increase in the response amplitude is very sharp, since the transition occurs in proximity of

the resonant peak; in these cases, small variations of r can lead to sudden and significant change in the displacement transmissibility. Finally, when $\beta \geq 1$, the frequency range where stick-slip occurs becomes larger and there are no significant resonant peaks; as a consequence, the variations of the displacement transmissibility occur very gradually. It has been observed that starting from $\beta = 1.06$ the maximum displacement transmissibility displayed in sliding regimes decreases below unity; therefore, it can be affirmed that no resonance occurs at all for larger values of the friction ratio.

- In Fig.3.14a, it is possible to observe that the transmissibility curve characterised by $\beta = 2$ does not pass through the point of inversion located at $r \cong 1.5$. More in general, it can be affirmed that the inversion phenomenon as described in Section 3.5 only regards the continuous transmissibility curves. When $\beta > 1.55$, the transition from stick-slip to continuous regime occurs after $r \cong 1.5$ and similar patterns to that of the curve $\beta = 2$ will be observed. Furthermore, also at lower frequencies, the stick-slip transmissibility curves do not respect the dependency of the continuous transmissibility on the friction ratio. For instance, in the range $1.23 < r < 1.5$, the amplitude of the continuous response decreases with β, but the amplitude of the stick-slip response increases if the curves $\beta = 1.25$ and $\beta = 1.5$ are considered. More regular patterns are observed in Fig.3.14b for the amplitude of the relative motion, which appears to decrease with the friction ratio independently of the motion regime.

Finally, the effect of the ratio μ on the displacement transmissibility and the relative motion amplitude is represented in Figs.3.15a-b for the case $\beta = 1$. It can be observed that, for $\mu > 1$, the starting point of the sliding motion is shifted to higher frequency ratios and the transition occurs with a discontinuity. The patterns displayed by the transmissibility curves when stick-slip motion occurs are quite similar among each others. Nonetheless, it can be observed that, starting from the case $\mu = 1.5$, there is a direct transition from permanent sticking to

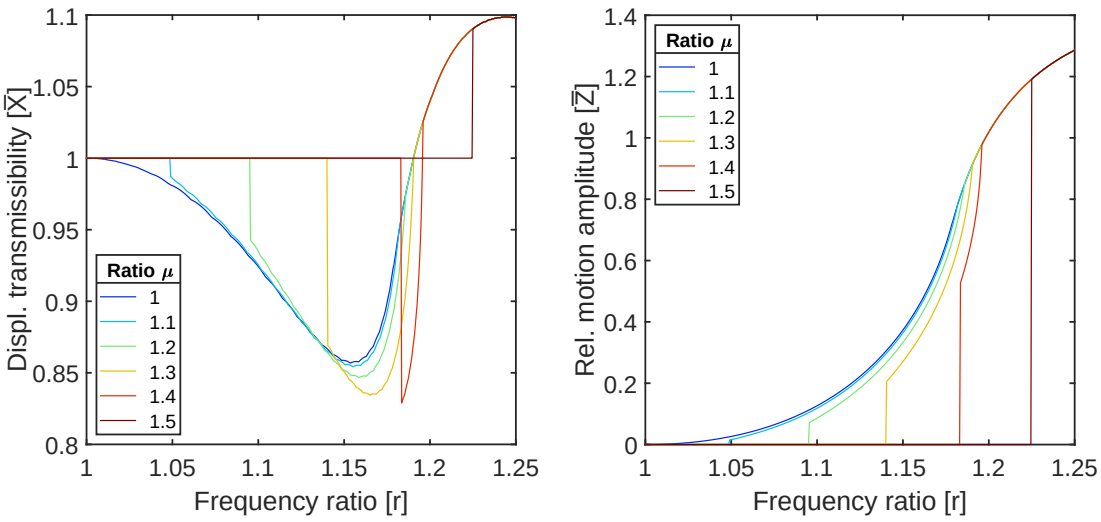

(a) **(b)**

Figure 3.15: Numerical response amplitude for $\beta = 1$ and varying ratio between static and kinetic friction forces: absolute mass motion (**a**) and relative motion in the contact (**b**).

continuous motion, in accordance with motion regimes scenario depicted in Fig.3.6c. Also in this case, the transition is characterised by a discontinuity, as shown in Figs.3.15a-b. The continuous transmissibility curves are instead unaffected by the variation of the static friction force.

3.7 Summary and concluding remarks

In this chapter, the dynamic response of a SDOF system with a Coulomb friction under joined base-wall motion has been investigated analytically and numerically.

In particular, analytical solutions have been derived for the continuous steady-state relative motion between the mass and the wall in contact and for the absolute motion of the mass. Closed-form expressions have also been obtained for the amplitude and the phase angle of the relative motion, while the displacement transmissibility and the phase angle between the excitation and the response have been evaluated numerically from the analytical expression of the time response. Furthermore, the domain of validity of the solutions presented for the continuous response has also been determined, providing an analytical formulation for the boundary between continuous and stick-slip regimes. The upper bound for the

presence of steady-state relative motion in the contact, either sticking or non-sticking, has also been derived analytically. These boundaries have been plotted in a two-dimensional parameter space for varying frequency and friction ratios, determining three different regions associated to the continuous, stick-slip and permanent sticking motion regimes. Different values of the static and the kinetic friction forces have also been taken into account in the formulation and their effect on these boundaries has been investigated.

A numerical approach has been introduced for validating the solutions presented for the continuous response and investigating the dynamic behaviour of the system when stick-slip occurs; the agreement observed between the analytical and the numerical results was very good for all the cases investigated.

The main results of this investigation were: (i) the development of a better understanding of how different motion regimes can occur depending on the frequency and friction ratios, particularly in the low- and high-frequency regions and at resonance; (ii) the presence of an inversion of the transmissibility curves, occurring across a narrow frequency range located around $r = 1.5$ and leading to the amplification of the transmissibility at high frequencies as an effect of Coulomb damping; (iii) a characterisation of the stick-slip responses, including how the patterns displayed by the transmissibility curves and the number of stops evolve depending on the kinetic and static friction forces.

Overall, the results presented in this chapter have contributed to the development of a more complete understanding of SDOF oscillators with Coulomb friction and revealed how the presence of a friction contact between two oscillating components has a significant impact on the dynamic behaviour of the system, which cannot be accounted for by simply assuming, for instance, a different reference system where one of the components is static. Nonetheless, the results obtained in this chapter, as well as those reported in Section 2.5.1 for SDOF systems with a fixed wall, are theoretical and based on important assumptions, first of all regarding the expression of the friction force according to the Coulomb's law. Therefore, in the next chapter, an experimental investigation will be introduced, aiming to verify

if these results can be reproduced in experimental conditions and to determine the main limitations to their validity.

A theory can be proved by experiment; but no path leads from experiment to the birth of a theory.

— Albert Einstein

4

Experimental investigation of a 1-storey frame with a metal-to-metal contact

Contents

4.1 Introduction

This chapter presents an experimental investigation of the dynamic behaviour of a SDOF system with a metal-to-metal contact under harmonic base or joined base-wall excitation. The main goal of the investigation is to provide an experimental validation for: (i) Den Hartog's analytical solutions for SDOF systems with a fixed wall; (ii) the solutions presented in Chapter 3 for SDOF systems with an

oscillating wall; (iii) the numerical results obtained in stick-slip regime with the approach presented in Section 3.6.

The experimental setup consists of a single-storey shear frame, where a harmonic excitation is imposed on the base plate and a friction contact is achieved between the steel top plate and a brass disc. The frequency and friction ratios can be selected by adjusting the driving frequency of the base motion and the normal force exerted by the disc on the top plate.

The experimental results are presented and compared to the analytical and numerical results using the displacement transmissibility and the phase angle as response metrics. The displacement of the top plate, corresponding to the mass motion in the SDOF model, is also shown in the time and the frequency domains for both continuous and stick-slip regimes. The setup does not allow to investigate the ratio between static and kinetic friction forces. Therefore, the analytical and numerical results used for the comparison have been derived assuming $\mu = 1$. Nonetheless, the potential role of different values of this ratio is considered in the discussion on the experimental results.

The chapter is structured as follows. The experimental setup is described in Section 4.2. Section 4.3 is dedicated to the description of the testing procedure, also including the preliminary tests for the estimation of the frequency and the friction ratio parameters and the processing of the results from the main forced vibration test. The results are presented in Section 4.4 in terms of the displacement transmissibility and the phase angle, while Section 4.5 shows a detailed comparison between the experimental and the numerical responses in the time and the frequency domains.

4.2 Experimental apparatus

The test rig used for the experimental investigations presented in this chapter is a single-storey shear frame composed of two metal plates connected through four metal bars, as shown in Fig.4.1. Each stanchion is doubly bolted to both floors. The main properties of these components are reported in Tab.4.1.

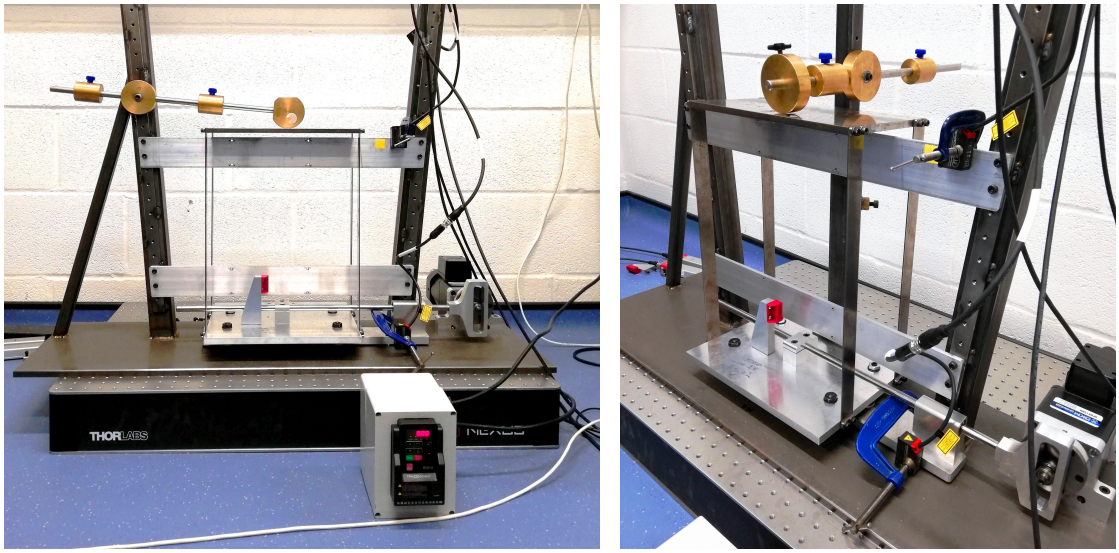

(a) Fixed wall configuration **(b)** Joined base-wall configuration

Figure 4.1: Pictures of the test rig. A rotor is connected to the base plate of a single-storey frame through a Scotch-yoke mechanism. A counterweight pinned to the external frame (**a**) or to the base plate (**b**) applies a normal force on the top plate.

Component	Size (mm)	Mass (kg)	Material
Top plate	$300 \times 153 \times 9.72$	3.372	Steel
Base plate	$300 \times 255 \times 12.7$	2.862	Aluminium
Bars	$410 \times 25.5 \times 1.60$	0.130	Steel

Table 4.1: Properties of the single-storey frame components.

A friction force is introduced in the system by means of a brass disc resting on the top plate producing a line metal-to-metal contact. The disc is mounted on a bar equipped with a counterweight system, so that the normal force, and therefore the friction force, applied to the plate can be modified by adjusting the position of the weights along the bar.

Two test configurations are considered by changing the location of the counterweight system. When the counterweight is pinned to the external frame (as shown in Fig.4.1a), the fixed-wall configuration is obtained. The joined base-wall configuration (shown in Fig.4.1b) is instead achieved by pinning the counterweight system to a post bolted to the base plate. A schematic representation of the test rig is reported in Fig.4.2.

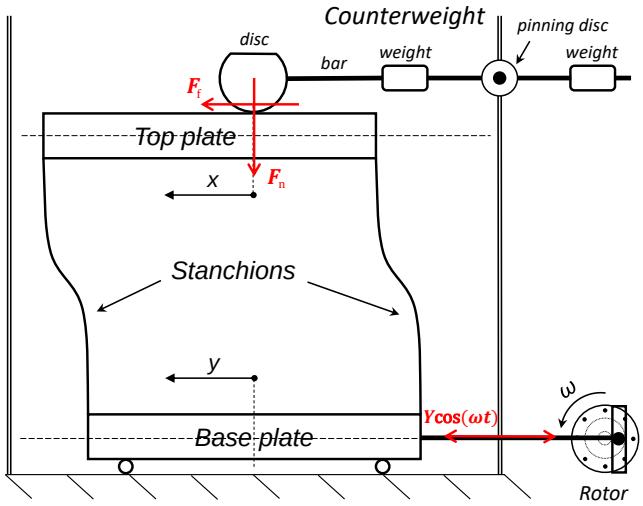

Figure 4.2: Schematic representation of the test rig in the fixed-wall configuration.

The single-storey frame is dynamically excited through the motion of the base plate. In particular, this motion is imposed by using an electric motor (DKM-9PBK) controlled through an inverter motor speed regulator (RS Pro RS510) and a Scotch-yoke mechanism in order to convert the rotating motion into a harmonic alternate motion. The frequency of the base displacement can be controlled by changing the input speed of the inverter, while the amplitude can be set by pinning the Scotch-yoke to different points of the rotor.

During the test, the displacements of the base and top plates are recorded with two separate laser displacement sensors (optoNCDT 1420, with a measuring range of 50mm [144]). These sensors are clamped to the external frame, as can be observed in Figs.4.1a-b.

4.3 Test procedure

The main purpose of this experimental investigation is the validation of the theoretical results obtained for the displacement transmissibility and phase angle of a SDOF system with Coulomb friction for varying frequency and friction ratios. To accomplish this goal, forced vibration tests have been run for different couples of values of r and β. However, preliminary tests were also needed to determine how these two parameters are related to the input driving frequency selected through

the inverter and to the normal force selected by shifting the weights along the counterweight axis. The suitability of the single-storey frame for reproducing a SDOF system, as well as the estimation of the frequency ratio are dealt within Section 4.3.1, while the experimental estimation of the friction ratio is presented in Section 4.3.2. Finally, in Section 4.3.3 it is shown how the aforementioned response metrics can be obtained by post-processing the experimental data.

4.3.1 SDOF model validation and frequency ratio estimation

The single-storey shear frame introduced in the previous section is meant to represent a SDOF mass-spring system. In a first approximation, the top plate corresponds to the mass of such a system, while the spring is represented by the four stanchions and characterised by their overall flexural stiffness. However, as a real structure, the frame has an infinite number of DOFs [24]. In order to determine if this structure can be modelled as SDOF system, it is required to verify whether one or more vibrating modes are excited within the frequency range explored in this experimental investigation.

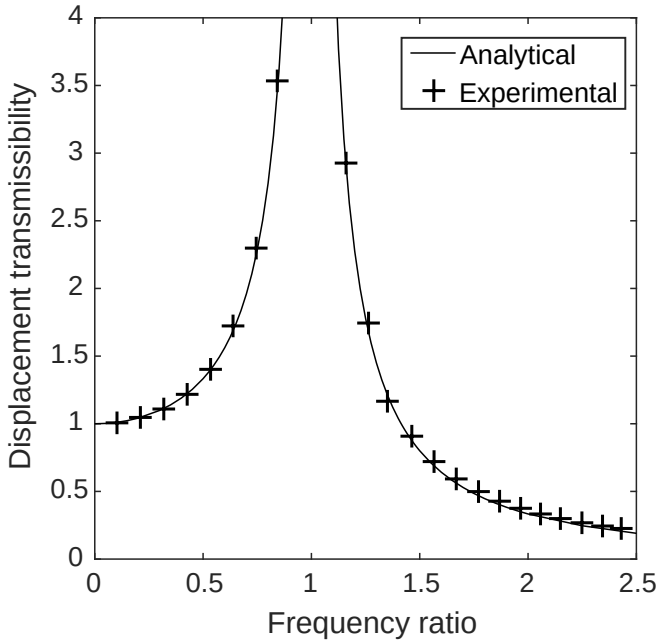

Figure 4.3: Displacement transmissibility of an undamped SDOF system: experimental results (markers) vs analytical results (continuous line).

The suitability of the SDOF model has been verified as follows. A series of tests were carried out in the absence of friction, i.e. by removing the counterweight from the setup, at different driving frequencies within the range $0 - 8$Hz, aiming to evaluate experimentally the displacement transmissibility. The procedure used to perform these tests and derive the transmissibility is the same used for the main forced vibration tests, which is described in detail in Section 4.3.3. The results from these tests, shown in Fig.4.3, have been fitted with the analytical curves:

$$\overline{X} = \frac{1}{|1 - r^2|} \tag{4.1}$$

corresponding to the displacement transmissibility of an undamped SDOF system [143], using a least-squares method. Two important conclusions can be drawn from the results of this preliminary test.

- The excellent agreement between the experimental results and the best-matching analytical curve implies that a SDOF model is a suitable representation of the single-storey frame.

- As shown in Eq.(2.15), estimating the frequency ratio requires the evaluation of the driving and natural frequencies. The driving frequency ω is specified by changing the input frequency of the inverter and can be visualised from the frequency spectrum of the excitation, which will exhibit a peak at $f = \omega/(2\pi)$. Therefore, the only unknown parameter in Eq.(4.1) is the natural frequency; the best agreement between experimental and analytical transmissibilities has been obtained for $f_n = 3.086$Hz. This value will be therefore considered as the natural frequency in the remaining of this chapter.

4.3.2 Friction ratio estimation

According to the definition introduced in Section 3.2, the friction ratio depends on the friction force F, the stiffness k and the amplitude of the base motion Y. Since k is a property of the frame and Y has been set to the fixed value of 1.75mm during the investigation, β could only be varied by adjusting the friction force

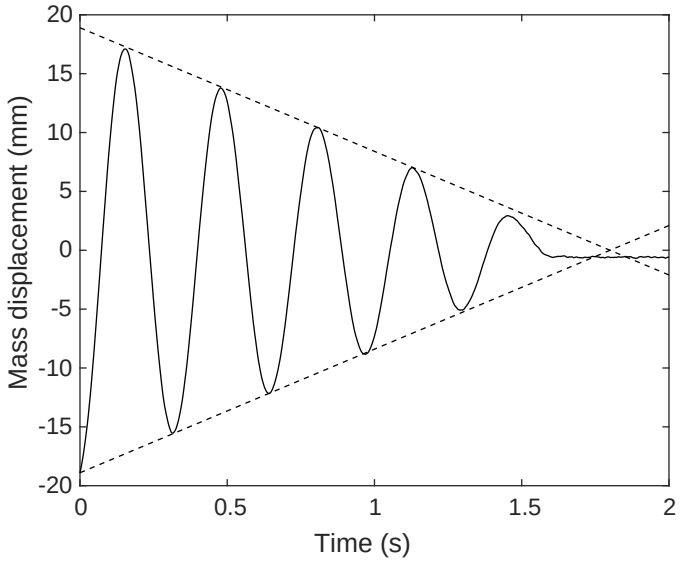

Figure 4.4: Experimental measurement of top plate free decay. The measured peaks show an approximatively linear slope (dashed line).

and, more specifically, by choosing a configuration of the counterweight masses producing the desired normal force on the top plate. The friction force acting between the disc and the top plate cannot be directly measured during the forced vibration test. Nevertheless, an experimental estimation can be obtained by using a *linear decrement* approach. A free vibration is generated in the frame by pulling and releasing the top mass. It has been observed that the peaks of each cycle of the freely decaying vibration have an approximatively linear slope, as shown in Fig.4.4. In accordance with the Coulomb model for free vibration. Therefore, the friction force can be evaluated as [143]:

$$F = \frac{k(x^{(1)} - x^{(2)})}{4} \tag{4.2}$$

where $x^{(1)}$ and $x^{(2)}$ are the displacements of two subsequent peaks. A better estimate can be obtained by averaging the force estimated for every pairs of subsequent peaks of the signal. Substituting Eq.(2.16) into Eq.(4.2), it is obtained that:

$$\beta = \frac{x^{(1)} - x^{(2)}}{4Y} \tag{4.3}$$

Since Y is known, the above formula can be used to calculate directly the friction ratio from the measured peaks, without need of estimating the stiffness value.

In order to validate each of the theoretical transmissibility and phase angle curves presented in Section 2.5.1 and in Section 3.5, it is required to run several forced vibration tests at different frequency ratios while keeping the friction ratio constant. However, variations of the friction ratio can occur either during a single test or among different tests due to several causes, which can lead to alterations in the normal force exerted by the disc on the top plate or in the friction coefficient between the surfaces in contact.

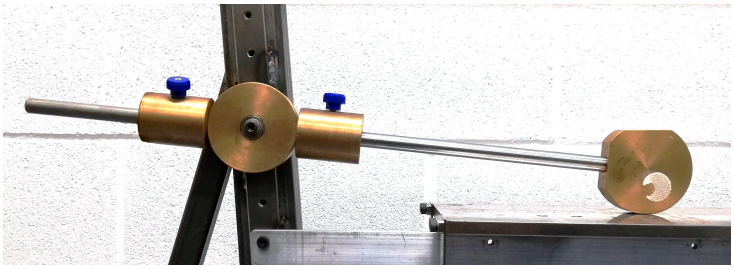

(a) Fixed wall configuration

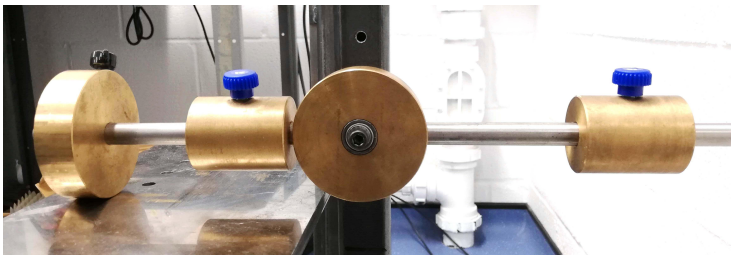

(b) Joined base-wall configuration

Figure 4.5: Counterweight system pinned to the external frame in the fixed-wall configuration (**a**) and to a base-fixed post in the joined base-wall configuration (**b**).

The variation of the normal force across different tests can be related to an imperfect pin connection between the counterweight bar and either the external frame (fixed-wall case, see Fig.4.5a) or the base-fixed post (joined base-wall case, shown in Fig.4.5b). In fact, this constraint should allow a free rotation around the pinning axis, preventing at the same time any horizontal or vertical displacement of the counterweight bar. Washers have been located on both sides of the pinning disc of the counterweight system in order to aid the rotation. Even so, pinning these components too tightly may partially prevent this free rotation, producing a reaction moment in the constraint, which would eventually alter the normal force

applied on the plate. On the other hand, an excessively loose tightening would allow an unacceptable horizontal displacement of the counterweight bar. Consequently, in order to limit both effects, care was taken when tightening.

The friction coefficient is an empirical parameter and its variation can be due to several underlying physical agents, including wear, debris formation, temperature, loading history and many others [2, 3]. These dependencies are still mostly unclear [137]; however, the focus of this investigation is not to quantify these variations but, as previously stated, to validate the presented theoretical results for varying frequency and friction ratios. Therefore, efforts have been made to reduce and control non-Coulomb phenomena which may occur during the test campaign. In particular, the setup allows the modification of the contact line between the disc and upper plate when significant wear has occurred; in fact, the brass disc can be rotated or shifted. Furthermore, debris has been removed after each test by thoroughly cleaning the surfaces in contact. Finally, the duration of each test was limited to 60s in the attempt of observing an approximatively constant value of the friction force throughout the experiment.

As a result, for each configuration of the weights along the counterweight bar, the friction force displayed only small variations from test to test, possibly due to a dependency on the exciting frequency or to a change in the external conditions. In addition, a fine tuning has been operated to refine the estimation of the friction ratio obtained from the linear decrement and to compensate for these possible friction force variations among different tests. Since both the displacement transmissibility and the phase angle were measured and compared to theoretical values, small adjustments have been applied to the normal force to yield simultaneously a good agreement for both response metrics. It is worth noting that, since it is possible to reproduce not only the magnitude but also the phase shift of the response, the fine tuning of the friction ratio does not affect the validation provided by the experiment.

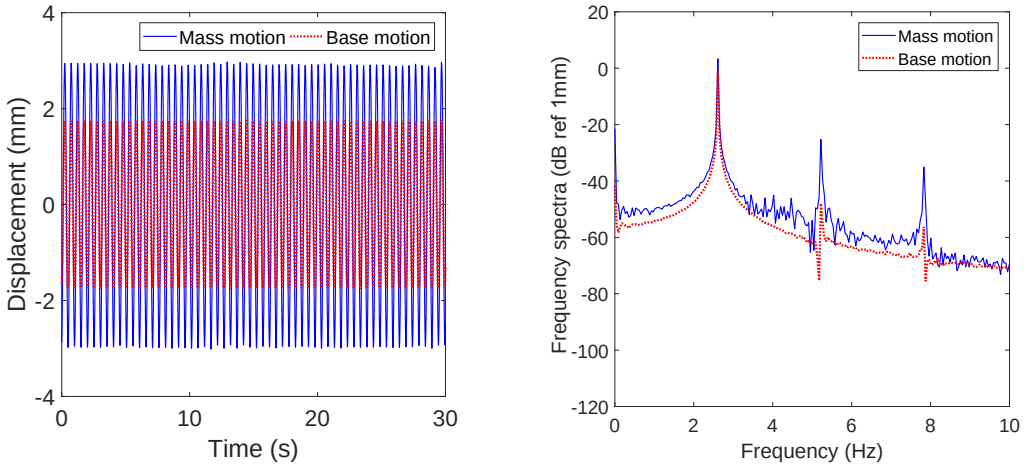

(a) Unprocessed signal

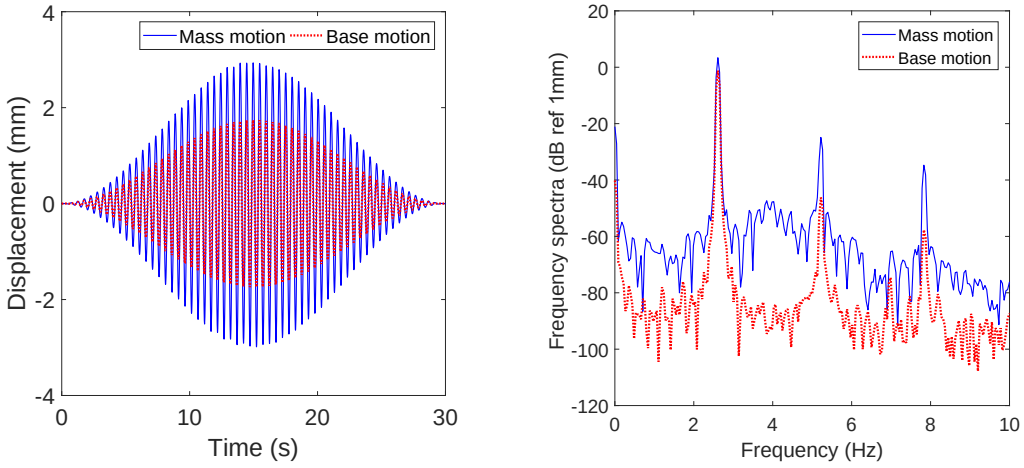

(b) Windowed signal

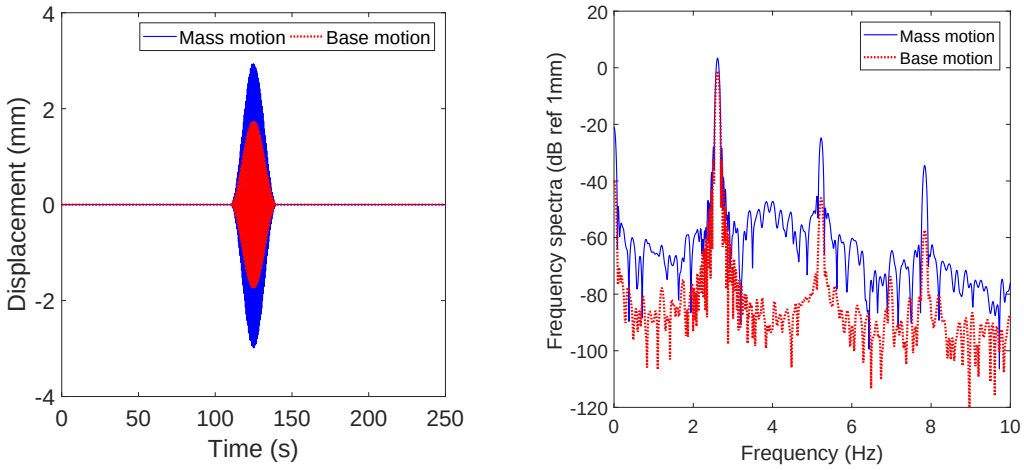

(c) Zero-padded signal

Figure 4.6: Base and mass displacements recorded for $r = 0.85$ and $\beta = 0.2$ in fixed-wall configuration and their frequency spectra before and after signal post-processing.

4.3.3 Signal processing for response metrics evaluation

In Chapter 3, the displacement transmissibility has been evaluated as the maximum absolute value of the non-dimensional steady-state response, while the phase angle has been defined as the non-dimensional time lag between the maxima of the excitation and of the response. Although correct, these time-domain based metrics are not suitable for experimental measurements. In fact, irregularities in the motion of the two plates might easily alter both the maximum value of their displacements and the time for which these maxima occurs. Moreover, as explained in Section 3.6.1, this definition of the phase angle cannot be applied when stick-slip occurs. Therefore, in this chapter, these quantities are evaluated from the frequency spectra of the displacements of the top plate $\texttt{fft}\{x\}$ and of the base plate $\texttt{fft}\{y\}$. In particular, the displacement transmissibility is evaluated as the ratio between the magnitude of the peaks displayed by these frequency spectra in correspondence of the driving frequency f:

$$\overline{X}_{\text{fft}} = \frac{|\texttt{fft}\{x\}(f)|}{|\texttt{fft}\{y\}(f)|} \tag{4.4}$$

while the phase angle is obtained as:

$$\phi_{\text{fft}} = \arg(\texttt{fft}\{x\}(f)) - \arg(\texttt{fft}\{y\}(f)) \tag{4.5}$$

In the remaining of this thesis, these quantities will be referred to as *frequency-based* displacement transmissibility and phase angle, as opposed to the previously considered *time-based* response metrics.

The signals acquired during the forced vibration test have to be processed in order to evaluate accurately the driving frequency, the displacement transmissibility and the phase angle. In particular, the signals from the laser displacement sensors have been recorded for 60s with a sampling frequency of 2kHz. This choice of duration for the recording window represents a compromise between obtaining an acceptable frequency resolution and, as previously mentioned, avoiding significant changes in the friction force due to wear and debris formation during a single test.

The acquired signals have been processed by applying a Hanning window (as defined in [145]) and zero-padding in order to reduce leakage and allow a more accurate resolution of the main peaks in the frequency spectrum. Fig.4.6 shows how post-processing affects a pair of recorded signals (with parameters specified in the figure caption) in the time and the frequency domains, respectively. It is worth noting that the frequency spectrum of the excitation displays not only a main peak in correspondence of the driving frequency, but also smaller peaks at other frequencies. This occurs because the base excitation generated by the setup is not perfectly monoharmonic and also other harmonics are excited, as inevitable when using a Scotch-yoke mechanism. Nevertheless, these additional frequency contents are typically more than 20dB below the fundamental peak so they do not affect the evaluation of the response metrics, which are referred to the main driving frequency. Conversely, the presence of secondary peaks in the response spectrum also depends on the nonlinearity of the friction force, as discussed in Section 4.5.

After the post-processing, the driving frequency can be evaluated as the frequency corresponding to the main peak of the excitation spectrum, while the transmissibility and the phase angle as finally obtained from Eqs.(4.4) and (4.5).

4.4 Transmissibility and phase angle results

In this section, the experimental results obtained from the forced vibration tests are presented for both fixed-wall and joined base-wall configurations and compared to the theoretical results presented in Section 2.5 and Chapter 3. These latter results have been obtained as follows.

- When $\beta < \beta_{\text{lim}}$, where the boundary friction ratio β_{lim} is obtained from Eq.(2.26) for the fixed-wall case and from Eq.(3.21) for the joined base-wall case, the analytical solutions for the continuous non-sticking response have been considered. The steady-state time responses, expressed in Eqs.(2.22) and (3.26) respectively, have been processed to obtain the frequency-based displacement transmissibilities and phase angles as defined in Eqs.(4.4) and (4.5).

- When $\beta \geq \beta_{\text{lim}}$, the stick-slip response has been evaluated numerically using the approach described in Section 3.6.1 and schematised in Fig.3.10 for the joined base-wall motion case. In the fixed-wall case, the same approach can be used by replacing the mass motion $\bar{x}$ to the relative motion $\bar{z}$ and expressing the forcing function as $\cos\tau$ rather than as $r^2\cos\tau$, as specified in the governing equation in Eq.(2.14). The same tolerances, initial conditions and number of cycles as those reported in Section 3.6.2 have been set. The numerical time responses have also been processed to obtain $\overline{X}_{\text{fft}}$ and ϕ_{fft}.

4.4.1 Base motion with fixed wall

The fixed-wall case has been investigated using the rig shown in Fig.4.1a. In addition to the two laser sensors mentioned in Section 4.2, the setup was equipped with a third laser sensor clamped to the external frame to measure the motion of the disc and ensure that it was negligible. For every test performed, it has been verified that the amplitude of the disc motion was at least two orders of magnitude smaller than the top plate vibration.

The parameter space investigated was $r = 0.025 : 2.5$ and $\beta = [0.2, 0.4, 0.6]$. Overall results for the displacement transmissibility and the phase angle from the experimental campaign are reported in Figs.4.7a-b, while the low-frequency ratio region is shown in detail in Figs.4.8a-b. For both quantities, the experimental results show a good agreement with the analytical and numerical results.

Comparing Figs.4.7a with Fig.2.4a, it can be observed that, despite the very similar patterns showed by the time-based and the frequency-based displacement transmissibilities in continuous regime, the latter does not always decrease with the friction ratio. In fact, it can be seen that a local inversion of the continuous transmissibility curves occur in the range $0.334 < r < 0.604$; it can be concluded that in this range, while the amplitude of the continuous responses decreases with β, there is an increase of amplitude in the main harmonic component of the response. Nonetheless, this inversion only concerns the continuous curves: in Fig.4.8, it can be observed the numerical stick-slip curves follow different patterns and generally appear

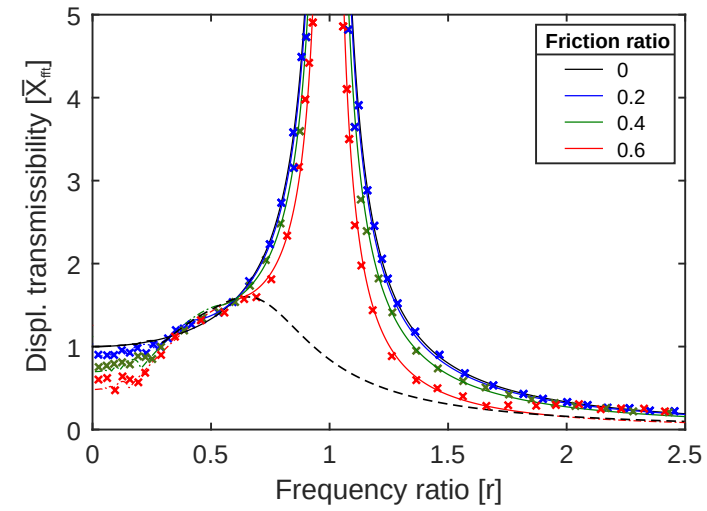

(a)

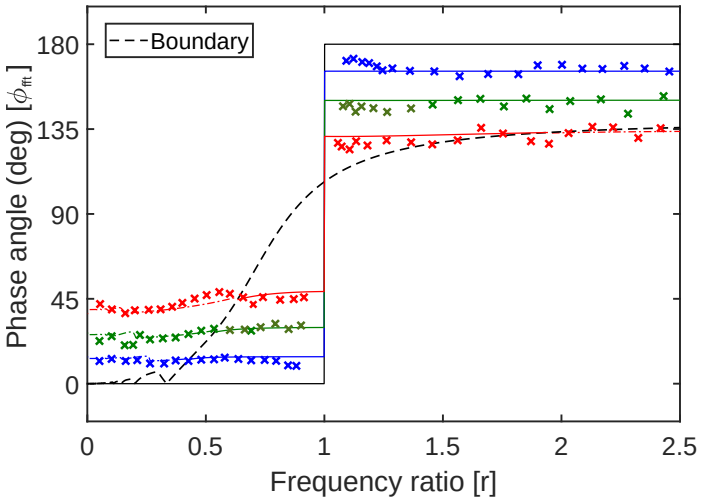

(b)

Figure 4.7: Displacement transmissibility (**a**) and phase angle (**b**) of a SDOF Coulomb friction oscillator with a fixed-wall under harmonic base excitation: experimental (markers) vs analytical (continuous lines) and numerical (dashed-dotted lines) results. The black dashed line represents the boundary between continuous and stick-slip regimes.

to decrease with β also in this frequency range. The experimental transmissibilities evaluated at these frequencies do not describe a clear pattern and only show very small variations with the friction ratio, independently of the motion regime.

Observing Figs.2.4b and 4.7b, it is possible to observe that the difference between the time-based and the frequency-based phase curves is more significant than that found for the transmissibility curves. In fact, the latter show a very low dependency on the frequency ratio, particularly in continuous regime. As a result, the frequency-

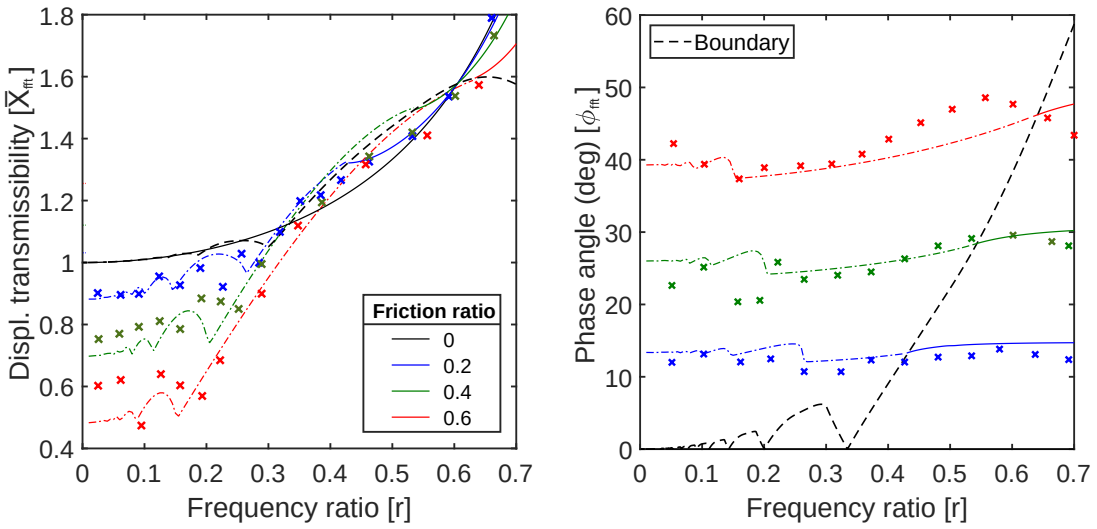

Figure 4.8: Displacement transmissibility (**a**) and phase angle (**b**) of a SDOF Coulomb friction oscillator with a fixed-wall under harmonic base excitation in low-frequency ratio region.

based phase angle is almost constant for varying r, while it shows significant variations for varying β. This sensitivity makes the frequency-based phase angle an interesting metric for measuring the friction ratio (and, therefore, the friction force) from the dynamic response of the structure. In other words, the evaluation of the phase angle from the measured displacement of the plates could be used to deduce the amount of Coulomb friction acting in the structure. The patterns displayed by the phase angle in stick-slip regime, depicted in Fig.4.8b, are slightly more irregular but the values remain very close to those displayed by the continuous curves.

Finally, it is worth noting that, according to the theoretical findings described in Section 2.5.1, stick-slip motion is expected at high frequency ratios only in the case $\beta = 0.6$, among those investigated. As can be seen in Fig.4.7a, although stick-slip could not be clearly observed during the experiments, there is an increase of the displacement transmissibility in the high-frequency range where stick-slip should occur; in the same frequency range, it can be seen from Fig.4.7b that the phase angle is still in good agreement with the numerical predictions.

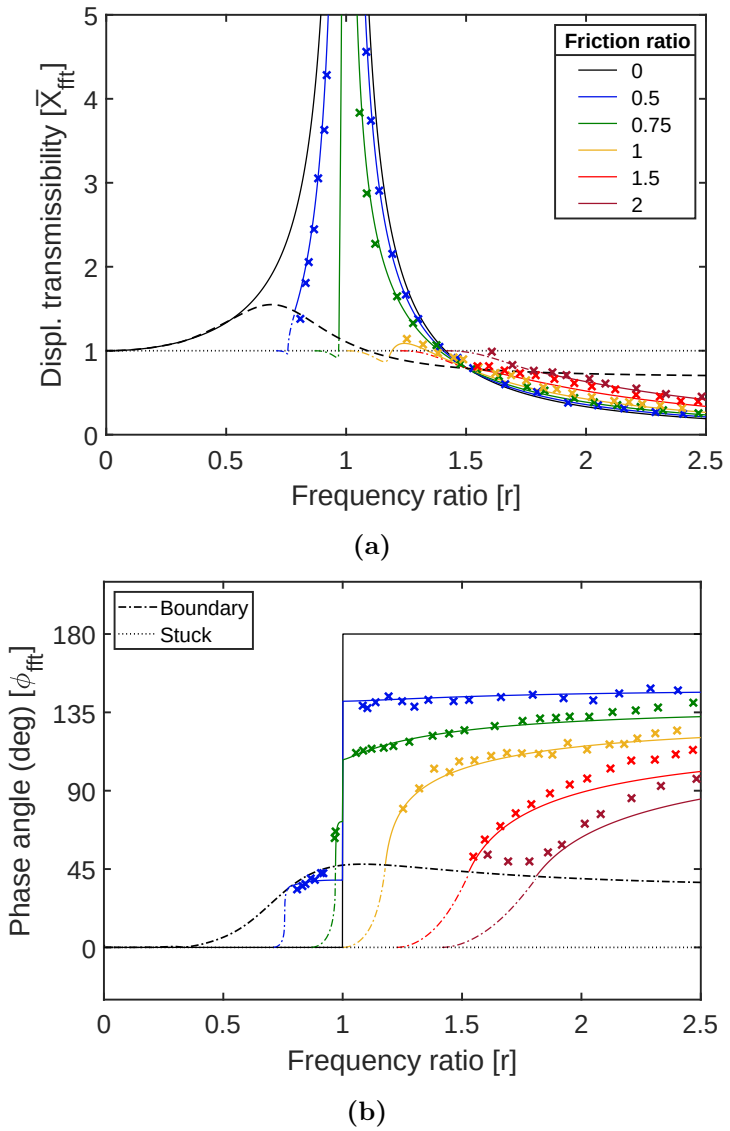

Figure 4.9: Displacement transmissibility (**a**) and phase angle (**b**) of a SDOF Coulomb friction oscillator under harmonic joined base-wall excitation: experimental (markers) vs analytical (continuous lines) and numerical (dashed-dotted lines) results. The black dashed line represents the boundary between continuous and stick-slip regimes.

4.4.2 Joined base-wall motion

The joined base-wall motion case has been investigated on the setup configuration shown in Fig.4.1b. An additional laser sensor clamped to the external frame has been used to measure the displacement of the disc to ensure that the wall was providing the same motion as the base. It has been observed that the disc motion is characterised by a negligible phase shift with respect to the base motion and a very low percentage increase in the level of noise.

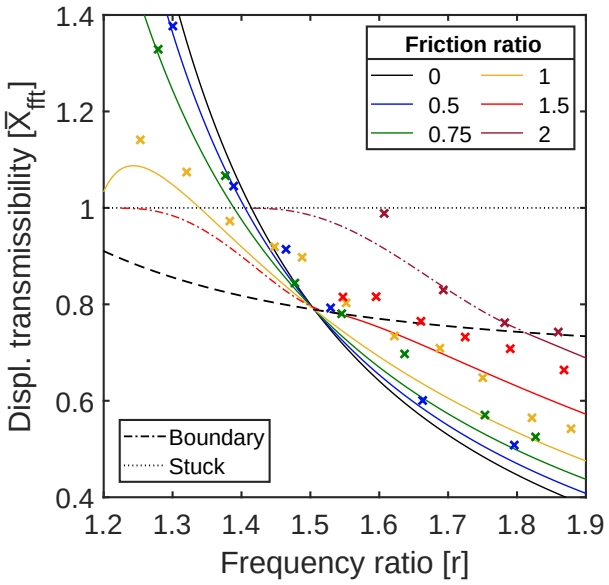

Figure 4.10: Detail of the inversion of transmissibility curves of a SDOF Coulomb friction oscillator under joined base-wall excitation at $r = 1.504$.

The parameters space investigated was such that $\beta = [0.5, 0.75, 1, 1.5, 2]$, while values for r ranged up to 2.5. The results of this experimental campaign are presented in Fig.4.9 and 4.10 and exhibit an overall good agreement with the analytical and the numerical results. In this configuration, the frequency-based transmissibility and phase angle curves are nearly the same as the time-based curves shown in Figs.3.7a and 3.8. A minor difference can be observed in the displacement transmissibility, where the inversion of the continuous curves occurs across a single point located at $r = 1.504$ rather than a narrow frequency range as observed in Section 3.5. This is well-visible in Fig.4.10, where it is also possible to observe that the experimental transmissibilities, despite assuming slightly larger values than the analytical ones, invert exactly at the frequency ratio predicted analytically in Section 3.5. The experiments have also confirmed that, while the amplitude of the response is not affected by friction ratio in proximity of the point of inversion, the same is not true for the phase angle, as shown in Fig.4.9b. The same figure also shows that, as in the fixed-wall case, the phase angle is very sensitive to variations in the friction ratio across a wide range of the frequency ratio. However, it is also shown that phase angle curves may overlap when $r < 1$, as in the cases of

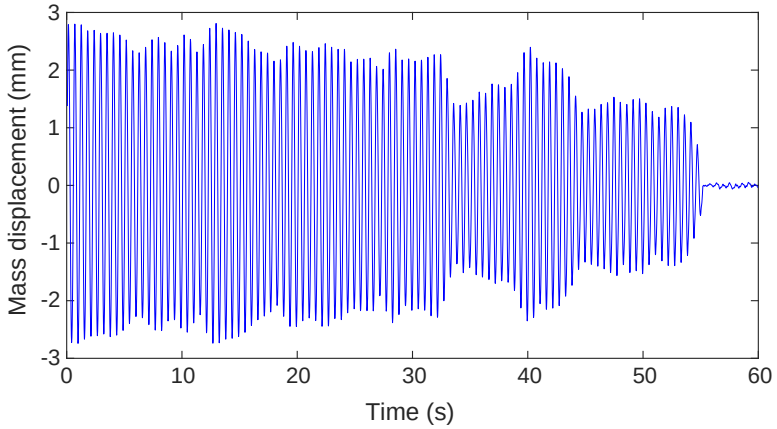

Figure 4.11: Experimental time response for $r = 1.15$ and $\beta = 0.7$, highlighting the occurrence of permanent sticking between mass and disc at $t = 54.8$s.

$\beta = 0.5$ and $\beta = 0.75$ of the current investigation.

In Fig.4.9, it is also possible to note that only a few tests could be carried out in stick-slip regime. Stick-slip was observed in the relative motion between the two plates only for $\beta = 2$, where a good agreement can observed between experimental and numerical transmissibilities but not in terms of the phase angle, where the experimental values are larger than the numerical predictions. The difficulties in investigating those stick-slip responses are discussed in the following subsection.

4.4.3 Limitations on the applicability of the setup

The results presented for the fixed-wall and the joined base-wall configurations have shown that the transmissibility and the phase angle of a SDOF Coulomb friction oscillator can be investigated with the proposed experimental setup.

Nonetheless, during the experimental campaign, it has been observed that for some particular conditions the top plate and the disc can become permanently stuck during the test. For example, Fig.4.11 shows the displacement of the top plate in a test where a permanent sticking occurs after about 55s. It is worth noting that a steady-state condition is apparently reached in a first stage but this is followed by a variation in the setup conditions which leads to a new transient ending with the permanent sticking. In order to further investigate this phenomenon, the test has been repeated under the same conditions. It has been found that the time at which

permanent sticking takes place can significantly vary across these tests. Moreover, it has been noted that, starting a new test directly from this stuck condition, no motion of the top plate would be observed; this is not true if the disc is removed and then reapplied onto the plate. It has not been possible to determine the causes of this phenomenon, which might include: (1) initial conditions variation; (2) contact properties variation, including temperature, wear and debris formation during the test; (3) setup imperfections; (4) transient chaotic behaviour.

The particular test conditions for which the permanent sticking has been observed are discussed in what follows. In the fixed-wall case, the sticking has occurred for values of the friction ratio above $\beta \cong 0.7$, independently of the exciting frequency. As for the joined base-wall motion case, the phenomenon was observed starting from $\beta \cong 0.7r^2$. This observation suggests that a difference between static and kinetic friction forces may be among the causes of the permanent sticking. Moreover, recent studies based on more advanced friction models [146] show that the boundary between sliding and permanent sticking regimes might also depend on frequency ratio in the fixed-wall case and occur at lower friction ratios within certain frequency ranges.

Due to the occurrence of permanent sticking, it is difficult to achieve an accurate experimental evaluation of the response metrics within the stick-slip region in the joined base-wall motion case, as already mentioned in Section 4.4.2. In particular, stick-slip motion has only been observed for $\beta = 2$, i.e. for the largest friction ratio investigated. This can be explained by recalling that, as shown in Figs.3.4 and 3.5, in the joined base-wall motion case the extension of the parameter space region associated to the stick-slip regimes becomes larger for high values of β.

In conclusion, this setup cannot be used to investigate with sufficient accuracy the displacement transmissibility and the phase angle when $\beta \geq 0.7$ in the fixed-wall configuration and $\beta \geq 0.7r^2$ in the joined base-wall motion configuration.

4.5 Mass motion analysis in the time and frequency domains

In this section, the experimental results obtained for fixed pairs of the parameters r and β are compared to the steady-state response yielded by the numerical approach in different motion regimes. Particularly, the response is investigated in the time and frequency domains to account for features such as the number of stops per cycle in stick-slip regime and their duration, as well as the multi-harmonic content, which cannot be captured by the response metrics presented in Section 4.4.

During the test, the signals were recorded for 60s only after a steady-state condition was reached. For this reason, in order to compare the numerical and the experimental time responses, the recorded displacement of the top plate has been shifted to match the first zero crossing of the numerical steady-state mass motion.

The comparison between the experimental and the numerical responses, achieved for the fixed-wall configuration, is shown in Figs.4.12 and 4.13 for different values of r and $\beta = 0.2$. In particular, Fig.4.12 presents the comparison between the time responses in a shorter and a longer time of observation. It is possible to observe that the experimental mass motions are well reproduced by the numerical simulations both in continuous and in stick-slip regimes, even when several stops occur during each period. Nonetheless, observing the comparison of the responses in a longer time window, it is possible to see that the displacement of the top plate can present a low-frequency variation not accounted by the numerical simulations; this is well-visible in Fig.4.12d. An asymmetric experimental response with one stop per cycle is shown in Fig.4.12b. The presence of asymmetries in the response in correspondence of the sub-resonant frequencies has been discussed from a theoretical point of view in Sections 2.5.1 and 3.6.2. In particular, in reference [70] it is specified that these asymmetric solutions are expected at $r = 0.5$ when $\beta < 1/3$. It is also worth noting that, if the static and the kinetic friction forces are equal, the solution should be non-sticking and the asymmetry is only expected at $r = 0.5$. The experimental response is instead characterised by the presence of one stop per cycle and it has been observed that this behaviour would also occur if the frequency

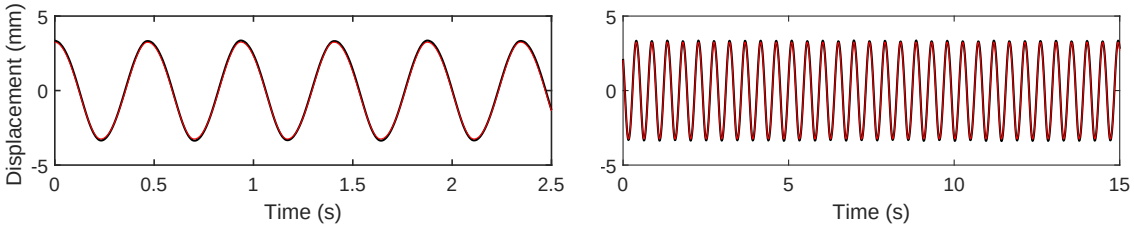

(a) Continuous motion ($r = 0.7$)

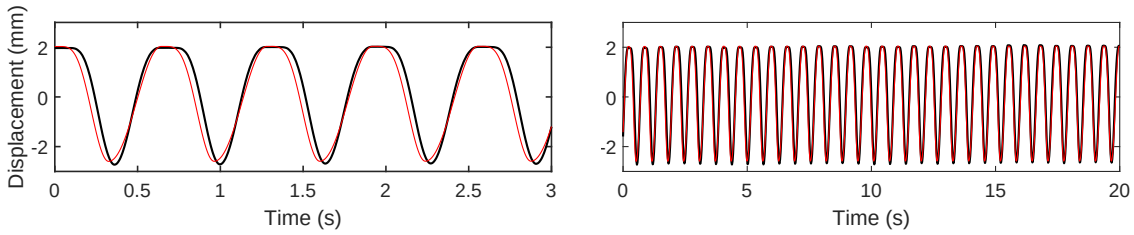

(b) One-stop stick-slip motion ($r = 0.5$)

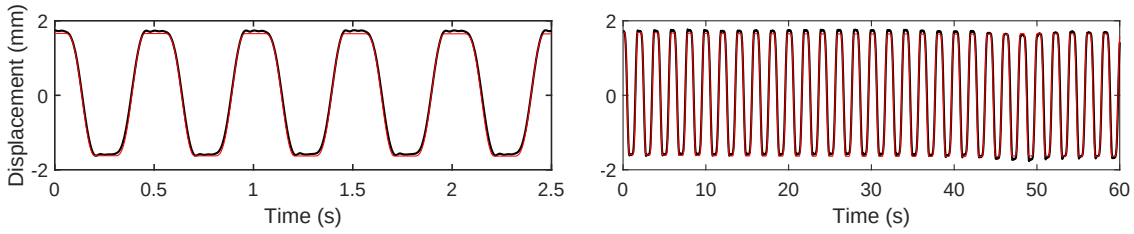

(c) two-stop stick-slip motion ($r = 0.35$)

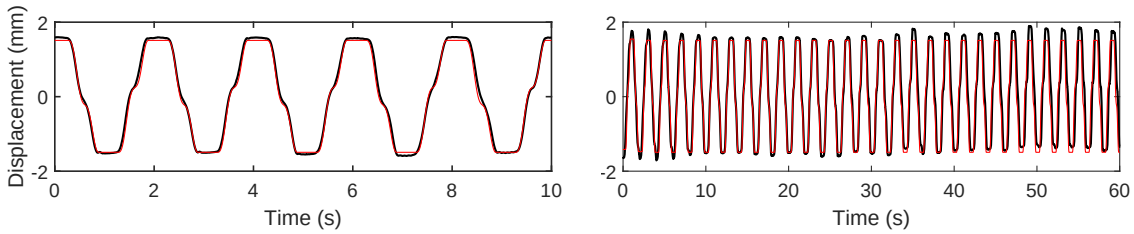

(d) Four-stops stick-slip motion ($r = 0.175$)

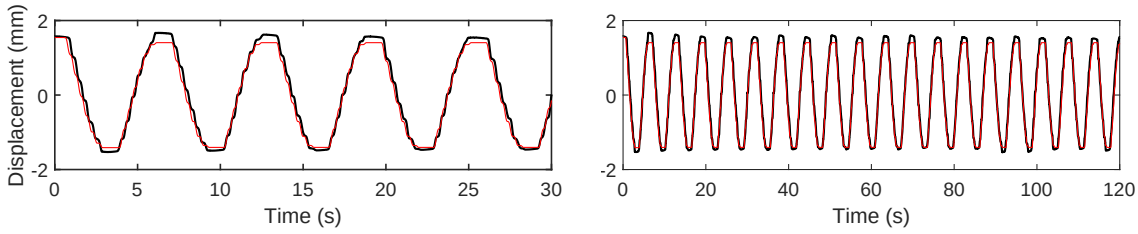

(e) multi-stop stick-slip motion ($r = 0.05$)

Figure 4.12: Steady-state time response for $\beta = 0.2$, short and long duration: experimental (black line) vs numerical (red line).

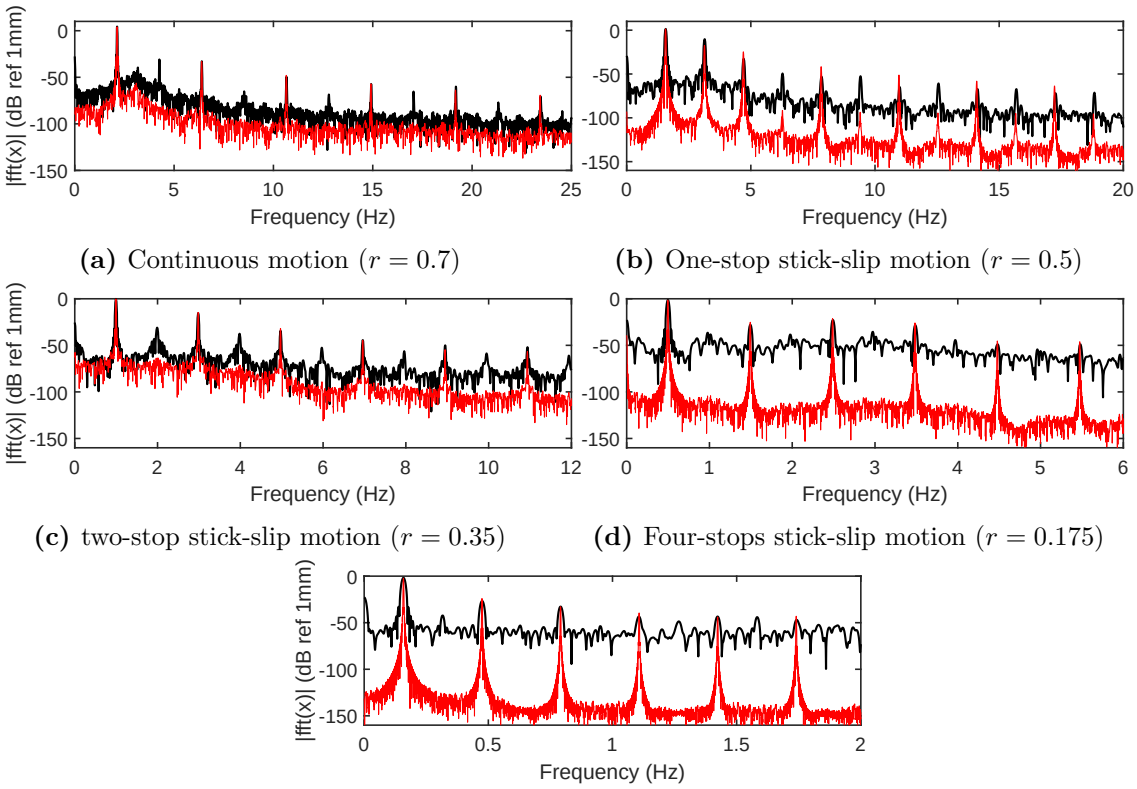

(a) Continuous motion ($r = 0.7$)

(b) One-stop stick-slip motion ($r = 0.5$)

(c) two-stop stick-slip motion ($r = 0.35$)

(d) Four-stops stick-slip motion ($r = 0.175$)

(e) multi-stop stick-slip motion ($r = 0.05$)

Figure 4.13: Frequency spectrum of the steady-state response for $\beta = 0.2$: experimental (black line) vs numerical (red line).

ratio is slightly changed. Following the discussion presented in Section 3.6.2 on the effect of μ on the sub-resonant behaviours, this might suggest that the static friction force is indeed larger than the kinetic one.

The comparison between the experimental and the numerical frequency spectra of the response is shown in Fig.4.13. It can be observed that the noise level in the experimental measurements is below -40dB in all the reported cases; this allows a clear observation of the peaks. A very good agreement is observed for the peaks related to the first six odd harmonics. These peaks are found both in the experimental and in the numerical responses because they are related to the nonlinearity of the problem, as explained in [60]. Conversely, peaks can only be observed in correspondence of the even harmonics in the experimental frequency spectra. As specified in Section 4.3.3, the peaks are due to the presence of higher harmonics in the base motion generated by the rotor through the Scotch-yoke

mechanism. It must be observed that, in Fig.4.13b, even peaks are also found in the numerical spectrum, due to the asymmetry of the response.

In conclusion, it has been shown that the proposed experimental setup also enables the investigation of the dynamic behaviour of a SDOF Coulomb friction oscillator in the time and the frequency domains. Particularly, the stick-slip motion has been observed with a very good accuracy.

4.6 Summary and concluding remarks

The experimental investigation of a SDOF Coulomb friction oscillator under either base excitation or joined base-wall harmonic excitation has been presented in this chapter.

A single-storey frame setup with a brass-to-steel contact has been designed to introduce a harmonic base excitation and a friction contact in the structure. Two different configurations of the test rig, corresponding to the fixed-wall and to the joined base-wall cases, have been explored. The response metrics considered were: (1) the displacement transmissibility and (2) the phase angle between the displacement of the two plates; (3) the steady-state time response of the top plate and (4) the corresponding frequency spectrum.

The analytical developments by Den Hartog [21], presented in Section 2.5.1, and those introduced in this thesis in Chapter 3 have been validated for different values of the frequency and friction ratios. An excellent agreement was found in terms of the response metrics (1) and (2) in continuous regime. In particular, it was confirmed that, in the joined base-wall case, an inversion of the transmissibility curves occurs at $r \cong 1.5$.

A very good agreement was also obtained between the experimental and the numerical results in stick-slip regime, in terms of the four response metrics. In particular, it has been shown that the numerical approach and the experimental setup allow the observation of features such as the number and the duration of the stops, as well as of the multi-harmonic content in the system response.

The limitations of the test setup have also been discussed. In particular, the parameter space which can be investigated is limited by the occurrence of permanent sticking between the disc and the top plate when $\beta \geq 0.7$ in the fixed-wall configuration and when $\beta \geq 0.7r^2$ in the joined base-wall configuration.

Overall, the experimental investigation presented in this chapter has shown that the analytical solutions and the numerical approaches proposed in the previous chapters for the steady-state response of a SDOF system with Coulomb friction can be reproduced in experimental conditions using the proposed setup. It has also been shown that certain response metrics, such as the frequency-based phase angle, which are easily be obtained from the measured displacements of the plates, offer a good degree of sensitivity with respect to the friction force variations. Therefore, these metrics could be used, in a inverse approach, to measure the friction force acting in the contact from the dynamic response of the structure.

In conclusion, the results presented in Chapters 3 and 4 offer a complete overview of the dynamic behaviour of SDOF systems with Coulomb friction. Nevertheless, although SDOF models can provide an adequate description of the dynamical behaviour of some systems, in most cases the dynamic analysis of a structure requires the use of MDOF models. The effects of the introduction of a Coulomb friction contact in such systems will be discussed in the following chapters.

Many of life's failures are people who did not realise they were close to success when they gave up

— Thomas Edison

5 Dynamic response of multi-degree-of-freedom systems with a Coulomb friction contact

Contents

5.1 Introduction

In this chapter, an exact solution is derived for the continuous steady-state response of MDOF systems with a Coulomb friction contact under harmonic loading. In particular, closed-form expressions are obtained for the time response of all the

masses of the system and for the response amplitude and phase of the mass in contact. Approximated analytical formulations are also proposed for the response amplitudes and phases of the other masses. Furthermore, the domain of validity of these solutions, i.e. the boundary between continuous and stick-slip regimes, is evaluated, also accounting for different static and kinetic friction forces.

All the presented solutions hold for any number of DOFs and take into account harmonic and friction forces applied to different masses of the system. Moreover, different contact configurations involving fixed or oscillating walls are explored. The latter case includes contacts occurring between either two masses of the system or one of the masses and the harmonically excited base. As mentioned in Section 3.1, systems with a contact between oscillating components are of interest for several engineering applications. Specific examples regarding MDOF models with a friction contact include the implementation of a friction damper in buildings [7], car suspensions [9], taxiing of airplanes models [15] and energy harvesters [14].

The general formulation of the problem and the relevant assumptions are discussed in Section 5.2, while the modal superposition approach used for deriving the solution is explained in Section 5.3. The closed-form expressions for the time response, displacement transmissibility and phase angle of each mass of the MDOF system are presented in Section 5.4 and the domain of validity of these solutions is derived in Section 5.5. Finally, all these results are extended to MDOF systems with a contact between oscillating parts in Section 5.6.

5.2 General formulation and assumptions

Let us consider a MDOF system where N masses m_i are connected between each other and to the base by N springs of stiffness k_i, as shown in Fig.5.1. The system is subjected to a harmonic load of amplitude P and frequency ω, applied to the l-th mass. The case of a harmonic base motion of amplitude Y can be accounted for by assuming that a harmonic load of amplitude $P = k_1 Y$ is applied to the mass m_1, as explained in Section 2.5.2 for SDOF systems. A Coulomb contact characterised

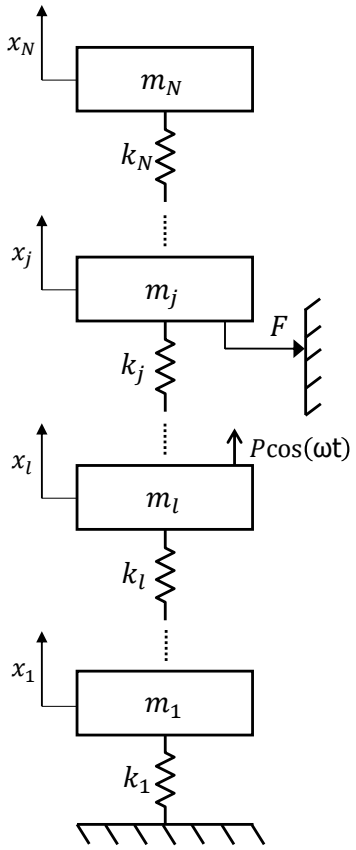

Figure 5.1: MDOF system with a friction contact on the j-th mass subjected to a harmonic excitation on the l-th mass.

by a friction force of amplitude F occurs on the j-th mass of the system. The generic ith governing equation of this system can be written as:

$$m_i\ddot{x}_i - k_i x_{i-1} + (k_i + k_{i+1})x_i - k_{i+1}x_{i+1} + \delta_{ji}F\mathrm{sgn}(\dot{x}_j) = \delta_{li}P\cos(\omega t) \qquad (5.1)$$

where $x_{i-1} = 0$ for $i = 1$, $x_{i+1} = k_{i+1} = 0$ for $i = N$ and:

$$\delta_{qs} = \begin{cases} 1 & \text{if } q = s \\ 0 & \text{otherwise} \end{cases} \qquad (5.2)$$

The sgn() function is defined in Eq.(2.11). It is worth recalling that the value assumed by this function when $\dot{x}_j = 0$ is included between -μ and μ and such that the system is in equilibrium when no motion occurs between the mass m_j and the wall.

The dynamic behaviour of this system can be described by referring to $2N + 1$ non-dimensional groups only:

- the frequency ratio $r_1 = \omega\sqrt{m_1/k_1}$;
- the friction ratio $\beta = F/P$;
- the ratio between static and kinetic friction forces μ;
- the $N-1$ mass ratios $\gamma_i = m_i/m_1$;
- the $N-1$ stiffness ratios $\kappa_i = k_i/k_1$.

It is worth noting that γ_1 and κ_1 are equal to 1, by definition, and therefore will not be considered as parameters of the system. By introducing the non-dimensional time τ defined in Eq.(2.12) and the non-dimensional mass displacements:

$$\bar{x}_i = \frac{x_i}{P/k_1} \tag{5.3}$$

it is possible to rewrite Eq.(5.1) in a non-dimensional form where these parameters appear explicitly:

$$\gamma_i r_1^2 \bar{x}_i'' - \kappa_i \bar{x}_{i-1} + (\kappa_i + \kappa_{i+1})\bar{x}_i - \kappa_{i+1}\bar{x}_{i+1} + \delta_{ji}\beta \mathrm{sgn}(\bar{x}_j') = \delta_{li}\cos\tau \tag{5.4}$$

The assumptions required for the analytical approach proposed in this chapter are the following::

- antiperiodic and continuous steady-state response
- presence of a single nonlinearity in the system

The first assumption is the same considered by Den Hartog [21] for the response of SDOF systems with a fixed wall and considered in Chapter 3 for the relative motion in the contact of SDOF systems under joined base-wall excitation. It is worth mentioning that, while the stability properties of SDOF systems have been investigated by several authors [23, 67, 70], to the best of the author's knowledge, they are unexplored for the MDOF systems investigated in this chapter. Nevertheless, the numerical investigations carried out in this study have shown a convergence of the response to a unique steady-state solution for most sets of parameters.

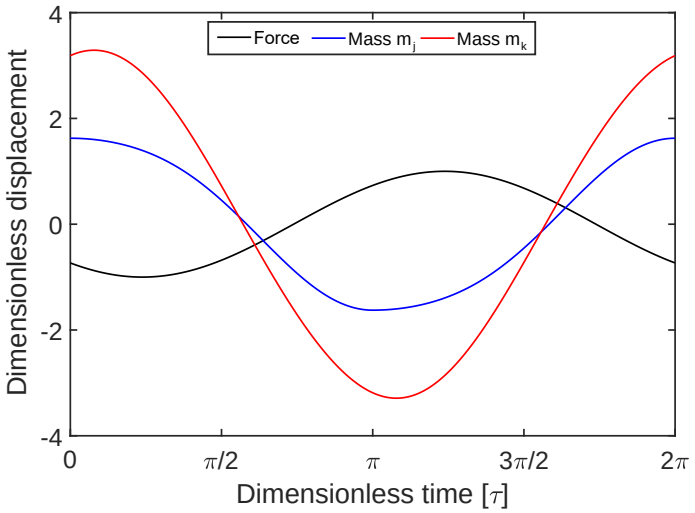

Figure 5.2: Harmonic excitation and continuous responses of the mass in contact m_j and of the generic mass not in contact m_k in the steady-state period included between two maxima of the response $\bar{x}_j$ of the mass in contact.

Specific exceptions, including the case of infinite resonant peaks, will be reported and discussed in Chapter 6.

The second assumption is satisfied if only a single contact is considered. Therefore, the proposed approach cannot deal with MDOF systems with multiple contacts occurring simultaneously on different masses.

The harmonic excitation and the motions of the mass in contact m_j and of a generic mass m_k are shown in Fig.5.2 in the steady-state period included between two maxima of $\bar{x}_j$. If the above assumptions are verified, the governing equations of the MDOF system will be linear in each half-period included between two subsequent stationary points of $\bar{x}_j$, independently of the number of DOFs of the system. If the non-dimensional time interval $[0, \pi]$ is considered, where $\tau = 0$ coincides with a maximum of the periodic displacement of the mass in contact and $\tau = \pi$ with the subsequent minimum, the velocity of m_j will be equal to zero at both ends of the interval and negative in all the internal points. Therefore, the non-dimensional friction force will be constant within the interval and equal to $-\beta$. Thus, it will be possible to rewrite Eq.(5.4) as:

$$\gamma_i r_1^2 \bar{x}_i'' - \kappa_i \bar{x}_{i-1} + (\kappa_i + \kappa_{i+1})\bar{x}_i - \kappa_{i+1}\bar{x}_{i+1} = \delta_{ji}\beta + \delta_{li}\cos(\tau + \phi_j) \qquad (5.5)$$

where it is assumed that an unknown phase angle ϕ_j is present between the maxima of the excitation and of the response of m_j when a steady-state condition is reached, as an effect of Coulomb damping. This phase angle is introduced here according to the definition used by Den Hartog [21], i.e. it refers to the maxima of the harmonic excitation and of the j-th response.

5.3 Modal superposition procedure

The linearity of Eq.(5.5) enables the use of standard approaches such as *modal superposition method*, which are typically used for the resolution of linear MDOF systems [24]. As a first step, it is possible to write the N governing equations of the system within the interval $[0, \pi]$ in the following matrix form:

$$\overline{\mathbf{M}}\bar{\mathbf{x}}'' + \overline{\mathbf{K}}\bar{\mathbf{x}} = \bar{\mathbf{f}} + \bar{\mathbf{p}} \tag{5.6}$$

where:

- $\overline{\mathbf{M}}$ is the mass matrix:

$$\overline{\mathbf{M}} = \begin{bmatrix} r_1^2 & 0 & \dots & 0 \\ 0 & \gamma_2 r_1^2 & \dots & 0 \\ \vdots & \vdots & \vdots & \vdots \\ 0 & 0 & \dots & \gamma_N r_1^2 \end{bmatrix} \tag{5.7}$$

- $\overline{\mathbf{K}}$ is the stiffness matrix:

$$\overline{\mathbf{K}} = \begin{bmatrix} 1+\kappa_2 & -\kappa_2 & 0 & \dots & 0 \\ -\kappa_2 & \kappa_2+\kappa_3 & -\kappa_3 & \dots & 0 \\ \vdots & \vdots & \vdots & \vdots & \vdots \\ 0 & 0 & \dots & -\kappa_N & \kappa_N \end{bmatrix} \tag{5.8}$$

- $\bar{\mathbf{f}}$ is the friction force vector, whose only non-zero component is β in the j-th position;

- $\bar{\mathbf{p}}$ is the harmonic force vector, whose only non-zero component is $\cos(\tau + \phi_j)$ in the l-th position;

The N non-dimensional natural frequencies Ω_i and the corresponding N mode shapes $\boldsymbol{\psi}_i = \begin{bmatrix}\psi_{1i} & \psi_{2i} & \dots & \psi_{Ni}\end{bmatrix}^T$ of the system described by Eq.(5.5) can be found as solutions of the generalised eigenvalue problem [24]:

$$(\overline{\mathbf{K}} - \Omega_i^2 \overline{\mathbf{M}})\boldsymbol{\psi}_i = \mathbf{0} \tag{5.9}$$

The obtained mode shapes $\boldsymbol{\psi}_i$ are defined up to a constant [24] and, therefore, they need to be normalised according to some criteria in order to have a unique definition. In the proposed approach, a mass-normalisation is considered, i.e. it is imposed that the modal mass:

$$\hat{m}_i = \boldsymbol{\psi}_i^T \overline{\mathbf{M}} \boldsymbol{\psi}_i \tag{5.10}$$

is unitary.

The modal superposition procedure allows the rewriting of the governing equations of a linear system with N DOFs as a set of N uncoupled equations, which can be considered as the governing equations of N separate SDOF systems [24]. This transformation is performed by using the modal matrix $\boldsymbol{\Psi} = \begin{bmatrix}\boldsymbol{\psi}_1 & \boldsymbol{\psi}_2 & \dots & \boldsymbol{\psi}_N\end{bmatrix}$, which is defined as the matrix whose columns are the mode shapes of the system. Thus, it is possible to introduce the modal coordinates η_i as the components of the vector $\boldsymbol{\eta}$ obtained from the linear transformation:

$$\bar{\mathbf{x}} = \boldsymbol{\Psi}\boldsymbol{\eta} \tag{5.11}$$

By introducing Eq.(5.11) into Eq.(5.6) and pre-multiplying both sides by $\boldsymbol{\Psi}^T$, it is possible to write:

$$\boldsymbol{\Psi}^T \overline{\mathbf{M}} \boldsymbol{\Psi} \boldsymbol{\eta}'' + \boldsymbol{\Psi}^T \overline{\mathbf{K}} \boldsymbol{\Psi} \boldsymbol{\eta} = \boldsymbol{\Psi}^T \bar{\mathbf{f}} + \boldsymbol{\Psi}^T \bar{\mathbf{p}} \tag{5.12}$$

Since the mode-shapes are mass-normalised, $\boldsymbol{\Psi}^T \overline{\mathbf{M}} \boldsymbol{\Psi}$ is equal to an identity matrix and $\boldsymbol{\Psi}^T \overline{\mathbf{K}} \boldsymbol{\Psi}$ is a diagonal matrix whose non-zero elements are equal to Ω_i^2. Therefore, the ith equation of the system in Eq.(5.12) can be written as:

$$\eta_i'' + \Omega_i^2 \eta_i = \psi_{ji}\beta + \psi_{li}\cos(\tau + \phi_j) \tag{5.13}$$

Eq.(5.13) can be seen as the governing equation of a SDOF system of unitary mass and stiffness equal to Ω_i^2, subjected to a constant force of amplitude $\psi_{ji}\beta$ and to a harmonic load $\psi_{li}\cos(\tau+\phi_j)$. This equation is therefore equivalent to that dealt with by Den Hartog [21] and reported in Eq.(2.18); its general solution can be written as:

$$\eta_i = A_i \cos\left(\frac{\tau}{R_i}\right) + B_i \sin\left(\frac{\tau}{R_i}\right) + \psi_{ji} R_i^2 \beta + \psi_{li} R_i^2 v_i \cos(\tau + \phi_j) \tag{5.14}$$

In this expression, the ith modal frequency ratio has been introduced as:

$$R_i = \frac{1}{\Omega_i} \tag{5.15}$$

while the function:

$$v_i = \frac{1}{1 - R_i^2} \tag{5.16}$$

is the response function associated to the ith mode. Finally, A_i and B_i are two unknown constants whose expressions can be determined by considering the initial conditions of this problem.

The initial and the final conditions to be imposed on η_i are, in general, different from those considered by Den Hartog for the response of a SDOF system. In fact, in the SDOF case, the non-dimensional time instants $\tau = 0$ and $\tau = \pi$ coincide with a maximum and a minimum of the response. However, this is not the case, in general, for the ith modal coordinate a MDOF system. Therefore, the initial conditions will be:

$$\begin{cases} \eta_i(0) = \eta_{i0} & \text{(5.17a)} \\ \eta_i'(0) = \eta_{i0}' & \text{(5.17b)} \end{cases}$$

where the terms η_{i0} and η_{i0}' are both unknown at this stage.

Substituting Eq.(5.14) into Eq.(5.17) and rearranging the terms, the expressions of A_i and B_i are obtained:

$$\begin{cases} A_i = \eta_{i0} - \psi_{ji} R_i^2 \beta - \psi_{li} R_i^2 v_i \cos\phi_j & \text{(5.18a)} \\ B_i = R_i \eta_{i0}' + \psi_{li} R_i^3 v_i \sin\phi_j & \text{(5.18b)} \end{cases}$$

Substituting these expressions into Eq.(5.14), it is possible to express the ith modal displacement as:

$$\eta_i = \eta_{i0}\cos\left(\frac{\tau}{R_i}\right) + \eta'_{i0}R_i\sin\left(\frac{\tau}{R_i}\right) + \psi_{ji}R_i^2\left[1-\cos\left(\frac{\tau}{R_i}\right)\right]\beta + \psi_{li}R_i^2 v_i\left\{\left[\cos\tau-\cos\left(\frac{\tau}{R_i}\right)\right]\cos\phi_j + \left[R_i\sin\left(\frac{\tau}{R_i}\right)-\sin\tau\right]\sin\phi_j\right\} \quad (5.19)$$

Due to the symmetry of the steady-state response, the final values of η_i and η'_i in the interval considered will be equal to:

$$\begin{cases}\eta_i(\pi) = -\eta_{i0} & (5.20a)\\ \eta'_i(\pi) = -\eta'_{i0} & (5.20b)\end{cases}$$

Therefore, substituting Eq.(5.19) into Eq.(5.20), a system of algebraic equations is obtained in the form:

$$\begin{cases}\mathcal{A}\cos\phi_j + \mathcal{B}\sin\phi_j + \mathcal{C} = 0 & (5.21a)\\ \mathcal{P}\cos\phi_j + \mathcal{Q}\sin\phi_j + \mathcal{R} = 0 & (5.21b)\end{cases}$$

where:

$$\begin{cases}\mathcal{A} = -\psi_{li}R_i^2 v_i\left[1+\cos\left(\frac{\pi}{R_i}\right)\right] & (5.22a)\\ \mathcal{B} = \psi_{li}R_i^3 v_i\sin\left(\frac{\pi}{R_i}\right) & (5.22b)\\ \mathcal{C} = \left[1+\cos\left(\frac{\pi}{R_i}\right)\right]\eta_{i0} + R_i\sin\left(\frac{\pi}{R_i}\right)\eta'_{i0} + \psi_{ji}R_i^2\left[1-\cos\left(\frac{\pi}{R_i}\right)\right]\beta & (5.22c)\\ \mathcal{P} = \psi_{li}R_i v_i\sin\left(\frac{\pi}{R_i}\right) & (5.22d)\\ \mathcal{Q} = \psi_{li}R_i^2 v_i\left[1+\cos\left(\frac{\pi}{R_i}\right)\right] & (5.22e)\\ \mathcal{R} = -\frac{1}{R_i}\sin\left(\frac{\pi}{R_i}\right)\eta_{i0} + \left[1+\cos\left(\frac{\pi}{R_i}\right)\right]\eta'_{i0} + \psi_{ji}R_i\sin\left(\frac{\pi}{R_i}\right)\beta & (5.22f)\end{cases}$$

The unknown values of $\cos\phi_j$ and $\sin\phi_j$ can be obtained from Eq.(5.21) as:

$$\cos\phi_j = \frac{\mathcal{B}\mathcal{R}-\mathcal{C}\mathcal{Q}}{\mathcal{A}\mathcal{Q}-\mathcal{B}\mathcal{P}} \qquad \sin\phi_j = \frac{\mathcal{C}\mathcal{P}-\mathcal{A}\mathcal{R}}{\mathcal{A}\mathcal{Q}-\mathcal{B}\mathcal{P}} \quad (5.23)$$

Substituting Eq.(5.22) into Eq.(5.23), it is obtained that:

$$\cos\phi_j = \frac{\eta_{i0}}{\psi_{li}R_i^2 v_i} \quad (5.24)$$

and:

$$\sin\phi_j = -\frac{\eta'_{i0}}{\psi_{li}R_i^2 v_i} - \frac{\psi_{ji}\sin(\pi/R_i)}{\psi_{li}R_i v_i\left[1+\cos(\pi/R_i)\right]}\beta \tag{5.25}$$

Let us introduce the damping function of the ith mode of the system as:

$$u_i = \frac{\sin(\pi/R_i)}{R_i\left[1+\cos(\pi/R_i)\right]} \tag{5.26}$$

in the same form as the damping function introduced in Eq.(2.25) for SDOF systems. Thus, it is possible to rewrite Eq.(5.25) as:

$$\sin\phi_j = -\frac{\eta'_{i0} + \psi_{ji}R_i^2 u_i\beta}{\psi_{li}R_i^2 v_i} \tag{5.27}$$

By substituting Eqs.(5.24) and (5.27) into Eq.(5.19), it is possible to express the ith modal coordinate as:

$$\eta_i = \eta_{i0}\cos\tau + (\eta'_{i0} + \psi_{ji}R_i^2 u_i)\sin\tau + \beta\psi_{ji}R_i^2\left[1-\cos\left(\frac{\tau}{R_i}\right) - u_i R_i \sin\left(\frac{\tau}{R_i}\right)\right] \tag{5.28}$$

In this expression, the initial values of the modal coordinate and of its derivative are still to be determined. However, differently from Den Hartog's procedure for SDOF systems, at this stage no conditions have been imposed related to how the non-dimensional time interval $[0,\pi]$ has been defined. In order to express such conditions, it is required to reintroduce the physical coordinates in the present analysis, as shown in the following section.

5.4 Evaluation of the steady-state response

5.4.1 Response of the mass in contact

As specified in Section 5.2, the extremes of the non-dimensional time interval $[0,\pi]$ coincide, respectively, with a maximum and a minimum of the response of the mass in contact m_j. Therefore, the initial conditions for this motion can be expressed as:

$$\begin{cases} \bar{x}_j(0) = \overline{X}_j & \text{(5.29a)} \\ \bar{x}'_j(0) = 0 & \text{(5.29b)} \end{cases}$$

where $\overline{X}_j$ indicates the amplitude of the non-dimensional displacement of the mass m_j. It is worth recalling that, since the amplitude of the non-dimensional excitation is unitary, this value also represents the j-th magnification factor or displacement transmissibility of the system. These initial conditions can be imposed to determine the unknown amplitude and phase angle of the response $\bar{x}_j$. By introducing the j-th coordinate transformation from Eq.(5.11) into Eq.(5.29), it is obtained that η_{i0} and η'_{i0} must verify the conditions:

$$\sum_{i=1}^{N} \psi_{ji}\eta_{i0} = \overline{X}_j \tag{5.30}$$

and:

$$\sum_{i=1}^{N} \psi_{ji}\eta'_{i0} = 0 \tag{5.31}$$

respectively. These relations can be used to eliminate η_{i0} and η'_{i0} from the expression of the phase angle ϕ_j. Let us multiply both numerator and denominator of the RHS of Eq.(5.24) by ψ_{ji}, obtaining:

$$\cos\phi_j = \frac{\psi_{ji}\eta_{i0}}{\psi_{ji}\psi_{li}R_i^2 v_i} \tag{5.32}$$

Since the value of ϕ_j does not depend on i, the RHS of the above equation is constant for each modal contribution. As a result, by taking the sum of the N modal contributions of the numerator and denominator, the ratio will remain unchanged:

$$\cos\phi_j = \frac{\sum\limits_{i=1}^{N} \psi_{ji}\eta_{i0}}{\sum\limits_{i=1}^{N} \psi_{ji}\psi_{li}R_i^2 v_i} \tag{5.33}$$

As shown in reference [24], the generic k-th response function of an undamped MDOF system of N masses subjected to a harmonic load acting on the l-th mass can be obtained, using the modal superposition approach, as:

$$V_k = \sum_{i=1}^{N} \psi_{ki}\psi_{li}R_i^2 v_i \tag{5.34}$$

Substituting Eqs.(5.30) and (5.34) for $j = k$, it is possible to rewrite Eq.(5.33) as:

$$\cos\phi_j = \frac{\overline{X}_j}{V_j} \tag{5.35}$$

In a similar fashion, starting from Eq.(5.27), it is possible to be obtain the relation:

$$\sin\phi_j = -\frac{\sum_{i=1}^{N}\psi_{ji}\eta'_{i0} + \beta\sum_{i=1}^{N}\psi_{ji}^2 R_i^2 u_i}{\sum_{i=1}^{N}\psi_{ji}\psi_{li}R_i^2 v_i} \tag{5.36}$$

Let us introduce the generic k-th damping function of a MDOF system of N masses with a contact on the j-th mass as:

$$U_k = \sum_{i=1}^{N}\psi_{ki}\psi_{ji}R_i^2 u_i \tag{5.37}$$

consistently with the formulation used in Eq.(5.34) for the response function. Substituting Eqs.(5.31), (5.34) and (5.37) into Eq.(5.36) for $j = k$, it can be obtained that:

$$\sin\phi_j = -\frac{\beta U_j}{V_j} \tag{5.38}$$

Substituting Eqs.(5.35) and (5.38) in the relation $\cos^2\phi_j + \sin^2\phi_j = 1$ and rearranging, it is possible to obtain the j-th displacement transmissibility as:

$$\overline{X}_j = \sqrt{V_j^2 - (\beta U_j)^2} \tag{5.39}$$

It is worth observing that these expressions of the displacement transmissibility and of the phase angle are formally identical to those obtained by Den Hartog for SDOF systems, reported in Eqs.(2.23) and (2.24) respectively, and reduce to the same expressions if $N = 1$.

Finally, the following expression is obtained for the non-dimensional time response of the mass m_j in the interval $[0, \pi]$ by applying the j-th equation of the transformation from modal to physical coordinates from Eq.(5.11) to Eq.(5.28):

$$\bar{x}_j = \sum_{i=1}^{N}\psi_{ji}\eta_{i0}\cos\tau + \left(\sum_{i=1}^{N}\psi_{ji}\eta'_{i0} + \beta\sum_{i=1}^{N}\psi_{ji}^2 R_i^2 u_i\right)\sin\tau + \beta\sum_{i=1}^{N}\psi_{ji}^2 R_i^2\left[1 - \cos\left(\frac{\tau}{R_i}\right) - u_i R_i \sin\left(\frac{\tau}{R_i}\right)\right] \tag{5.40}$$

Considering Eqs.(5.30), (5.31) and (5.37), it is possible to rewrite the above expression as:

$$\bar{x}_j = \overline{X}_j\cos\tau + \beta U_j\sin\tau + \beta\sum_{i=1}^{N}\psi_{ji}^2 R_i^2\left[1 - \cos\left(\frac{\tau}{R_i}\right) - u_i R_i\sin\left(\frac{\tau}{R_i}\right)\right] \tag{5.41}$$

Also in this case, Den Hartog's expression for the time response of a SDOF system, expressed in Eq.(2.22), is retrieved for $N = 1$.

5.4.2 Response of a generic mass of the system

The time response of the generic mass m_k of the MDOF system can be found with a similar approach. In fact, by introducing the k-th equation from Eq.(5.11) into Eq.(5.28), it is obtained that:

$$\bar{x}_k = \bar{x}_{k0}\cos\tau + (\bar{x}'_{k0} + \beta U_k)\sin\tau + \beta\sum_{i=1}^{N}\psi_{ji}\psi_{ki}R_i^2\left[1 - \cos\left(\frac{\tau}{R_i}\right) - u_i R_i \sin\left(\frac{\tau}{R_i}\right)\right] \tag{5.42}$$

where $\bar{x}_{k0}$ and $\bar{x}'_{k0}$ are, respectively, the initial values of the displacement and of the velocity of m_k in the interval considered; these values are unknown at this stage.

In order to determine $\bar{x}_{k0}$ and $\bar{x}'_{k0}$, let us multiply numerator and denominator of the RHS of Eqs.(5.24) and (5.27) by ψ_{ki} and consider their summations from $i = 1$ to N, proceeding as in Section 5.4.1. The expressions obtained are:

$$\cos\phi_j = \frac{\sum\limits_{i=1}^{N}\psi_{ki}\eta_{i0}}{\sum\limits_{i=1}^{N}\psi_{ki}\psi_{li}R_i^2 v_i} = \frac{\bar{x}_{k0}}{V_k} \tag{5.43}$$

from Eq.(5.24) and:

$$\sin\phi_j = -\frac{\bar{x}'_{k0} + \beta U_k}{V_k} \tag{5.44}$$

from Eq.(5.27). The initial displacement of m_k can be determined by substituting Eq.(5.35) into Eq.(5.43):

$$\bar{x}_{k0} = \frac{V_k}{V_j}\overline{X}_j = \frac{V_k}{V_j}\sqrt{V_j^2 - (\beta U_j)^2} \tag{5.45}$$

Similarly, considering Eqs.(5.38) and (5.44), the initial velocity can be formulated as:

$$\bar{x}'_{k0} = \beta\left(\frac{V_k}{V_j}U_j - U_k\right) \tag{5.46}$$

The time response of the generic mass m_k can now be evaluated by substituting Eqs.(5.45) and (5.46) into Eq.(5.42), obtaining:

$$\bar{x}_k = \frac{V_k}{V_j}\left(\overline{X}_j\cos\tau + \beta U_j\sin\tau\right) + \beta\sum_{i=1}^{N}\psi_{ji}\psi_{ki}R_i^2\left[1 - \cos\left(\frac{\tau}{R_i}\right) - u_i R_i\sin\left(\frac{\tau}{R_i}\right)\right] \tag{5.47}$$

It can be observed that this expression reduces to Eq.(5.41) if $j = k$.

The amplitude and the phase angle cannot be easily determined for the generic mass from the expression of the time response $\bar{x}_k$. In general, the evaluation of the maximum absolute value of $\bar{x}_k$ within the non-dimensional time interval $[0, \pi]$ can be performed numerically and its value will coincide with the k-th displacement transmissibility. Moreover, if the maximum value of $|\bar{x}_k|$ is verified at $\tau = \tau_{k,\max}$, the phase angle between the excitation and the displacement of the mass m_k can be calculated as:

$$\begin{cases} \phi_k = \phi_j + \tau_{k,\max} & \text{if } \bar{x}_k(\tau_{k,\max}) \geq 0 \quad (5.48a) \\ \phi_k = \phi_j + \tau_{k,\max} + \pi & \text{if } \bar{x}_k(\tau_{k,\max}) < 0 \quad (5.48b) \end{cases}$$

This approach for the determination of $\overline{X}_k$ and ϕ_k does not yield information on their dependency on the parameters of the problem. Therefore, an approximated approach for determining explicit analytical expressions for the displacement transmissibility and the phase angle of a generic mass of the system is proposed in what follows.

A monoharmonic approximation of the motion of the mass m_j in the interval $[0, \pi]$ could simply be obtained as $\bar{x}_j \cong \overline{X}_j \cos\tau$. Such a formulation would neglect the non-harmonic behaviour of the response due to nonlinearity but would agree with the exact solution from Eq.(5.41) at both ends of the interval, thus providing the exact amplitude of the response. Nevertheless, the same approximation cannot be directly introduced for the motion of the generic mass m_k. In fact, a certain phase shift ϕ_{kj} is generally present between the displacements of m_j and m_k; as a consequence, the initial and the final points of $\bar{x}_k$ in $[0, \pi]$ are not stationary points. Comparing Eq.(5.41) and Eq.(5.42), it is possible to observe that this effect is expressed by the term $\bar{x}'_{k0} \sin\tau$, which is equal to zero in the case $j = k$. This term cannot be disregarded in a monoharmonic approximation. Thus, the formulation hereby proposed is:

$$\bar{x}_k \cong \bar{x}_{k0} \cos\tau + \bar{x}'_{k0} \sin\tau = \overline{X}_k \cos(\tau - \phi_{kj}) \quad (5.49)$$

where:

$$\overline{X}_k = \sqrt{\bar{x}_{k0}^2 + \bar{x}_{k0}'^2} = \sqrt{V_k^2 + \left(1 - 2\frac{V_k}{V_j}\frac{U_j}{U_k}\right)(\beta U_k)^2} \quad (5.50)$$

is the approximated k-th displacement transmissibility of the MDOF system, while the phase angle ϕ_{kj} can be determined as:

$$\cos\phi_{kj} = \frac{\bar{x}_{k0}}{\overline{\overline{X}}_k} \qquad \sin\phi_{kj} = \frac{\bar{x}'_{k0}}{\overline{\overline{X}}_k} \tag{5.51}$$

The phase angle between the excitation and the displacement of the k-th mass will be finally obtained as $\phi_k = \phi_j + \phi_{kj}$. It was verified that Eqs.(5.50) and (5.51) offer a very good approximation of the exact transmissibilities and phase angles of the mass not in contact; in fact, the motion of these masses tends to have a lower contribution from other harmonic components compared to that of the mass in contact. Therefore, Eqs.(5.50) and (5.51) will be considered in the evaluations of the transmissibility and of the phase angle reported in Chapter 6. The absolute errors introduced with respect to the exact quantities were negligible for all the cases investigated.

5.5 Boundaries between continuous and stick-slip motion regimes

The solutions presented in the previous sections have been determined under the assumption of continuous non-sticking response. In Section 5.2, it has been specified that the proposed mathematical procedure only holds if the velocity of the mass in contact m_j is negative in all the internal points of the non-dimensional time interval $[0, \pi]$. As explained in Section 3.4.1, this condition cannot rule out the occurrence of stops at the ends of the interval, where the velocity of the mass in contact must be equal to zero. Therefore, in these points it is required to impose explicitly that the overall dynamic loading acting on the mass m_j is larger than the static friction force. Thus, these non-sticking conditions can be expressed as:

$$\begin{cases} \bar{x}'_j < 0 & \text{if } 0 < \tau < \pi \qquad (5.52a) \\ \left| \sum_{k=1}^{N} \overline{K}_{jk} \bar{x}_k - \delta_{lj} \cos(\tau + \phi_j) \right| > \mu\beta & \text{if } \tau = 0 \text{ or } \tau = \pi \qquad (5.52b) \end{cases}$$

and will be used to obtain the maximum value of the friction ratio for which the steady-state response is non-sticking.

Let us consider the derivative of the j-th mass motion from Eq.(5.41), so that Eq.(5.52a) can be rewritten as:

$$-\overline{X}_j \sin\tau + \beta U_j \cos\tau + \beta \sum_{i=1}^{N} \psi_{ji}^2 R_i^2 \left[\frac{1}{R_i} \sin\left(\frac{\tau}{R_i}\right) - u_i \cos\left(\frac{\tau}{R_i}\right) \right] < 0 \tag{5.53}$$

from which:

$$\overline{X}_j > \beta \sum_{i=1}^{N} \psi_{ji}^2 \frac{R_i \sin(\tau/R_i) + u_i R_i^2 \left[\cos\tau - \cos(\tau/R_i)\right]}{\sin\tau} \tag{5.54}$$

This relation is verified if $\overline{X}_j$ is larger than the maximum value assumed by the RHS in the interval $]0, \pi[$. Thus, introducing the function:

$$S_j = \sum_{i=1}^{N} \psi_{ji}^2 s_i \tag{5.55}$$

where:

$$s_i = \max_{0<\tau<\pi} \frac{R_i \sin(\tau/R_i) + u_i R_i^2 \left[\cos\tau - \cos(\tau/R_i)\right]}{\sin\tau} \tag{5.56}$$

it is possible to rewrite Eq.(5.54) as:

$$\overline{X}_j > \beta S_j \tag{5.57}$$

Substituting Eq.(5.39) into Eq.(5.57) and rearranging, it is possible to express this relation in terms of the friction ratio as:

$$\beta < \sqrt{\frac{V_j^2}{U_j^2 + S_j^2}} \tag{5.58}$$

Regarding the second non-sticking condition, expressed in Eq.(5.52b), only the case $\tau = 0$ needs to be considered, due to the symmetry of the steady-state response. Therefore, the equation reduces to:

$$\left| \sum_{k=1}^{N} \overline{K}_{jk} \bar{x}_{k0} - \delta_{lj} \cos\phi_j \right| > \mu\beta \tag{5.59}$$

and, substituting Eqs.(5.43) and (5.45):

$$\left| \frac{\overline{X}_j}{V_j} \left(\sum_{k=1}^{N} \overline{K}_{jk} V_k - \delta_{lj} \right) \right| > \mu\beta \tag{5.60}$$

Let us now consider the undamped MDOF system described by the equation:

$$\overline{\mathbf{M}}\bar{\mathbf{x}}'' + \overline{\mathbf{K}}\bar{\mathbf{x}} = \bar{\mathbf{p}} \tag{5.61}$$

If the j-th equation of the above system is considered and the response of the generic mass m_k is expressed as $\bar{x}_k = V_k e^{it}$, consistently with the definition of V_k, the following relation can be obtained:

$$\gamma_j r_1^2 V_j = \sum_{k=1}^{N} \overline{K}_{jk} V_k - \delta_{lj} \tag{5.62}$$

Substituting Eq.(5.62) into Eq.(5.60), it is obtained that:

$$\overline{X}_j > \frac{\mu\beta}{\gamma_j r_1^2} \tag{5.63}$$

Introducing Eq.(5.39), it is possible to express this condition in terms of the friction ratio as:

$$\beta < \sqrt{\frac{V_j^2}{U_j^2 + \left(\frac{\mu}{\gamma_j r_1^2}\right)^2}} \tag{5.64}$$

Finally, Eq.(5.58) and Eq.(5.64) can be merged in the following overall condition for obtaining a continuous non-sticking response:

$$\beta < \sqrt{\frac{V_j^2}{U_j^2 + \left[\max\left(S_j, \frac{\mu}{\gamma_j r_1^2}\right)\right]^2}} \tag{5.65}$$

The RHS of the above inequality represents the value β_{lim} assumed by the friction ratio at the boundary between continuous and stick-slip motion regimes. Furthermore, it is possible to express the boundary between continuous and stick-slip motion in terms of any of the displacement transmissibilities or phase angles of the MDOF system by simply substituting Eq.(5.65) into their expression.

Similarly to Section 3.4.1, an approximated expression of the boundary can be proposed in order to avoid the time-consuming evaluation of the function S_j for each value of r_1. In fact, the function $s_i(R_i)$ expressed in Eq.(5.56) coincides with the function $S(r)$ reported in Eq.(2.27) and plotted in Fig.3.3. This means that s_i will be unitary for most values of the frequency ratio. Therefore, since $\mu \geq 1$, Eq.(5.64) can be used as an approximated formulation of the boundary. This expression was considered, for the case $\mu = 1$, in reference [147], while a comparison

between the exact and the approximate formulations has been presented in reference [148] for different MDOF systems, only highlighting minor discrepancies at low frequency ratios. Nonetheless, the exact formulation introduced in Eq.(5.65) will be considered in the remaining of this thesis.

5.6 Extension to systems with a contact between oscillating parts

In this section, the analytical solutions derived in the previous sections for the continuous steady-state response of a MDOF system with a Coulomb friction contact between one of the masses and a fixed wall is extended to address the cases where the contact occurs: (i) between two different masses of the system; (ii) between a mass and a harmonically excited base.

5.6.1 Contact between two masses

Evaluation of the continuous steady-state response

Let us consider a MDOF system with N masses and N springs excited by the harmonic load $P\cos(\omega t)$ applied to the l-th mass, where a friction contact occurs between the masses m_A and m_B, with $A < B$, as shown in Fig.5.3. The generic ith governing equation can be written as:

$$m_i\ddot{x}_i - k_i x_{i-1} + (k_i + k_{i+1})x_i - k_{i+1}x_{i+1} + (\delta_{Bi} - \delta_{Ai})F\mathrm{sgn}(\dot{x}_B - \dot{x}_A) = \delta_{li}P\cos(\omega t) \tag{5.66}$$

or, in non-dimensional terms, as:

$$\gamma_i r_1^2 \bar{x}_i'' + \sum_{k=1}^{N} \overline{K}_{ik}\bar{x}_k + (\delta_{Bi} - \delta_{Ai})\beta\mathrm{sgn}(\bar{x}_B' - \bar{x}_A') = \delta_{li}\cos\tau \tag{5.67}$$

In order to apply to this system the analytical procedure introduced for MDOF systems with a fixed wall, let us indicate the relative motion in the friction contact as:

$$\bar{z} = \bar{x}_B - \bar{x}_A \tag{5.68}$$

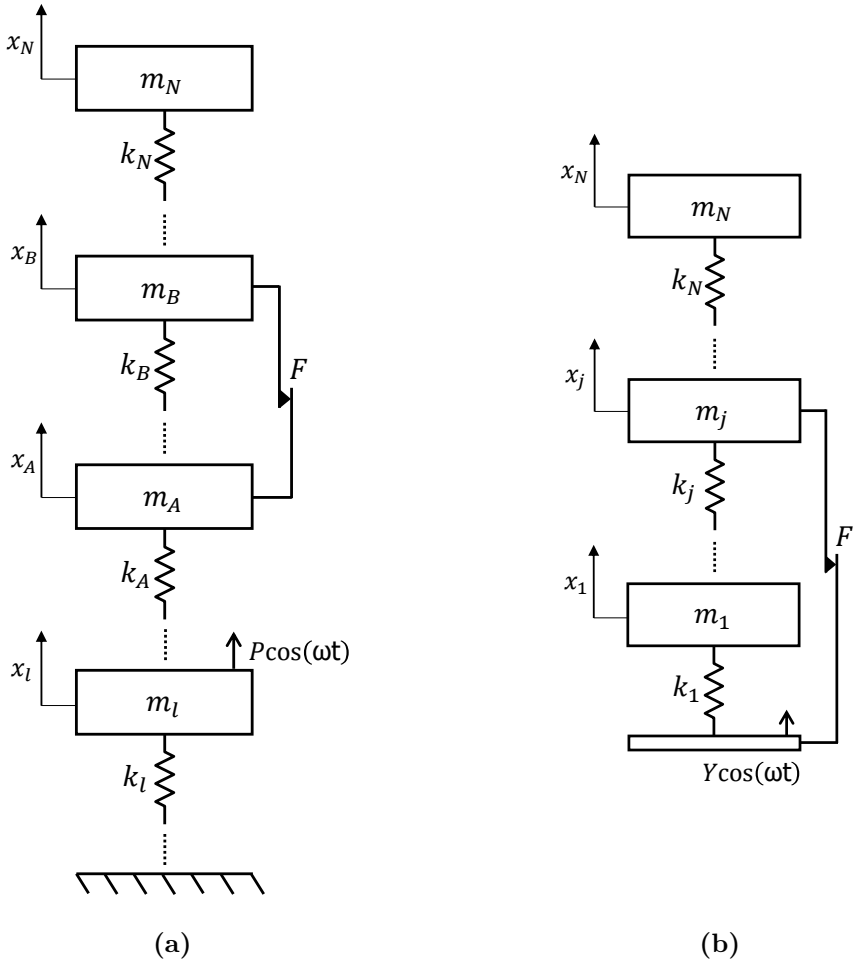

Figure 5.3: MDOF systems under harmonic excitation with a friction contact between (**a**) the A-th and the B-th masses and (**b**) the j-th mass and the excited base.

and consider the non-dimensional time interval $[0, \pi]$ included between a maximum and the subsequent minimum of $\bar{z}$, under the assumption of continuous steady-state motion. Eq.(5.67) will then reduce to the linear equation:

$$\gamma_i r_1^2 \bar{x}_i'' + \sum_{k=1}^{N} \overline{K}_{ik} \bar{x}_k = (\delta_{Bi} - \delta_{Ai})\beta + \delta_{li} \cos(\tau + \phi_z) \tag{5.69}$$

where ϕ_z is the phase angle between the excitation and the relative motion $\bar{z}$. Introducing the coordinate transformation from Eq.(5.11), it is possible to write the governing equation for the generic ith modal coordinate as:

$$\eta_i'' + \Omega_i^2 \eta_i = (\psi_{Bi} - \psi_{Ai})\beta + \psi_{li} \cos(\tau + \phi_z) \tag{5.70}$$

Comparing Eq.(5.70) with Eq.(5.13), it can be noted that the term ψ_{ji} is here replaced by $\psi_{Bi} - \psi_{Ai}$. This can also be observed in the initial conditions for

the relative motion:

$$\begin{cases} \bar{z}(0) = \sum_{i=1}^{N} (\psi_{Bi} - \psi_{Ai}) \eta_{i0} = \overline{Z} & \text{(5.71a)} \\ \bar{z}'(0) = \sum_{i=1}^{N} (\psi_{Bi} - \psi_{Ai}) \eta'_{i0} = 0 & \text{(5.71b)} \end{cases}$$

if compared to the initial conditions for the mass in contact written in Eq.(5.29). In the above conditions, $\overline{Z}$ indicates the amplitude of the non-dimensional relative motion. Therefore, it can easily be shown that the phase angle ϕ_z and the amplitude $\overline{Z}$ of the relative motion, as well as the steady-state time response, can be obtained from Eqs.(5.35), (5.38), (5.39) and (5.41) by replacing ψ_{ji} with $\psi_{Bi} - \psi_{Ai}$. The expression of time response of the generic k-th mass of the system will be:

$$\bar{x}_k = \frac{V_k}{V_z} \left(\overline{Z} \cos\tau + \beta U_z \sin\tau \right) + \beta \sum_{i=1}^{N} (\psi_{Bi} - \psi_{Ai}) \psi_{ki} R_i^2 \left[1 - \cos\left(\frac{\tau}{R_i}\right) - u_i R_i \sin\left(\frac{\tau}{R_i}\right) \right] \quad \text{(5.72)}$$

where:

$$\overline{Z} = \sqrt{V_z^2 - (\beta U_z)^2} \quad \text{(5.73)}$$

The response and the damping functions V_z and U_z are obtained from Eqs.(5.34) and (5.37) respectively by applying the substitution specified above. Similarly, the displacement transmissibility of the generic mass m_k of the system could be written in a closed-form, from Eq.(5.50), as:

$$\overline{X}_k \cong \sqrt{V_k^2 + \left(1 - 2\frac{V_k}{V_z}\frac{U_z}{U_k}\right)(\beta U_k)^2} \quad \text{(5.74)}$$

following the monoharmonic approximation introduced at the end of Section 5.4.2. However, it has been observed that Eq.(5.74) does not describe accurately the transmissibility curves of the masses in contact. In fact, the response of these masses is more markedly non-monoharmonic compared to that of the other masses. Therefore, it is not advised to refer to Eq.(5.74) if an accurate evaluation of the displacement transmissibility is required; in this case, the numerical calculation of the maximum absolute value of Eq.(5.72) within the half-period $[0, \pi]$ is preferred

and will be considered when plotting the transmissibility curves in Chapter 6. Nonetheless, Eq.(5.74) can be used for other purposes, such as the investigation of certain features of the dynamic response, which will be presented in Section 6.2.

Boundary between continuous and stick-slip regimes

In order to observe the continuous non-sticking response described in the previous paragraph, two conditions need to be met:

- the relative velocity in the contact must be different from zero in all the internal points of the time interval $[0, \pi]$. This condition is met under the assumption of $\bar{z}' < 0$ specified in Section 5.6.1;
- the amplitude of the resultant dynamic load acting in the contact must overcome the static friction force when the relative velocity is zero, i.e. at $\tau = 0$ and $\tau = \pi$.

While the first condition will simply lead to the boundary expressed by Eq.(5.58) if ψ_{ji} is replaced by $\psi_{Bi} - \psi_{Ai}$, more attention needs to be paid to the second condition. As shown in Section 3.4 for the SDOF case, the valuation of the overall dynamic load acting in the contact when $\bar{z}' = 0$ is easily carried out if a governing equation has been written for the relative motion $\bar{z}$. In the MDOF case dealt with in this section, this governing equation can be obtained by subtracting from the B-th equation of the system described by Eq.(5.66) the A-th equation multiplied by the ratio between the two masses in contact:

$$\gamma_{AB} = \frac{m_B}{m_A} = \frac{\gamma_B}{\gamma_A} \tag{5.75}$$

The resulting equation is expressed as:

$$\gamma_B r_1^2 \bar{z}'' + \sum_{k=1}^{N} \left(\overline{K}_{Bk} - \gamma_{AB} \overline{K}_{Ak} \right) \bar{x}_k + \beta(1+\gamma_{AB}) \mathrm{sgn}(\bar{z}') = (\delta_{lB} - \gamma_{AB}\delta_{lA}) \cos\tau \tag{5.76}$$

and, therefore, the second non-sticking condition can be written as:

$$\left| \sum_{k=1}^{N} \left(\overline{K}_{Bk} - \gamma_{AB} \overline{K}_{Ak} \right) \bar{x}_k - (\delta_{lB} - \gamma_{AB}\delta_{lA}) \cos(\tau + \phi_z) \right| > \mu\beta(1+\gamma_{AB}) \tag{5.77}$$

Imposing that $\tau = 0$ and introducing the expressions of $\bar{x}_{k0}$ and $\cos\phi_z$ obtained from Eqs.(5.35) and (5.39) by replacing V_j with V_z and $\overline{X}$ with $\overline{Z}$, it is obtained that:

$$\left| \left(\sum_{k=1}^{N} \overline{K}_{Bk} - \delta_{lB} \right) - \gamma_{AB} \left(\sum_{k=1}^{N} \overline{K}_{Ak} V_k - \delta_{lA} \right) \right| > \mu\beta(1 + \gamma_{AB}) \tag{5.78}$$

The remainder of the procedure is similar to that introduced in Section 5.5 and consists in taking into account the A-th and the B-th equations of the undamped system in Eq.(5.61). The final expression obtained is:

$$\beta < \sqrt{\frac{V_z^2}{U_z^2 + \left[\left(\frac{1}{\gamma_A} + \frac{1}{\gamma_B} \right) \frac{\mu}{r_1^2} \right]^2}} \tag{5.79}$$

The boundary between continuous and stick-slip regimes can finally be obtained by merging Eq.(5.58), rewritten posing $\psi_{ji} = \psi_{Bi} - \psi_{Ai}$, and Eq.(5.79):

$$\beta < \sqrt{\frac{V_z^2}{U_z^2 + \left[\max\left(S_z, \left(\frac{1}{\gamma_A} + \frac{1}{\gamma_B} \right) \frac{\mu}{r_1^2} \right) \right]^2}} \tag{5.80}$$

All the considerations reported at the end of Section 5.5 also apply to this contact configuration.

5.6.2 Joined base-wall excitation

Evaluation of the continuous steady-state response

Let us consider a MDOF mass-spring system excited by the harmonic base motion $y = Y\cos(\omega t)$. A Coulomb contact characterised by the friction force F occurs between the oscillating base and the mass m_j, as shown in Fig.5.3b. The ith governing equation of the system is given by:

$$m_i\ddot{x}_i - k_i x_{i-1} + (k_i + k_{i+1})x_i - k_{i+1}x_{i+1} + \delta_{ji} F \mathrm{sgn}(\dot{x}_j - \dot{y}) = \delta_{1i} k_1 Y \cos(\omega t) \tag{5.81}$$

Considering $P = k_1 Y$ in Eq.(5.3), Eq.(5.81) can also be expressed in a non-dimensional form as:

$$\gamma_i r_1^2 \bar{x}_i'' + \sum_{k=1}^{N} \overline{K}_{ik} \bar{x}_k + \delta_{ji} \beta \mathrm{sgn}(\bar{x}_j' - \bar{y}') = \delta_{1i} \cos\tau \tag{5.82}$$

The procedure proposed to determine the continuous steady-state response of this system is similar to that described in Section 5.6.2. If the relative motion between the mass in contact and the base is denoted as:

$$\bar{z} = \bar{x}_j - \bar{y} \tag{5.83}$$

then Eq.(5.82) can be rewritten in the non-dimensional time interval $[0, \pi]$ included between a maximum and a minimum of $\bar{z}$ as:

$$\gamma_i r_1^2 \bar{x}_i'' + \sum_{k=1}^{N} \overline{K}_{ik} \bar{x}_k = \delta_{ji}\beta + \delta_{1i}\cos(\tau + \phi_z) \tag{5.84}$$

Applying the modal transformation from Eq.(5.11), the same set of modal equations as that expressed by Eq.(5.13) is obtained from Eq.(5.82). The initial conditions for the relative motion will instead be given by:

$$\begin{cases} \bar{z}(0) = \sum_{i=1}^{N} \psi_{ji}\eta_{i0} - \cos\phi_z = \overline{Z} & \text{(5.85a)} \\ \bar{z}'(0) = \sum_{i=1}^{N} \psi_{ji}\eta'_{i0} + \sin\phi_z = 0 & \text{(5.85b)} \end{cases}$$

Substituting Eqs.(5.85a) and (5.85b) into Eqs.(5.35) and (5.38) respectively, it is possible to obtain the following expressions for the phase angle between the excitation and the relative motion $\bar{z}$:

$$\cos\phi_z = \frac{\overline{Z}}{V_j - 1} \tag{5.86}$$

$$\sin\phi_z = \frac{-\beta U}{V_j - 1} \tag{5.87}$$

while the non-dimensional amplitude of the relative motion will be obtained from the relation $\cos^2\phi_z + \sin^2\phi_z = 1$ as:

$$\overline{Z} = \sqrt{(V_j - 1)^2 - (\beta U)^2} \tag{5.88}$$

It can be observed that these expressions are equivalent to those obtained in the previous sections for the fixed-wall case if V_j is substituted with $V_j - 1$. The

response of the generic mass m_k can also be obtained from Eq.(5.41), introducing the same substitution, as:

$$\bar{x}_k = \frac{V_k}{V_j - 1}\left(\overline{Z}\cos\tau + \beta U_j \sin\tau\right) + \beta \sum_{i=1}^{N} \psi_{ji}\psi_{ki} R_i^2 \left[1 - \cos\left(\frac{\tau}{R_i}\right) - u_i R_i \sin\left(\frac{\tau}{R_i}\right)\right] \quad (5.89)$$

It can be noted that Eqs.(5.86)-(5.89) reduce to the expressions provided in Eqs.(3.11), (3.12) and (3.26) for SDOF systems under joined base-wall excitation when $N = 1$.

Also for this contact configuration, a closed-form expression can be obtained for the generic k-th displacement transmissibility, by using the monoharmonic approximation introduced in Section 5.4.2, as:

$$\overline{X}_k \cong \sqrt{V_k^2 + \left(1 - 2\,\frac{V_k}{V_j - 1}\frac{U_j}{U_k}\right)(\beta U_k)^2} \quad (5.90)$$

However, as in the case of the friction contact occurring between two masses, this approximation does not provide an accurate result for the mass in contact m_j and, therefore, its use is not advised for obtaining an accurate evaluation of the response amplitudes, while it can similarly be used for investigating the presence of invariant points across the transmissibility curves. It is worthwhile observing that, for $N = 1$, the above equation reduce to Levitan's formulation for the displacement transmissibility of SDOF systems under joined base-wall excitation [28], shown in Eq.(3.30), whose limitations have already been discussed at the end of Section 3.5.

Boundary between continuous and stick-slip regimes

The assumption of continuous steady-state response is verified, as in the previously considered contact configurations, when the relative velocity in the contact is negative in all the internal points of the time interval $[0, \pi]$ and, simultaneously, overall dynamic loading acting in the contact is larger than the static friction force at both ends of this interval.

Following the procedure described in Section 5.5, it can be shown that the first condition can be expressed in terms of the friction ratio by substituting $V_j - 1$ to

V_j in Eq.(5.58). In order to write the second condition, it is necessary to derive the governing equation for the relative motion $\bar{z}$. This equation can be obtained by substituting Eq.(5.83) into Eq.(5.82), written for $i = j$:

$$\gamma_j r_1^2 \bar{z}'' + \sum_{k=1}^{N} \overline{K}_{jk} \bar{x}_k + \beta \mathrm{sgn}(\bar{z}') = (\delta_{1j} + \gamma_j r_1^2) \cos\tau \tag{5.91}$$

Therefore, the second non-sticking condition can be expressed as:

$$\left| \sum_{k=1}^{N} \overline{K}_{jk} \bar{x}_k - (\delta_{1j} + \gamma_j r_1^2) \cos(\tau + \phi_z) \right| > \mu\beta \tag{5.92}$$

Imposing that $\tau = 0$ and introducing $\cos\phi_z$ from Eq.(5.86), as well as the expression of x_{k0} obtained by replacing $V_j - 1$ with V_j into Eq.(5.45), it is obtained that:

$$\left| \frac{\overline{Z}}{V_j - 1} \left[\sum_{k=1}^{N} \overline{K}_{jk} V_k - (\delta_{1j} + \gamma_j r_1^2) \right] \right| > \mu\beta \tag{5.93}$$

Also in this case, considering the undamped system described by Eq.(5.61) for $l = 1$, it is possible to obtain the following relation:

$$\sum_{k=1}^{N} \overline{K}_{jk} V_k - \delta_{1j} = \gamma_j r_1^2 V_j \tag{5.94}$$

which, substituted in Eq.(5.93), yields:

$$\overline{Z} > \frac{\mu\beta}{\gamma_j r_1^2} \tag{5.95}$$

With a similar procedure to that introduced in Section 5.5, this equation can be formulated in terms of the friction ratio in the same form as in Eq.(5.64), where V_j is replaced with $V_j - 1$. Finally, the boundary between continuous and stick-slip motion can be expressed, merging the two conditions derived, as:

$$\beta < \sqrt{\frac{(V_j - 1)^2}{U_j^2 + \left[\max\left(S_j, \frac{\mu}{\gamma_j r_1^2} \right) \right]^2}} \tag{5.96}$$

Approximated expressions of this boundary can also be obtained as described at the end of Section 5.5.

5.7 Summary and concluding remarks

In this chapter, analytical solutions have been derived for the continuous steady-state response of a harmonically excited MDOF system with a Coulomb friction contact between: (1) a mass and a fixed wall; (2) two different masses; (3) a mass and an oscillating base.

In particular, these solutions have been obtained by introducing a generalisation of the Den Hartog's approach for SDOF systems [21], presented in Section 2.5.1, which enables the use of the modal superposition method despite the nonlinearity of the problem. Closed-form expressions of the displacement transmissibility, the phase angle and the time response have been obtained for all the masses of the system. It has been observed that, for the case of the mass in contact, the formulations derived for all these quantities present the same form as those obtained by Den Hartog for SDOF systems, while more general expressions are observed for the other masses. In all these solutions, the response and the damping functions of the MDOF system can be written as a modal superposition of those regarding each vibrating mode of the system.

Finally, the domain of validity of these solutions has also been determined, providing an analytical formulation for the boundary between continuous and stick-slip regimes which also takes into account the case where different static and kinetic friction forces are considered.

Overall, the presented results can be used for exploring design solutions of structures that can be modelled as MDOF mass-spring systems with a friction damper required to operate in a non-sticking continuous vibration regime. Moreover, the proposed analytical solutions could be exploited for carrying out parameter investigations, optimisations and statistical model updating with a reduced computational cost compared to numerical approaches. More generally, these solutions can be used to investigate how the dynamic behaviour of a MDOF system is affected by the presence of Coulomb damping, as described in the next chapter.

Nothing in life is to be feared; it is only to be understood. Now is the time to understand more, so that we may fear less.

— Marie Curie

6

Coulomb damping effects on the response features of multi-degree-of-freedom systems

Contents

6.1 Introduction

In this chapter, the analytical solutions derived in Chapter 5, along with the numerical and experimental approaches introduced in Chapter 3 and Chapter 4, are used to investigate the effects of the presence of a Coulomb friction contact on the dynamic behaviour of a MDOF system. The main goal of this investigation is to understand how the motion regimes and the features of the dynamic response of these systems evolve depending on parameters such as the frequency of the harmonic loading, the amount of friction generated in the contact or the location of the sources of excitation and friction in the system. Different contact configurations are also explored, including contacts between a mass and a fixed wall, between two masses or between a mass and the oscillating base.

The analytical expressions obtained in Chapter 5 for the displacement transmissibilities, the phase angles and the boundaries between continuous and stick-slip regimes are further investigated in this chapter to explore the behaviour of Coulomb damped systems at resonance, at low and high frequency ratios and to reveal the presence of invariant points with respect to friction across the transmissibility and phase angle curves. In addition, a general approach is proposed for determining the conditions for which permanent sticking occurs in the contact and the response of the system in the stuck configuration. The formulation of a boundary between sliding and permanent sticking regimes allows the representation of the motion regimes scenario for MDOF systems in the two-dimensional maps introduced for SDOF systems in the previous chapters. Numerical approaches based on that proposed in Section 3.6 for the investigation of SDOF systems under joined base-wall motion have also been developed to validate the analytical results and to investigate the response of MDOF systems when stick-slip occurs. Finally, an experimental validation is proposed for 2DOF systems with a contact between either mass and a fixed wall and between the lower mass and the excited base, using a modified version of the setup proposed in Chapter 4.

The chapter is structured as follows. Section 6.2 presents the analytical investigation of the resonant, low- and high-frequency behaviour of MDOF systems

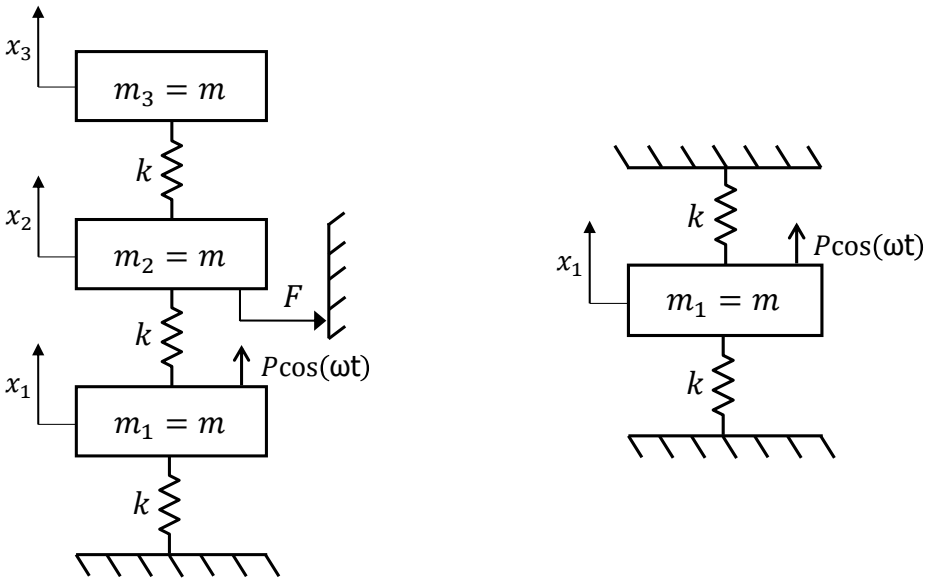

(a) **(b)**

Figure 6.1: 3DOF system with unitary mass and stiffness ratios, a Coulomb friction contact on m_2 and harmonic excitation on m_1 (**a**) and its stuck configuration (**b**).

with a contact between a mass and a fixed wall. In Section 6.3, the numerical validation and extension to stick-slip regime is proposed for 2DOF and 5DOF systems with the harmonic and the friction forces applied to the same or to different masses. The experimental validation performed on a two-storey frame setup is described in Section 6.4. Finally, the investigation of the response features, the numerical and the experimental validation are also proposed for MDOF systems with a contact between two oscillating parts in Section 6.5.

6.2 Features of the dynamic response

This section focuses on investigating the features of the dynamic response of a MDOF system with a contact on the j-th mass and subjected to a harmonic excitation acting on the l-th mass. This investigation is based on the analytical solutions derived in Chapter 5 for its continuous steady-state response and the boundaries between continuous and stick-slip motion regimes and focuses on:

- resonant, low- and high-frequency behaviours

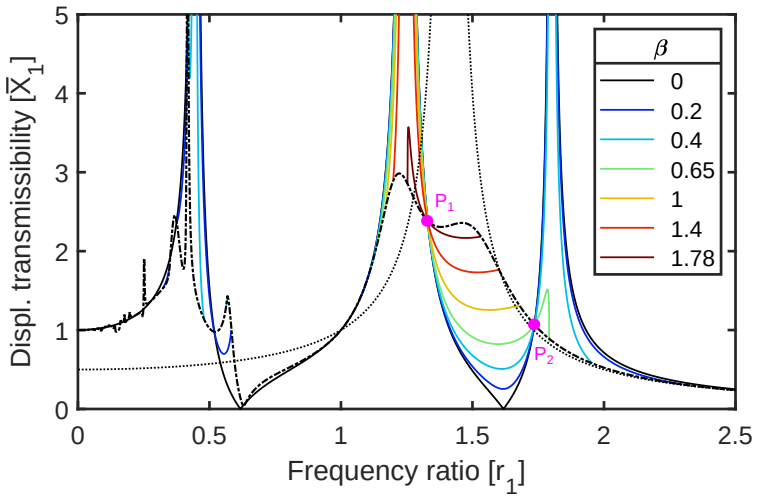

Figure 6.2: Continuous transmissibility curves for the mass m_1 of a 3DOF system with $\gamma_i = \kappa_i = 1$, $\mu = 1$, a Coulomb friction contact on m_2 and harmonic excitation on m_1 for varying r_1 and β. The black dashed line represents the boundary between continuous and stick-slip regimes, while the black dotted line portrays the transmissibility in stuck configuration. The invariant points P_1 and P_2 are highlighted in magenta.

- the presence of invariant points in the transmissibility curves
- the effect of stuck friction contacts on the response of the system

The 3DOF system shown in Fig.6.1a, which is characterised by unitary stiffness and mass ratios, a harmonic load applied on m_1, a friction contact occurring on m_2 and equal static and kinetic friction forces will be used as an example to show these response features. In particular, the displacement transmissibility displayed by the mass m_1 in continuous regime, shown in Fig.6.2, will be considered.

6.2.1 Resonant behaviour

As discussed in Sections 2.5.1 and 3.5, Coulomb friction is not able to provide a finite resonance in SDOF systems if $\beta < \pi/4$. This value represents the minimum friction ratio for which stick-slip occurs in the response at $r = 1$.

Let us then denote with $\beta_{n,i}$ the threshold value of the friction ratio for which the ith resonant peak of a Coulomb damped MDOF system with a fixed wall becomes finite. Similarly to the SDOF case, $\beta_{n,i}$ can be determined by evaluating the value of the boundary between continuous and stick-slip motion from Eq.(5.65) for $R_i \to 1$.

Observing that in the expressions of the response and of the damping functions, in Eqs.(5.34) and (5.37) respectively, only the ith terms of the summations tend to infinity, it is possible to write:

$$\beta_{n,i} = \lim_{R_i \to 1} \beta_{\lim} = \left| \frac{\psi_{li}}{\psi_{ji}} \right| \lim_{R_i \to 1} \frac{\dfrac{1}{1 - R_i^2}}{\dfrac{\sin(\pi/R_i)}{R_i[1 + \cos(\pi/R_i)]}} \tag{6.1}$$

Therefore, after evaluating the above limit, the minimum friction ratio required for observing a finite ith resonant peak is obtained as:

$$\beta_{n,i} = \frac{\pi}{4} \left| \frac{\psi_{li}}{\psi_{ji}} \right| \tag{6.2}$$

It must be observed that, in the above equation, the ratio between ψ_{li} and ψ_{ji} is always independent of the frequency ratio.

In the 3DOF system shown in Fig.6.1a, the threshold values of the friction ratio calculated from Eq.(6.2) are equal to $\beta_{n,1} = 0.436$, $\beta_{n,2} = 1.765$ and $\beta_{n,3} = 0.630$. These results are in agreement with the resonant behaviour exhibited by the continuous transmissibility curves shown in Fig.6.2 for the mass m_1 of this system.

Eq.(6.2) shows that, in general, the different resonant peaks of a MDOF system will become finite for different values of β. However, if the harmonic excitation and the friction force act on the same mass, i.e. if $j = l$, $\beta_{n,i}$ will be equal to:

$$\beta_{n,i} = \frac{\pi}{4} \cong 0.785 \tag{6.3}$$

for any i, meaning that all the resonant peaks of the system will become finite for the same threshold value of the friction ratio.

6.2.2 Quasi-static conditions

In quasi-static conditions, the dynamic response of SDOF systems with a fixed wall is usually characterised by the occurrence of stick-slip motion. Moreover, when the frequency ratio approaches to zero, the number of stops per cycle can increase significantly, as shown by many authors (see, e.g., [22, 65]).

It can be shown that stick-slip motion usually occurs at very low frequency ratios also in the MDOF case. In fact, the evaluation of the boundary friction ratio from Eq.(5.65) for $\omega \to 0$ and, therefore, for $R_i \to 0$ yields:

$$\beta_0 = \lim_{R_i \to 0} \beta_{\text{lim}} = 0 \tag{6.4}$$

This equation reveals that any non-zero value of the friction ratio would lead to stick-slip in quasi-static conditions.

The numerical investigations carried out in this study showed that the dynamic response of MDOF systems is characterised, as in the SDOF case, by an increasing number of stops for $r_1 \to 0$. However, the starting point of the transmissibility curves at $r_1 = 0$ can be evaluated analytically, avoiding the complications which may arise in numerical approaches due to the large number of stops per cycle.

Let us rewrite the governing equations of the problem from Eq.(5.6) in static conditions. If $\omega = 0$, then both r_1 and τ will also be equal to zero. Thus, the harmonic excitation will reduce to a constant force, which will be opposed by a constant friction force. Therefore, the governing equations will reduce to:

$$\overline{\mathbf{K}}\bar{\mathbf{x}}_\mathbf{0} = \bar{\mathbf{p}}_\mathbf{0} - \bar{\mathbf{f}}_\mathbf{0} \tag{6.5}$$

where:

- $\bar{\mathbf{x}}_\mathbf{0} = \left[\overline{X}_{10}, \ldots, \overline{X}_{N0}\right]^T$ is the vector of the displacement transmissibilities for $r_1 = 0$;
- $\bar{\mathbf{p}}_\mathbf{0}$ is a vector whose only non-zero component is equal to 1 in the l-th position;
- $\bar{\mathbf{f}}_\mathbf{0}$ is a vector whose only non-zero component is equal to β in the j-th position.

The starting points of the transmissibilities curves can be evaluated as solutions of the linear algebraic system expressed in Eq.(6.5). In the case of a SDOF system, the solution is given by $\overline{X}_0 = 1 - \beta$, in agreement with the starting value observed by Csernak et al. in reference [70], while for the 3DOF system in Fig.6.1a the values obtained are $\overline{X}_{10} = 1 - \beta$, $\overline{X}_{20} = 1 - 2\beta$ and $\overline{X}_{30} = 1 - 2\beta$.

The validity of these results is limited to the cases where a sliding motion can be observed in the contact in quasi-static conditions. However, depending on the system investigated and on the value of β, permanent sticking may occur; in this case, a different approach is required. This will be discussed in Section 6.2.5.

6.2.3 High-frequency behaviour

In Section 2.5.1, it has been observed that, although the response amplitude of a SDOF system with a fixed wall always tends to zero when $r \to \infty$, the response can exhibit different motion regimes depending on the value of the friction ratio. More specifically, continuous motion will be observed below the threshold value specified in Eq.(2.31), while stick-slip is expected if β is included between such a value and $1/\mu$, for which permanent sticking occurs.

The occurrence of stick-slip motion at high frequency ratios in the response of a MDOF system can be investigated by evaluating the limit of the boundary friction ratio from Eq.(5.64) for $\omega \to \infty$, recalling that $\mu/(\gamma_j r_1^2) \geq S_j$ at high frequencies. Considering that R_i will also tend to infinity in this case, it is possible to write:

$$\beta_\infty = \lim_{R_i \to \infty} \beta_{\lim} = \sqrt{\frac{\left(\sum_{i=1}^{N} \psi_{li}\psi_{ji}\right)^2}{\left(\mu + \frac{\pi^2}{4}\right)\left(\sum_{i=1}^{N} \psi_{ji}^2\right)^2}} \tag{6.6}$$

Given the orthogonality conditions of the mode shapes and that, from Eq.(5.10):

$$\sum_{i=1}^{N} \psi_{ji}^2 = \frac{1}{\gamma_j r_1^2} \tag{6.7}$$

the boundary friction ratio will be equal to:

$$\beta_\infty = \begin{cases} \dfrac{2}{\sqrt{4\mu + \pi^2}} & \text{if } j = l \\ 0 & \text{if } j \neq l \end{cases} \tag{6.8}$$

Therefore:

- if the harmonic and the friction forces act on the same mass of the MDOF system, stick-slip will occur at high frequencies only if the friction ratio is larger than the above value, which is equal to 0.537 if $\mu = 1$;
- otherwise, stick-slip will occur for $r_1 \to \infty$ for any non-zero value of β , as long as permanent sticking does not occur.

In the case of the 3DOF system shown in Fig.6.1a, the harmonic load and the friction contact are applied to different masses and, therefore, stick-slip occurs at high frequencies for any value of the friction ratio; this can also be observed from Fig.6.2.

6.2.4 Invariant points

In Fig.6.2, it can be observed that the continuous transmissibility curves of the bottom mass of the 3DOF system pass through two points denoted as P_1 and P_2, which are commonly defined as invariant points. In these points, the response amplitude is independent of the damping, which is represented in this case by the friction ratio.

The presence of invariant points in the transmissibility curves is regarded as an important aspect in the design of mechanical systems such as dynamic vibration absorbers [149, 150, 151] and car suspensions [152, 153]. In particular, according to the Den Hartog's theory illustrated in reference [154], these points can be used to determine the optimal configuration of a viscous damper acting as vibration absorber for a main undamped SDOF system. An approach for determining the presence of invariant points in the transmissibilities of MDOF systems with Coulomb friction is proposed in what follows.

Let us consider the expression of the displacement transmissibility provided by Eq.(5.39) for mass in contact of the MDOF system. It appears clear that the transmissibility will not depend on the friction ratio if:

$$U_j = 0 \tag{6.9}$$

Thus, this equation can be used to find the invariant points for the response of the mass m_j. From Eq.(5.39), it can also be deduced that, at any other frequency ratios,

$\overline{X}_j$ will always decrease with β; therefore, no inversion of the transmissibility curves will be observed across the invariant points in this case. Moreover, from Eq.(5.35) and Eq.(5.38), it is possible to observe that the points determined from Eq.(6.9) will also be invariant for the phase angle ϕ_j. Particularly, from Eq.(5.38), it can be deduced that the corresponding value of ϕ_j will be equal to 0 or 180 degrees, i.e. the excitation and the j-th mass motion will be in phase or in phase-opposition. The phase angle curves will also exhibit an inversion across these points.

Let us now consider the generic k-th displacement transmissibility of the system. From Eq.(5.50), it is possible to deduce that the invariant points can be obtained not only from the equation $U_k = 0$, but also from:

$$1 - 2\frac{V_k}{V_j}\frac{U_j}{U_k} = 0 \tag{6.10}$$

The points determined as solutions of the latter equation are associated to an inversion of the transmissibility curves. This behaviour can only be observed in the transmissibilities of the masses not in contact. Furthermore, these points are not invariant for the phase angle ϕ_k.

It is important to note that Eq.(6.9) and Eq.(6.10) hold only for the continuous response of the MDOF system. In general, transmissibility curves will not pass through an invariant point if stick-slip or permanent sticking of the mass in contact occur at the corresponding frequency ratio. Finally, it is worth observing that Eqs.(6.9) and (6.10) are transcendental equations and have infinitely many possible solutions. Nevertheless, as shown in Section 6.3, the vast majority of these solutions are characterised by very small values of frequency ratio, where usually stick-slip motion or permanent sticking occur, and can therefore be disregarded.

6.2.5 Stuck configurations

In friction damped systems, sliding can occur between two components in contact either continuously or in alternation with sticking phases. However, friction contacts can also become permanently stuck when the amplitude of the dynamic load acting

in the contact is smaller than the static friction force, as discussed for SDOF systems in Sections 2.5.1 and 3.4.

The same principle holds, more in general, for the mass in contact of a MDOF system. However, even when the mass in contact is stuck, some masses of the system can still exhibit a dynamic response, depending on where the harmonic and the friction forces are applied. The reduced system which remains active when m_j is stuck will be referred to as *stuck configuration* of the MDOF system and its response can be evaluated as follows:

- if $j > l$, only the masses $m_1, \ldots, m_{j-1}$ will be excited. Thus, the stuck configuration of the system will be represented by an undamped system with $j-1$ DOFs, where the stuck j-th mass is replaced by a fixed wall. The response of this system can be evaluated from standard modal analysis and will be characterised by the presence of $j-1$ infinite resonant peaks located, in general, at different frequencies from those of the original system;

- if $j < l$, only the masses $m_{j+1}, \ldots, m_N$ will be excited and, therefore, the stuck configuration of the system will include $N-j$ DOFs. All the above considerations apply, except that, in this case, the stuck system will exhibit $N-j$ infinite resonant peaks;

- finally, if $j = l$, the harmonic excitation is applied to the stuck mass and, therefore, is not transmitted to any of the other masses, leaving the MDOF system fully stuck. Obviously, this is also the case for a SDOF system.

Denoting with $\overline{X}_i^*$ the ith displacement transmissibility of the system in stuck configuration, it is therefore possible to write the conditions for observing sliding motion between the mass m_j and the wall as:

$$\begin{cases} \beta < (\kappa_j \overline{X}_{j-1}^*)/\mu & \text{if } j > l \quad (6.11a) \\ \beta < (\kappa_{j+1} \overline{X}_{j+1}^*)/\mu & \text{if } j < l \quad (6.11b) \\ \beta < 1/\mu & \text{if } j = l \quad (6.11c) \end{cases}$$

In the example of the 3DOF system in Fig.6.1a, the stuck configuration consists in the SDOF system shown in Fig.6.1b, where the bottom mass is the only remaining active DOF, while the intermediate mass is replaced by a fixed wall. The displacement transmissibility for m_1 in stuck conditions can be obtained as:

$$\overline{X}_1^* = \frac{1}{|2 - r_1^2|} \tag{6.12}$$

and is represented by a dotted line in Fig.6.1b. According to Eq.(6.11a), sliding occurs between the mass m_2 and the wall if $\overline{X}_1^* > \beta$. This implies that, for each value of β, the system will operate in a non-stuck configuration only in the frequency ratio range:

$$\sqrt{\frac{2\beta - 1}{\beta}} < r_1 < \sqrt{\frac{1 + 2\beta}{\beta}} \tag{6.13}$$

The lower bound of Eq.(6.13) reduces to $r_1 = 0$ if $\beta \leq 0.5$, while the upper bound is defined for any non-zero value of β. Therefore, in the presence of friction damping, the mass m_2 will always become stuck at high frequency ratios beyond the threshold expressed in the above inequality. Moreover, these bounds will converge to a single point at $r_1 = \sqrt{2}$ only for $\beta \to \infty$. Therefore, even when the friction ratio is very large, sliding motion will always occur in the contact in a small range of frequencies around the resonance of the stuck configuration and the transmissibility will assume a finite value in this range; this behaviour will be shown in Section 6.3, where stick-slip responses are also investigated.

The last two properties, regarding the high-frequency and the resonant behaviours of the stuck configuration, can easily be generalised to any MDOF systems with $j \neq l$. In fact, it can be observed that:

- at high frequencies, all the displacement transmissibilities tend to zero and, therefore, Eqs.(6.11a) and (6.11b) are never verified, leading to permanent sticking when $r_1 \to \infty$;

- in proximity of a resonance of the stuck configuration, the transmissibility curves tend to infinity leading to Eqs.(6.11a) and (6.11b) being always verified.

6.3 Numerical validation and stick-slip response

In this section, the analytical solutions introduced in Chapter 5 for the continuous response of MDOF systems with a fixed wall are compared to the results yielded by a numerical approach. Moreover, the response is also evaluated numerically in stick-slip regimes, providing a validation of the analytical boundaries between continuous and stick-slip motion regimes and a complete overview of the dynamic behaviour for varying frequency and friction ratios. The stick-slip responses have been evaluated, for simplicity, in the case of $\mu = 1$; different results would be obtained, in general, if a different value of the static friction force were considered.

In Section 6.2, it has been shown that the continuous response features can be significantly different depending on whether the friction and the harmonic forces are applied on the same or on different masses. Therefore, these two different classes of MDOF systems will be dealt with separately. In each case, analytical and numerical results will be first compared and discussed in detail for the 2DOF case and then generalised to systems with a larger number of DOFs, referring to the case of a 5DOF system. Moreover, for each of these systems, the analytical boundaries among continuous, stick-slip and permanent sticking regimes will be represented in a 2-D parameter space for varying frequency and friction ratios and taking into account different values of the parameter μ.

6.3.1 Numerical approach

The numerical approach used for evaluating the time response of MDOF systems with Coulomb friction via time integration is an extended version of the algorithm presented in Section 3.6.1, as can be seen from its flowchart represented in Fig.6.3. The main differences with the algorithm shown in Fig.3.10 are described in what follows.

- Similarly to the SDOF case, the algorithm requires as an input the parameters r_1, β and μ. However, a MDOF system is also described by the $N-1$ mass ratios and the $N-1$ stiffness ratios introduced in Section 5.2, which therefore need to be specified by the user. Alternatively, the non-dimensional matrices

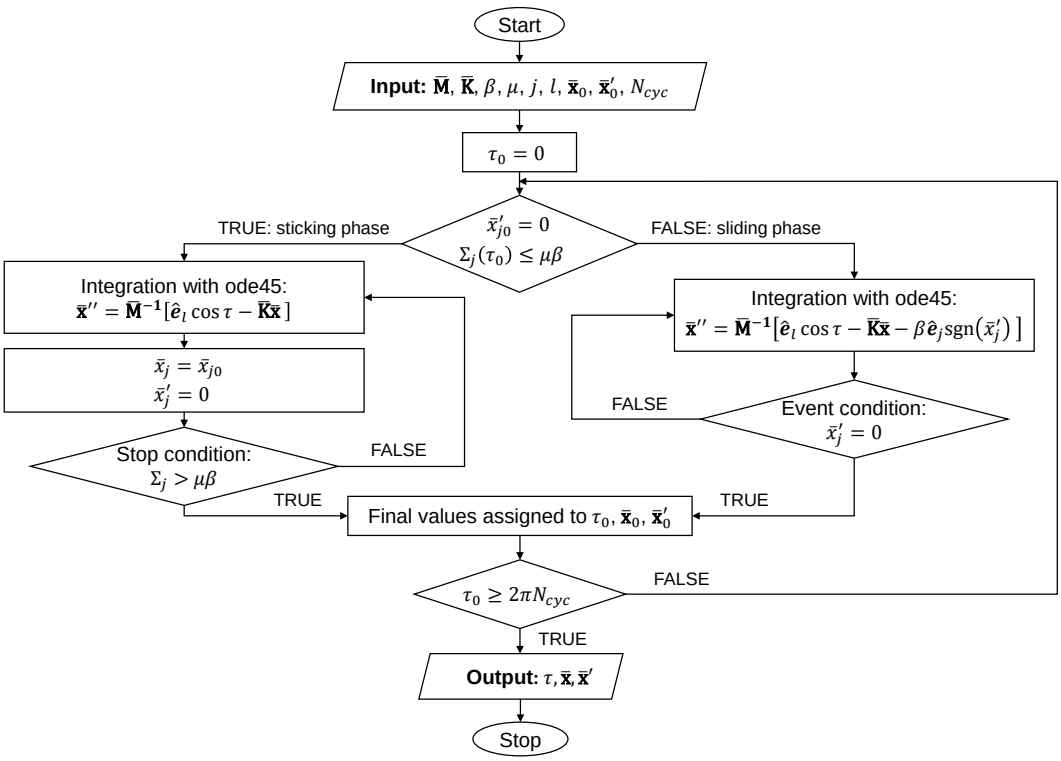

Figure 6.3: Flowchart of the numerical algorithm implemented for the calculation of the response of a MDOF system with a Coulomb friction contact under harmonic excitation.

$\overline{\mathbf{M}} = \mathbf{M}\omega^2/k_1$ and $\overline{\mathbf{K}} = \mathbf{K}/k_1$ can directly be provided, which is particularly practical if the dimensional mass and stiffness matrices of the system are known; in this case, the mass, stiffness and frequency ratios will not be needed. In addition, it is required to select the number of DOFs of system and to specify which are the masses in contact and under harmonic excitation.

- While the sliding phases present no significant differences compared to the SDOF case, it must be considered that during the sticking phases the masses not in contact will keep oscillating; therefore, numerical integration is also needed at this stage. Despite the displacement and the velocity of the mass in contact are known during the stop, it is convenient to integrate all the N equations of the system, disregarding the friction force, and imposing the displacement and the velocity of the mass m_j at each step, as shown in Fig.6.3. In fact, this procedure allows the use of the same mass and stiffness matrices used during the sliding stages.

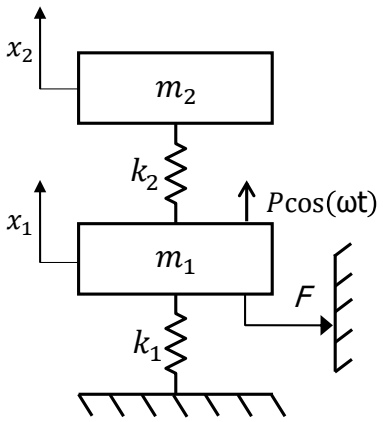

Figure 6.4: 2DOF system with a friction contact and a harmonic load applied to the lower mass.

The remaining steps coincide with those described for SDOF systems; their explanation can be found in Section 3.6.1. All the numerical analyses carried out in the next paragraphs have been obtained by considering $N_{cyc} = 200$ cycles and with absolute and relative tolerances equal to 10^{-6} and 10^{-12} respectively.

6.3.2 Systems with excitation and contact on the same mass

2DOF system with excitation and contact on m_1

The analytical and numerical results for the dynamic response of the 2DOF system with $j = l = 1$ shown in Fig.6.4 are discussed in what follows.

Figs.6.5a-b present a comparison between the analytical and numerical time responses of the masses m_1 and m_2. These results have been plotted in the non-dimensional time interval $[0, \pi]$ for two different sets of the parameters r_1, β, κ, γ and μ, exhibiting in both cases an excellent agreement. The harmonic excitation $\cos(\tau + \phi_1)$ is also represented and appears perfectly aligned to the numerical forcing function, showing that a very good agreement is also achieved for the phase angle ϕ_1.

The analytical and the numerical displacement transmissibilities and phase angles are shown in Figs.6.6a-b for $\gamma = \kappa = 1$ and varying frequency and friction ratios. Specifically, the frequency ratio varies in the range $0 : 2.5$ and the friction ratios $0 : 0.2 : 0.8$ are considered. In these figures, it is possible to observe an excellent

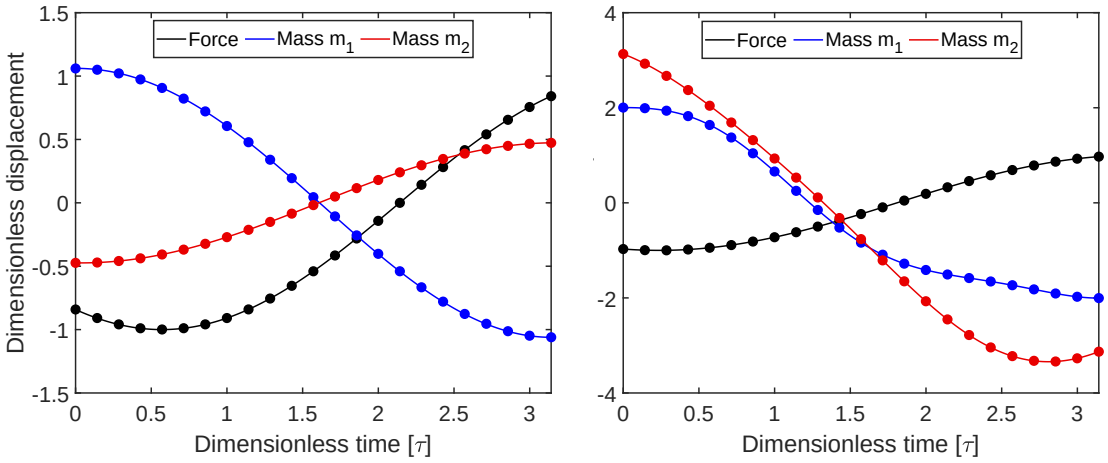

(a) $\gamma = 1$, $\kappa = 1$, $\mu = 1$, $\beta = 0.4$, $r_1 = 1.8$ **(b)** $\gamma = 2$, $\kappa = 2$, $\mu = 1$, $\beta = 0.4$, $r_1 = 0.6$

Figure 6.5: Steady-state time response of a 2DOF system with a friction contact and a harmonic load on the lower mass for two different sets of parameters: comparison between analytical (continuous lines) and numerical (round markers).

agreement between the analytical (continuous lines) and numerical results (rounded markers) when the motion of m_1 is continuous. The analytical boundaries between continuous and stick-slip regimes are represented by a black dashed line. Numerical transmissibilities for stick-slip responses are also included (diamond markers). It can be observed that stick-slip motion occurs in the numerical responses only when the transmissibility is smaller than the boundary value, showing that the motion regimes occurring in the numerical results are in agreement with the analytical prediction.

The following features of the dynamic response of this 2DOF system can be observed from Fig.6.6.

- Both resonant peaks are finite only in the case $\beta = 0.8$, in agreement with Eq.(6.3).

- From Eq.(6.5), it can be calculated the starting values of the transmissibility curves at $r_1 = 0$ are $\overline{X}_{10} = \overline{X}_{20} = 1 - \beta$. These values are in agreement with those displayed in both transmissibility plots.

- At low frequency ratios, the response of the system is characterised by the occurrence of stick-slip motion. For most values of the friction ratio, the response is continuous starting from $r_1 = 0.559$. Among those displayed, only

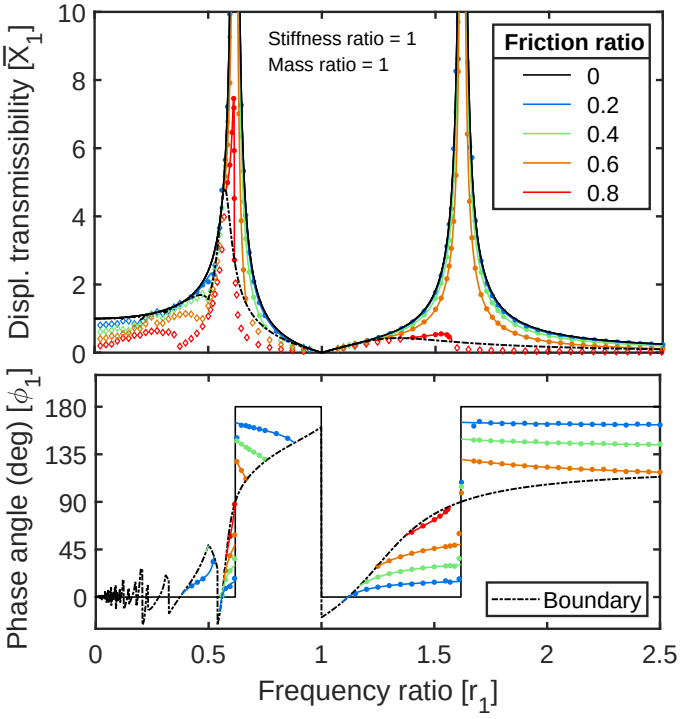

(a) Mass m_1

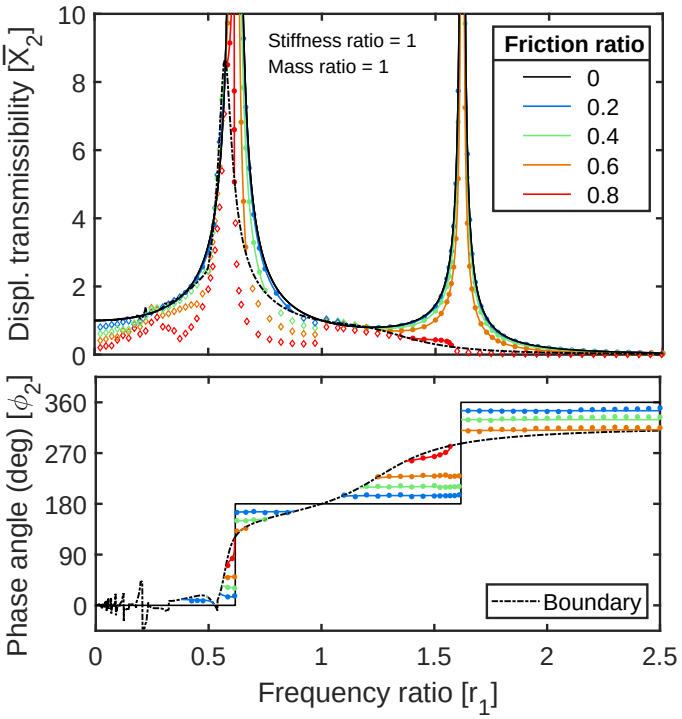

(b) Mass m_2

Figure 6.6: Displacement transmissibilities and phase angles of a 2DOF system with a Coulomb contact and a harmonic load on m_1 for $\gamma = \kappa = \mu = 1$ and varying friction ratio. Analytical results are represented by the continuous lines, while numerical results are represented with round (continuous motion) and diamond markers (stick-slip motion).

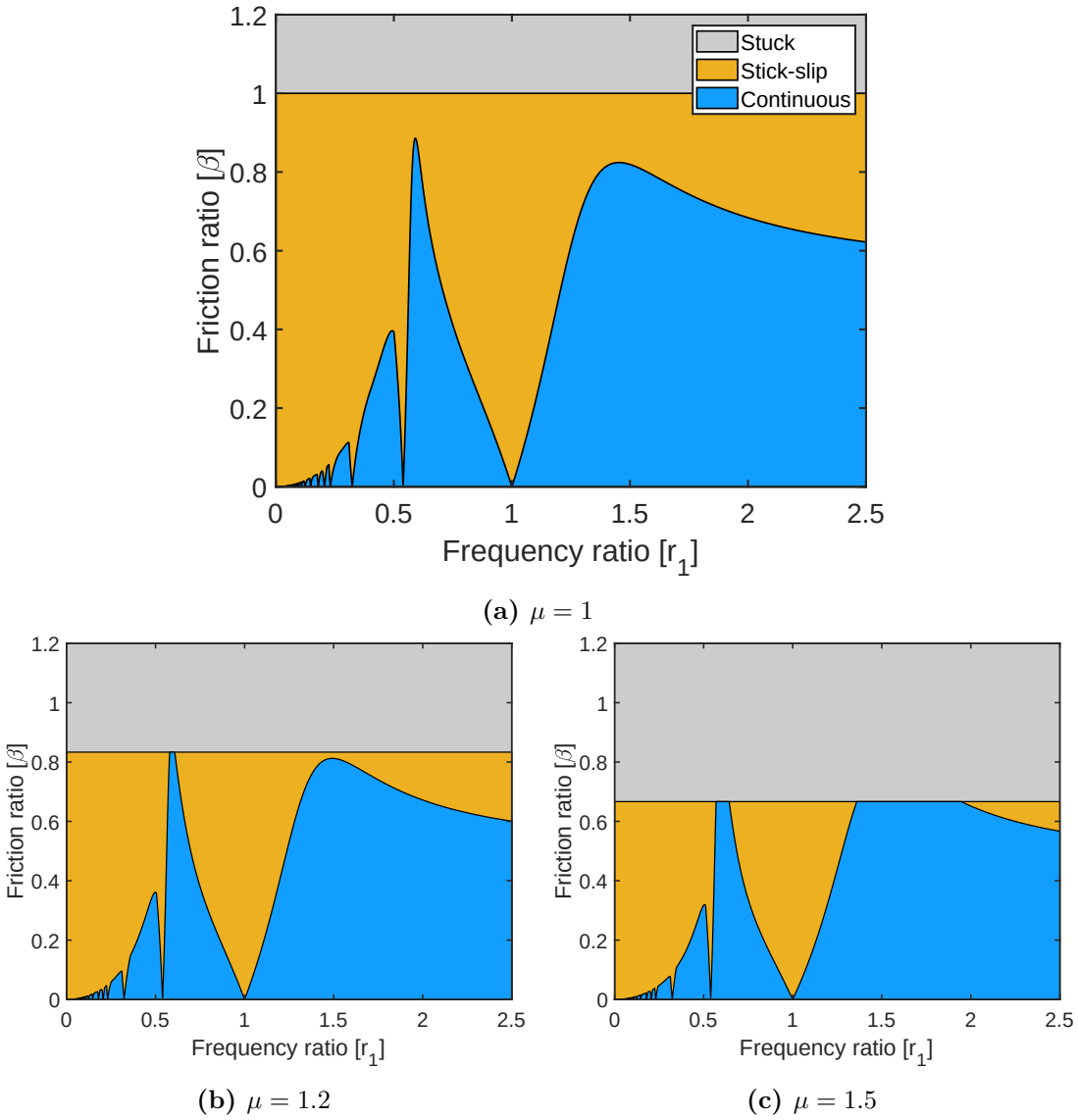

(a) $\mu = 1$

(b) $\mu = 1.2$

(c) $\mu = 1.5$

Figure 6.7: Motion regimes of a 2DOF system with a Coulomb contact and a harmonic load on m_1 for $\gamma = \kappa = 1$ and varying frequency and friction ratios.

in the case $\beta = 0.2$ continuous motion occurs at lower frequencies, specifically in the range $0.372 < r_1 < 0.524$. The patterns exhibited by the transmissibility curves in the low frequency ratio range are very similar to those observed for SDOF systems by several authors (see, e.g, [64, 65]).

- It can be observed that stick-slip motion occurs at high frequencies for $\beta = 0.8$ and it has been verified that this is also the case for $\beta = 0.6$, even though the transition from continuous to stick-slip regime does not occur within the range of frequencies displayed in Fig.6.6. This behaviour is in agreement with

Eq.(6.8).

- The invariant points of $\overline{X}_1$ can be evaluated from Eq.(6.9). These points can be observed in Fig.6.6a as the intersections between the undamped and the boundary curves, which are particularly well-visible in the phase angle plot. As anticipated in Section 6.2.4, most of these points are located in the low-frequency region, where the response is discontinuous for most values of β. Since Eq.(6.9) only holds for continuous regime, the transmissibility and the phase angle curves will not pass through these points, which can therefore be disregarded. The only relevant solutions are $r_1 = 0.559$ and $r_1 = 1.123$, which represent the main points of transition from continuous to stick-slip regime for most curves.

- The invariant points of $\overline{X}_2$, which can be obtained from Eq.(6.10), are associated to local inversions of the transmissibility curves, occurring at $0.527 < r_1 < 0.576$ and $1 < r_1 < 1.201$. However, as can be seen in Fig.6.6b, none of these show a significative increase of $\overline{X}_2$ with β.

- It can be observed that $\phi_2 \cong \phi_1$ for $r_1 < \sqrt{\kappa/\gamma}$ and $\phi_2 \cong \phi_1 + \pi$ for $r_1 \geq \sqrt{\kappa/\gamma}$. This result can be explained by observing that mass m_2 is only excited, through the upper spring, by the motion of the mass m_1. Since the contact occurs on m_1 only, no damping and, consequently, no phase delay is introduced in the vibration transmission between the two masses. Small differences between these phase angles are justified by the non-monoharmonic motion of the mass m_1.

Finally, Fig.6.7 shows the analytical boundaries among continuous, stick-slip and permanent sticking motion regimes, obtained by using Eq.(5.65) and Eq.(6.11) respectively. Fig.6.7a, obtained for $\mu = 1$, presents a similar pattern to that displayed by the boundaries of a SDOF system with a fixed wall, shown in Fig.2.5. In particular, the boundary between sliding and permanent sticking regimes is unchanged, while the boundary between continuous and stick-slip regimes displays a

slightly more complicated pattern, particularly for $r < 1$. However, most properties, including the asymptotic value at high frequencies and the maximum value assumed by the curves are the same as in the SDOF case. An antiresonance can be observed at $r_1 = 1$, in correspondence of the antiresonance displayed by $\overline{X}_1$; it has been verified that, more in general, this antiresonance occurs at $r_1 = \sqrt{\kappa/\gamma}$. The effect of the parameter μ is also investigated in Fig.6.7. By observing Figs.6.7b-c, it is possible to observe as, for increasing values of μ, the boundary β^*_{lim} occurs at smaller and smaller values of the friction ratio, eventually intersecting with the boundary β_{lim}, which appears to be more lightly affected by the variation of the static friction force.

5DOF system with excitation and contact on m_1

Most of the response features discussed for the 2DOF case can also be observed in systems with a larger number of DOFs if excitation and contact are applied to the same mass.

Let us consider, for instance, the case of a 5DOF system with unitary stiffness and mass ratios where both forces are applied to the bottom mass m_1. The analytical transmissibilities and phase angles are plotted in Figs.6.8a-b, for the same frequency ratio range and values of friction ratio considered in the 2DOF case; in Fig.6.8a, the numerical transmissibilities in stick-slip regime have also been included. The analytical and the numerical time responses of this system are shown, for a specific set of parameters, in Fig.6.9a, exhibiting an excellent agreement. Analytical and numerical phase angles curves, associated to the different masses of the system, are shown in Fig. 6.9b for varying r_1 and $\beta = 0.4$; also in this case, a very good agreement can be observed. Finally, the boundaries among continuous, stick-slip and permanent sticking motion regimes are represented in Fig.6.10.

From these figures, the following behaviours can be observed:

- the transmissibility curves present finite resonant peaks only in the case $\beta = 0.8$, among those considered;

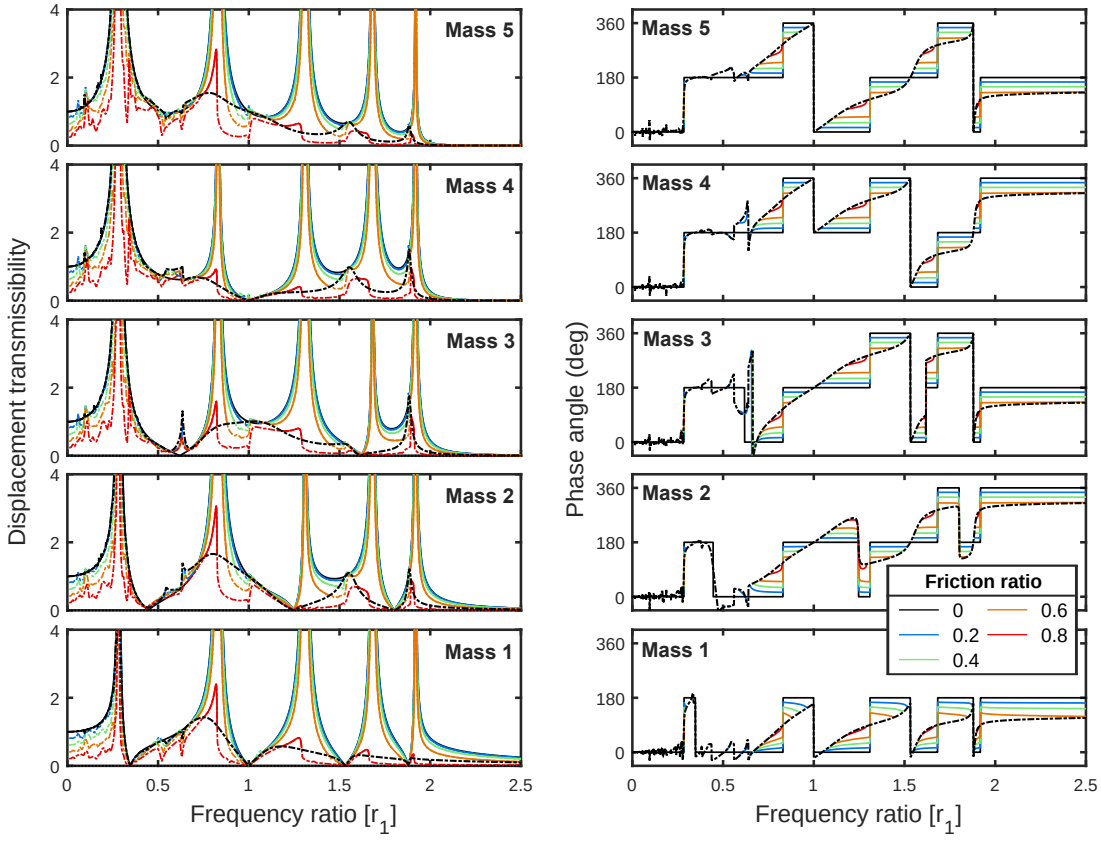

Figure 6.8: Displacement transmissibilities (**a**) and phase angles (**b**) of a 5DOF system with a Coulomb contact and a harmonic load on m_1, unitary mass and stiffness ratios and varying friction ratio. Analytical results for continuous motions are represented with continuous lines, while numerical results for stick-slip motions with dashed lines. The black dashed line represents the boundary between continuous and stick-slip regimes.

- the displacement transmissibilities are generally decreasing for increasing values of β. Local inversions can be observed for the masses not in contact, but they always occur in small intervals of r_1 and only present a slight increase in the transmissibility;

- the motion of each mass of the system is approximatively in phase or in phase-opposition with the motion of the other masses. This can be clearly observed from Figs.6.9a-b.

- the boundary between continuous and stick-slip regimes exhibits a similar pattern to that observed for the 2DOF case in Fig.6.7a. In particular, the boundary has an irregular behaviour at low frequency ratios and presents

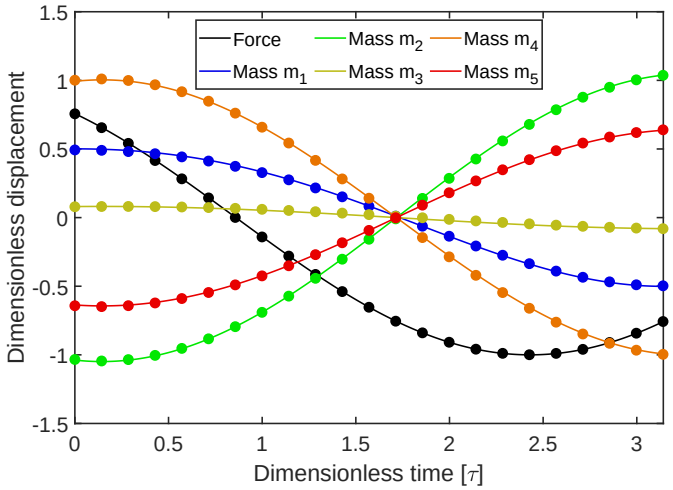

(a) $r_1 = 1.6$, $\beta = 0.6$

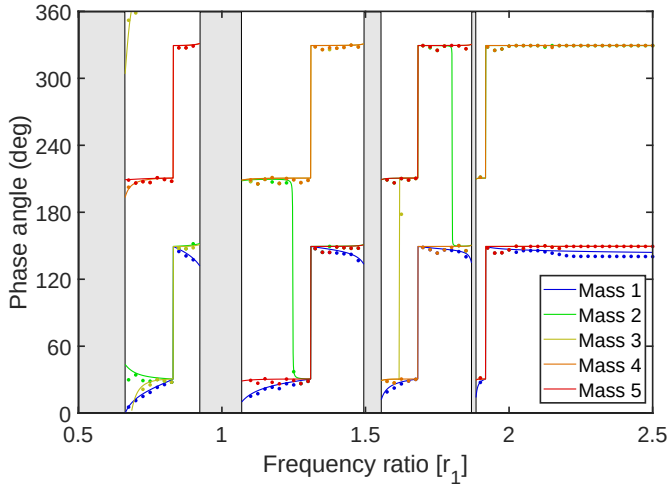

(b) $\beta = 0.4$

Figure 6.9: Analytical (continuous lines) and numerical (round markers) steady-state time response (**a**) and phase angle curves (**b**) of a 5DOF system with a Coulomb contact and a harmonic load on m_1 and $\gamma = \kappa = \mu = 1$. The grey regions indicate stick-slip and stuck regimes.

five maxima which are all characterised by the friction ratio $\beta \cong 0.83$. All these maxima are reached smoothly, except the one occurring at the lowest frequency ratio.

Fig.6.9b shows that the phase angle curves, particularly those of the mass in contact m_1, present slightly different patterns only in proximity of the transition to stick-slip regimes and at high frequency ratios. This behaviour can be explained observing that in these two cases the response of the mass in contact, which is usually nearly

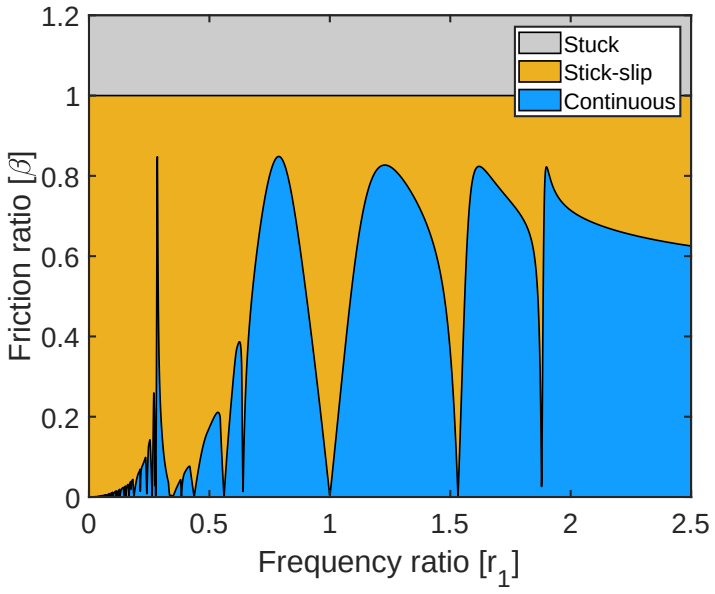

Figure 6.10: Motion regimes of a 5DOF system with equal masses and springs and $\mu = 1$, with a Coulomb contact and a harmonic load on m_1 for varying frequency and friction ratios.

monoharmonic in continuous regime, is significantly affected by the higher harmonics.

6.3.3 Systems with excitation applied to a mass not in contact

2DOF system excited on m_1 with m_2 in contact

Let us consider a 2DOF system with a friction contact on the mass m_2 and excited by a harmonic load applied on m_1, as shown in Fig.6.11. A comparison between the analytical and the numerical time responses of this system in the non-dimensional time interval $[0, \pi]$ is portrayed in Figs.6.12a-b for two different sets of parameters, showing an excellent agreement. Analytical and numerical results for the displacement transmissibilities and the phase angles are compared in Figs.6.13a-b, for varying frequency ratios within the range $0 : 2.5$ and for the friction ratios $[0, 0.2, 0.4, 0.5, 1, 1.5, 2, 5]$. Also in this case, the agreement between analytical and numerical results in continuous motion regime is very good. Furthermore, stick-slip motion occurs in the numerical responses only when the transmissibility of the mass in contact is smaller than the boundary value, as expected.

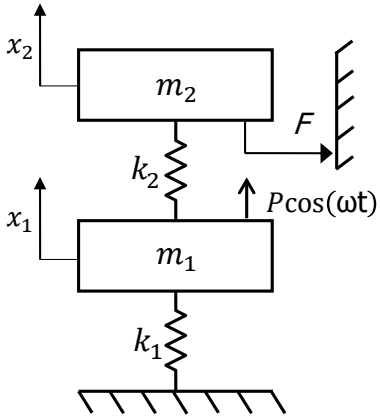

Figure 6.11: 2DOF system with a friction contact on m_1 and a harmonic load on m_2.

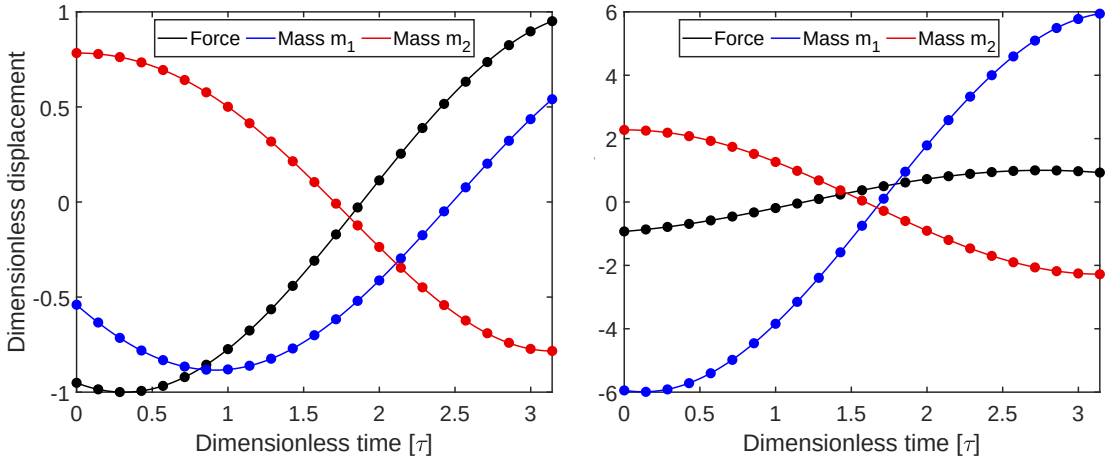

(a) $\gamma = 1$, $\kappa = 1$, $\mu = 1$, $\beta = 0.5$, $r_1 = 1.3$ **(b)** $\gamma = 2$, $\kappa = 2$, $\mu = 1$, $\beta = 1$, $r_1 = 1.9$

Figure 6.12: Steady-state time response of a 2DOF system with a friction contact on m_1 and a harmonic load on m_2 for two different sets of parameters: comparison between analytical (continuous lines) and numerical (round markers).

The main features of the dynamic response of this 2DOF system, which can be observed from Fig.6.13, are summarised in what follows.

- It can be observed that the first and the second resonant peaks become finite starting from the cases $\beta = 0.5$ and $\beta = 1.5$, respectively. This result agrees with the values obtained from Eq.(6.3), which are $\beta_{n,1} = 0.485$ and $\beta_{n,2} = 1.271$.

- The stuck configuration of this 2DOF system is represented by an undamped SDOF system where the mass m_1 is connected to a fixed wall on both sides

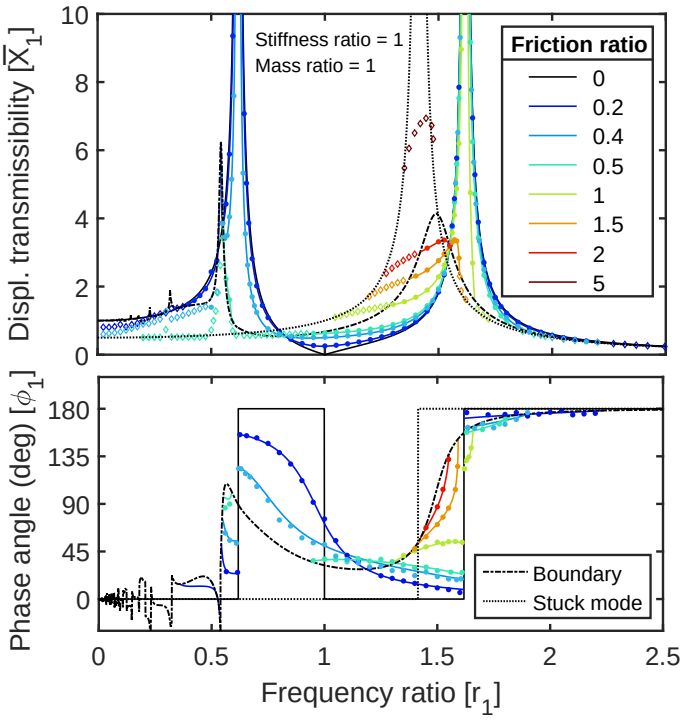

(a)

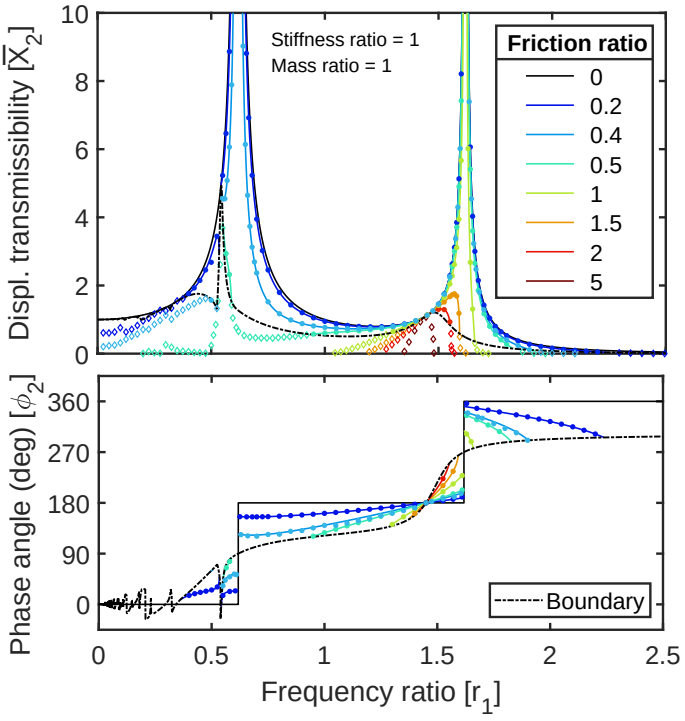

(b)

Figure 6.13: Displacement transmissibilities and phase angles of a 2DOF system with a contact on m_2 and a harmonic load on m_1 for varying friction ratio and unitary mass and stiffness ratios, displayed on m_1 (**a**) and on m_2 (**b**). Analytical results are represented by the continuous lines, while numerical results are represented with round (continuous motion) and with diamond markers (stick-slip motion).

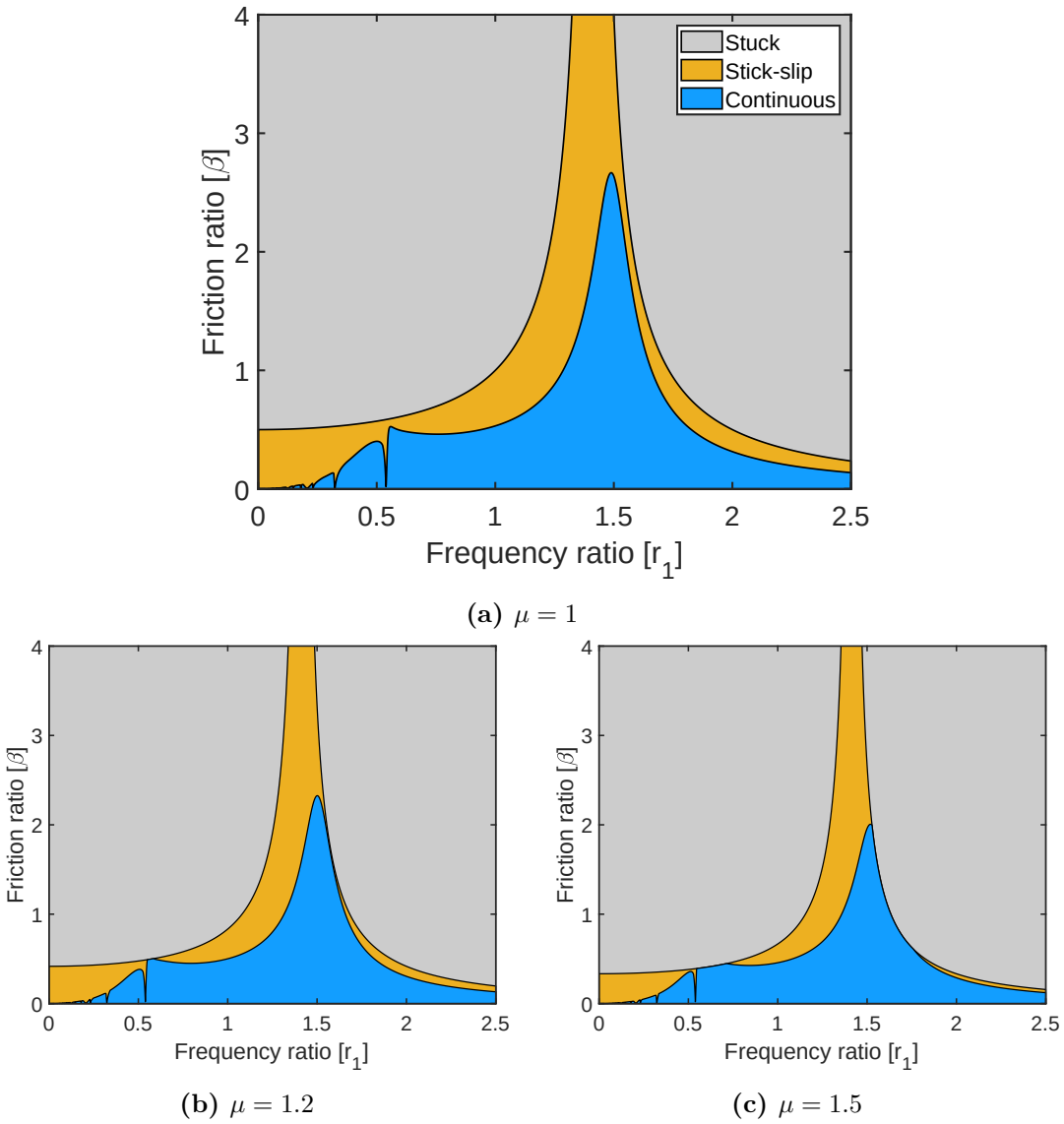

(a) $\mu = 1$

(b) $\mu = 1.2$

(c) $\mu = 1.5$

Figure 6.14: Motion regimes of a 2DOF system with a Coulomb contact on m_2 and a harmonic load on m_1 for $\gamma = \kappa = 1$ varying frequency and friction ratios.

through the springs k_1 and k_2, respectively. The transmissibility and the phase angle associated to this stuck configuration are represented in Fig.6.13a with a black dotted line. Particularly, the displacement transmissibility can be expressed as:

$$\overline{X}_1^* = \frac{1}{|1 + \kappa - r_1^2|} \tag{6.14}$$

and the phase angle is equal to 0 degrees before the natural frequency ratio $r_1 = \sqrt{1+\kappa}$ and 180 degrees afterwards. It can be observed that the transitions between stuck and sliding configurations always occur at $\overline{X}_1^* = \mu\beta/\kappa$, as

predicted from Eq.(6.11a).

- According to Eq.(6.5), the starting values of the transmissibility curves are $\overline{X}_{10} = 1 - \beta$ and $\overline{X}_{20} = 1 - (1 + \kappa)\beta/\kappa$. These values agree well with those shown from the transmissibilities curves up to $\beta = 0.4$. Starting from $\beta = 0.5$, the mass m_2 will be stuck for $r_1 \to 0$.

- As discussed in Sections 6.2.3 and 6.2.5 respectively, both boundaries between continuous and stick-slip regimes and between sliding and stuck regimes tend to zero for $r_1 \to \infty$ when $j \neq l$. In Figs.6.13 and 6.14, it is possible to observe that stick-slip motion always occurs at high frequencies before the transition to the stuck configuration.

- All the transmissibility and the phase angle curves associated to the mass in contact m_2, shown in Fig.6.13b, intersect at $r_1 = 1.450$. This value corresponds to the larger solution of Eq.(6.9), while the other solutions of this equation represent the other intersections occurring between the undamped and the boundary curves, as already observed in the 2DOF case discussed in Section 6.3.2.

- Two main invariant points for $\overline{X}_1$ can be observed in Fig.6.13a at $r_1 = 0.828$ and $r_1 = 1.549$. These values of r_1 correspond to the two largest solutions of Eq.(6.10) and are associated to a significant inversion of the transmissibility curves. In fact, in the frequency ratio interval included between these points, the transmissibility increases with β, leading the gradual onset of the resonant peak associated to the stuck configuration.

- The evolution of the phase angle ϕ_1 is quite irregular for varying friction ratios. However, it can be observed that its value is always smaller than ϕ_2, showing that m_1 oscillate with an intermediate phase angle between those of the excitation and of the response of m_2.

Finally, Fig.6.14 shows the boundaries among continuous and stick-slip regimes and between sliding and permanent sticking regimes. It can be observed that the boundary between sliding and permanent sticking regimes exhibits the same infinite peak shown in the transmissibility curves of the stuck configuration, as expected from Eq.(6.11a). Also in this configuration, intersections between the boundaries only occurs when $\mu > 1$, leading to direct transition between continuous and permanent sticking regimes.

5DOF system excited on m_1 with m_3 in contact

Let us consider a 5DOF system with a contact on m_3 and a harmonic load on m_1 as a more general example of MDOF system with $j \neq l$. The displacement transmissibility curves, obtained analytically for continuous motion and numerically in stick-slip regime, are plotted in Fig.6.15a, while the analytical phase angles are depicted in Fig.6.15b for continuous response only. Analytical and numerical time responses are compared in Fig.6.16b for a specified set of parameters, showing an excellent agreement. Analytical and numerical phase angles on the different masses of the system are represented in Fig.6.16b. Finally, the boundaries among continuous, stick-slip and permanent sticking regimes are shown in Fig.6.17. In these figures, many of the patterns and features described in the 2DOF case can be observed. In particular:

- the transmissibility of the mass in contact m_3 always decreases with β, except that in the invariant points. In fact, in Fig.6.15a, it can be observed that all the transmissibility curves $\overline{X}_3$ pass through two invariant points, located in proximity of the natural frequencies of the stuck configuration. In general, it has been verified that the number of these invariant points for the mass in contact is always equal to the number of peaks of the stuck configuration. Despite this, invariant points and stuck resonant peaks occur at close but not coincident frequency ratios;

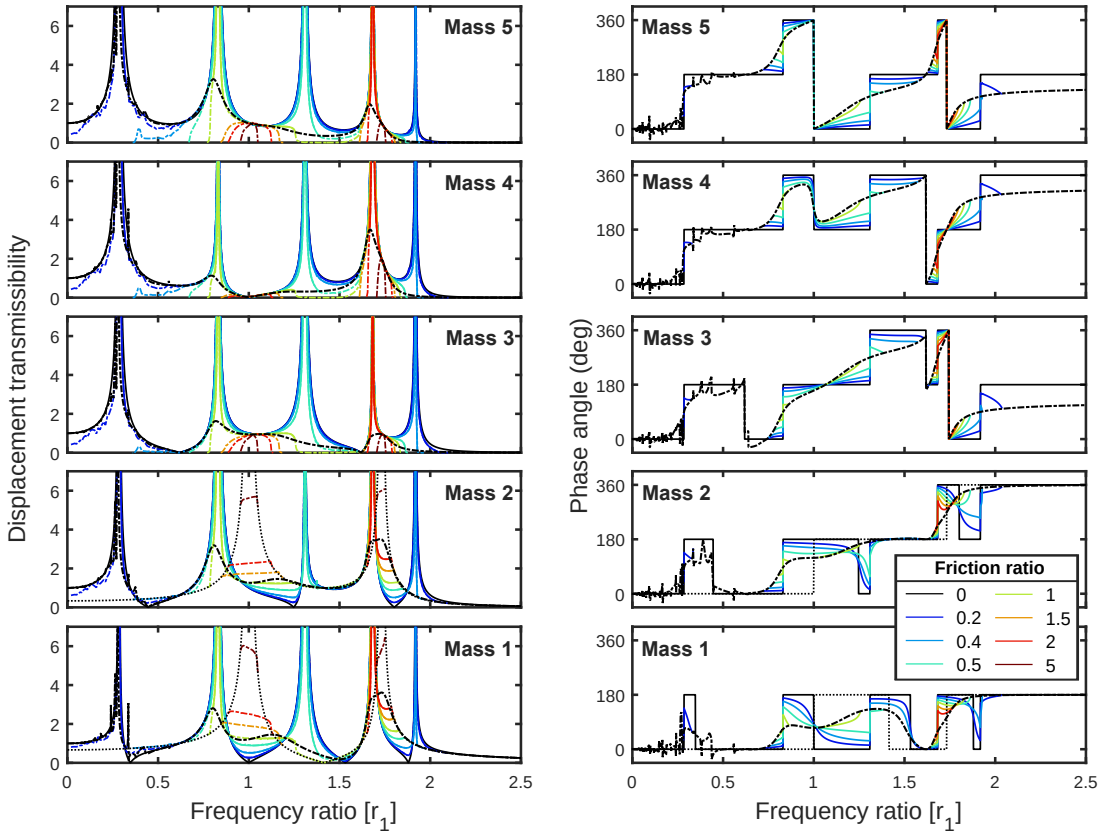

(a) **(b)**

Figure 6.15: Displacement transmissibilities (**a**) and phase angles (**b**) of a 5DOF system with a Coulomb contact on m_3, a harmonic load on m_1 , unitary mass and stiffness ratios and varying friction ratio. Analytical results for continuous motions are represented with continuous lines, while numerical results for stick-slip motions with dashed lines. The black dashed line represents the boundary between continuous and stick-slip regimes, while the dotted black line represents the response in stuck configuration.

- the masses m_4 and m_5 oscillate in phase or in-phase opposition with m_3 for most values of frequency and friction ratios and their transmissibility curves have similar patterns to those of $\overline{X}_3$. This behaviour is typical of the masses located on the opposite side of the harmonic excitation with respect to the mass in contact and has already been described for the 5DOF system investigated in Section 6.3.2.

- the masses m_1 and m_2 do not oscillate in phase with m_3 or between each other. Their transmissibility curves exhibit significant inversions which lead to the onset of the two resonant peaks of the stuck configuration. In general, this

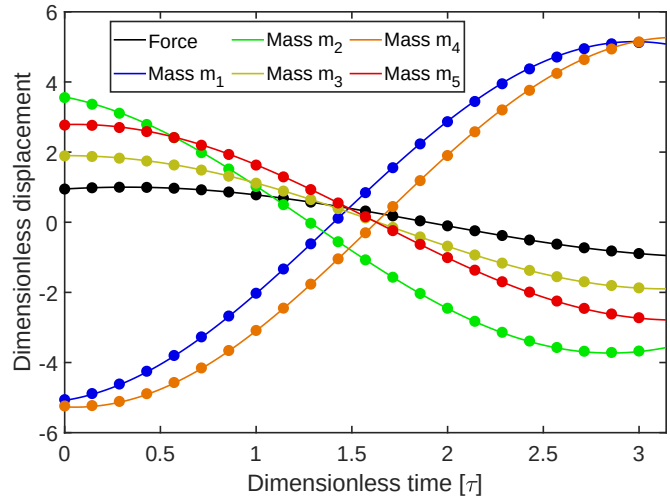

(a) $r_1 = 1.7$, $\beta = 1$

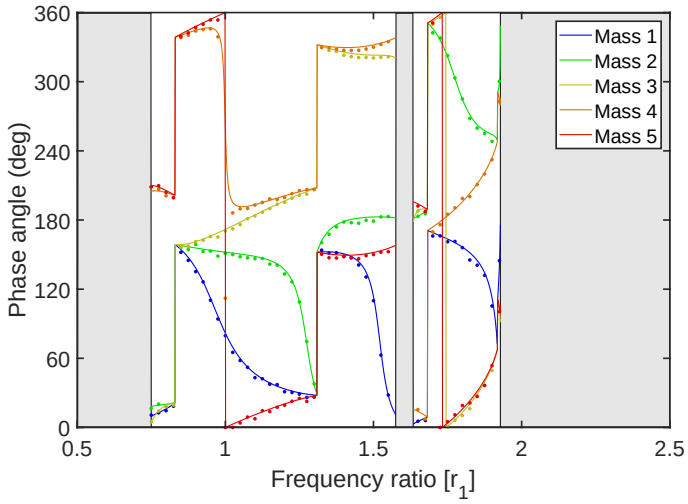

(b) $\beta = 0.4$

Figure 6.16: Analytical (continuous lines) and numerical (round markers) steady-state time response (**a**) and phase angle curves (**b**) of a 5DOF system with a Coulomb contact on m_3, a harmonic load on m_1 and $\gamma = \kappa = \mu = 1$. The grey regions indicate stick-slip and stuck regimes.

behaviour is observed in the masses located on the same side of the excitation with respect to the mass in contact. The inversions of the transmissibility curves leading to the stuck resonant peaks always occur through two invariant points.

Overall, it can be concluded that, despite MDOF systems can present several different configurations depending on the number of DOFs and the location of the exciting and the friction forces, they tend to present similar dynamic behaviours

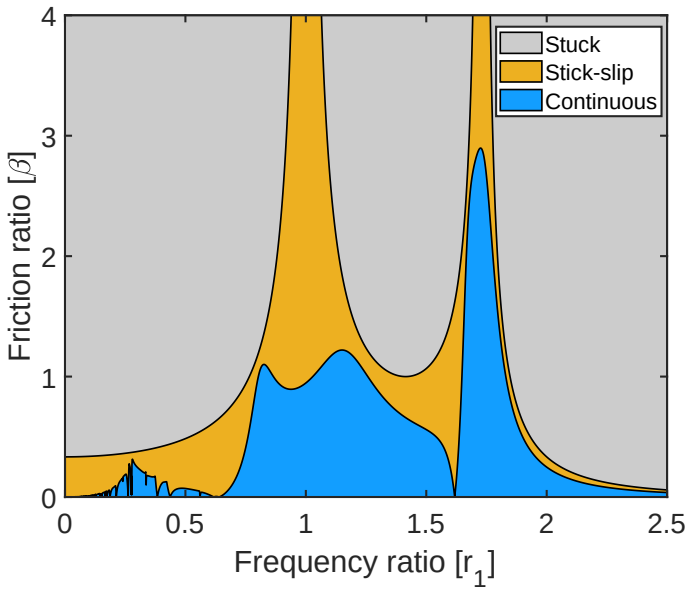

Figure 6.17: Motion regimes of a 5DOF system with equal masses and springs, with a Coulomb contact on m_3 and a harmonic load on m_1 for varying frequency and friction ratios.

depending on whether these forces are applied on the same or on different masses. Furthermore, all the numerical results shown in this section present an excellent agreement with the analytical values obtained for the continuous responses from the solutions proposed in Chapter 5. As in the SDOF case, all these results have been obtained within a specific set of assumptions regarding the use of Coulomb's law for modelling the friction force and the presence of a single friction contact as the only source of damping. An experimental validation is introduced in what follows to verify if the dynamic behaviours described by analytical and numerical results can also be observed in a real structure.

6.4 Experimental validation for 2DOF systems

This section presents an experimental investigation of the dynamic behaviour of a MDOF system with a metal-to-metal contact under harmonic base motion, aiming to provide an experimental validation for the results presented in Chapter 5 and in the first part of this chapter. In particular, the single-storey frame setup, described in Section 4.2 and used for reproducing a SDOF system, has been modified to

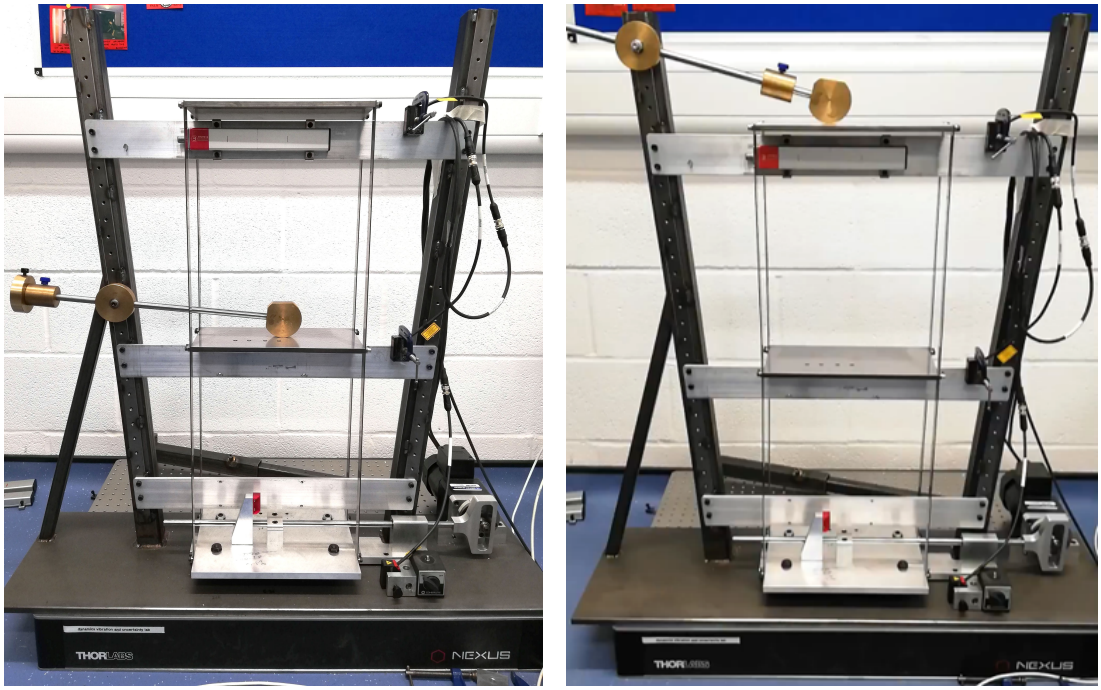

(a) Lower floor in contact **(b)** Upper floor in contact

Figure 6.18: Pictures of the two-storeys frame test rig. A counterweight pinned to the external frame applies a normal force on the lower (**a**) or the upper (**a**) plate.

include a second storey so that a 2DOF system could be represented.

6.4.1 Apparatus

The test rig used for this experimental investigation is a two-storey shear frame where three plates are connected by four metal bars, as shown in Fig.6.18. The properties of these components are reported in Tab.6.1. The bottom plate is harmonically excited by an electric rotor connected through a Scotch-yoke mechanism and the exciting frequency is selected using an inverter motor speed regulator, as described in Section 4.2 for the single-storey configuration.

Component	Size (mm)	Mass (kg)	Material
Base plate	$300 \times 255 \times 12.7$	2.860	Aluminium
Lower plate	$300 \times 153 \times 9.55$	3.270	Steel
Upper plate	$300 \times 153 \times 9.48$	3.250	Steel
Bars	$410 \times 25.5 \times 1.60$	0.130	Steel

Table 6.1: Properties of the two-storey frame components.

A friction force is generated by the relative motion in the contact achieved between one of the steel plates and a brass disc. The normal force exerted by the disc on the plate in contact is adjusted by using the counterweight system described in Section 4.2. Two different contact configurations have been explored by placing the brass disc on either the lower (Fig.6.18a) or the upper (Fig.6.18b) storey. These configurations aim to reproduce the 2DOF systems with a contact either on the lower or on the upper mass shown in Figs.6.4 and 6.11 respectively.

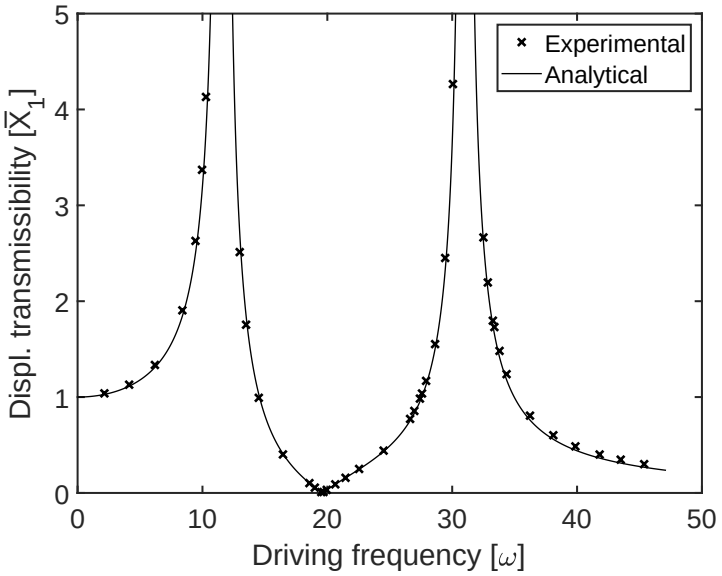

Figure 6.19: Displacement transmissibility of the lower mass of an undamped 2DOF system for $r_1 = (0.3419s)\omega$, $\gamma = 0.9772$ and $\kappa = 1.1119$: experimental results (markers) vs analytical results (continuous line).

6.4.2 Parameter estimation

The procedure used in this experimental campaign consists of two main stages: the preliminary parameters estimation and the main forced vibration test. In fact, as a first step, it is necessary to determine if the setup can be modelled as a 2DOF system and to estimate the parameters of problem.

As specified in Section 4.1 for the SDOF case, the proposed experimental approach cannot be used to directly investigate different static and friction forces; therefore, it will be assumed that $\mu = 1$ and the potential role of different values of this ratio will be debated in the discussion of the experimental results. Therefore,

according to the formulation provided in Section 5.2, four parameters are needed to fully describe the dynamic behaviour of a 2DOF system: the frequency ratio r_1, the friction ratio β, the mass ratio γ and stiffness ratio κ.

Similarly to Section 4.3.1, a series of tests were carried out in the absence of friction, removing the counterweight from the system, and the displacement transmissibilities were evaluated at different driving frequency in the range $0-8$Hz, as shown in Fig.6.19. The frequency, mass and stiffness ratios, which are not related to friction, have been determined, by using the optimisation process implemented in Matlab by the function fmincon and the algorithm sqp [141], so that the best agreement between the experimental and analytical transmissibilities shown in Fig.6.19 could be achieved.

The process has been implemented as follows. As shown in Appendix A, the displacement transmissibility of the mass m_1 of a 2DOF system can be written as:

$$\overline{X}_1 = \left(\frac{\omega_1\omega_2}{\omega_0}\right)^2 \frac{\omega_0^2-\omega^2}{(\omega_1^2-\omega^2)(\omega_2^2-\omega^2)} \tag{6.15}$$

where ω_1 and ω_2 are the natural frequencies of the system and $\omega_0 = \sqrt{k_2/m_2}$ is the frequency of the antiresonance of $\overline{X}_1$. While it has not been possible to observe a convergence of the optimisation process using r_1, γ and κ as parameters, a quick convergence has been obtained by referring to ω_0, ω_1 and ω_2 and minimising the cost function:

$$J = \sum_{i=1}^{N_t} \frac{[\overline{X}_{1,\exp}(\omega^{(i)}) - \overline{X}_1(\omega^{(i)})]^2}{\overline{X}_{1,\exp}(\omega^{(i)})^2} \tag{6.16}$$

where $\omega^{(i)}$ is the driving frequency used in the ith test and N_t the number of tests performed. Finally, the frequency, mass and stiffness ratios have been determined using the following relations:

$$r_1 = \left(\frac{\omega_0}{\omega_1\omega_2}\right)\omega \tag{6.17}$$

$$\gamma = \left(\frac{\omega_{z0}}{\omega_0}\right)^2 - 1 \tag{6.18}$$

$$\kappa = \gamma\left(\frac{\omega_0^2}{\omega_1\omega_2}\right)^2 \tag{6.19}$$

where:

$$\omega_{z0} = \sqrt{\frac{k_2(m_1 + m_2)}{m_1 m_2}} \tag{6.20}$$

is the antiresonance of the amplitude $\overline{Z}$ of the relative motion between the lower plate and the base. A mathematical demonstration of these relations is provided in Appendix A. The final values obtained from this process were $r_1 = (0.3419s)\omega$, $\gamma = 0.9772$ and $\kappa = 1.1119$. In Fig.6.19, it is also possible to observe that only two vibrating modes are displayed within the frequency range considered during these tests. Therefore, the proposed setup can be modelled as 2DOF system if the driving frequency range up to 8Hz.

Regarding the estimation of the friction ratio, the linear decrement technique described in Section 4.3.2 cannot be easily applied to systems with more than one DOF. However, four different response metrics have been measured during the main forced vibration test, i.e. the displacement transmissibilities and the phase angles of the two masses of the system. Therefore, the following procedure has been followed.

- Before reproducing experimentally the curves associated to each friction ratio, a series of tests has been performed at a specific value of the frequency ratio, adjusting the position of the weights along the counterweight bar until a good agreement between the experimental and the theoretical values of the phase angle of the mass in contact was obtained.

- After this tuning operation, forced vibration tests have been performed at different frequency ratios maintaining the same setting of the counterweight, so that the experimental transmissibility and phase angle curves could be obtained.

The same procedures described in Section 4.3.2 for limiting the non-Coulomb phenomena have been followed in the present investigation and the post-processing described in Section 4.3.3 has been used for obtaining the frequency-based transmissibilities and phase angles. The results obtained from this investigation are presented in what follows.

6.4.3 Results and discussion

The forced vibration test has been performed for both configurations of the setup at different values of the frequency ratio in the range 0:2.5; the friction ratio values explored were [0.2, 0.4, 0.6] for the case of the lower mass in contact and [0.2, 0.5, 1, 1.5, 2] with the upper mass in contact. For each combination of the parameters r_1 and β, the displacement of the plates has been recorded for 50s with a sampling frequency of 2kHz. The experimental results are compared to the analytical and numerical results in Figs.6.20 and 6.21. As in the SDOF case presented in Chapter 4, the frequency-based transmissibilities and phase angles have been evaluated by post-processing the analytical solutions obtained in Chapter 5 when $\beta < \beta_{\text{lim}}$ and numerically when stick-slip is expected in the response, i.e. for $\beta \geq \beta_{\text{lim}}$; the analytical expression of the boundary friction ratio β_{lim} is reported in Eq.(5.65).

In Fig.6.20, it is possible to observe that the agreement between the experimental and the theoretical results is excellent in terms of all the response metrics investigated. As mentioned in Section 6.4.2, the desired value has been selected, prior to reproducing each of the curves, by performing a tuning of the counterweight at a specified value of r_1 such that a good agreement is obtained between the experimental and the analytical values of $\phi_{1,\text{fft}}$. As can be seen in Fig.6.20a, this phase angle presents a good degree of sensitivity to the friction ratio variations independently of the value of r_1. Therefore, it has been arbitrarily chosen to operate the tuning at $r_1 \cong 1.25$ for each curve. It is also possible to note that, as in the SDOF case, the phase angle curves show an almost constant value for varying frequency ratio; small variations can only be seen at low frequencies, where stick-slip occurs. These are well reproduced by the experimental observations. Another noteworthy behaviour can be observed from the response of the upper mass, in Fig.6.20b. Consistently with the analytical results presented in Section 6.3.1, it has been observed that the motion of the upper mass is approximatively in phase or in phase-opposition with respect to the motion of the lower mass. This implies that the phase angle of the mass m_2 might also be used, in a reverse approach, to measure the friction ratio and, eventually, the friction force acting in the contact.

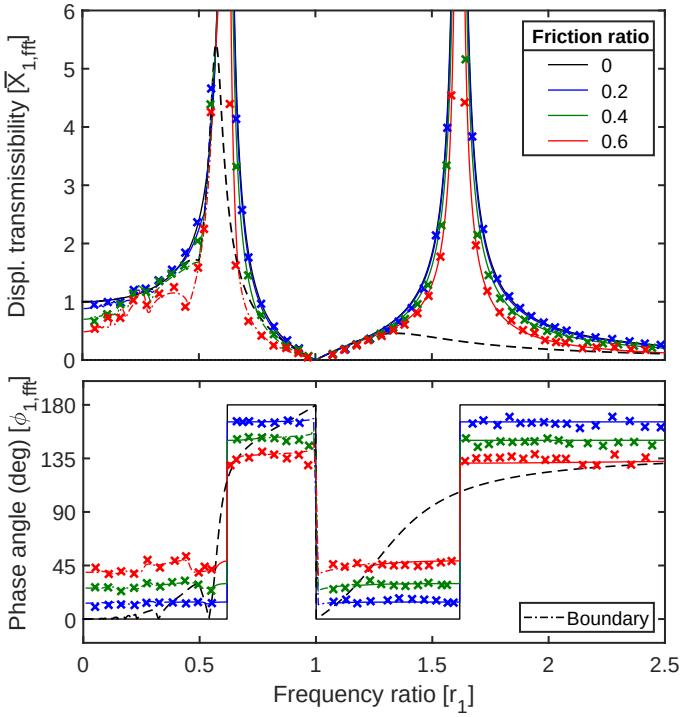

(a) Mass m_1

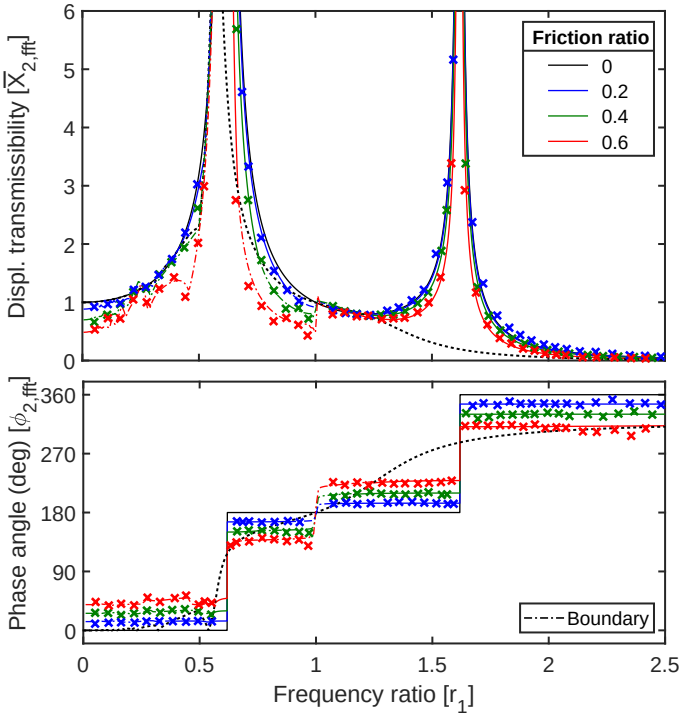

(b) Mass m_2

Figure 6.20: Displacement transmissibility and phase angle of a 2DOF system with a fixed-wall contact on m_1 under harmonic base excitation: experimental (markers) vs analytical (continuous lines) and numerical (dashed-dotted lines) results. The black dashed line represents the boundary between continuous and stick-slip regimes.

Therefore, these results indicate that the friction force generated in a contact might be measured from the response of a structure even not observing directly one of the components involved in the contact.

From Fig.6.21, it can be seen that a very good agreement between experimental and theoretical results is also obtained when the upper mass is in contact, despite the more complex patterns observed due to the harmonic and the friction forces acting on different masses of the system. Differently from the case discussed above, the phase angles of both masses show a significant dependence on the frequency ratio. While the patterns described by $\phi_{1,\text{fft}}$ are particularly complicated and the different curves overlap in a wide frequency ratio range, the curves $\phi_{2,\text{fft}}$ present a more regular behaviour. In particular, the phase angle of the upper mass increases with β for $0 < r_1 < 0.618$ and $1.414 < r_1 < 1.618$ and decreases in the remaining frequency ranges. The point $r_1 = \sqrt{2}$ is invariant for both $\overline{X}_{2,\text{fft}}$ and $\phi_{2,\text{fft}}$, meaning that the main harmonic component of the motion of the upper mass is completely independent of friction at this frequency ratio. An important implication is that it is not always possible to use this phase angle for measuring the friction ratio and the tuning of the counterweight must be necessarily performed at a different frequency. In the current investigation, it has been chosen to operate the tuning at $r_1 \cong 1.5$.

The limitations encountered during the experimental campaign were similar to those highlighted in Section 4.4.3 for the SDOF case. In fact, the response of the system becomes more unstable as the amount of friction is increased. Eventually, this leads to the occurrence of permanent sticking in the contact when the friction ratio is $\beta \cong 0.7\beta^*_{\text{lim}}$. Therefore, when the lower plate is in contact, the current setup cannot be used to investigate friction ratios that exceeds 0.7. Similarly, if the upper plate is contact, it is not possible to evaluate the transmissibility and the phase angle in proximity of the boundary between stick-slip and permanent sticking regimes. As discussed in Section 4.4.3, this could partially be explained by different values of the static and kinetic friction forces; nonetheless, the good agreement between the experimental and the numerical results observed in stick-slip regime suggests that μ could only be slightly larger than unity.

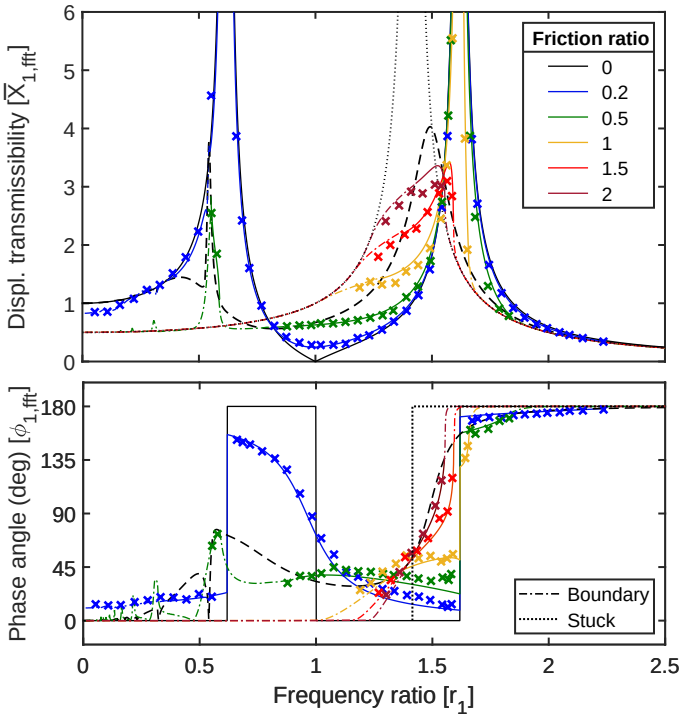

(a) Mass m_1

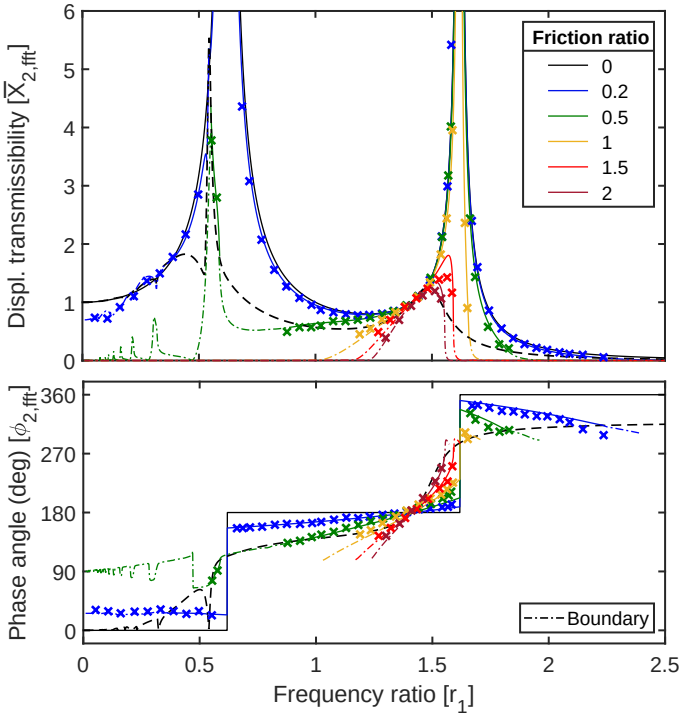

(b) Mass m_2

Figure 6.21: Displacement transmissibility and phase angle of a 2DOF system with a fixed-wall contact on m_2 under harmonic base excitation: experimental (markers) vs analytical (continuous lines) and numerical (dashed-dotted lines) results. The black dashed line represents the boundary between continuous and stick-slip regimes, the black dotted line the transmissibility in the stuck configuration.

In conclusion, it is confirmed that the analytical and numerical results obtained in Chapter 5 and in this chapter can be reproduced, in most cases, in experimental conditions and that the proposed setup can be used for this purpose. However, further investigations are needed to fully explain the unstable behaviours and the occurrence of permanent sticking observed for large amounts of friction. In the remaining of this chapter, the investigation of the response features and the numerical and experimental validations presented for MDOF systems with a fixed wall will be extended to systems with a contact between oscillating parts.

6.5 Systems with a contact between oscillating parts

In this section, the solutions derived in Section 5.6 for the response of MDOF systems with a contact between two masses or a mass and the oscillating base are validated numerically and extended to include stick-slip responses, referring as an example to the 2DOF systems shown in Fig.6.22. In addition, these analytical and numerical results are used to investigate the features of dynamic response of these systems and the boundaries of their motion regimes. Finally, an experimental validation is also presented for the case of a 2DOF system with a contact between the lower mass and the base.

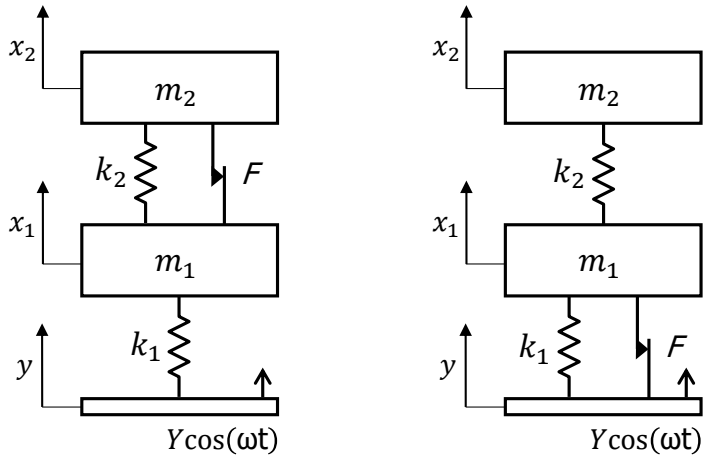

Figure 6.22: 2DOF systems under harmonic base excitation with a Coulomb contact: (**a**) between the m_1 and the mass m_2 and (**b**) between the m_1 and the base.

6.5.1 2DOF system with a contact between the masses

The numerical approach used for evaluating the time response of MDOF systems with a contact between the masses m_A and m_B is similar to that presented in Section 6.3.1 and schematised in Fig.6.3. Nonetheless, a few modifications are needed when implementing the sticking conditions and for evaluating the response of the system during the sticking stages. In fact, a sticking phase will take place when, simultaneously, $\bar{x}'_A = \bar{x}'_B$ and:

$$\left| \sum_{k=1}^{N} \left(\overline{K}_{Bk} - \gamma_{AB} \overline{K}_{Ak} \right) \bar{x}_k - (\delta_{lB} - \gamma_{AB} \delta_{lA}) \cos \tau \right| > \mu\beta(1 + \gamma_{AB}) \tag{6.21}$$

The latter condition has been derived in Section 5.6.1. During the sticking phases, the masses m_A and m_B will oscillate jointly so that their relative displacement $\bar{z} = \bar{x}_B - \bar{x}_A$ remains constant and their relative velocity $\bar{z}' = 0$. In order to describe this joined motion, it is useful to introduce the coordinate of the centroid of the masses in contact:

$$\bar{x}_c = \frac{m_A \bar{x}_A + m_B \bar{x}_B}{m_A + m_B} \tag{6.22}$$

so that the motion of these masses can be described in terms of the motion of their centroid and of their relative motion as:

$$\begin{cases} \bar{x}_A = \bar{x}_c - \dfrac{m_B}{m_A + m_B} \bar{z} & \text{(6.23a)} \\ \bar{x}_B = \bar{x}_c + \dfrac{m_A}{m_A + m_B} \bar{z} & \text{(6.23b)} \end{cases}$$

While $\bar{z}$ is constant during the sticking phase, the displacement of the centroid must be determined. A governing equation for $\bar{x}_c$ can be obtained by summing the equations governing the motion of the masses m_A and m_B and substituting Eq.(6.22):

$$(m_A + m_B)\bar{x}''_c + \sum_{k=1}^{N} \left(\overline{K}_{Ak} + \overline{K}_{Bk} \right) \bar{x}_i = (\delta_{Ai} + \delta_{Bi}) \cos \tau \tag{6.24}$$

Eq.(6.24) can be coupled with the governing equations of the masses not involved in the contact, obtaining a system of $N - 1$ linear equations in the form:

$$\overline{\mathbf{M}}^* \bar{\mathbf{x}}^{*\prime\prime} + \overline{\mathbf{K}}^* \bar{\mathbf{x}}^* = \bar{\mathbf{p}}^* \tag{6.25}$$

where the matrices $\overline{\mathbf{M}}^*$ and $\overline{\mathbf{K}}^*$ can be obtained from $\overline{\mathbf{M}}$ and $\overline{\mathbf{K}}$, in Eq.(5.7) and Eq.(5.8) respectively, by replacing the original A-th and B-th rows and columns with the terms provided in Eq.(6.24). Similarly, the vector $\bar{\mathbf{p}}^*$ can be obtained by replacing the A-th and the B-th components with the term $(\delta_{Ai}+\delta_{Bi})\cos\tau$ given by Eq.(6.24). Eq.(6.25) is a linear second-order ODE and can be integrated using the function ode45. In the resulting vector $\bar{x}^*$, the A-th and the B-th component will coincide with the position of the centroid; therefore, it is necessary to impose Eq.(6.23) explicitly at during each time step, so that the actual displacement of m_A and m_B is obtained. Finally, the sticking phase will end when Eq.(6.21) is no longer verified.

The analytical results obtained from the solutions presented in Section 5.6.1 have been compared, for varying parameters, with the results obtained using the integration approach described above. The agreement was excellent in all the cases investigated. In particular, the comparison between analytical and numerical transmissibilities is shown in Fig.6.23 for the 2DOF system shown in Fig.6.22a, in the frequency ratio range $0:2.5$ and for varying friction ratio, assuming both stiffness and mass ratios equal to 0.5 and a unitary ratio between static and kinetic friction forces. The agreement between the transmissibilities is very good when the response is continuous. The motion regimes occurring in the numerical response are always in accordance with the analytical predictions. The analytical boundaries of these motion regimes are also shown in the parameter space $r_1-\beta$ in Fig.6.23.

The general features of the dynamic response of MDOF systems with a Coulomb contact between two masses are discussed in what follows.

- The value $\beta_{n,i}$ of the friction ratio for which the ith resonant peak becomes finite can be evaluated by calculating the limit of Eq.(5.80) for $R_i \to 1$, as proposed in Sect.6.2.1, and is given by:

$$\beta_{n,i} = \frac{\pi}{4}\left|\frac{\psi_{li}}{\psi_{Bi}-\psi_{Ai}}\right| \tag{6.26}$$

  In the 2DOF case considered in this section, the values obtained from Eq.(6.26) are $\beta_{n,1}=0.785$ and $\beta_{n,2}=0.393$, in agreement with the curves shown in Fig.6.23.

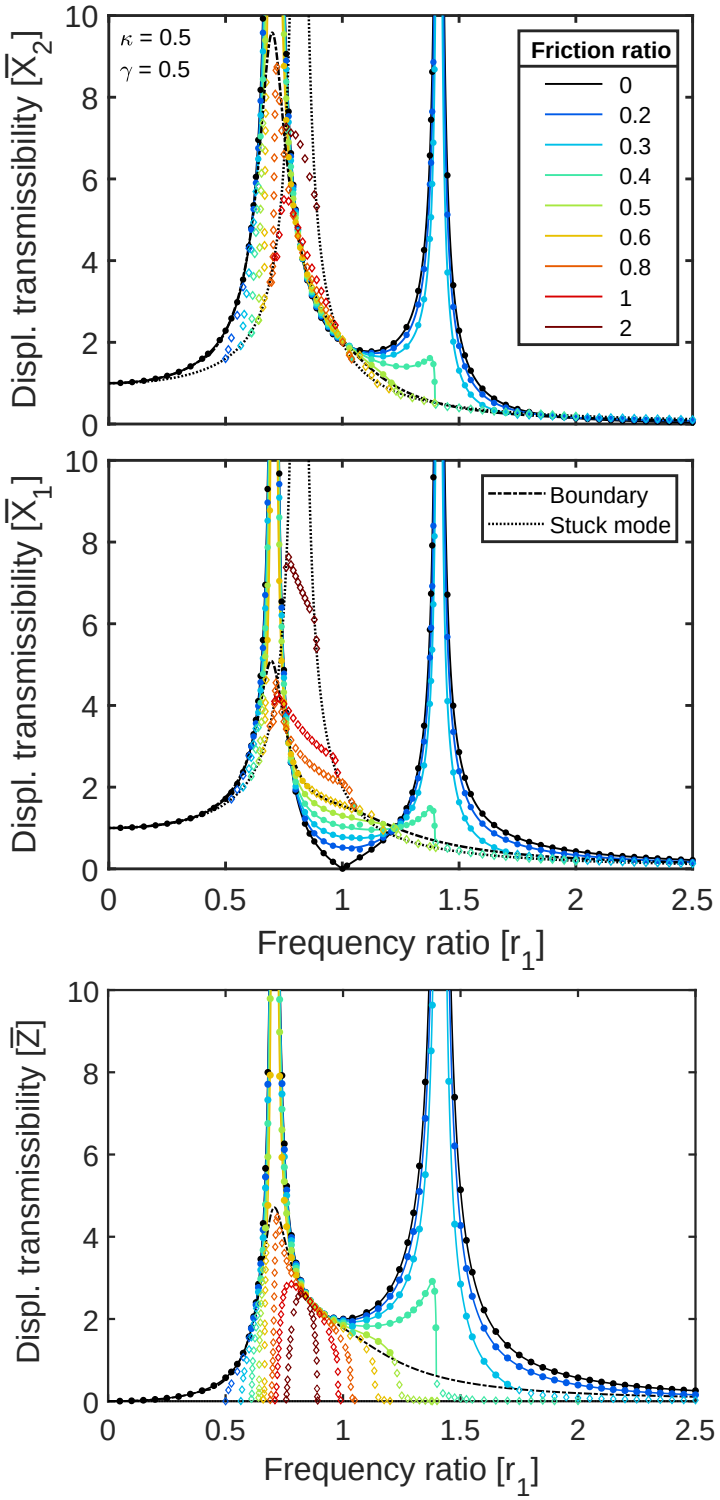

Figure 6.23: Displacement transmissibilities of a harmonically excited 2DOF system with a contact between m_1 and m_2 for varying friction ratio and γ=κ=0.5: (**a**) absolute motions of m_1 and m_2 and (**b**) relative motion in the contact. Analytical results are represented by the continuous lines, while numerical results are represented with round (continuous motion) and with diamond markers (stick-slip motion).

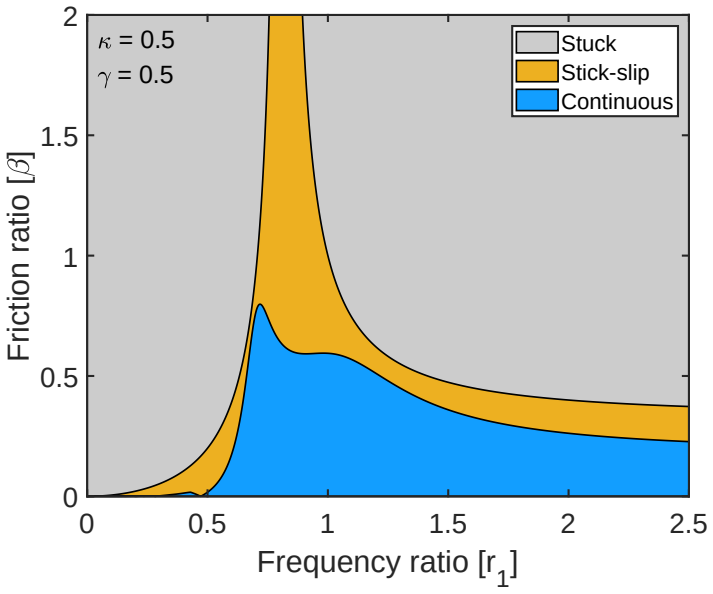

Figure 6.24: Motion regimes of a 2DOF system with a Coulomb friction contact between m_1 and m_2 and a harmonic load on m_1 for varying frequency and friction ratios.

- Permanent sticking between the masses m_A and m_B will occur if the amplitude of the dynamic load acting in the contact when $\bar{z} = 0$ does not overcome the static friction force. Considering the governing equation of the relative motion introduced in Eq.(5.76), it is possible to write this condition as:

$$\beta < \frac{1}{\mu(1+\gamma_{AB})} \left| \sum_{k=1}^{N} \left(\overline{K}_{Bk} - \gamma_{AB} \overline{K}_{Ak} \right) \overline{X}_k^* - (\delta_{lB} - \gamma_{AB} \delta_{lA}) \right| \tag{6.27}$$

  where the response amplitudes in stuck configuration $\overline{X}_1^*$, ..., $\overline{X}_N^*$ can be determined from Eq.(6.25) using a standard modal superposition approach. It is worth underlining that, since the relative motion between m_A and m_B is equal to zero in permanent sticking regime, these masses will both oscillate jointly to their centroid $\bar{x}_c$ in the stuck configuration.

- Evaluating the limit value of the boundary between continuous and stick-slip motion for $r_1 \to 0$, it can be shown that, as in the fixed-wall case, any non-zero value of the friction ratio will prevent the relative motion in the contact from being continuous in quasi-static conditions. The starting value of the boundary between sliding and permanent sticking regimes can instead be evaluated from Eqs.(6.25) and (6.27), imposing that $r_1 = 0$. While this is

not true in general, it has been observed that the system is always stuck in quasi-static conditions if $l = 1$. This behaviour also occurs in the example presented in this section, as can be observed from Fig.6.24.

- The high-frequency behaviour of these MDOF systems can significantly change depending on where the friction contact and the harmonic load are applied. In fact, when $r_1 \to \infty$, the boundary between continuous and stick-slip regimes expressed in Eq.(5.80) tends to:

$$\beta_\infty = \begin{cases} \dfrac{2\gamma_{AB}}{(1+\gamma_{AB})\sqrt{4\mu^2+\pi^2}} & \text{if } l = A \quad (6.28a) \\ \dfrac{2}{(1+\gamma_{AB})\sqrt{4\mu^2+\pi^2}} & \text{if } l = B \quad (6.28b) \\ 0 & \text{if } l \neq \{A, B\} \quad (6.28c) \end{cases}$$

Furthermore, evaluating Eq.(6.27) for $r_1 \to \infty$, it can be determined that the boundary between sliding and permanent sticking regimes tends to:

$$\beta^*_\infty = \begin{cases} \dfrac{\gamma_{AB}}{\mu(1+\gamma_{AB})} & \text{if } l = A \quad (6.29a) \\ \dfrac{1}{\mu(1+\gamma_{AB})} & \text{if } l = B \quad (6.29b) \\ 0 & \text{if } l \neq \{A, B\} \quad (6.29c) \end{cases}$$

In the 2DOF case dealt within this section, since $l = A = 1$ and $\gamma_{AB} = \gamma = 0.5$, it is obtained that $\beta_\infty = 0.179$ and $\beta^*_\infty = 0.333$, in agreement with Fig.6.24. It can be concluded that if the harmonic excitation is applied to one of the masses in contact, both boundaries will tend to non-zero asymptotic values, below which continuous and stick-slip motions can be observed respectively. Conversely, if the excitation is applied to any other masses, both boundaries will tend to zero, meaning that the contact will always get stuck at high frequencies.

- In Fig.6.23a, it can be observed that for both masses an inversion of the transmissibility curves occurs across two invariant points and leads to the onset of the resonant peak associated to the stuck configuration. It is possible to obtain an estimate of the position of these points from Eq.(5.74), as explained

in Section 5.6.1. For instance, the points estimated for $\overline{X}_1$ are $r_1 = 0.778$ and $r_1 = 1.213$, while it has been observed that the actual inversion occurs between two small regions (rather than single points) located at $r_1 \cong 0.770$ and $r_1 \cong 1.226$. Finally, the amplitude of the relative motion in the contact (from Fig.6.23b) always decreases with β, similarly to the motion of the mass in contact in systems with a fixed wall. In this case, the invariant points can be evaluated exactly from the condition $U_z = 0$.

6.5.2 2DOF system with a contact between the lower mass and the base

The time response of MDOF systems under joined base-wall excitation can also be evaluated numerically with a similar approach to that introduced in Section 6.3.1. However, as in the case investigated in Section 5.1, it is necessary to introduce in the algorithm the appropriate sticking conditions and to determine the governing equations of the system to be integrated during the sticking stages. In this contact configuration, stops occur when the relative motion between the mass in contact m_j and the wall is $\bar{z} = 0$ and, as shown in Section 5.6.2:

$$\left| \sum_{k=1}^{N} \overline{K}_{jk} \bar{x}_k - (\delta_{1j} + \gamma_j r_1^2) \cos\tau \right| > \mu\beta \tag{6.30}$$

During the sticking stages, as in the fixed-wall case, the response can still be obtained by integrating the governing equations considered during the sliding stages. However, also in this case, it will be necessary to impose the position and the velocity of the mass in contact as:

$$\begin{cases} \bar{x}_j = \bar{z}_0 + \cos\tau & \text{(6.31a)} \\ \bar{x}'_j = -\sin\tau & \text{(6.31b)} \end{cases}$$

The analytical results based on the solutions derived in Section 5.6.2 have been compared to the results obtained with this numerical approach for varying frequency, friction, mass and stiffness ratios, showing a very good agreement in all the cases investigated. The comparison between the analytical and numerical response amplitudes for the 2DOF system represented in Fig.6.22b is reported in

Fig.6.25; the results shown in these plots have been obtained for unitary mass, stiffness and static/kinetic friction force ratios. An excellent agreement is observed for both absolute mass motions (in Fig.6.25a) and for the relative motion in the contact (in Fig.6.25b). Numerical results obtained in stick-slip regime are also reported in Figs.6.25a-b to provide a complete overview of the dynamic behaviour of the system, while the boundaries among continuous, stick-slip and stuck motion regimes are depicted in Fig.6.26.

The main dynamic response features are presented for MDOF systems under joined base-wall excitation in what follows, referring as example to the results shown in Figs.6.25 and 6.26.

- The evaluation of limit value assumed by the boundary between continuous and stick-slip regimes when $R_i \to 1$ provides the same result obtained in Section 6.2.1 for the fixed-wall configuration and reported in Eq.(6.2). Therefore, all the resonant peaks exhibited by systems undergoing joined base-wall excitation also become finite at $\beta = \pi/4$ if the friction contact occurs on the mass m_1. This can also be observed from Figs.6.25a-b, where both peaks are finite starting from the curves associated to the case $\beta = 0.8$.

- As shown in Sections 6.2.5 and 6.5.1, two main steps are required for deriving the boundary between sliding and permanent sticking motion regimes: (i) deriving the steady-state response of the system in the stuck configuration and (ii) using the derived response amplitudes for determining the maximum dynamic load acting in the contact and comparing it to the static friction force. In this contact configuration, when sticking occurs, the mass in contact will oscillate jointly to the wall. Therefore, its motion can simply be written as $\bar{x}_j = \cos\tau$. The motion of the remaining masses can be determined from a linear system of $N-1$ equations written in the form expressed in Eq.(6.25), where the stuck mass and stiffness matrices are obtained by removing the j-th rows and columns from $\overline{\mathbf{M}}$ and $\overline{\mathbf{K}}$, while the generic ith component of

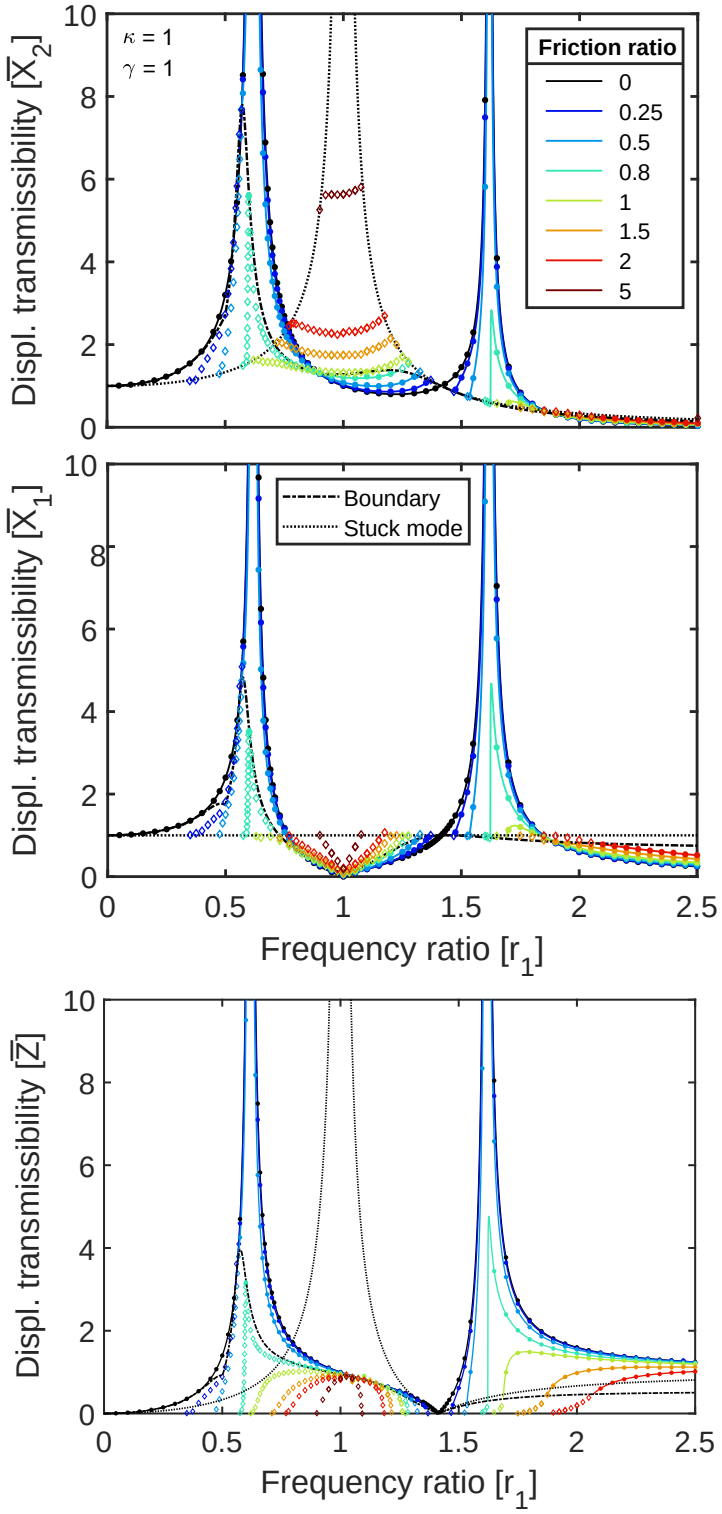

Figure 6.25: Displacement transmissibilities of a 2DOF system with a contact on m_1 under harmonic joined base-wall motion for varying friction ratio and unitary mass and stiffness ratios: (**a**) absolute motions of m_1 and m_2 and (**b**) relative motion in the contact. Analytical results are represented by the continuous lines, while numerical results are represented with round (continuous motion) and with diamond markers (stick-slip motion).

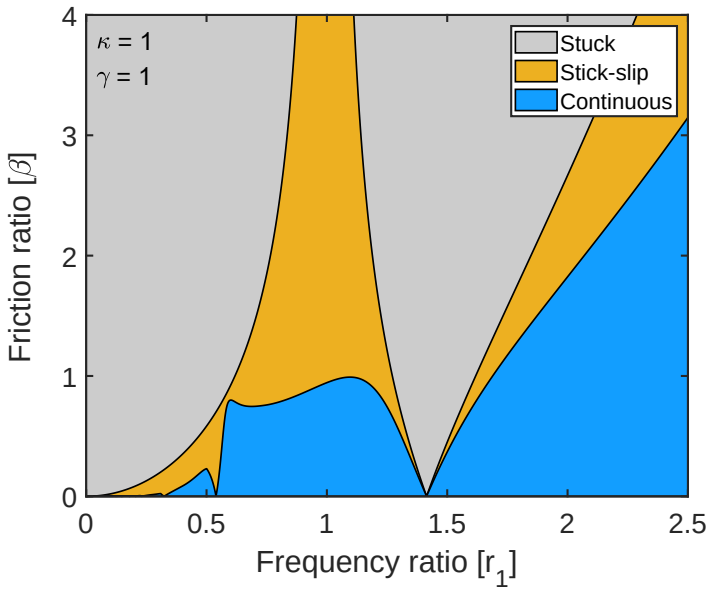

Figure 6.26: Motion regimes of a 2DOF system with a Coulomb friction contact between m_1 and the harmonically excited base for varying frequency and friction ratios.

the stuck force vector will be:

$$\bar{p}_i^* = (\delta_{1i} + \delta_{j-1,i}\kappa_j + \delta_{ji}\kappa_{j+1}) \cos\tau \tag{6.32}$$

In other words, since its motion is already known, the mass m_j will act as a further source of harmonic excitation in the stuck system. Therefore, a harmonic load $\kappa_j \cos\tau$ will be applied onto the mass m_{j-1} and a load $\kappa_{j+1} \cos\tau$ will act on the mass m_{j+1}.

The formulation of the upper bound for the sliding motion regime can be obtained, at this stage, from Eq.(6.30), considering the maximum amplitude of the resultant force acting in the friction contact:

$$\beta < \frac{1}{\mu} \left| \sum_{k=1}^{N} \overline{K}_{jk} \overline{X}_k^* - \delta_{1j} - \gamma_j r_1^2 \right| \tag{6.33}$$

where the RHS represents the boundary value β_{lim}^* of the friction ratio.

- The behaviour of these systems at low frequency ratios can easily be explained by evaluating the values assumed by both boundaries for $r_1 \to 0$. As in all the contact configurations explored in this paper, also in this case the boundary between continuous and stick-slip regimes tends to zero. It can be

demonstrated that also the boundary between sliding and permanent sticking regimes is equal to zero at $r_1 = 0$. In fact, when permanent sticking occurs, the static response of the system can simply be obtained by the equation $\overline{\mathbf{K}}^* \bar{\mathbf{x}}^* = \bar{\mathbf{p}}^*$. However, it can be observed that substituting the response amplitudes obtained from this equation into Eq.(6.33) and imposing $r_1 = 0$, the resulting value of the boundary will be equal to zero. Therefore, it can be concluded that systems under joined base-wall motion are always stuck in quasi-static conditions, as already observed for the SDOF case in Chapter 3.

- The behaviour of MDOF systems under joined base-wall motion is also similar to that described for the SDOF case in Chapter 3 at high frequency ratios. In fact, both boundaries grows to infinity when $r_1 \to 0$. This means that, increasing the driving frequency, it will always be possible to observe a sliding motion in the friction contact at some point.

- Inversions of the transmissibility curves can be seen for both masses in Fig.6.25a. In particular, two different kinds of inversions can be observed. In the case of the mass not in contact, inversions are mostly similar to those described in the other contact configurations, i.e. they occur across two invariant points and show the gradual onset of a new resonant peak associated to the stuck configuration of the system. However, it can also be noted that another inversion occurs for all the masses of the system after the last resonant peak, so that the transmissibility always increases with the friction ratio at high frequency ratios. This inversion occurs across a small region rather than a single invariant point. This behaviour had already been observed in SDOF systems, where such an inversion occurs at $r_1 \cong 1.5$.

6.5.3 Experimental validation

An experimental validation has been carried out also for MDOF systems with a contact between oscillating parts, using a modified version of the setup presented in Section 6.4.1 to reproduce a 2DOF system with a contact between the lower

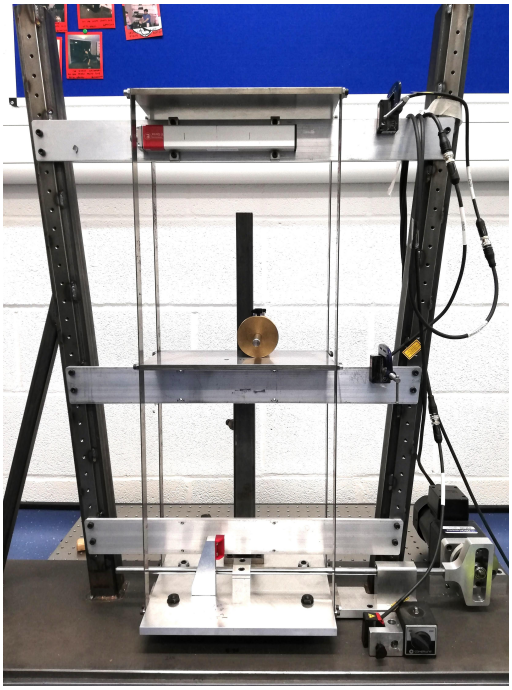

Figure 6.27: Picture of the two-storeys frame test rig with the counterweight pinned to a pole rigidly mounted on the base and applying a normal force on the lower plate.

mass and the excited base. The test rig is shown in Fig.6.27. In this figure, it can be observed that the contact between the base and the lower storey has been achieved by mounting a rigid post on the base and pinning the counterweight to this post so that the brass disc could rest on the lower plate. This configuration has already been used in Chapter 4 to reproduce a SDOF system under joined base-wall excitation, as shown in Fig.4.1b.

Since the parameters r_1, γ and κ have already been estimated in Section 6.4.2, no further preliminary tests were needed. The forced vibration test has been performed at different values of the frequency ratio within the range 0:2.5 and the displacement transmissibility and phase angle curves associated to the friction ratios [0.5, 0.75, 1, 2] have been reproduced. The experimental results are shown in Figs.6.28 and 6.29, where it is possible to observe a good agreement with the analytical results when the response is continuous and with the numerical curves when stick-slip occurs. The tuning of the friction ratio has been operated referring to the phase angle of the relative motion between the lower plate and the base, shown in Fig.6.29, at $r_1 \cong 1.2$. In fact, it can be observed that these phase angle curves present a regular pattern

and always show a monotonic dependence on the friction ratio. However, it must also be noted that $\phi_{z,\text{fft}}$ has a significant dependence on r_1 and, therefore, its sensitivity to the variations of the friction ratio may vary at different driving frequencies. In particular, an invariant point for both amplitude and phase of the relative motion is observed at $r_1 = 1.09$, in correspondence of the antiresonance of the transmissibility of m_1. It can also be observed that, for this value of r_1, the response of m_2 is still affected by friction, as shown by Fig.6.28b. Finally, looking at the phase angles $\phi_{1,\text{fft}}$ and $\phi_{2,\text{fft}}$, it is possible to see that, also in this contact configuration, the plates oscillate in phase or phase-opposition, as predicted by the analytical solutions.

During the tests, the motion of the brass disc has been monitored and compared to the motion of the base plate; it has been verified that the error introduced by the setup between the base motion and the wall motion is negligible in the frequency ratio range investigated. Conversely, it was found that the current setup cannot reproduce well the behaviour of a 2DOF system with a contact between the base and the upper plate. In fact, if the post is extended so that the brass disc can rest on the top plate, the wall motion results amplified in comparison to the base motion. This effect becomes particularly significant at higher frequencies, showing that further modes are being activated within the frequency range investigated. Regarding the current experiment, the same limitations highlighted in the previous investigations have been encountered. In fact, it has not been possible to reproduce the transmissibility and the phase angle in proximity of the boundary between sliding and permanent sticking regimes due to the frequent occurrence of permanent sticking between the disc and the plate in contact within the observed time window. Nonetheless, it can be concluded that, except that for very large amounts of friction, the proposed setup can reproduce well the behaviour of a 2DOF system with a contact between the base and m_1.

6.6 Summary and concluding remarks

In this chapter, the analytical solutions derived in Chapter 5 for the continuous response of MDOF systems with a Coulomb friction contact have been validated

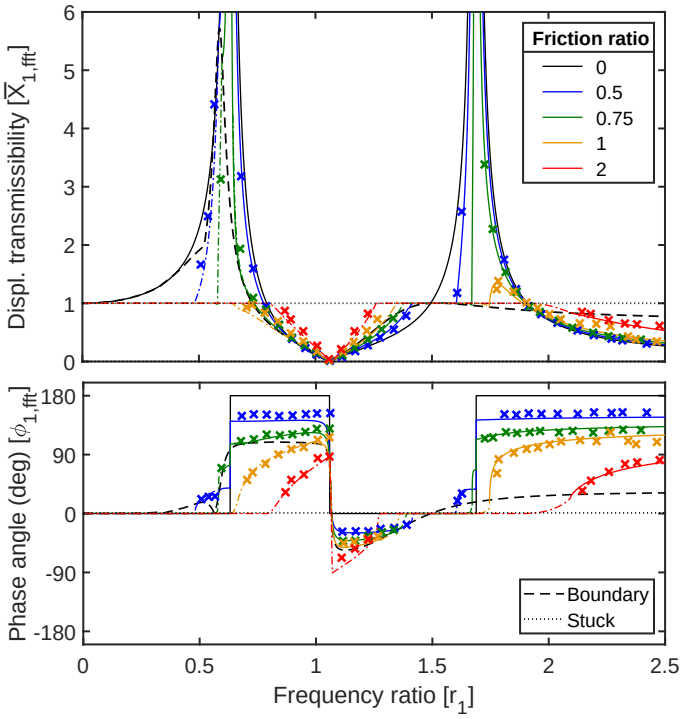

(a) Mass m_1

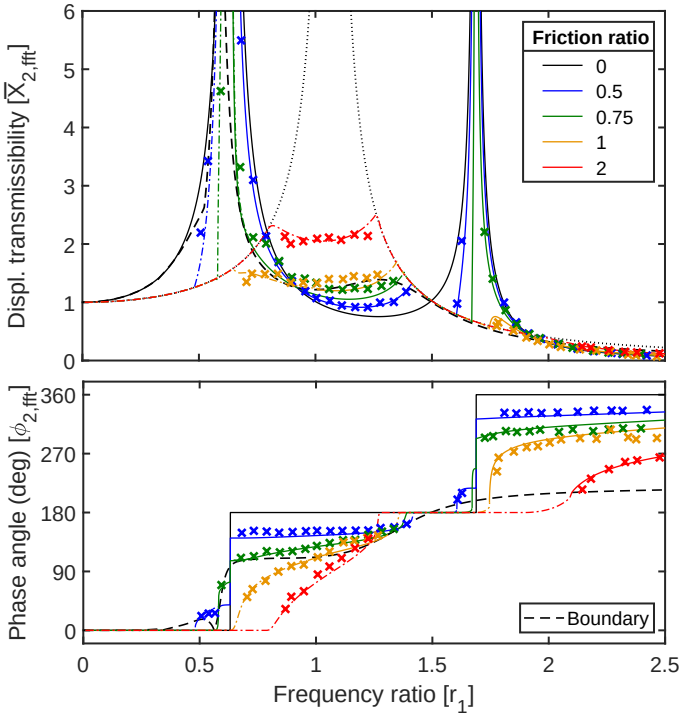

(b) Mass m_2

Figure 6.28: Displacement transmissibility and phase angle of a 2DOF system with a contact between m_1 and the harmonically excited base: experimental (markers) vs analytical (continuous lines) and numerical (dashed-dotted lines) results. The black dashed line represents the boundary between continuous and stick-slip regimes, the black dotted line the transmissibility in the stuck configuration.

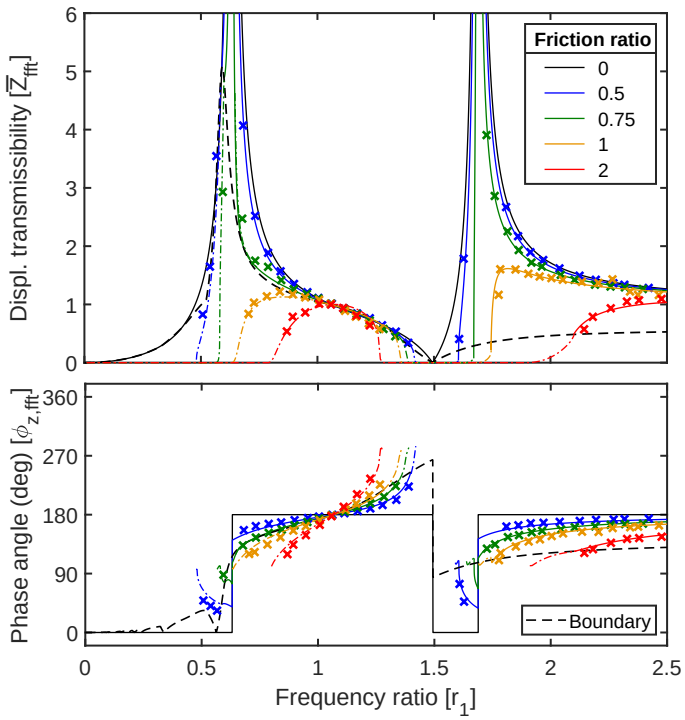

Figure 6.29: Non-dimensional amplitude and phase angle of the relative motion in the contact between m_1 and the harmonically excited base of a 2DOF system: experimental (markers) vs analytical (continuous lines) and numerical (dashed-dotted lines) results. The black dashed line represents the boundary between continuous and stick-slip regimes, the black dotted line the transmissibility in the stuck configuration.

numerically and experimentally. Moreover, the analytical expressions of the displacement transmissibilities, of the phase angles and of the boundaries between continuous and stick-slip regimes have been used to investigate the features of the dynamic response of these MDOF systems. Specifically, the resonant, low- and high-frequency behaviours have been analysed and an analytical approach for the determination of the invariant points for the transmissibility and the phase angle curves has been proposed. Finally, analytical formulations have also been obtained for the boundaries between the sliding and the permanent sticking regimes and for the response of the system in stuck conditions. The boundaries among the different motion regimes have been represented in a two-dimensional parameter space to visualise how these regimes occur for varying non-dimensional driving frequencies and friction forces.

The numerical validation has been presented for: (i) a 2DOF system with a

harmonic load on the lower mass and a friction contact between either the lower or the upper mass and a fixed wall; (ii) a 5DOF system with a harmonic load on the bottom mass and a friction contact between either the bottom or the third mass and a fixed wall; (iii) a base-excited 2DOF system with a contact either between the two masses or between the lower mass and the base. Numerical transmissibilities have also been evaluated in stick-slip regime for all these systems, providing a complete overview of their dynamic behaviour across the different motion regimes. The comparison between analytical and numerical results yielded an excellent agreement in all the cases investigated.

The experimental validation has been performed on a two-storeys shear frame setup with a brass-to-steel contact, where different configurations have been realised to reproduce the behaviour of a 2DOF system with a contact between either mass and a fixed wall and between the lower mass and the excited base. The experimental transmissibilities and phase angles observed during this investigation were in good agreement with the analytical and the numerical results in all the cases investigated, showing that the behaviour of MDOF systems with a Coulomb friction contact can also be observed in experimental conditions using the approach introduced in Chapter 4. However, as in the SDOF case, it emerged that the setup cannot be used to investigate the response of the system in proximity of the boundary between sliding and stuck regimes due to the frequent occurrence of permanent sticking between the parts in contact.

The main results obtained from the investigation of the response features were: (i) the determination of the minimum friction ratio for which the generic ith resonant peak of the response becomes finite; (ii) the determination of starting values of the transmissibility curves in quasi-static regime; (iii) the evaluation of the asymptotic values assumed by the boundary between continuous and stick-slip regimes when the exciting frequency tends to infinity. In addition, the presence of invariant points, inversions across the transmissibility curves for varying non-dimensional friction force and the onset of additional resonant peaks due to the transition from the sliding to the stuck configurations have been observed in the analytical, numerical

and experimental curves. All these results have shown that MDOF systems can exhibit a significantly different dynamic behaviour depending on whether the contact and the harmonic excitation occur on the same or on different masses.

One of the most important assumptions introduced in the MDOF models investigated in Chapters 5 and 6 is that the Coulomb friction generated in a single and localised contact can be regarded as the only source of damping of the system. In real structures, although Coulomb damping may have a predominant role, other forms of damping are always present, for instance due to the presence of joints or to the internal dissipation in the material. Nonetheless, it has been possible to reproduce experimentally most of the theoretical results using the proposed setup, meaning that it can be reasonable to neglect these other forms of damping when dealing with a very lightly-damped structure. However, it has also been shown that considering Coulomb friction as the only source of damping can lead to non-physical behaviours such as the presence of infinite resonant peaks. Therefore, in order to further understand how Coulomb friction can affect the resonant behaviour of real structures, including those cases where the structural damping is more significant, an investigation of systems with combined modal and Coulomb damping is presented in the following chapter.

Research is seeing what everybody else has seen and thinking what nobody else has thought.

— Albert Szent-Györgyi

7

Systems with combined modal and Coulomb damping

Contents

7.1 Introduction

In Chapters 5 and 6, the dynamic response of MDOF systems with a Coulomb friction contact has been explored considering the dry friction generated by the relative motion in the contact as the only source of damping in the system. The

experimental investigations carried out on a two-storey frame setup in Chapter 6, as well as those presented in Chapter 4 for the SDOF case, have shown that most of the behaviours described under this assumption by the analytical solutions and the numerical results can also be observed in a real structure. Nonetheless, assuming Coulomb friction as the only source of dissipation in a vibrating system can also lead to unrealistic results. In particular, in the previous chapters it has been observed that Coulomb damped systems always present infinite resonant peaks, unless stick-slip or permanent sticking occur at resonance. Since one of the main goals of the use of friction dampers is to avoid large stresses at resonance [8], it is essential to further investigate the resonant behaviour of these systems, also accounting for the general damping levels of the structure in the mechanical model.

As the exact nature of damping in real structures is often unknown, the viscous damping model is usually preferred when dealing with SDOF models because of its linearity [24]. However, even the introduction of viscous damping notably increases the complexity of the analysis of MDOF systems. In fact, in the presence of viscous damping, the modal superposition procedure cannot be used for determining the dynamic response in the form presented in Chapter 5. In fact, viscous damping can lead, in general, to non-diagonal modal damping matrices and, therefore, to coupling between the normal modes of the system. This is typically the case viscous damping is generated by localised sources, such as the shock absorbers in a car suspension, or the behaviour of structures with highly non-homogeneous damping levels, e.g., the building models accounting for the soil-structure interaction. However, this coupling effect, which would lead to the presence of complex mode shapes, is usually negligible when viscous damping is used to model the damping resulting in structures by non-localised sources such as internal dissipation in the materials, junctions or interfaces between parts of the structure and non-structural elements [24, 143]. These forms of damping are usually defined at a system level rather than in terms of individual element properties [24] and can be modelled using specific damping models, such as modal damping, where the damping of each vibrating mode is expressed by a modal damping ratio, assigned by measurement or based on experience [143]..

This chapter explores the dynamic behaviour of mechanical systems with combined modal and Coulomb damping, aiming to establish how the response features and the motion regimes observed in the previous chapters for SDOF and MDOF systems with Coulomb damping only evolve when the general damping of a structure is also introduced in the models.

The analytical procedure introduced in Chapter 5 is applied to MDOF systems with modal and Coulomb damping in Section 7.2, where closed-form expressions are derived for the continuous steady-state time response, displacement transmissibility and phase angle of all the masses of a MDOF system. Furthermore, an analytical formulation is provided for the boundary between continuous and stick-slip regimes. In Section 7.3, the numerical approach introduced in Section 6.3.1 is used for validating the analytical results and providing an insight on the behaviour of these systems in stick-slip regime. Finally, the resonant, low- and high-frequency behaviours, as well as the dynamic response in permanent sticking regime, are explored in Section 7.4.

7.2 Analytical evaluation of the continuous response

7.2.1 General formulation and assumptions

Let us consider a discrete MDOF system characterised by the $N \times N$ mass, damping and stiffness matrices $\mathbf{M}$, $\mathbf{C}$ and $\mathbf{K}$ respectively, where a harmonic load $P\cos(\omega t)$ is applied to the l-th DOF and a Coulomb contact occurs between the j-th mass and a fixed wall, generating a kinetic friction force of amplitude F and a static friction force equal to μF. The governing equation of this system can be written as:

$$\mathbf{M}\ddot{\mathbf{x}} + \mathbf{C}\dot{\mathbf{x}} + \mathbf{K}\mathbf{x} + \mathbf{f}\mathrm{sgn}(\dot{x}_j) = \mathbf{p} \tag{7.1}$$

or, in a non-dimensional form, as:

$$\overline{\mathbf{M}}\bar{\mathbf{x}}'' + \overline{\mathbf{C}}\bar{\mathbf{x}}' + \overline{\mathbf{K}}\bar{\mathbf{x}} + \bar{\mathbf{f}}\mathrm{sgn}(\bar{x}_j') = \bar{\mathbf{p}} \tag{7.2}$$

where $\overline{\mathbf{M}}$, $\overline{\mathbf{K}}$, $\bar{\mathbf{f}}$ and $\bar{\mathbf{p}}$ have been introduced in Section 5.3. From the nondimensionalisation process, described in detail in Section 5.2, it is also possible to express the relation between $\overline{\mathbf{C}}$ and $\mathbf{C}$ as:

$$\overline{\mathbf{C}} = \frac{\omega}{k_1}\mathbf{C} \tag{7.3}$$

The problem described by Eqs.(7.1) and (7.2) is piecewise linear and can be solved with the analytical approach presented in Chapter 5, i.e. by investigating the continuous steady-state response in the half-period included between two stationary points of $\bar{x}_j$. In fact, Eq.(7.2) is linear in this time interval and a modal superposition procedure can be applied. However, this approach can only be used if specific assumptions are made on the formulation of the linear damping matrix $\overline{\mathbf{C}}$. In fact, while the mass and the stiffness matrices can be diagonalised by introducing the modal transformation described in Section 5.3, this is not generally the case for the damping matrix. As a consequence, if a generic linear damping matrix $\overline{\mathbf{C}}$ is considered, modal analysis cannot be used to reduce Eq.(7.2) to a set of N uncoupled equations. Nonetheless, it is common in the engineering practice to assume that this damping matrix can be expressed as a linear combination of the mass and the stiffness matrices [155] or that, more in general, it satisfies the conditions derived in references [156, 157] for which a diagonal modal damping matrix is obtained. As specified in Section 7.1, the modal damping model will be considered, i.e. it will be assumed that the matrix $\overline{\mathbf{C}}$ is such that:

$$\hat{\mathbf{C}} = \mathbf{\Psi}^T\overline{\mathbf{C}}\mathbf{\Psi} = \mathrm{diag}(2\zeta_i\Omega_i) \tag{7.4}$$

where $\zeta_1, ..., \zeta_N$ represent the modal damping ratios of the N vibrating modes of the system. The modal damping ratios can be considered as further N input parameters of the problem, in addition to the $2N + 1$ non-dimensional groups introduced in Section 5.2. Once the values of the modal damping ratios are assigned, the non-dimensional linear damping matrix $\overline{\mathbf{C}}$ can be obtained from $\hat{\mathbf{C}}$ using the following relationship [24]:

$$\overline{\mathbf{C}} = \mathbf{\Psi}^{-T}\hat{\mathbf{C}}\mathbf{\Psi}^{-1} = \sum_{i=1}^{N} 2\zeta_i\Omega_i(\overline{\mathbf{M}}\boldsymbol{\psi}_i)(\overline{\mathbf{M}}\boldsymbol{\psi}_i)^T \tag{7.5}$$

The assumption of a modal damping model allows the use of modal analysis for determining the steady-state response of the system in continuous regime. This procedure is detailed in what follows.

7.2.2 Modal superposition procedure

Modal damping does not affect either the natural frequencies or the mode-shapes of the system. Therefore, considering Eqs.(5.13) and (7.4), it is possible to write the governing equation of the ith modal coordinate as:

$$\eta_i'' + 2\zeta_i\Omega_i\eta_i' + \Omega_i^2\eta_i = \psi_{ji}\beta + \psi_{li}\cos(\tau + \phi_j) \tag{7.6}$$

The general solution of Eq.(7.6) can be obtained as:

$$\eta_i = e^{-\frac{\zeta_i\tau}{R_i}}\left[A_i\cos\left(\frac{\tau\sqrt{1-\zeta_i^2}}{R_i}\right) + B_i\sin\left(\frac{\tau\sqrt{1-\zeta_i^2}}{R_i}\right)\right] + \psi_{ji}R_i^2\beta + \psi_{li}R_i^2 v_{di}\cos(\tau + \phi_j) \tag{7.7}$$

where:

$$v_{di} = \frac{1}{1 - R_i^2 + i2\zeta_i R_i} \tag{7.8}$$

represents the complex response function of the ith vibrating mode of the system in the absence of Coulomb damping. The initial and final conditions written in Eqs.(5.17) and (5.20) for the ith modal coordinate and its derivative can be used to determine the unknown integration constants A_i and B_i and to define a relation between the phase angle ϕ_j and the initial values η_{i0} and η_{i0}', which are still unknown at this stage. This procedure is similar to that introduced in Section 5.3 in the absence of modal damping and is therefore reported in detail in Appendix B. The resulting expressions for $\cos\phi_j$ and $\sin\phi_j$ can be written as:

$$\cos\phi_j = \frac{\eta_{i0} + \psi_{ji}R_i^2 g_i\beta}{\psi_{li}R_i^2 v_{di}} \tag{7.9}$$

$$\sin\phi_j = -\frac{\eta_{i0}' + \psi_{ji}R_i^2 u_{di}\beta}{\psi_{li}R_i^2 v_{di}} \tag{7.10}$$

where the functions:

$$u_{di} = \frac{\sin\left(\dfrac{\pi\sqrt{1-\zeta_i^2}}{R_i}\right)}{R_i\sqrt{1-\zeta_i^2}\left[\cosh\left(\dfrac{\zeta_i\pi}{R_i}\right)+\cos\left(\dfrac{\pi\sqrt{1-\zeta_i^2}}{R_i}\right)\right]} \tag{7.11}$$

and:

$$g_i = \frac{\sinh\left(\dfrac{\zeta_i\pi}{R_i}\right) - \dfrac{\zeta_i}{\sqrt{1-\zeta_i^2}}\sin\left(\dfrac{\pi\sqrt{1-\zeta_i^2}}{R_i}\right)}{\cosh\left(\dfrac{\zeta_i\pi}{R_i}\right)+\cos\left(\dfrac{\pi\sqrt{1-\zeta_i^2}}{R_i}\right)} \tag{7.12}$$

have been introduced as the first and the second damping functions of the ith mode of the system. In particular, in the limit case of $\zeta_i = 0$, the first damping function reduces to the damping function formulated for the ith mode of a MDOF system with Coulomb damping only in Eq.(5.26), while $g_i = 0$. When $N = 1$, the formulations of both damping functions reduce to those derived by Den Hartog for SDOF systems with combined viscous and Coulomb damping [21], which are reported in Eqs.(2.36) and (2.37).

7.2.3 Response amplitude and phase of the mass in contact

Multiplying by ψ_{ji} the numerators and the denominators of Eqs.(7.9) and (7.10), considering their sums from 1 to N and introducing Eqs.(5.30) and (5.31), it is possible to express $\cos\phi_j$ and $\sin\phi_j$ as:

$$\cos\phi_j = \frac{\sum\limits_{i=1}^{N}\psi_{ji}\eta_{i0} + \beta\sum\limits_{i=1}^{N}\psi_{ji}^2 R_i^2 g_i}{\sum\limits_{i=1}^{N}\psi_{ji}\psi_{li}R_i^2 v_{di}} = \frac{\overline{X}_j + \beta G_j}{V_{dj}} \tag{7.13}$$

and:

$$\sin\phi_j = -\frac{\sum\limits_{i=1}^{N}\psi_{ji}\eta'_{i0} + \beta\sum\limits_{i=1}^{N}\psi_{ji}^2 R_i^2 u_{di}}{\sum\limits_{i=1}^{N}\psi_{ji}\psi_{li}R_i^2 v_{di}} = -\frac{\beta U_{dj}}{V_{dj}} \tag{7.14}$$

where the generic k-th complex response function, the first and the second damping functions of the MDOF systems have been introduced as the modal superpositions of

the expressions provided for the ith mode in Eqs.(7.8), (7.11) and (7.12) respectively:

$$V_{dk} = \sum_{i=1}^{N} \psi_{ki}\psi_{li}R_i^2 v_{di} \tag{7.15}$$

$$U_{dk} = \sum_{i=1}^{N} \psi_{ki}\psi_{ji}R_i^2 u_{di} \tag{7.16}$$

$$G_k = \sum_{i=1}^{N} \psi_{ki}\psi_{ji}R_i^2 g_i \tag{7.17}$$

It is necessary to observe that, due to the presence of the function V_{dj}, the expressions derived for $\cos\phi_j$ and $\sin\phi_j$ are complex. However, expressing the complex response function as $V_{dj} = |V_{dj}|e^{i\angle V_{dj}}$ and after performing some algebraic manipulations, it is possible to rewrite Eqs.(7.13) and (7.14) as:

$$\cos(\phi_j + \angle V_{dj}) = \frac{\overline{X}_j + \beta G_j}{|V_{dj}|} \tag{7.18}$$

and:

$$\sin(\phi_j + \angle V_{dj}) = -\frac{\beta U_{dj}}{|V_{dj}|} \tag{7.19}$$

Using the relation $\cos^2(\phi_j + \angle V_{dj}) + \sin^2(\phi_j + \angle V_{dj}) = 1$, it can be obtained that the non-dimensional response amplitude of the mass in contact m_j is given by:

$$\overline{X}_j = -\beta G_j + \sqrt{|V_{dj}|^2 - (\beta U_{dj})^2} \tag{7.20}$$

It can be observed that this expression is formally identical to that derived by Den Hartog for a SDOF system with combined viscous and Coulomb damping [21], which is reported in Eq.(2.34), and reduces to that formulation when $N = 1$. The phase angle ϕ_j can finally be obtained from Eqs.(7.18) and (7.19) or, more synthetically, from:

$$\phi_j = \text{atan2}\left(-\frac{\beta U_{dj}}{|V_{dj}|}, \sqrt{1 - \left(\frac{\beta U_{dj}}{|V_{dj}|}\right)^2}\right) - \angle V_{dj} \tag{7.21}$$

where the function atan2 is defined according to the expression provided in [141].

7.2.4 Steady-state time response of all masses

In Appendix B, the following expression has been derived for the ith modal displacement:

$$\eta_i = (\eta_{i0} + \psi_{ji} R_i^2 g_i \beta)\cos\tau + (\eta'_{i0} + \psi_{ji} R_i^2 u_{di}\beta)\sin\tau + \beta\psi_{ji}R_i^2 \left\{ 1 - (1+g_i)e^{-\frac{\zeta_i \tau}{R_i}} \left[\sin\left(\frac{\tau\sqrt{1-\zeta_i^2}}{R_i}\right) + \frac{\zeta_i}{\sqrt{1-\zeta_i^2}}\cos\left(\frac{\tau\sqrt{1-\zeta_i^2}}{R_i}\right)\right] - u_{di}R_i \frac{1}{\sqrt{1-\zeta_i^2}} e^{-\frac{\zeta_i\tau}{R_i}} \sin\left(\frac{\tau\sqrt{1-\zeta_i^2}}{R_i}\right)\right\} \quad (7.22)$$

The time response of the generic mass m_k of the system in the non-dimensional time interval $[0, \pi]$ can be obtained from Eq.(7.22), by multiplying both sides by ψ_{ki} and introducing the k-th equation from Eq.(5.11), as:

$$\bar{x}_k = (\bar{x}_{k0} + \beta G_k)\cos\tau + (\bar{x}'_{k0} + \beta U_{dk})\sin\tau + \beta \sum_{i=1}^{N} \psi_{ki}\psi_{ji} R_i^2 \left\{ 1 - (1+g_i)e^{-\frac{\zeta_i \tau}{R_i}} \left[\sin\left(\frac{\tau\sqrt{1-\zeta_i^2}}{R_i}\right) + \frac{\zeta_i}{\sqrt{1-\zeta_i^2}}\cos\left(\frac{\tau\sqrt{1-\zeta_i^2}}{R_i}\right)\right] - u_{di}R_i \frac{1}{\sqrt{1-\zeta_i^2}} e^{-\frac{\zeta_i\tau}{R_i}} \sin\left(\frac{\tau\sqrt{1-\zeta_i^2}}{R_i}\right)\right\} \quad (7.23)$$

The response of the mass in contact m_j is completely known at this stage, since the initial values of its displacement and velocity are equal to $\overline{X}_j$ and to zero respectively, as expressed in Eq.(5.29). However, these values are still unknown for all the other masses of the system. In order to determine them, let us multiply by ψ_{ki} the numerators and the denominators of Eqs.(7.9) and (7.10) and consider their sums from 1 to N. The following relationships are obtained:

$$\cos\phi_j = \frac{\bar{x}_{k0} + \beta G_k}{V_{dk}} \quad (7.24)$$

$$\sin\phi_j = -\frac{\bar{x}'_{k0} + \beta U_{dk}}{V_{dk}} \quad (7.25)$$

Comparing Eqs.(7.24) and (7.25) with Eqs.(7.13) and (7.14) respectively, it can be obtained that:

$$\bar{x}_{k0} = -\beta G_k + \frac{|V_{dk}|}{|V_{dj}|}\sqrt{|V_{dj}|^2 - (\beta U_{dj})^2}\; e^{i(\angle V_{dk} - \angle V_{dj})} \quad (7.26)$$

and:

$$\bar{x}'_{k0} = \beta \left[\frac{|V_{dk}|}{|V_{dj}|} U_{dj} \, e^{i(\angle V_{dk} - \angle V_{dj})} - U_{dk} \right] \tag{7.27}$$

Introducing these expressions into Eq.(7.23) and considering the real part only, the response of the generic mass m_k can be finally written as:

$$\begin{aligned} \bar{x}_k = {} & \frac{|V_{dk}|}{|V_{dj}|} \left[\sqrt{|V_{dj}|^2 - (\beta U_{dj})^2} \cos(\tau + \angle V_{dk} - \angle V_{dj}) + \beta U_{dj} \sin(\tau + \angle V_{dk} - \angle V_{dj}) \right] \\ & + \beta \sum_{i=1}^{N} \psi_{ki} \psi_{ji} R_i^2 \left\{ 1 - (1+g_i) e^{-\frac{\zeta_i \tau}{R_i}} \left[\sin\left(\frac{\tau \sqrt{1-\zeta_i^2}}{R_i} \right) + \frac{\zeta_i}{\sqrt{1-\zeta_i^2}} \cos\left(\frac{\tau \sqrt{1-\zeta_i^2}}{R_i} \right) \right] \right. \\ & \left. - u_{di} R_i \frac{1}{\sqrt{1-\zeta_i^2}} e^{-\frac{\zeta_i \tau}{R_i}} \sin\left(\frac{\tau \sqrt{1-\zeta_i^2}}{R_i} \right) \right\} \end{aligned} \tag{7.28}$$

7.2.5 Response amplitude and phase of the masses not in contact

The amplitude and the phase angle of the response of the generic mass m_k of the system cannot be determined in a closed form from Eq.(7.28). In general, it is possible to calculate them numerically, determining the amplitude as the maximum absolute value of $\bar{x}_k$ and the phase angle as:

$$\begin{cases} \phi_k = \phi_j + \tau_{k,\max} & \text{if } \bar{x}_k(\tau_{k,\max}) \geq 0 \quad (7.29a) \\ \phi_k = \phi_j + \tau_{k,\max} + \pi & \text{if } \bar{x}_k(\tau_{k,\max}) < 0 \quad (7.29b) \end{cases}$$

where $\tau_{k,\max}$ is the time instant where such a maximum is reached. Nonetheless, as shown in Section 5.4.2 in the absence of modal damping, approximated closed-form expressions for these quantities can be obtained by considering the monoharmonic approximation of the response provided in Eq.(5.49). In particular, it has been observed that, in continuous non-sticking regime, modal damping further reduces the non-monoharmonic effects introduced by Coulomb friction. While these effects can still be significant for the response of the mass in contact, Eq.(5.49) offers a very good approximation of the response $\bar{x}_k$. Substituting Eqs.(7.26) and (7.27) into Eq.(5.49), it can be obtained that:

$$\begin{aligned} \bar{x}_k &\cong \mathrm{Re}\{\bar{x}_{k0} \cos\tau + \bar{x}'_{k0} \sin\tau\} \\ &= \mathrm{Re}\{(\bar{x}_{k0} - i\bar{x}'_{k0})(\cos\tau + i\sin\tau)\} = \overline{X}_{k_C} \cos\tau + \overline{X}_{k_S} \sin\tau \end{aligned} \tag{7.30}$$

where:

$$\overline{X}_{k_C} = \left[\frac{|V_{dk}|}{|V_{dj}|}\sqrt{|V_{dj}|^2 - (\beta U_{dj})^2}\cos(\angle V_{dk} - \angle V_{dj}) + \beta U_{dj}\sin(\angle V_{dk} - \angle V_{dj})\right] - \beta G_k \tag{7.31}$$

and:

$$\overline{X}_{k_S} = \frac{|V_{dk}|}{|V_{dj}|}\left[\beta U_{dj}\cos(\angle V_{dk} - \angle V_{dj}) - \sqrt{|V_{dj}|^2 - (\beta U_{dj})^2}\sin(\angle V_{dk} - \angle V_{dj})\right] - \beta U_{dk} \tag{7.32}$$

Therefore, the response amplitude can be obtained as:

$$\begin{aligned}\overline{X}_k &\cong \sqrt{\overline{X}_{k_C}^2 + \overline{X}_{k_S}^2} \\ &= \left\{|V_{dk}|^2 + \beta^2(G_k^2 + U_{dk}^2) - 2\beta\frac{|V_{dk}|}{|V_{dj}|}\left[\sqrt{|V_{dj}|^2 - (\beta U_{dj})^2}\left(G_k\cos(\angle V_{dk} - \angle V_{dj})\right.\right.\right. \\ &\left.\left.\left. + U_{dk}\sin(\angle V_{dk} - \angle V_{dj})\right) + \beta U_{dj}\left(G_k\sin(\angle V_{dk} - \angle V_{dj}) + U_{dk}\cos(\angle V_{dk} - \angle V_{dj})\right)\right]\right\}^{\frac{1}{2}}\end{aligned} \tag{7.33}$$

while the phase angle between the maxima of the displacements of m_j and m_k within the time interval $[0, \pi]$ is given by:

$$\cos\phi_{kj} = \frac{\overline{X}_{k_C}}{\overline{X}_k} \qquad\qquad \sin\phi_{kj} = \frac{\overline{X}_{k_S}}{\overline{X}_k} \tag{7.34}$$

The phase angle of the response of the generic k-th mass can be finally calculated as $\phi_k = \phi_j + \phi_{kj}$, where ϕ_j is obtained from Eq.(7.21). It can be demonstrated that Eq.(7.33) reduces to Eq.(7.20) when $k = j$.

7.2.6 Domain of validity of the solution

The domain of validity of the solutions derived in this section can be determined with a similar procedure to that introduced in Section 5.5. In fact, these solutions only hold if the steady-state response of the system is continuously non-sticking. The response has been investigated in the half-period $[0, \pi]$ included between a maximum and a minimum of $\bar{x}_j$, assuming that $\bar{x}'_j < 0$ in all the internal points of this interval. In addition, the occurrence of a stop must also be ruled out at the ends of the interval, where $\bar{x}'_j = 0$, imposing explicitly that the overall dynamic

loading acting in the contact has a larger amplitude than the static friction force. Therefore, the following non-sticking conditions can be formulated:

$$\begin{cases} \bar{x}'_j < 0 & \text{if } 0 < \tau < \pi \quad (7.35a) \\ \left| \sum_{k=1}^{N} \overline{C}_{jk} \bar{x}'_k + \sum_{k=1}^{N} \overline{K}_{jk} \bar{x}_k - \delta_{lj} \cos(\tau + \phi_j) \right| > \mu\beta & \text{if } \tau = 0 \text{ or } \tau = \pi \quad (7.35b) \end{cases}$$

In order to express the domain of validity in terms of the friction ratio, let us substitute Eq.(7.28) into Eq.(7.35a). The following inequality is obtained:

$$\overline{X}_j + \beta G_j > \beta S_{dj} \tag{7.36}$$

where:

$$S_{dj} = \sum_{i=1}^{N} \psi_{ji}^2 s_{di} \tag{7.37}$$

and:

$$s_{di} = \max_{0<\tau<\pi} \frac{1}{\sin\tau} \left\{ (1+g_i) e^{-\frac{\zeta_i \tau}{R_i}} \frac{R_i}{\sqrt{1-\zeta_i^2}} \sin\left(\frac{\tau\sqrt{1-\zeta_i^2}}{R_i} \right) \right. \\ \left. - u_{di} R_i^2 e^{-\frac{\zeta_i \tau}{R_i}} \left[\sin\left(\frac{\tau\sqrt{1-\zeta_i^2}}{R_i} \right) + \frac{\zeta_i}{\sqrt{1-\zeta_i^2}} \cos\left(\frac{\tau\sqrt{1-\zeta_i^2}}{R_i} \right) \right] \right\} \tag{7.38}$$

From Eq.(7.20) and Eq.(7.36), it can be obtained that the condition expressed in Eq.(7.35a) is verified when:

$$\beta < \sqrt{\frac{|V_{dj}|^2}{U_{dj}^2 + S_{dj}^2}} \tag{7.39}$$

In order to derive a similar expression from Eq.(7.35b), it is possible to rewrite it in modal terms by introducing the coordinate transformation in Eq.(5.11) and considering the generic ith modal coordinate:

$$|2\zeta_i \Omega_i \eta'_{i0} + \Omega_i^2 \eta_{i0} - \psi_{li} \cos\phi_j| > \psi_{ji} \mu\beta \tag{7.40}$$

It is useful to express the term $\cos\phi_j$ in the above expression as a function of η_{i0} and η'_{i0}. From Eqs.(7.9) and (7.10), it is obtained that:

$$\begin{cases} \cos(\phi_j + \angle v_{di}) = \dfrac{\eta_{i0} + \psi_{ji} R_i^2 g_i \beta}{\psi_{li} R_i^2 |v_{di}|} & (7.41a) \\ \sin(\phi_j + \angle v_{di}) = -\dfrac{\eta'_{i0} + \psi_{ji} R_i^2 u_{di} \beta}{\psi_{li} R_i^2 |v_{di}|} & (7.41b) \end{cases}$$

Furthermore, it is easily obtained from the definition of v_{di}, provided in Eq.(7.8), that:

$$\begin{cases} \cos(\angle v_{di}) = |v_{di}|(1 - R_i^2) & \text{(7.42a)} \\ \sin(\angle v_{di}) = -|v_{di}|(2\zeta_i R_i) & \text{(7.42b)} \end{cases}$$

Thus, it follows that:

$$\cos\phi_j = \frac{\eta_{i0} + \psi_{ji} R_i^2 g_i \beta}{\psi_{li} R_i^2}(1 - R_i^2) + \frac{\eta'_{i0} + \psi_{ji} R_i^2 u_{di} \beta}{\psi_{li} R_i^2}(2\zeta_i R_i) \tag{7.43}$$

Introducing Eq.(7.43), it is possible to rewrite Eq.(7.40) as:

$$\left|\eta_{i0} - \beta\psi_{ji}[(1 - R_i^2)g_i + 2\zeta_i R_i u_{di}]\right| > \psi_{ji}\mu\beta \tag{7.44}$$

Let us now consider the sums of both sides of Eq.(7.44), multiplied by ψ_{ji}. Introducing the function:

$$H_j = \sum_{i=1}^{N} \psi_{ji}^2 (g_i + 2\zeta_i R_i u_{di}) \tag{7.45}$$

and substituting Eq.(6.7),it is possible to rewrite the above inequality as:

$$\left|\overline{X}_j + \beta G_j - \beta H_j\right| > \frac{\mu\beta}{\gamma_j r_1^2} \tag{7.46}$$

The condition expressed in Eq.(7.46) is verified if:

$$\beta < \sqrt{\frac{|V_{dj}|^2}{U_{dj}^2 + \left(H_j + \dfrac{\mu}{\gamma_j r_1^2}\right)^2}} \tag{7.47}$$

or:

$$\beta > \sqrt{\frac{|V_{dj}|^2}{U_{dj}^2 + \left(H_j - \dfrac{\mu}{\gamma_j r_1^2}\right)^2}} \tag{7.48}$$

In order to obtain a continuous non-sticking response, the inequalities expressed in Eq.(7.39) and one between Eq.(7.47) and Eq.(7.48) must be simultaneously verified. However, it has been observed that Eq.(7.39) and Eq.(7.48) never occur concurrently. Therefore, the domain of validity of the mathematical solution presented in this section can be expressed as:

$$\beta < \sqrt{\frac{|V_{dj}|^2}{U_{dj}^2 + \left[\max\left(S_{dj}, H_j + \dfrac{\mu}{\gamma_j r_1^2}\right)\right]^2}} \tag{7.49}$$

where the RHS represents the value β_{lim} of the friction ratio at the boundary between continuous and stick-slip regimes.

Due to the presence of the function S_{dj}, the evaluation of the boundary described by Eq.(7.49) requires the numerical calculation of the maximum of the time-dependant expression in Eq.(7.38) for each sets of parameters. In order to reduce the computational cost associated to this procedure, the following approximation can be considered. It has been observed numerically that, in most cases, the maximum value of the function s_{di} occurs at $\tau = 0$. This effect is due to the presence of the exponential term $e^{-\frac{\zeta_i \tau}{R_i}}$ in the expression of s_{di} and, therefore, exceptions are only observed when ζ_i is nearly zero. Thus, a first-order expansion of the function s_{di} around $\tau = 0$ can be considered:

$$s_{di} \cong \frac{1}{\tau}\left\{(1+g_i)\left(1-\frac{\zeta_i\tau}{R_i}\right)\tau - u_{di}R_i^2\left[1-\left(1-\frac{\zeta_i\tau}{R_i}\right)^2\right]\right\} \tag{7.50}$$

Neglecting the second-order terms in the above equation, it is obtained that:

$$s_{di} \cong 1 + g_i + 2\zeta_i R_i u_{di} \tag{7.51}$$

and, by substituting this expression into Eq.(7.37), it is possible to write an approximated expression of the function S_{dj} as:

$$S_{dj} \cong H_j + \frac{1}{\gamma_j r_1^2} \tag{7.52}$$

Introducing this approximated formulation into Eq.(7.49), it can be observed that the term $H_j + \mu/(\gamma_j r_1^2)$ coincides with S_{dj} if $\mu = 1$ and becomes larger if $\mu > 1$. Therefore, Eq.(7.47) can directly be considered as an approximation of the boundary between continuous and stick-slip regimes. In particular, it has been observed that discrepancies between the exact and the approximated expressions can arise at low frequency ratios only when the modal damping ratios are nearly zero, consistently with the above observations. The case $\zeta_i = 0$, discussed in Section 5.5, is therefore the case where the most significant disagreement is observed between the exact and the approximated boundary.

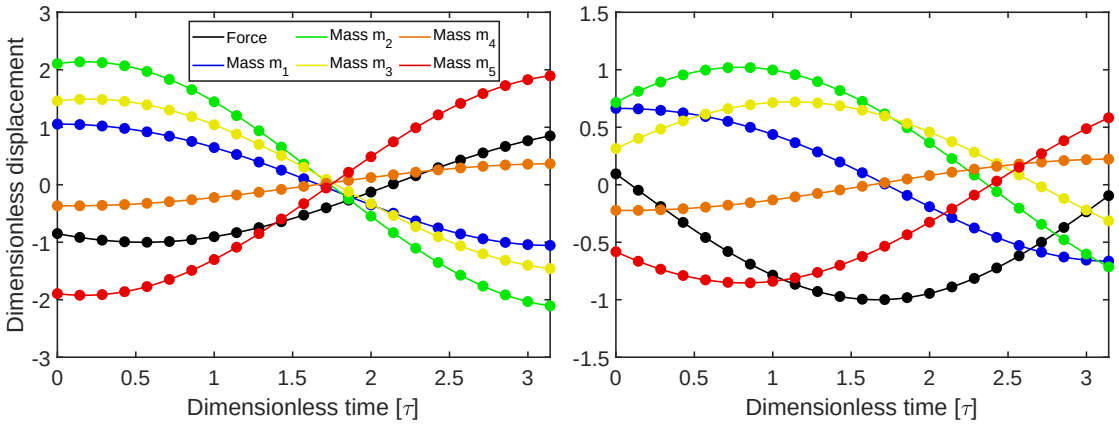

(a) $\zeta_i = 0.01$ **(b)** $\zeta_i = 0.1$

Figure 7.1: Steady-state time response of a 5DOF system with equal masses and springs where a friction contact and a harmonic load are applied to m_1 for $\mu = 1$, $\beta = 0.2$, $r_1 = 0.9$ and modal damping ratios 0.01 (**a**) and 0.1 (**b**): comparison between analytical (continuous lines) and numerical (round markers).

7.3 Numerical validation and extension to stick-slip regime

This section presents the numerical validation and extension to the stick-slip regime of the solutions derived in Section 7.2 for the response of discrete mechanical systems with combined modal and Coulomb damping.

The numerical approach used for the current investigation is the same described in Section 6.3.1 and illustrated in Fig.6.3, provided that the term $\overline{\mathbf{C}}\bar{\mathbf{x}}'$ is introduced in the governing equations of the sticking and of the sliding stages. The linear damping term must also be taken into account when comparing the overall dynamic loading acting on the mass in contact and the static friction force, as suggested by the non-sticking condition reported in Eq.(7.35b). The matrix $\overline{\mathbf{C}}$ can be directly specified by the user or, alternatively, the modal damping ratios $\zeta_1, ..., \zeta_N$ can be provided as an input. In the latter case, the damping matrix is evaluated by using Eq.(7.5). In the following numerical analyses, the same settings indicated in Section 3.6.1 and Section 6.3.1 for the number of cycles and the tolerances have been considered.

A comparison between the analytical and numerical steady-state time responses in continuous regime is obtained in Figs.7.1 and 7.2, referring to the case of a 5DOF system excited on m_1 and with a contact applied on either m_1 (in Fig.7.1) or m_3

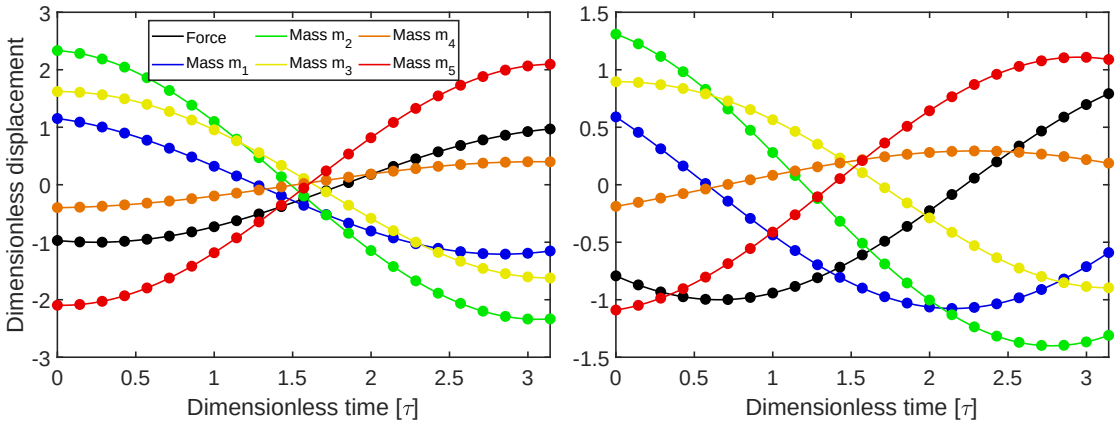

(a) $\zeta_i = 0.01$ **(b)** $\zeta_i = 0.1$

Figure 7.2: Steady-state time response of a 5DOF system with equal masses and springs where a friction contact occurs on m_3 and a harmonic load is applied to m_1 for $\mu = 1$, $\beta = 0.2$, $r_1 = 0.9$ and modal damping ratios 0.01 (**a**) and 0.1 (**b**): comparison between analytical (continuous lines) and numerical (round markers).

(in Fig.7.1) for two different amounts of modal damping. It can be observed that the agreement between the analytical and the numerical results is excellent in all the cases investigated. From Fig.7.1, it can also be noted that, while for $\zeta_i = 0.01$ the response of all the masses is nearly in phase or phase-opposition, as in the undamped case discussed in Section 6.3.2, this property is lost when larger modal damping ratios are considered. This can also be observed from Fig.7.2, where a phase shift gradually appears among the responses of the mass in contact m_3 and of the masses located above the contact, i.e. m_4 and m_5.

The numerical validation of the transmissibility and phase angle curves has been performed for a (i) SDOF system and for (ii) the 2DOF system shown in Fig.6.11. These two case-studies represent the simplest configurations where the harmonic and the friction forces are applied on the same and on different masses, respectively. While the SDOF behaviour has been investigated for the values [0.001, 0.01, 0.1] of the damping ratio ζ, for the 2DOF system it has been chosen to refer to the values $\zeta_i = [0.001/r_{n,i}, 0.01/r_{n,i}, 0.1/r_{n,i}]$ in order to observe a similar damping effect for both vibrating modes in each case. A very good agreement can be observed from the comparison between the analytical and the numerical results, shown in Fig.7.3 for (i) and in Figs.7.5 and 7.6 for (ii). In the same figures, the numerical transmissibilities

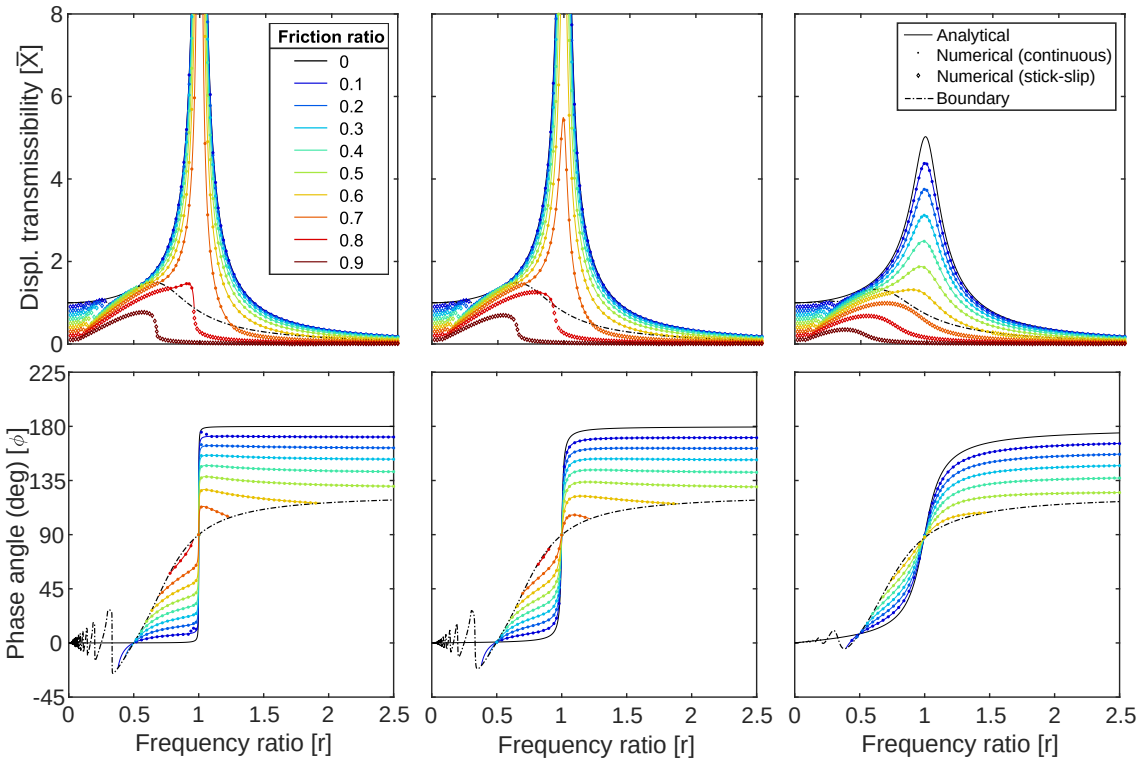

(a) $\zeta = 0.001$ **(b)** $\zeta = 0.01$ **(c)** $\zeta = 0.1$

Figure 7.3: Displacement transmissibility and phase angle of a SDOF system with combined modal and Coulomb damping under harmonic excitation for $\mu = 1$ and varying frequency, friction and modal damping ratios: analytical vs numerical.

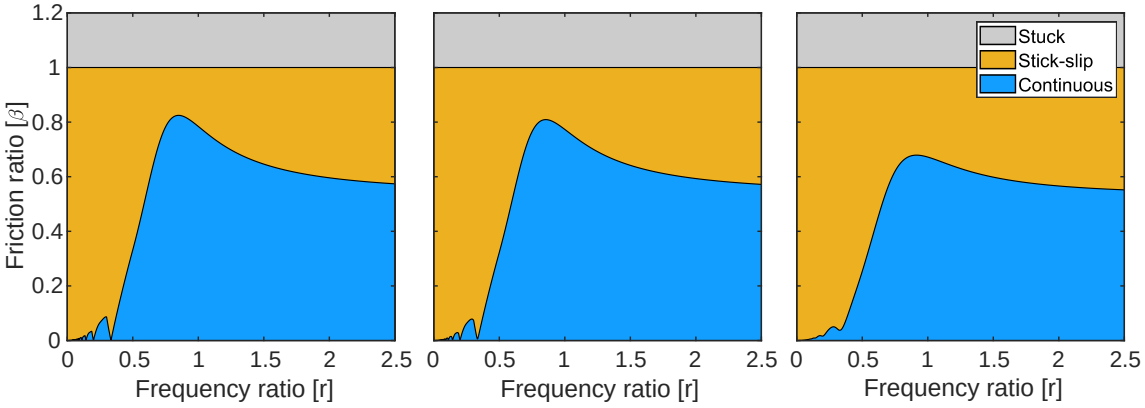

(a) $\zeta = 0.001$ **(b)** $\zeta = 0.01$ **(c)** $\zeta = 0.1$

Figure 7.4: Motion regimes of a SDOF system with combined modal and Coulomb damping under harmonic excitation in the parameter space r-β for $\mu = 1$ and varying modal damping ratio.

have also been represented for stick-slip responses. Finally, the analytical boundaries of the motion regimes are depicted in Figs.7.4 and 7.7 for varying amounts of modal damping. All these results are further discussed in the following section, where the

response features of systems with modal and Coulomb damping are explored.

7.4 Features of the dynamic response

In Section 6.2, the main features characterising the dynamic response of a MDOF system with a Coulomb friction contact between a mass and a fixed wall have been discussed, including the resonant, the low- and the high-frequency behaviours, the presence of invariant points and inversions across the transmissibility curves and the behaviour of these systems in permanent sticking regime. This section presents a discussion on how these response features are affected by the presence of modal damping.

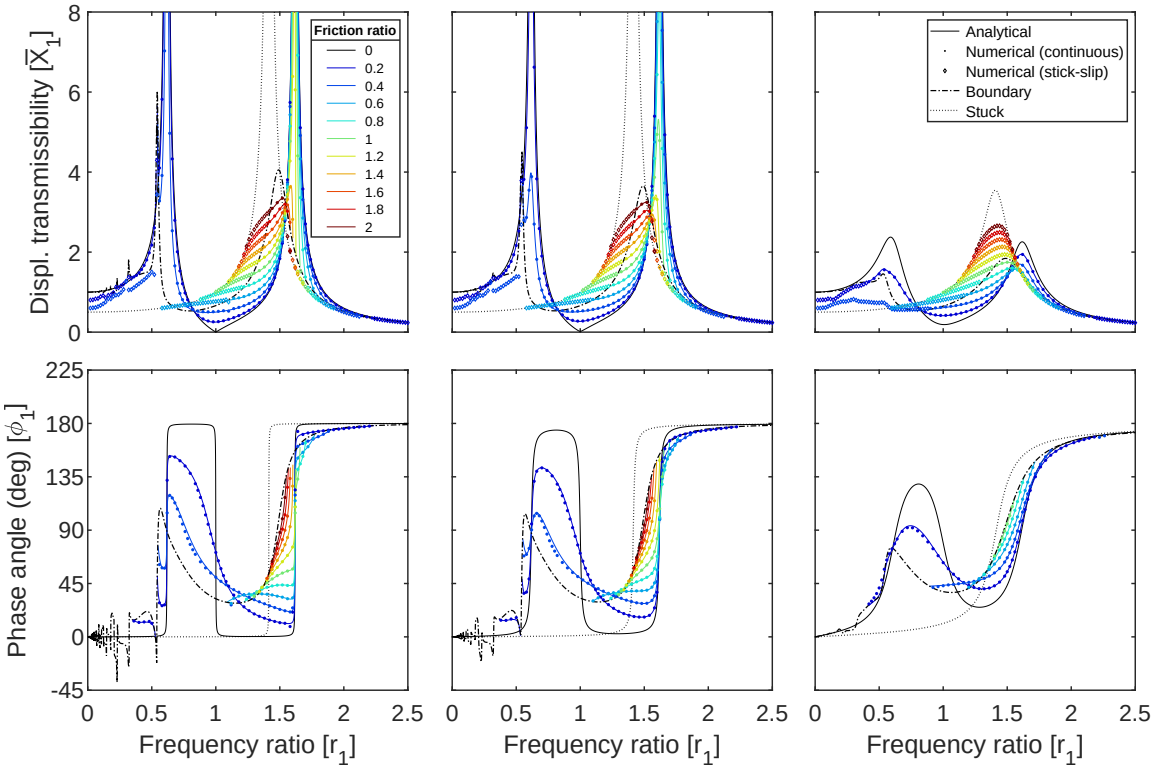

(a) $\zeta_i = 0.001/r_{n,i}$ **(b)** $\zeta_i = 0.01/r_{n,i}$ **(c)** $\zeta_i = 0.1/r_{n,i}$

Figure 7.5: Displacement transmissibility and phase angle of the lower mass of a 2DOF system with a Coulomb friction contact on m_2 and a harmonic excitation on m_1 for $\gamma = \kappa = \mu = 1$ and varying frequency, friction and modal damping ratios: analytical vs numerical.

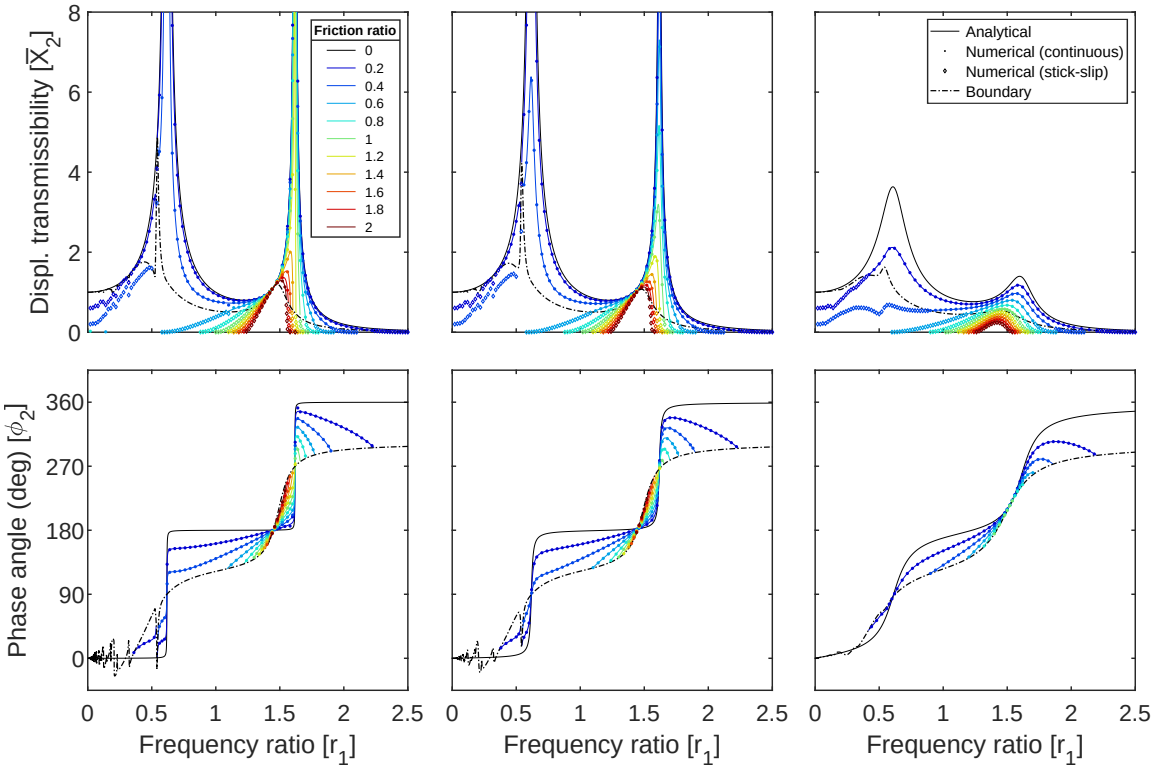

(a) $\zeta_i = 0.001/r_{n,i}$ **(b)** $\zeta_i = 0.01/r_{n,i}$ **(c)** $\zeta_i = 0.1/r_{n,i}$

Figure 7.6: Displacement transmissibility and phase angle of the upper mass of a 2DOF system with a Coulomb friction contact on m_2 and a harmonic excitation on m_1 for $\gamma = \kappa = \mu = 1$ and varying frequency, friction and modal damping ratios: analytical vs numerical.

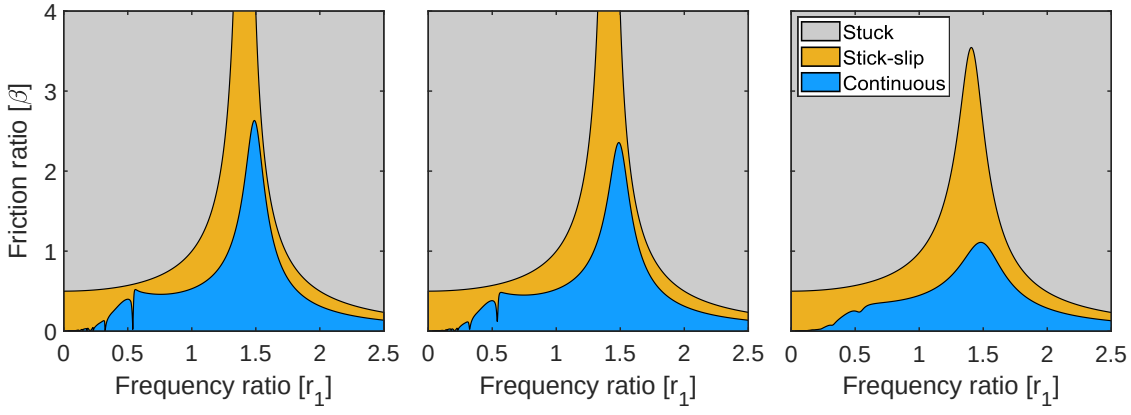

(a) $\zeta_i = 0.001/r_{n,i}$ **(b)** $\zeta_i = 0.01$ **(c)** $\zeta_i = 0.1$

Figure 7.7: Motion regimes of a 2DOF system with a Coulomb friction contact on m_2 and a harmonic excitation on m_1 in the parameter space r_1-β for $\gamma = \kappa = \mu = 1$ and varying modal damping ratio.

7.4.1 Resonant behaviour

As discussed in Section 6.2.1, in the absence of modal damping, Coulomb friction cannot provide finite resonant peaks in discrete mechanical systems unless stick-slip or permanent sticking occur at resonance. However, the resonant behaviour of these systems is deeply affected by the presence of modal damping. In fact, in Figs.7.3, 7.5 and 7.6, it can be observed that systems with combined modal and Coulomb damping present finite resonances in continuous motion regime. A procedure for determining an approximated expression for the amplitude of these finite resonant peaks is presented in what follows.

According to Craig [24], the values of the modal damping ratios typically lie in the range $0 \leq \zeta_i \leq 0.1$; therefore, it can generally be assumed that $\zeta_i \ll 1$. Based on this consideration, it can also be assumed, at this stage, that resonant peaks occur in correspondence of the undamped natural frequencies of the system. Under these assumptions, an approximated expression can be derived for the amplitude of the ith resonant peak of the response of the generic mass m_k by evaluating Eq.(7.33) for $R_i \to 1$ and $\zeta_i \ll 1$. As a first step, let us determine how the complex response function V_{dk} and the damping functions G_k and U_{dk} are affected by these assumptions.

- Regarding the complex response function, in proximity of the ith resonant peak, the ith term of the summation in Eq.(7.15) becomes significantly larger than the other $N-1$ terms. Therefore, it can be written that:

$$V_{dk} \cong \lim_{R_i \to 1} \psi_{ki}\psi_{li}R_i^2 v_{di} = -i\frac{\psi_{ki}\psi_{li}}{2\zeta_i} \tag{7.53}$$

  where the expression of v_{di} is provided in Eq.(7.8). When the ith resonance occurs, the amplitude of the complex response function is therefore given by:

$$|V_{dk}| \cong \frac{|\psi_{ki}\psi_{li}|}{2\zeta_i} \tag{7.54}$$

  while the phase of this function will be equal to $-\pi/2$ or $\pi/2$ depending on the sign of the product $\psi_{ki}\psi_{li}$. Thus, it can be demonstrated that, in Eq.(7.33):

$$\begin{cases} \cos(\angle V_{dk} - \angle V_{dj}) = \mathrm{sgn}(\psi_{ki}\psi_{ji}) & \text{(7.55a)} \\ \sin(\angle V_{dk} - \angle V_{dj}) = 0 & \text{(7.55b)} \end{cases}$$

- Let us now evaluate the second damping function of the ith vibrating mode for $R_i \to 1$. If $\zeta_i \ll 1$, it is obtained from Eq.(7.12) that:

$$g_i = \frac{\sinh(\zeta_i \pi)}{\cosh(\zeta_i \pi) - 1} \tag{7.56}$$

  It can be demonstrated that the above expression tends to infinity when $\zeta_i \to 0$. Therefore, since $\zeta_i \ll 1$, the ith term of the summation in Eq.(7.17) will also grow much larger than the other terms when $R_i \to 1$. Thus, in proximity of the ith resonance, the second damping function will assume the value:

$$G_k \cong \lim_{R_i \to 1} \psi_{ki}\psi_{ji} R_i^2 g_i = \psi_{ki}\psi_{ji} \frac{\sinh(\zeta_i \pi)}{\cosh(\zeta_i \pi) - 1} \tag{7.57}$$

- Finally, the first damping function U_{dk} does not present any peculiar behaviours at resonance. In fact, although it can be shown from Eq.(7.11) that $u_{di} = 0$ for $R_i \to 1$, the other $N - 1$ terms of the summation from Eq.(7.16) will generally have different values. Nonetheless, since the response functions V_{dk} tend to assume large amplitudes in proximity of the resonances, it will be assumed in what follows that $\sqrt{|V_{dj}|^2 - (\beta U_{dj})^2} \cong |V_{dj}|$.

Considering this assumption and substituting Eq.(7.55) into Eq.(7.33), it is obtained that, for $r_1 = r_{n,i}$:

$$\overline{X}_k \cong \left[|V_{dk}^2 + \beta^2 (G_k^2 + U_{dk}^2) - \beta (2|V_{dk}||G_k| - |U_{dj}||U_{dk}|) \right]^{\frac{1}{2}} \tag{7.58}$$

Since at resonance, as previously stated, the functions $|V_{dk}|$ and G_k becomes much larger than the damping functions U_{dk}, the above equation can be approximated as:

$$\overline{X}_k \cong \left| V_{dk} - \beta |G_k| \right| \tag{7.59}$$

Finally, substituting Eqs.(7.54) and (7.57) into Eq.(7.59), it is possible to write:

$$\overline{X}_k \cong \frac{|\psi_{ki}\psi_{li}|}{2\zeta_i} - |\psi_{ki}\psi_{ji}| \frac{\sinh(\zeta_i \pi)}{\cosh(\zeta_i \pi) - 1} \beta \tag{7.60}$$

Eq.(7.60) can be used for estimating the response amplitude of each mass of the system in correspondence of each resonant peak of the system. The most important

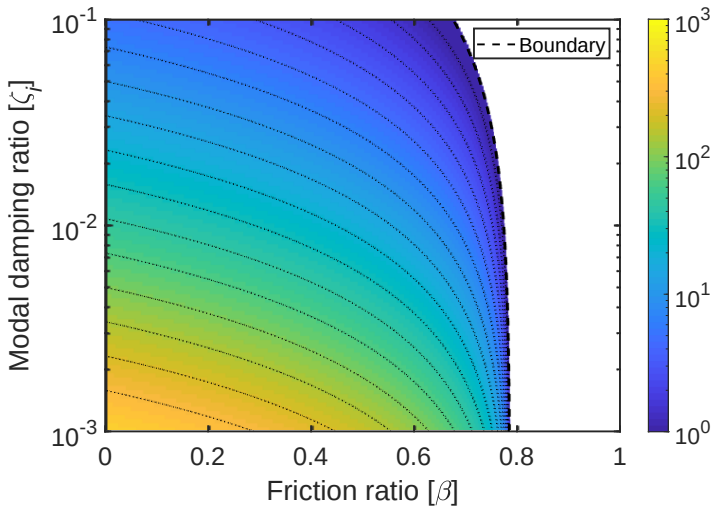

Figure 7.8: Non-dimensional amplitude of the resonant peak of a SDOF system in continuous non-sticking regime for varying friction and modal damping ratio.

implication of this expression is that, in the presence of modal damping, Coulomb friction also reduces the resonant amplitudes without introducing stick-slip in the response. Furthermore, it can be observed that the amplitude of these peaks decreases linearly with the friction ratio. To the best of the author's knowledge, this latter phenomenon has never been discussed in previous publications. However, it is worthwhile mentioning that Den Hartog investigated experimentally the response amplitude at resonance for a SDOF system with Coulomb friction and a small amount of viscous damping; in his results, the resonant amplitude shows an approximatively linear reduction with the friction ratio [21].

The dependence of the resonant peak amplitude on ζ and β is shown in Fig.7.8 for the SDOF case; similar patterns have also been observed for the resonances of more complex systems. For a SDOF system, Eq.(7.60) reduces to:

$$\overline{X} = \frac{1}{2\zeta} - \frac{\sinh(\zeta\pi)}{\cosh(\zeta\pi) - 1}\beta \tag{7.61}$$

In Fig.7.8, a boundary has also been represent to delimit the domain of validity of this formula, which is only valid in continuous motion regime. Based on the above observations on the response and damping functions, an approximated expression of this boundary can be determined by evaluating Eq.(7.49) for $R_i \to 1$. After

some algebraic manipulations, it is obtained that:

$$\beta_{n,i} \cong \left|\frac{\psi_{li}}{\psi_{ji}}\right| \frac{\cosh(\zeta_i \pi) - 1}{2\zeta_i \sinh(\zeta_i \pi)} \tag{7.62}$$

It can be verified that the above expression reduces to Eq.(6.2) when $\zeta_i \to 0$. In the SDOF case, the boundary friction ratio at resonance is equal to $\pi/4$ in the absence of modal damping. Fig.7.8 shows how the value of $\beta_{n,i}$ remains approximatively constant for $\zeta \leq 0.01$ and only decreases significantly for larger values of the modal damping ratio. Therefore, while it is important to take modal damping into account when evaluating the amplitude of the resonant peaks, Eq.(6.2) can be considered a good estimation of the minimum value of the friction ratio for which stick-slip occurs at resonance in lightly-damped systems.

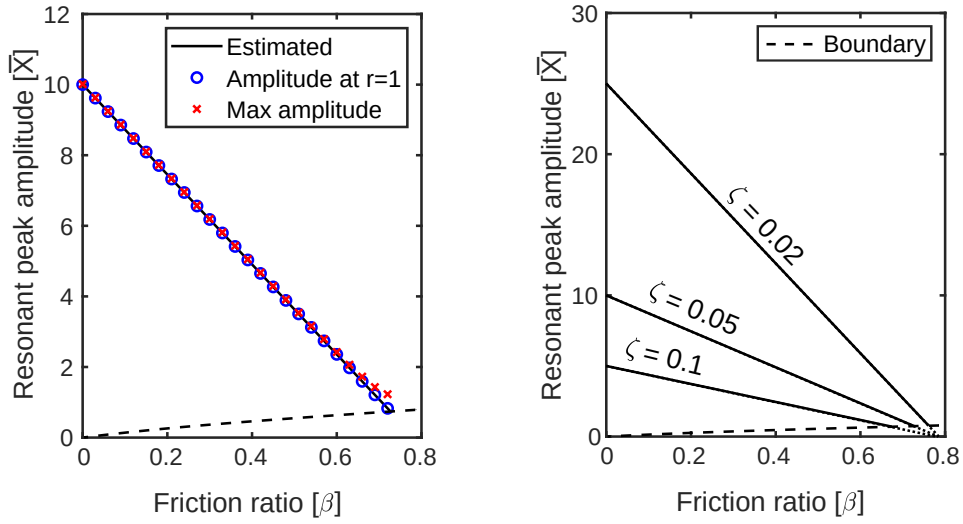

Figure 7.9: Non-dimensional amplitude of the resonant peak of a SDOF system in continuous non-sticking regime for varying friction ratio: comparison between the estimated and the actual amplitudes (**a**) and estimated value for varying modal damping ratio (**b**).

In Fig.7.9, the estimation of the resonant amplitude provided by Eq.(7.60) is compared to the amplitude of the response at $r = 1$ and to the actual resonant amplitude evaluated from Eq.(7.33), showing an excellent agreement with both quantities. It can also be observed that, in proximity of the boundary between continuous and stick-slip regimes, the actual value of the resonant amplitude becomes

slightly larger than the estimated one. In Figs.7.3, 7.5 and 7.6, it can be seen that, for large amounts of the friction ratio, the resonant peak is slightly shifted to the left and, therefore, it can be underestimated by Eq.(7.60). Nonetheless, the actual and the estimated values of the resonant peak have been compared for several MDOF systems and for different amounts of modal damping; their agreement was very good in all the cases investigated. The linear dependency of $\overline{X}_k$ on the friction ratio is also shown in Fig.7.9b for different values of the damping ratio. It can be observed that the slope of the curves decreases with ζ; however, the rate of variation of this slope also becomes smaller as the damping ratio is increased.

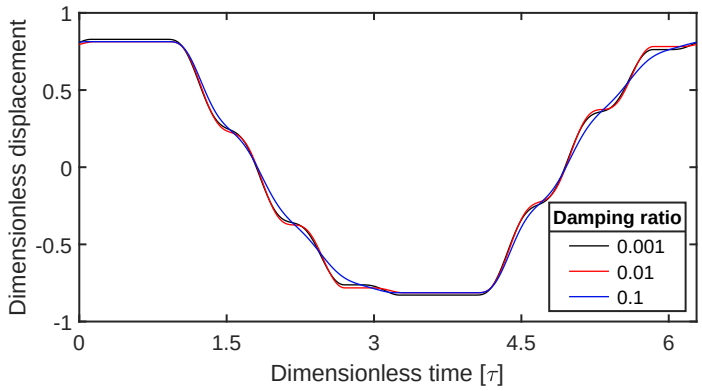

Figure 7.10: Steady-state stick-slip response of a SDOF system with combined modal and Coulomb damping for $r = 0.1$, $\beta = 0.2$ and $\mu = 1$.

7.4.2 Low- and high-frequency behaviours

As can be observed from Figs.7.3-7.7, the dynamic behaviour of SDOF and MDOF systems at low and high frequency ratios is not significantly affected by the presence of modal damping.

Regarding the low-frequency behaviour, it can be easily verified that the boundary expressed in Eq.(7.49) tends to zero for $r_1 \to 0$; therefore, the quasi-static behaviour of systems with combined modal and Coulomb damping will also be characterised by the occurrence of stick-slip in the response. However, as shown in Fig.7.10, modal damping can have a smoothing effect on the quasi-static response of these systems; this is particularly evident from the curve corresponding to $\zeta = 0.1$. The patterns displayed in the transmissibility curves in Figs.7.3, 7.5

and 7.6 at low frequencies do not generally show significant differences for varying damping ratios. This implies that, in most cases, modal damping can reduce the number of stops but does not change significantly the amplitude of the stick-slip responses, in agreement with Fig.7.10.

The behaviour of these systems at high frequency ratios is also similar to that observed in the absence of modal damping in Section 6.2.3. In the above figures, it can be clearly observed that the transmissibilities always tends to zero when $r_1 \to \infty$, as expected. Therefore, also in this case, the discussion focuses on determining if stick-slip or permanent sticking can occur in these systems at high frequencies. Evaluating the limit value β_∞ of the boundary between continuous and stick-slip regimes from Eq.(7.49)) for $R_i \to \infty$, it can be verified that the response and the first damping functions tend to the same values as in the undamped case, while $H_j \to 0$. Therefore, the resulting expression of β_∞ will be same expressed in Eq.(6.8), meaning that only systems with the harmonic and the friction forces applied to the same mass can display a continuous response at high frequencies, independently of the presence of modal damping. This can also be observed from Fig.7.4, where all the boundaries between continuous and stick-slip regimes displayed for varying ζ tend to the asymptotic value $\beta_\infty = 0.537$. Conversely, in Fig.7.7 these boundaries tend to zero, meaning that stick-slip is always expected for high frequency ratios.

7.4.3 Invariant points and stuck configurations

In Fig.7.5, it is possible to observe how the inversion process of the transmissibility curves and the onset of the resonant peaks of the stuck configuration are not heavily affected by the presence of modal damping. From a mathematical point of view, it can be observed that invariant points are not admitted by Eq.(7.33) unless $\zeta_i = 0$. However, it can be observed that the inversions of the transmissibility curves still occur in a small region located in proximity of the invariant points determined in the absence of modal damping. Therefore, the points determined from Eq.(6.10) can also be considered, with good approximation, when modal damping is taken into account in the mechanical model.

Permanent sticking between the mass and the wall in contact can also occur in mechanical systems with combined modal and Coulomb damping; stuck configurations and the corresponding new resonant peaks are still observed in MDOF systems with $j \neq l$, as can be seen from Fig.7.5. Although the procedure for evaluating the response of system in stuck conditions and the boundary between the sliding and the permanent sticking regimes is the same described in Section 6.2.5, it must be considered that modal damping will also be present in the stuck configurations.

Let us consider, for instance, the case $j > l$. As specified in Section 6.2.5, when permanent sticking occurs, the masses $m_1, ..., m_{j-1}$ will keep oscillating. Therefore, the response of the system can be determined from the linear equation:

$$\overline{\mathbf{M}}^* \bar{\mathbf{x}}^{*\prime\prime} + \overline{\mathbf{C}}^* \bar{\mathbf{x}}^{*\prime} + \overline{\mathbf{K}}^* \bar{\mathbf{x}}^* = \bar{\mathbf{p}}^*$$

with a standard modal superposition procedure. In the above equation, the stuck mass, damping and stiffness matrices are determined considering the first $j-1$ rows and columns of the matrices $\overline{\mathbf{M}}$, $\overline{\mathbf{C}}$ and $\overline{\mathbf{K}}$. If needed, the modal damping ratios $\zeta_1^*, ..., \zeta_{j-1}^*$ of the stuck configuration can be determined by using Eq.(7.4), after that the stuck natural frequencies and mode-shapes have been determined from Eq.(5.9), referring to the matrices $\overline{\mathbf{M}}^*$ and $\overline{\mathbf{K}}^*$. Finally, the boundary $\beta_{\lim}^*$ can be evaluated from Eq.(6.11a). The same procedure can be used for the case $j < l$, taking into account the masses $m_{j+1}, ..., m_N$, while the system will be fully stuck if $j = l$. From Figs.7.5 and 7.7, it can be observed that modal damping only affects $\overline{X}_k^*$ and $\beta_{\lim}^*$ at resonance, while the starting values at $r_1 = 0$ and the asymptotic behaviour at high frequencies remain unchanged.

7.5 Summary and concluding remarks

In this chapter, an analytical solution has been derived for the continuous response of a MDOF system with combined modal and Coulomb damping under harmonic excitation. In particular, closed-form expressions have been obtained for the steady-state time response, the displacement transmissibility and the phase angle of all

the masses of the system. Furthermore, exact and approximated formulations have been provided for the boundary between continuous and stick-slip regimes.

The results obtained from these analytical solutions have been validated with a numerical approach, taking into account: (i) a 5DOF system with excitation and contact on m_1; (ii) a 5DOF system excited on m_1 and with a contact on m_3; (iii) a SDOF system; (iv) a 2DOF system excited on m_1 and with a contact on m_2. The cases (i) and (ii) have shown that an excellent agreement can be obtained between the analytical and the numerical time responses even when several DOFs are involved. For the systems (iii) and (iv), a very good agreement has been observed for the transmissibilities and the phase angles.

The features and the motion regimes exhibited by the dynamic response of these systems have been investigated, including the resonant, low- and high-frequency behaviours, the presence of invariant points and inversions of the transmissibility curves and the stuck configurations determined by the occurrence of permanent sticking. This investigation has revealed that, while most of the response features are not significantly altered by the presence of modal damping, the resonant behaviour is very different from that observed in SDOF and MDOF systems with Coulomb damping only. The most important novel finding is that, when modal damping is accounted for in the mechanical models, the resonant peaks are also finite in continuous motion regime and the amplitude of such peaks decreases linearly with the intensity of the friction force. This implies that Coulomb friction can be particularly effective for avoiding large resonances in structures with non-negligible levels of damping.

Overall, the present investigation has shown that the SDOF and MDOF models introduced in the previous chapters can provide an acceptable description of lightly-damped structures where a Coulomb friction contact is the predominant source of damping, consistently with the results obtained from the experimental campaigns presented in Chapters 4 and 6. Structures with higher levels of damping will still present most of the behaviours described by mechanical models with Coulomb damping only. However, modal damping is needed for an accurate description of the

resonant behaviour of these structures. Finally, the results presented this chapter can be extended to systems with a contact between two oscillating components using the substitutions introduced in Section 5.5.

As for the future, your task is not to foresee it, but to enable it.

— Antoine de Saint Exupery

8 Conclusions and future work

Contents

8.1 Main conclusions

This thesis was devoted to the improvement of the current understanding of how the damping introduced by dry friction in mechanical vibrating systems affects their dynamic behaviour. The dynamic response of different lumped mechanical models including a Coulomb friction contact and subjected to harmonic excitation was investigated analytically, numerically and experimentally. In particular, the behaviour of SDOF and MDOF systems with a contact between (1) a mass and a fixed wall, (2) a mass and an oscillating wall and (3) two different masses was studied, aiming to establish the effect of the different parameters of the problem, of the presence of multiple DOFs and of the different contact configurations on the features and the motion regimes observed in the response of these systems.

The main outcomes of the research work presented in this thesis can be summarised as follows:

1. Analytical solutions were derived for the continuous steady-state response of these systems and closed-form expressions were provided for their response amplitude and phase. These solutions can be applied to the analysis of early design stages of engineering systems where SDOF and MDOF models with a single contact are of interest. Moreover, they enabled the development of a general understanding of the effect of Coulomb friction on response features such as the resonant, the low- and the high-frequency behaviours, the presence of invariant points and inversions of the transmissibility curves.

2. Closed-form formulations were also obtained for the boundaries (i) between continuous and stick-slip motion regimes and (ii) between the sliding and the permanent sticking regimes. These boundaries have been represented in a two-dimensional parameter space as functions of the non-dimensional exciting frequency and friction force. These 2-D maps offer a handy and cost-effective tool for predicting the motion regimes during the early stages of the design process. In fact, thanks to the low computational cost required for generating those maps, different mechanical models and contact configurations can quickly be explored by the designer and the right set of parameters can be chosen, for instance, to prevent stick-slip or permanent sticking in operation.

3. A shear frame setup with a brass-to-steel contact has been developed for investigating experimentally the dynamic response of SDOF and 2DOF systems with a Coulomb friction contact between one of the masses and either a fixed or oscillating wall. The proposed experimental procedure includes a preliminary estimation of the frequency and friction ratio parameters and a main forced vibration test, which is run at different pairs of these values for reproducing the transmissibility and phase angle curves of these systems. Measures were also taken to limit non-Coulomb phenomena such as wear and debris formation during and between the tests.

4. Closed-form solutions were also derived for the continuous steady-state response of systems with combined modal and Coulomb damping, aiming

to evaluate how the damping effects due to Coulomb friction are altered by non-negligible damping levels in a structure. The analytical expressions obtained for the response amplitude and phase, as well as for the boundaries of motion regimes, allowed the investigation of the response features of these systems.

The analytical solutions derived in this thesis, together with the numerical results obtained with ad-hoc time integration approaches, allowed to establish how the features and the motion regimes of the dynamic response of a Coulomb damped system evolve in the presence of multiple DOFs and depending on the contact configuration, i.e. if the contact occurs between two oscillating parts rather than between a mass and a fixed wall. The key results are detailed in what follows.

The dynamic analysis of MDOF systems with a Coulomb friction contact was presented in Chapters 5 and 6. It was concluded that the main factor affecting the dynamic behaviour of these systems is the location of the excitation and of the friction sources in the system. In particular:

- MDOF systems behave similarly to SDOF systems when the harmonic load and the friction contact are applied to the same mass. In fact, in this case, all the masses oscillate nearly in phase or phase-opposition with the mass in contact and, therefore, exhibit similar resonant, low- and high-frequency behaviours. Inversions are generally not observed across the transmissibility curves for varying friction force, meaning that the response amplitude of all the masses is decreased by friction. Finally, when the amplitude of the harmonic load is not larger than the static friction force, the whole system becomes permanently stuck.

- On the contrary, MDOF systems where the harmonic and the friction forces are applied to different masses show a much richer dynamic behaviour. Nonetheless, a few general conclusions can also be drawn for these system. In fact, it can be observed that those masses which are only excited through the mass in contact still present similar behaviours to those described above.

However, the masses located between the exciting and the friction sources, will also be excited when the mass in contact is stuck. This leads to the presence of inversions of the transmissibility curves, which occur across invariant points, and to the onset of further resonant peaks corresponding to the stuck configuration of the system, i.e., that subsystem which is still excited in permanent sticking regime.

As described in Chapter 3 for the SDOF case and in Chapters 5 and 6 for the MDOF case, the dynamic behaviour of Coulomb damped systems is significantly affected by the motion of the parts in contact. The investigation of SDOF systems subjected to joined base-wall harmonic excitation revealed two main differences with respect to fixed-wall case: (i) in terms of motion regimes, permanent sticking in the contact easily occurs at low frequency ratios, while a sliding relative motion can be observed at higher frequencies even in the presence of large amounts of friction; (ii) at high frequency ratios, Coulomb friction magnifies the displacement transmissibility of the mass in contact. In particular, an inversion of the continuous transmissibility curves is observed when the driving frequency is about 1.5 times the natural frequency of the system. This behaviour recalls that displayed by base-excited viscous damped systems. Similar patterns are also observed in the boundaries of the motion regimes and in the response amplitudes of MDOF systems under joined base-wall motion. However, the behaviour of these systems, as well as that of systems with a contact between two masses, is also affected by the location of the harmonic and friction forces, similarly to the fixed-wall case.

The dynamic behaviour of systems with combined modal and Coulomb damping was explored in Chapter 7, leading to two major observations:

- Most response features are not significantly affected by the damping levels of a vibrating structure. In fact, modal damping does not change either the starting points of the transmissibility curves or the asymptotic behaviours displayed at high frequency ratios. The effects on the invariant points are also mostly negligible. Therefore, it can be concluded that modal damping can be neglected when these behaviours are investigated.

- Modal damping must be necessarily kept into account when investigating the resonant behaviour of a vibrating system. In fact, the resonant peaks of systems with Coulomb damping only are solely finite when stick-slip or permanent sticking occur in the contact; this does not allow a proper investigation of the real effect of dry friction on the resonant amplitudes. It was shown that, when modal damping is accounted for in the mechanical model, these amplitudes decrease linearly with the friction force generated in the contact. Therefore, not only Coulomb friction can reduce the resonant peaks in the response of real structures, but this effect is also enhanced by the general damping levels of such structures.

The experimental investigations carried out on the single-storey and 2-storey configurations of the shear frame setup were presented in Chapters 4 and 6 respectively. For most configurations and parameters, a very good agreement was observed between the experimental and the analytical transmissibilities and phase angles in continuous motion regimes and between the experimental and numerical values for stick-slip responses. More irregular behaviours were only observed when larger levels of friction were introduced in the system; in this case, permanent sticking can suddenly occur in the contact. Nonetheless, these experiments showed that the Coulomb friction model can be used, in most conditions, for describing the dynamic behaviour of structures with a metal-to-metal contact. In general, it also emerged that the phase angle evaluated from the FFTs of the excitation and the response could be a particularly suitable metric for detecting and measuring the friction force from the response of the structure.

Overall, the work presented in this thesis advanced the fundamental knowledge of the dynamic behaviour of mechanical systems with Coulomb friction. While most of this knowledge was previously limited to the case of SDOF systems with a fixed wall, a more complete understanding, based on analytical, numerical and experimental results, was developed for a much wider range of mechanical models, including those with multiple DOFs and/or with a contact between two oscillating components. The presented results give information relevant to the design and

the analysis of engineering structures and, in particular, can support the early stages of the mechanical design, enhancing the exploration of innovative and more efficient solutions. Possible directions for the future research in the field are proposed in the next section.

8.2 Suggestions for further works

The research findings presented in this thesis offer an interesting insight into the behaviour of mechanical systems with friction damping. Nonetheless, these results have been obtained within a specific set of assumptions, regarding the choice of the mechanical and of the friction models, the nature of the dynamic loading and the presence of a single friction contact. To address the more complex behaviours shown by engineering structures with frictional interfaces, future research on friction damped systems should aim at overcoming these assumptions, as suggested in what follows.

- **MDOF systems with multiple friction contacts.** Structures such as bladed-disks and civil buildings typically include several friction joints and dampers. Even during the earliest stages, the design process should be informed of the dynamic behaviour introduced by the presence of multiple interfaces. Therefore, it would be essential to explore the response features, the motion regimes and the stability properties of MDOF systems with more than one contact.

- **Continuous multi-modal systems with friction damping.** A further step for understanding the dynamic behaviour of more complex structures is the investigation of friction damping effects on continuous systems. From a theoretical point of view, it would be interesting to extend the results presented in this thesis to mechanical models such as beams and plates with a friction contact. Moreover, the experimental investigation of a built-up system including, for instance, a beam connected to a friction damper would be

particularly relevant in view of finding suitable response metrics for detecting and monitoring friction in real structures.

- **Different input waveforms.** Real structures are often subjected to complex dynamic loadings, different from the monoharmonic excitation considered in this thesis. For instance, rotating machines such as bladed-disks typically experience multi-harmonic forces, while in civil structures the excitation provided by earthquakes and wind is usually modelled as random. Because of nonlinearity, the dynamic response under such loading conditions can differ significantly from that observed in the harmonic case and, therefore, further investigation is needed.

- **More advanced friction models.** Another aspect requiring further investigation is the presence of several friction related phenomena (wear, debris formation, hysteresis and many others) which are not accounted for by Coulomb model. Despite its simplicity, the experimental setup proposed in this thesis could be used for further investigating these phenomena and validating more advanced friction models. This could be done, for instance, by testing different materials or by observing the response of the structure during longer time windows. The experimental procedure could also be improved by developing new techniques for investigating parameters such the static friction coefficient, which are not available in the current approach.

A

Analytical background of the parameter estimation for base-excited 2DOF systems

In Chapter 6, the frequency, mass and stiffness ratios of the 2DOF model of the two-storey frame setup have been determined, in the absence of friction, from the experimental transmissibilities by implementing an optimisation process. In this process, the cost function defined in Eq.(6.16) is minimised referring to variables ω_0, ω_1 and ω_2, i.e, to the antiresonant frequency for the response of the lower mass and to the natural frequencies of the system. Therefore, in this appendix, it is shown how the displacement transmissibility $\overline{X}_1$, required for evaluating the cost function J, and the parameters r_1, κ and γ can be expressed as functions of ω_0, ω_1 and ω_2.

First of all, the governing equations of an undamped 2DOF system under harmonic base excitation can be written as:

$$\begin{cases} m_1\ddot{x}_1 + (k_1+k_2)x_1 - k_2x_2 = k_1Y\cos(\omega t) & \text{(A.1a)} \\ m_2\ddot{x}_2 - k_2x_1 + k_2x_2 = 0 & \text{(A.1b)} \end{cases}$$

The expression of the natural frequencies ω_1 and ω_2 can be determined from the stiffness and mass matrices of the system by using Eq.(5.9), yielding:

$$\omega_{1,2}^2 = \frac{(k_1+k_2)m_2 + k_2m_1}{2m_1m_2} \pm \sqrt{\left[\frac{(k_1+k_2)m_2 + k_2m_1}{2m_1m_2}\right]^2 - \frac{k_1k_2}{m_1m_2}} \qquad \text{(A.2)}$$

The antiresonant frequency ω_0 can be evaluated by imposing that the displacement transmissibility of the lower mass is $\overline{X}_1 = 0$. Such displacement transmissibility can

be determined from Eq.(A.1) by assuming that $x_1 = X_1\cos(\omega t)$ and $x_2 = X_2\cos(\omega t)$. After some algebraic manipulations, it is obtained that:

$$\overline{X}_1 = \frac{X_1}{Y} = \frac{k_1(k_2 - \omega^2 m_2)}{(k_1 + k_2 - \omega^2 m_1)(k_2 - \omega^2 m_2) - k_2^2} \tag{A.3}$$

Thus, $\overline{X}_1$ will be equal to zero if:

$$k_1(k_2 - \omega^2 m_2) = 0 \tag{A.4}$$

hence:

$$\omega_0 = \sqrt{\frac{k_2}{m_2}} \tag{A.5}$$

It is now possible to derive an expression of r_1 as a function of ω_0, ω_1 and ω_2. From Eq.(A.2), it can be found that:

$$\frac{\omega_1^2 + \omega_2^2}{2} = \frac{(k_1 + k_2)m_2 + k_2 m_1}{2m_1 m_2} \tag{A.6}$$

and:

$$\frac{\omega_1^2 - \omega_2^2}{2} = \sqrt{\left[\frac{(k_1 + k_2)m_2 + k_2 m_1}{2m_1 m_2}\right]^2 - \frac{k_1 k_2}{m_1 m_2}} \tag{A.7}$$

Substituting Eqs.(A.5) and (A.6) into Eq.(A.7), it is obtained that:

$$\left(\frac{\omega_1^2 - \omega_2^2}{2}\right)^2 = \left(\frac{\omega_1^2 + \omega_2^2}{2}\right)^2 - \frac{k_1}{m_1}\omega_0 \tag{A.8}$$

from which:

$$\frac{k_1}{m_1} = \left(\frac{\omega_1\omega_2}{\omega_0}\right)^2 \tag{A.9}$$

Finally, the frequency ratio can be expressed as:

$$r_1 = \omega\sqrt{\frac{m_1}{k_1}} = \left(\frac{\omega_0}{\omega_1\omega_2}\right)\omega \tag{A.10}$$

as reported in Eq.(6.17). Introducing Eqs.(A.2), (A.5) and (A.10) into Eq.(A.3), it is also possible to obtain the expression of the displacement transmissibility $\overline{X}_1$ provided in Eq.(6.15):

$$\overline{X}_1 = \left(\frac{\omega_1\omega_2}{\omega_0}\right)\frac{\omega_0^2 - \omega^2}{(\omega_1^2 - \omega^2)(\omega_2^2 - \omega^2)} \tag{A.11}$$

As mentioned in Chapter 6, a further parameter is needed to express the mass and the stiffness ratios as functions of ω_0, ω_1 and ω_2, i.e., the antiresonant frequency ω_{z0} of the relative displacement between the lower mass and the excited base:

$$z = x_1 - Y\cos(\omega t) \tag{A.12}$$

In order to determine the expression of this further antiresonant frequency, let us introduce z in the governing equations from Eq.(A.1):

$$\begin{cases} m_1\ddot{z} + (k_1+k_2)z - k_2x_2 = (\omega^2 m_1 - k_2)Y\cos(\omega t) & \text{(A.13a)} \\ m_2\ddot{x}_2 - k_2 z + k_2 x_2 = k_2 Y\cos(\omega t) & \text{(A.13b)} \end{cases}$$

Assuming that $z = Z\cos(\omega_t)$, it is possible to determine the non-dimensional amplitude of the relative motion as:

$$\overline{Z} = \frac{Z}{Y} = \frac{(\omega^2 m_1 - k_2)(k_2 - \omega^2 m_2) + k_2^2}{(k_1 + k_2 - \omega^2 m_1)(k_2 - \omega^2 m_2) - k_2^2} \tag{A.14}$$

Therefore, the antiresonant frequency can be determined as that value of ω such that $\overline{Z} = 0$, i.e.:

$$(\omega^2 m_1 - k_2)(k_2 - \omega^2 m_2) + k_2^2 = 0 \tag{A.15}$$

hence:

$$\omega_{z0} = \sqrt{\frac{k_2(m_1+m_2)}{m_1 m_2}} \tag{A.16}$$

as specified in Eq.(6.20). From Eq.(A.16), it can be obtained that:

$$\omega_{z0}^2 = \frac{k_2(1+\gamma)}{m_2} = \omega_0^2(1+\gamma) \tag{A.17}$$

and, therefore, the mass ratio can be expressed as:

$$\gamma = \left(\frac{\omega_{z0}}{\omega_0}\right)^2 - 1 \tag{A.18}$$

Finally, from Eq.(A.5), it can be written that:

$$\omega_0^2 = \frac{k_2}{k_1}\frac{k_1}{m_1}\frac{m_1}{m_2} = \frac{\kappa}{\gamma}\left(\frac{\omega_1\omega_2}{\omega_0}\right)^2 \tag{A.19}$$

from which the stiffness ratio is obtained as:

$$\kappa = \left(\frac{\omega_0}{\omega_1\omega_2}\right)^2 \gamma \tag{A.20}$$

The final expressions of γ and κ coincide with those proposed in Eqs.(6.18) and (6.19).

B

Modal solution for MDOF systems with combined modal and Coulomb damping

This appendix presents a step-by-step solution of the modal problem introduced in Chapter 7. The governing equation of the i-th modal coordinate of a MDOF system with combined modal and Coulomb damping has been written in Eq.(7.6) as:

$$\eta_i'' + 2\zeta_i\Omega_i\eta_i' + \Omega_i^2\eta_i = \psi_{ji}\beta + \psi_{li}\cos(\tau + \phi_j) \tag{B.1}$$

This equation holds in the non-dimensional time interval $[0, \pi]$, included between a maximum and the subsequent minimum of the continuous steady-state response of the mass in contact m_j. The general solution of Eq.(B.1), also reported in Eq.(7.7), is:

$$\eta_i = e^{-\frac{\zeta_i\tau}{R_i}}\left[A_i\cos\left(\frac{\tau\sqrt{1-\zeta_i^2}}{R_i}\right) + B_i\sin\left(\frac{\tau\sqrt{1-\zeta_i^2}}{R_i}\right)\right] + \psi_{ji}R_i^2\beta + \psi_{li}R_i^2 v_{di}\cos(\tau + \phi_j) \tag{B.2}$$

In the above solution, the integration constants A_i and B_i and the phase angle ϕ_j between the excitation and the displacement $\bar{x}_j$ of the mass in contact are unknown. As in the procedure described in Chapter 5, these values can be determined by imposing the following initial and the final conditions on η_i and on its derivative

η_i' in the interval $[0, \pi]$:

$$\begin{cases} \eta_i(0) = \eta_{i0} & \text{(B.3a)} \\ \eta_i'(0) = \eta_{i0}' & \text{(B.3b)} \end{cases}$$

and:

$$\begin{cases} \eta_i(\pi) = -\eta_{i0} & \text{(B.4a)} \\ \eta_i'(\pi) = -\eta_{i0}' & \text{(B.4b)} \end{cases}$$

where the assumption of symmetry of the steady-state response has been taken into account. Substituting Eq.(B.3) into Eq.(B.2) and rearranging the terms, the expressions of A_i and B_i can be obtained as:

$$\begin{cases} A_i = \eta_{i0} - \psi_{ji} R_i^2 \beta - \psi_{li} R_i^2 v_{di} \cos\phi_j & \text{(B.5a)} \\ B_i = \dfrac{R_i}{\sqrt{1-\zeta_i^2}} (\eta_{i0}' + \psi_{li} R_i^2 v_{di} \sin\phi_j) + \dfrac{\zeta_i A_i}{\sqrt{1-\zeta_i^2}} & \text{(B.5b)} \end{cases}$$

Introducing these expressions, Eq.(B.2) can be rewritten as:

$$\eta_i = d_i \eta_{i0} + R_i q_i \eta_{i0}' + \psi_{ji} R_i^2 (1-d_i)\beta + \psi_{li} R_i^2 v_{di} [(\cos\tau - d_i)\cos\phi_j + (R_i q_i - \sin\tau)\sin\phi] \quad \text{(B.6)}$$

and, therefore, η_i' will be equal to:

$$\eta_i' = -d_i' \eta_{i0} + R_i q_i' \eta_{i0}' - \psi_{ji} R_i^2 d_i' \beta - \psi_{li} R_i^2 v_{di} [(\sin\tau + d_i')\cos\phi_j + (\cos\tau - R_i q_i')\sin\phi] \quad \text{(B.7)}$$

In the above equations, the functions:

$$\begin{cases} d_i(\tau) = e^{-\frac{\zeta_i \tau}{R_i}} \left[\cos\left(\dfrac{\tau\sqrt{1-\zeta_i^2}}{R_i} \right) + \dfrac{\zeta_i}{\sqrt{1-\zeta_i^2}} \sin\left(\dfrac{\tau\sqrt{1-\zeta_i^2}}{R_i} \right) \right] & \text{(B.8a)} \\ q_i(\tau) = \dfrac{1}{\sqrt{1-\zeta_i^2}} e^{-\frac{\zeta_i \tau}{R_i}} \sin\left(\dfrac{\tau\sqrt{1-\zeta_i^2}}{R_i} \right) & \text{(B.8b)} \end{cases}$$

and their derivatives:

$$\begin{cases} d_i'(\tau) = -\dfrac{q_i}{R_i} & \text{(B.9a)} \\ q_i'(\tau) = \dfrac{1}{R_i} e^{-\frac{\zeta_i \tau}{R_i}} \left[\cos\left(\dfrac{\tau\sqrt{1-\zeta_i^2}}{R_i} \right) - \dfrac{\zeta_i}{\sqrt{1-\zeta_i^2}} \sin\left(\dfrac{\tau\sqrt{1-\zeta_i^2}}{R_i} \right) \right] & \text{(B.9b)} \end{cases}$$

have been introduced. Substituting the final conditions from Eq.(B.4) into Eqs.(B.6) and (B.7), a system of algebraic equations is obtained in the form:

$$\begin{cases} \mathcal{A}\cos\phi_j + \mathcal{B}\sin\phi_j + \mathcal{C} = 0 & \text{(B.10a)} \\ \mathcal{P}\cos\phi_j + \mathcal{Q}\sin\phi_j + \mathcal{R} = 0 & \text{(B.10b)} \end{cases}$$

where:

$$\begin{cases} \mathcal{A} = -\psi_{li} R_i^2 v_{di}[1 + d_i(\pi)] & \text{(B.11a)} \\ \mathcal{B} = \psi_{li} R_i^3 v_{di} q_i(\pi) & \text{(B.11b)} \\ \mathcal{C} = [1 + d_i(\pi)]\eta_{i0} + R_i q_i(\pi)\eta'_{i0} + \psi_{ji} R_i^2 [1 - d_i(\pi)]\beta & \text{(B.11c)} \\ \mathcal{P} = \psi_{li} R_i v_{di} q_i(\pi) & \text{(B.11d)} \\ \mathcal{Q} = \psi_{li} R_i^2 v_{di}[1 + R_i q'_i(\pi)] & \text{(B.11e)} \\ \mathcal{R} = -\dfrac{q_i(\pi)}{R_i}\eta_{i0} + [1 + R_i q'_i(\pi)]\eta'_{i0} + \psi_{ji} R_i q_i(\pi)\beta & \text{(B.11f)} \end{cases}$$

The solutions of the system in Eq.(B.10) can be obtained as:

$$\cos\phi_j = \frac{\mathcal{B}\mathcal{R} - \mathcal{C}\mathcal{Q}}{\mathcal{A}\mathcal{Q} - \mathcal{B}\mathcal{P}} \qquad \sin\phi_j = \frac{\mathcal{C}\mathcal{P} - \mathcal{A}\mathcal{R}}{\mathcal{A}\mathcal{Q} - \mathcal{B}\mathcal{P}} \tag{B.12}$$

resulting in the following expressions:

$$\cos\phi_j = \frac{\eta_{i0} + \psi_{ji} R_i^2 g_i \beta}{\psi_{li} R_i^2 v_{di}} \tag{B.13}$$

and:

$$\sin\phi_j = -\frac{\eta'_{i0} + \psi_{ji} R_i^2 u_{di} \beta}{\psi_{li} R_i^2 v_{di}} \tag{B.14}$$

as reported in Eqs.(7.9) and (7.10). The functions u_{di} and g_i introduced in the above expressions have been defined in Eqs.(7.11) and (7.12)

Introducing Eqs.(B.12) and (B.14) into Eq.(B.6), it is also possible to obtain the following expression for i-th the modal coordinate:

$$\begin{aligned} \eta_i = {} & (\eta_{i0} + \psi_{ji} R_i^2 g_i \beta)\cos\tau + (\eta'_{i0} + \psi_{ji} R_i^2 u_{di}\beta)\sin\tau \\ & + \beta\psi_{ji} R_i^2 \left\{ 1 - (1 + g_i) e^{-\frac{\zeta_i \tau}{R_i}} \left[\sin\left(\frac{\tau\sqrt{1-\zeta_i^2}}{R_i} \right) + \frac{\zeta_i}{\sqrt{1-\zeta_i^2}} \cos\left(\frac{\tau\sqrt{1-\zeta_i^2}}{R_i} \right) \right] \right. \\ & \left. - u_{di} R_i \frac{1}{\sqrt{1-\zeta_i^2}} e^{-\frac{\zeta_i \tau}{R_i}} \sin\left(\frac{\tau\sqrt{1-\zeta_i^2}}{R_i} \right) \right\} \end{aligned} \tag{B.15}$$

which has also been written in Eq.(7.22) and represents the solution of the modal problem dealt within this appendix. It is worth observing that the initial values η_{i0} and η'_{i0} are not known at this stage. Nonetheless, they can be obtained by imposing further conditions on the initial displacements and velocities of the masses, after considering the transformation from modal to physical coordinates written in Eq.(5.11). This is done in Sections 7.2.3 and 7.2.4.

If I have seen further, it is by standing on the shoulders of giants.

— Sir Isaac Newton

Bibliography

[1] Berman, A.D., Ducker, W.A., Israelachvili, J.N.: Experimental and theoretical investigations of stick-slip friction mechanisms. In: Persson, B.N.J., Tosatti E.: Physics of Sliding Friction. NATO ASI Series (Series E: Applied Sciences), vol. 311. Springer, Dordrecht (1996)

[2] Brake, M.R.W.: The mechanics of jointed structures. Springer, Houston, TX (2018)

[3] Ferri, A.A.: Friction damping and isolation systems. Trans. Am. Soc. Mech. Eng. **117**, 196-206 (1995)

[4] Ibrahim, R.A., Friction-induced vibration, chatter, squeal, and chaos. Part II: Dynamics and modeling. **47**(7), 227-253 (1994)

[5] Gagnon L., Morandini M. and Ghiringhelli G.. A review of friction damping modeling and testing. Arch. Appl. Mech. **90**, 107-126 (2020)

[6] Colajanni, P., Papia, M.: Seismic response of braced frames with and without friction dampers. Eng. Struct. **17**, 129–140 (1995)

[7] Pisal, A.Y., Jangid, R.S.: Dynamic response of structure with tuned mass friction damper. Int. J. Adv. Struct. Eng. **8**, 363-377 (2016)

[8] Griffin, J.H.: Friction damping of resonant stresses in gas turbine engine airfoils. ASME J. Eng. Power **102**, 329-333 (1980)

[9] Guglielmino, E., Edge, K.A.: A controlled friction damper for vehicle applications. Control Eng. Pract. **12**, 431-443 (2004)

[10] Lyu, D., Zhang, Q., Lyu, K., Liu, J., Li, Y.: Influence of the dry friction suspension system characteristics on the stick-slip of vertical vibration of a three-piece bogie. Shock Vib., 8868996 (2021).

[11] Qian, H.P., De Schutter, J.: The role of damping and low pass filtering in the stability of discrete time implemented robot force control. In: Proc. IEEE ICRA **2**, 1368-1373 (1992)

[12] Biglari, H., Golmohammadi1, M., Hayati1, S., Hemmati, S.: Vibration reduction of a flexible robot link using a frictional damper. J. Vib. Control **27**, 985-997 (2020)

[13] Green, P.L., Worden, K., Sims, N.D.: On the identification and modelling of friction in a randomly excited energy harvester. J. Sound Vib. **332**(19), 4696-4708 (2013)

[14] Thein, C.K., Foong, F.M., Shu, Y.-C.: Spring amplification and dynamic friction modelling of a 2DOF/2SDOF system in an electromagnetic vibration energy harvester – Experiment, simulation, and analytical analysis. Mech. Syst. Signal Process. **132**, 232-252 (2019)

[15] Huang., M., Ochieng, W.Y., Nie, H., Zhang, M.: Main wheel prerotation and ground taxi driven by electric taxi system. J. Aerosp. Eng. **32** (2019)

[16] Chen, S. *et al.*: Parallel load-bearing and damping system design and test for satellite vibration suppression. Appl. Sci. **10**, 1-12 (2020)

[17] Kerschen ,G., Worden, K., Vakakis, A.F., Golinval, J.-C.: Past, present and future of nonlinear system identification in structural dynamics. Mech. Syst. Signal Process. **20**, 505–592 (2006)

[18] Noël, J.P., Kerschen, G.: Nonlinear system identification in structural dynamics: 10 more years of progress. Mech. Syst. Signal Process. **83**, 2-35 (2017)

[19] Yuan, J., Scarpa, F., Titurus, B., Allegri, G., Patsias, S., Rajasekaran, R.: Novel frame model for mistuning analysis of bladed disk systems. ASME J. Vib. Acoust. **139**(3), 031016 (2017)

[20] Feiner, D.M., Griffin, J.: A fundamental model of mistuning for a single family of modes. ASME J. Turbomach. **124**(4), 597-605 (2002)

[21] Den Hartog, J.P.: Forced vibrations with combined viscous and Coulomb damping. Trans. Am. Soc. Mech. Eng. **53**(9), 107-115 (1931)

[22] Hong, H.-K., Liu, C.-S.: Non-sticking oscillation formulae for Coulomb friction under harmonic loading. J. Sound Vib. **244**, 883-898 (2001)

[23] Shaw, S.W.: On the dynamic response of a system with dry friction. J. Sound Vib. **108**, 305-325 (1986)

[24] Craig, R.R., Kurdila, A.J.: Fundamentals of structural dynamics, 302-305. Wiley (2006)

[25] Feeny, B., Guran, A., Hinrichs, N., Popp, K.: A historical review on dry friction and stick-slip phenomena. ASME. Appl. Mech. Rev. **51**(5), 321–341 (1998)

[26] Toufine, A., Barrau, J.J., Berthillier M.: Dynamic study of a simplified mechanical system with presence of dry friction. J. Sound Vib. **225**(1), 95-109 (1999)

[27] Jaisee, S., Yue, F., Ooi, Y.H.: A state-of-the-art review on passive friction dampers and their applications. Eng. Struct. **235**, 1-22 (2021)

[28] Levitan, E.S.: Forced oscillation of a spring-mass system having combined Coulomb and viscous damping. J. Acoust. Soc. Am. **32**, 1265-1269. (1960)

[29] Rao, S.S.: Mechanical Vibrations (6th edition), 320-322. Reading, Mass: Addison-Wesley (1993).

[30] Jacobsen., L.S.: Steady forced vibration as influenced by damping: an approximate solution of the steady forced vibration of a system of one degree of freedom under the influence of various types of damping. Trans. Am. Soc. Mech. Eng. **52**, 169-181 (1930)

[31] Marui, E., Kato, S.: Forced vibration of a base-excited single-degree-of-freedom system with Coulomb friction. Trans. Am. Soc. Mech. Eng. **106**, 280-285 (1984)

[32] Pitenis, A.A., Dowson, D., Gregory Sawyer, W.: Leonardo da Vinci's friction experiments: an old story acknowledged and repeated. Tribol. Lett. **56**(3), 509-515 (2014)

[33] Popova, E., Popov, V.L.: The research works of Coulomb and Amontons and generalized laws of friction. Friction **3**, 183-190 (2015).

[34] Euler, L.: Sur le frottement des corps solides. Mémoires de l'académie des sciences de Berlin, Volume 4, pp. 122-133 (1750)

[35] Segner, J.A.: De adfrictu solidorum in motu constitatorum. Thesis, Paris (1758)

[36] Tijani Ismaila, B., Salami, M.J E., Akmeliawati, R., Alfaro, H.M. Artificial intelligent based friction modelling and compensation in motion control system. INTECH Open Access Publisher (2011)

[37] Awrejcewicz, J., Olejnik, P.: Analysis of dynamic systems with various friction laws. Appl. Mech. Rev. **58**, 389-411 (2005)

[38] Woydt, M., Wäsche, R.: The history of the Stribeck curve and ball bearing steels: The role of Adolf Martens. Wear **268**, 1542–1546 (2010)

[39] Stribeck, R.: Kugellager für beliebige Belastungen (Ball Bearings for any Stress), Zeitschrift des Vereins Deutscher Ingenieure **45** (1901)

[40] Stribeck, R.: Die wesentlichen Eigenschaften der Gleit- und Rollenlager (Characteristics of Plain and Roller Bearings), Zeit. des VDI **46** (1902)

[41] Pennestri, E., Rossi, V., Salvini, P., Valentini, P.P.: Review and comparison of dry friction force models. Nonlinear Dyn. **83**, 1785-1801 (2016)

[42] Qi, Z., Xu, Y., Luo, X., Yao, S.: Recursive formulations for multibody systems with frictional joints based on the interaction between bodies. Multibody Syst. Dyn. **24**, 133-166 (2010)

[43] Threlfall, D.: The inclusion of Coulomb friction in mechanisms programs with particular reference to DRAM. Mech. Mach. Theory **13**(4), 475-483 (1978)

[44] Duan, C., Singh, R.: Dynamics of a 3DOF torsional system with a dry friction controlled path. J. Sound Vib. **289**, 657-688 (2006)

[45] Mostaghel, N.: A non-standard analysis approach to systems involving friction. J. Sound Vib. **284**, 583-595 (2005)

[46] Wang, D., Rui, Y.: Simulation of the stick–slip friction between steering shafts using ADAMS. International ADAMS User Conference, 1-11 (2000)

[47] Karnopp, D.: Computer simulation of stick slip friction in mechanical dynamic systems. J. Dyn. Syst. Meas. Control **107**, 100-103 (1985)

[48] Armstrong-Helouvry, B.: Frictional lag and stick-slip. In: Proceedings IEEE international conference on robotics and automation (1992)

[49] Åström, K,J., Canudas de Wit, C.: Revisiting the LuGre friction model. IEEE Control Syst. **28**(6), 101-114 (2008)

[50] Dahl, P.R.: Solid friction damping of spacecraft oscillations. AIAA Guidance and Control Conf. 1975-1104 (1975)

[51] Dahl, P.R.: Solid friction damping of mechanical vibrations. AIAA J. **14**(12), 1675-1682 (1976)

[52] Piatkowski, T.: Dahl and LuGre dynamic friction models - the analysis of selected properties. Mech. Mach. Theory **73**, 91-100 (2014)

[53] Canudas de Wit, C., Lischinsky, P.: Adaptive friction compensation with partially known dynamic friction model. Int. J. Adapt. Control Signal Process **11**(1), 65-80 (1997)

[54] Lischinsky, P., Canudas de Wit, C., Morel, G.: Friction compensation for an industrial hydraulic robot. IEEE Control Syst Technol **19**(1), 25-33 (1999)

[55] Shiriaev, A., Robertsson, A., Johansson, R.: Friction compensation for passive systems based on the LuGre model. In Proc. 2nd IFAC Workshop on Lagrangian and Hamiltonian Methods for Nonlinear Control, 183-188 (2003)

[56] Bouc, R.: Forced vibration of mechanical systems with hysteresis. In: Proc. of the 4th Conf. on Non-linear Oscillation (1967)

[57] Wen, Y.-K.: Method for random vibration of hysteretic systems. J. Eng. Mech. Div. **102**, 249-263 (1976)

[58] Dupont, P., Hayward, V., Armstrong, B., Altpeter, F.: Single state elastoplastic friction models. IEEE Trans. Autom. Control **47**(5), 787-792 (2002)

[59] Al-Bender, F., Lampaert, V., Swevers, J.: The generalized Maxwell-slip model: a novel model for friction simulation and compensation. IEEE Trans. Autom. Control **50**(11), 1883-1887 (2005)

[60] Worden, K., Tomlinson, G.R.: Nonlinearity in structural dynamics. Institute of Physics, Bristol, UK (2001)

[61] Caughey, T.K.: Equivalent linearisation techniques. J. Acoust. Soc. Am. **35**, 1706-1711 (1963)

[62] Iwan, W.D.: A generalization of the concept of equivalent linearization. Int. J. Non Linear Mech. **8**, 279–287 (1973)

[63] Den Hartog, J.P.: Forced vibrations with combined viscous and Coulomb damping. Phil. Mag. VII **9**(59), 801–817 (1930)

[64] Hong, H.-K., Liu, C.-S.: Coulomb friction oscillator: modelling and responses to harmonic loads and base excitations. J. Sound Vib. **229**, 1171-1192 (2000)

[65] Papangelo, A., Ciavarella, M.: On the limits of quasi-static analysis for a simple Coulomb frictional oscillator in response to harmonic loads. J. Sound Vib. **339**, 280-289 (2014)

[66] Brake, M.R, Hills, D.A.: Determination of the limits of quasi-static/rigid and dynamic solutions for problems with frictional interfaces. Tribol. Int. **76**, 45-56 (2014)

[67] Natsiavas, S.: Stability of piecewise linear oscillators with viscous and dry friction damping. J. Sound Vib. **217**, 507-522 (1998)

[68] Deimling, K.: Multivalued Differential Equations. de Gruyter Series in Nonlinear Analysis and Applications, Vol.1. Berlin, New York (1992)

[69] Csernak, G., Stepan, G.: On the periodic response of a harmonically excited dry friction oscillator. J. Sound Vib. **295**, 649–658 (2006)

[70] Csernak, G., Stepan, G., Shaw, S.W.: Sub-harmonic resonant solutions of a harmonically excited dry friction oscillator. Nonlinear Dyn. **50**, 93-109 (2007)

[71] Filippov, A.F.: Differential Equations with Discontinuous Righthand Sides. Kluwer Academic Publishers, Dordrecht (1988)

[72] Kowalczyk, P., Di Bernardo, M.: Two-parameter degenerate sliding bifurcations in Filippov systems. Physica D **204**, 204–229 (2005)

[73] Kowalczyk, P., Piiroinen, P.: Two-parameter sliding bifurcations of periodic solutions in a dry-friction oscillator. Physica D **237**, 1053–1073 (2008)

[74] Acary, V., Brogliato, B.: Numerical methods for nonsmooth dynamical systems: applications in mechanics and electronics. Lecture notes in applied and computational mechanics, Vol.35. Springer Verlag, Berlin (2008)

[75] Leine, R., Nijmeijer, H.: Dynamics and bifurcations of non-smooth mechanical aystems. Lecture notes in applied and computational mechanics, Vol.18. Springer, Berlin (2004)

[76] Licsko, G., Csernak, G.: On the chaotic behaviour of a simple dry-friction oscillator. Math. Comput. Simulat. **95**, 55-62 (2013)

[77] Csernak, G., Licsko, G.: Asymmetric and chaotic responses of dry friction oscillators with different static and kinetic coefficients of friction. Meccanica **56**, 2401—2414 (2021)

[78] Sorge, F.: On the frequency behaviour, stability and isolation properties of dry friction oscillators. Meccanica **42**(1), 61-75 (2007)

[79] I. López, J.M. Busturia, H. Nijmeijer Energy dissipation of a friction damper J Sound Vib, 278 (2004), pp. 539-561

[80] Dai, W., Yang, J., Wiercigroch, M.: Vibration energy flow transmission in systems with Coulomb friction. Int. J. Mech. Sci. **214**, 106932 (2022)

[81] Hundal, M.S.: Response of a base excited system with Coulomb and viscous friction. J. Sound Vib. **64**, 371-378 (1979)

[82] Yeh, G.C.K.: Forced vibrations of a two-degree-of-freedom system with combined Coulomb and viscous damping. J. Acoust. Soc. Am. **39**, 1424 (1966)

[83] Pascal, M.: New limit cycles of dry friction oscillators under harmonic load. Nonlinear Dyn. **70**, 1435-1443 (2012)

[84] Pascal, M.: Sticking and nonsticking orbits for a two-degree-of-freedom oscillator excited by dry friction and harmonic loading. Nonlinear Dyn. **77**, 267-276 (2014)

[85] Pascal, M.: Dynamics of coupled oscillators excited by dry friction. ASME J. Comput. Nonlinear Dyn. **3**, 20-26 (2008)

[86] Nayfeh, A.H., Mook, D.T.: Nonlinear oscillations. Wiley-VCH, New York (1995)

[87] Rizvi, A., Smith, C.W., Rajasekaran R., Evans, K.E.: Dynamics of dry friction damping in gas turbines: literature survey. J. Vib. Control **22**, 296-305 (2016)

[88] Sinha, A., Griffin, J.H.: Effects of static friction on the forced response of frictionally damped turbine blades. J. Eng. Power **106**, 65-69 (1984)

[89] Griffin, J.H., Sinha, A.: The interaction between mistuning and friction in the forced response of bladed disk assemblies. J. Eng. Gas Turbines Power **107**, 205-211 (1985)

[90] Dowell, E.H.: The behavior of a linear, damped modal system with a non-linear spring-mass-dry friction damper system attached. J. Sound Vib. **89**, 65-84 (1983)

[91] Ferri, A.A., Dowell, E.H.: The behavior of a linear, damped modal system with a non-linear spring-mass-dry friction damper system attached, part II. J. Sound Vib. **101**(1), 55-74 (1985)

[92] Ferri, A.A., Bindemann, A.C.: Damping and vibration of beams with various types of frictional support conditions. ASME J. Vib. Acoust. **114**(3), 289-296 (1992)

[93] Ferri, A.A., Dowell, E.H.: Frequency domain solutions to multi-degree-of-freedom, dry friction damped systems. J. Sound Vib. **124**, 207-224 (1988)

[94] Petrov, E.P., Ewins, D.J.: Analytical formulation of friction interface elements for analysis of nonlinear multi-harmonic vibrations of bladed disks. J. Turbomach. **125**, 364-371 (2003)

[95] Legrand, M., Roques, S., Pierre, C., Cartraud, P., Peseux B.: n-dimensional harmonic balance method extended to non-explicit nonlinearities. Eur. J. Comp. Mech. **15**, 269-280 (2006)

[96] Lau, S.L., Cheung, Y.K.: Amplitude incremental variational principle for nonlinear vibration of elastic systems. J. Applied Mech. **48**(4), 959-964 (1981)

[97] Dowell, E.H.: Damping in beams and plates due to slipping at the support boundaries. J. Sound Vib. **105**, 243-253 (1986)

[98] Cameron, T.M., Griffin, J.H.: An alternating frequency/time domain method for calculating the steady-state response of nonlinear dynamic systems. J. Applied Mech. **56**, 149-154 (1989)

[99] Thomsen, J.J., Fidlin, A.: Analytical approximations for stick–slip vibration amplitudes. Int. J. Nonlinear Mech. **38**(3), 389-403 (2003)

[100] Bryne, G.D., Hindmarsh, A.C.: Stiff ODE solvers: A review of current and coming attractions. J. Comp. Phys. **70**(1), 1-62 (1987)

[101] Moreau, J.J. Unilateral contact and dry friction in finite freedom dynamics. In: Moreau J.J., Panagiotopoulos P.D.: Nonsmooth Mechanics and Applications, vol. 302, pp. 1–82. Springer Verlag, Wien-New York (1988)

[102] Jean, M.: The non smooth contact dynamics method. Comput. Methods Appl. Mech. Eng. **177**, 235–257 (1999)

[103] Acary, V.: Projected event-capturing time-stepping schemes for nonsmooth mechanical systems with unilateral contact and Coulomb's friction. Comput. Methods Appl. Mech. Eng. **256**, 224-250 (2013)

[104] Ferri, A.A., Heck, B.S.: Vibration analysis of dry friction damped turbine blades using singular perturbation theory. In: Proc. ASME Int. Mech. Eng. Congress Expo. **192**, 47-56 (1994)

[105] Klepp, H.J.: Steady-state and irregular motions of a system with friction under harmonic excitation. Mech. Struct. Mach. **19**(3), 327-356, (1991)

[106] Pfeiffer, F., Hajek, M.: Stick-slip motion of turbine blade dampers. Philos. Trans. R. Soc. Lond. **338**, 503-517 (1992)

[107] Pfeiffer, F.: Complementarity problems of stick-slip vibration. In: Proc. ASME 14th Biennial Conf. Mech. Vib. Noise **56**, 43-50 (1993)

[108] Ahn, Y.J., Barber, J.: Response of frictional receding contact problems to cyclic loading. Int. J. Mech. Sci. **50**, 1519–1525 (2008)

[109] Barber, J.R.: Frictional systems subjected to oscillating loads. Ann. Solid Struct. Mech. **2**, 45-55 (2011)

[110] Barber, J., Wang, X.: Numerical algorithms for two-dimensional dynamic frictional problems. Tribol. Int. **80**, 141–146 (2014)

[111] Allgower, E.L., Georg, K.: Numerical continuation methods: an introduction. Springer Verlag, Berlin, Heidelberg (1990)

[112] Bernardo, M., Budd, C., Champneys, A.R., Kowalczyk, P.: Piecewise-smooth dynamical systems—theory and applications. Applied mathematical sciences, vol. 163. Springer Verlag, London (2008)

[113] Arnoux, J.J., Sutter, G., List, G., Molinari, A.: Friction experiments for dynamical coefficient measurement. Adv. Tribol., 613581, (2011)

[114] Kelemenová, T. *et al*: Specific problems in measurement of coefficient of friction using variable incidence tribometer. Symmetry **12**(8), 1235 (2020)

[115] Dickey, R.D.I., Jackson, R., Flowers, G.T.: Measurements of the static friction coefficient between tin surfaces and comparison to a theoretical model. J. Tribol. **133**(3), 031408 (2011)

[116] Liu, Y., Jiang, H., Pavlovskaia, E., Wiercigroch, M.: Experimental investigation of the vibro-impact capsule system. Nonlinear Dyn. **83**(1), 1029-1041 (2016)

[117] Canudas de Wit, C., Lischinsky, P.: Adaptive friction compensation with partially known dynamic friction model. Int. J. Adapt. Control Signal Process. **11**, 65–80 (1997)

[118] Liu, L.L., Wu, Z.Y.: A new identification method of the Stribeck friction model based on limit cycles. J. Mech. Eng. Science **228**(15), 2678-2683 (2014)

[119] Cabboi, A., Putelat, T., Woodhouse, J.: The frequency response of dynamic friction: enhanced rate-and-state models. J. Mech. Phys. Solids **92**, 210-236 (2016)

[120] Rizos, D., Fassois, S.: Friction identification based upon the LuGre and Maxwell slip models. IEEE Trans. Control Syst. Technol. **17**(1), 153-160 (2009)

[121] Boegli, M., Laet, T.D., Schutter, J.D., Swevers, J.: A smoothed GMS friction model suited for gradient-based friction state and parameter estimation. IEEE/ASME Trans. Mech. **1**9(5), 1593-1602 (2014)

[122] Worden, K., Barthorpe, R.J., Cross, E.J., Dervilis, N., Holmes, G.R., Mnson, G., Rogers, T.J.: On evolutionary system identification with applications to nonlinear benchmarks. Mech. Syst. Signal Pr. **112**, 194-232 (2018).

[123] Liu, Y.F., Li, J., Zhang, Z.M., Hu, X.H., Zhang, W.J.: Experimental comparison of five friction models on the same test-bed of the micro stick-slip motion system. Mech. Sci. **6**(1), 15–28 (2015)

[124] Cabboi, A., Woodhouse, J.: Validation of a constitutive law for friction-induced vibration under different wear conditions. Wear **396**, 107-125 (2018)

[125] Ferretti G., *et al*: Friction model validation in sliding and presliding regimes with high resolution encoders. Exp. Robot. VIII **5**, 328-337 (2003)

[126] Jacobsen, L.S.: An approximate solutions of the steady forced vibration of a system of one degree of freedom under the influence of various types of damping. Bull. Seismol. Soc. Am. **20**(3), 196-223 (1930)

[127] Jacobsen, L.S., Ayre, R.S.: Engineering vibrations. McGraw-Hill, NY (1958)

[128] Watari, A.: Kikai-rikigaku. Kyouritsu publisher (1969)

[129] Feeny, B.F., Liang,J.-W.: A decrement method for the simultaneous estimation of Coulomb and viscous friction. J. Sound Vib. **195**, 149-154 (1996)

[130] Liang,J.-W., Feeny, B.F.: Identifying Coulomb and viscous friction from free-vibration decrements. Nonlinear Dyn. **16**, 337–347 (1998)

[131] Tomlinson, G.R., Hibbert, J.H.: Identification of the dynamic characteristics of a structure with Coulomb friction. J. Sound Vib. **64**, 233–242 (1979)

[132] Tomlinson, G.R.: An analysis of the distortion effects of Coulomb damping on the vector plots of lightly damped system. J. Sound Vib. **71**, 443–451 (1980)

[133] Chen, Q.,Tomlinson, G.R.: Parametric identification of systems with dry friction and nonlinear stiffness using a time series model. ASME J. Vibr. Acoust. **118**, 252–263 (1996)

[134] Iourtchenko, D.V., Dimentberg, M.F.: In-service identification of nonlinear damping from measured random vibration. J. Sound Vib. **255**, 549–554 (2002)

[135] Yao, G. Z., Meng, G., Fang, T.: Parameter estimation and damping performance of electro-rheological dampers. J. Sound Vib. **204**, 575-584 (1997)

[136] Liang, J., Feeny, B.F.: Identifying Coulomb and viscous friction in forced dual-damped oscillators. ASME. J. Vib. Acoust. **126**(1), 118–125 (2004)

[137] Wang S., Woodhouse, J.: The frequency response of dynamic friction: a new view of sliding interfaces. J. Mech. Phys. Solids **59**, 1020-1036 (2011)

[138] Woodhouse, J., Wang S.: The frequency response of dynamic friction: model comparisons. J. Mech. Phys. Solids **59**, 2294-2306 (2011)

[139] Marino, L., Cicirello, A., Hills, D.A.: Displacement transmissibility of a Coulomb friction oscillator subject to joined base-wall motion. Nonlinear Dyn. **98**, 2595-2612 (2019)

[140] Sonin, A.A: A generalization of the π-theorem and dimensional analysis. In: Proc. Natl. Acad. Sci. **101**(23), 8525-8526 (2004)

[141] MATLAB Release 2019a, The MathWorks, Inc., Natick, MA, US.

[142] Sun, D., Liao, R.: Damping prediction technique of the bolted joint structure considering pretension force. Open J. Civ. Eng. **9**, 622-626 (2015)

[143] Inman, D.J.: Engineering Vibration 4th edition. Pearson Education, London (2014)

[144] Micro-epsilon: optoNCDT 1420. https://www.micro-epsilon.com/download/manuals/man–optoNCDT-1420–en.pdf

[145] Brandt, A.: Noise and Vibration Analysis: Signal analysis and experimental procedures. Wiley, Hoboken (2011)

[146] Scholl, M., Tiesler, B., Müller, G.: Statistical evaluation of experimental and numerical data of stick–slip effects in harmonically excited systems. J. Sound Vib., 116536 (2021)

[147] Marino, L., Cicirello, A.: Multi-degree-of-freedom systems with a Coulomb friction contact: analytical boundaries of motion regimes. Nonlinear Dyn. **104**, 35–63 (2021)

[148] Marino, L., Cicirello, A.: Dynamic response of multi-degree-of-freedom systems with a Coulomb friction contact under harmonic excitation. Nonlinear Dyn. **106**, 1675–1709 (2021)

[149] Ormondroyd, J., Den Hartog, J.P.: The theory of the dynamic vibration absorber. ASME J. Appl. Mech. **50**, 9-22 (1928)

[150] Warburton, G.B., Ayorinde, E.O.: Optimum absorber parameters for simple systems. Earthq. Eng. Struct. Dyn. **8**, 197-217 (1980)

[151] Ozer, M.B., Royston, T.J.: Extending Den Hartog's vibration absorber technique to multi-degree-of-freedom systems. ASME J. Vib. Acoust. **127**, 341-350 (2005)

[152] Hurel, J., Mandow, A., García-Cerezo,A.: Kinematic and dynamic analysis of the McPherson suspension with a planar quarter-car model. Vehicle Syst. Dyn. **51**, 1422-1437 (2013)

[153] Nie, S., Zhuang, Y., Chen, F., Xie, J.: Invariant points of semi-active suspensions. Adv. Mech. Eng. **10**, 1-14 (2018)

[154] Den Hartog, J.P.: Mechanical Vibration (Chap. 3). McGraw Hill, NY (1934)

[155] Adhikari, S.: Damping modelling using generalized proportional damping. J. Sound Vib. **293**(1), 156-170 (2006)

[156] Caughey, T.K., O'Kelly, M.E.J.: Classical normal modes in damped linear dynamic systems. J. Applied Mech. **27**, 269-271 (1960)

[157] Caughey, T.K., O'Kelly, M.E.J.: Classical normal modes in damped linear dynamic systems. J. Applied Mech. **32**(3), 583-588 (1965)